AAAS

Science

21 AUGUST 2025

The neglected disease that plagues 190 million women
p. 771

Light pollution alters songbird activity
p. 818

More people exposed to wildfire globally
p. 826

RIPPLE BUGS
FAN OUT

Rapid automatic deployment of flat-ribbon fans enables agile motion on a water surface **pp. 779 & 811**

Science AAAS

TIANQIAO & CHRISSY CHEN INSTITUTE

CO-HOST

ETH zürich

AI & MENTAL HEALTH

SEPTEMBER 8–9, 2025 | ZURICH

Mental health is a vast and growing worldwide problem. In addition to the suffering experienced by individuals and their affected family members it also has an enormous economic impact. Because it can affect people at a young age they will often need treatment for many years and during that period they will not be able to participate to their full potential in society.

REGISTER TODAY!

CONTENTS

21 AUGUST 2025 | VOLUME 389 | ISSUE 6762

762

Along Alaska's Yukon River, scientists are probing why Chinook salmon runs have plummeted in recent years.

PHOTO: NATHAN HOWARD/AP

EDITORIAL

NEWS

FEATURES

COMMENTARY

PERSPECTIVES

POLICY FORUM

BOOKS ET AL.

LETTERS

REVIEWS

REVIEW SUMMARY

RESEARCH

HIGHLIGHTS

RESEARCH SUMMARIES

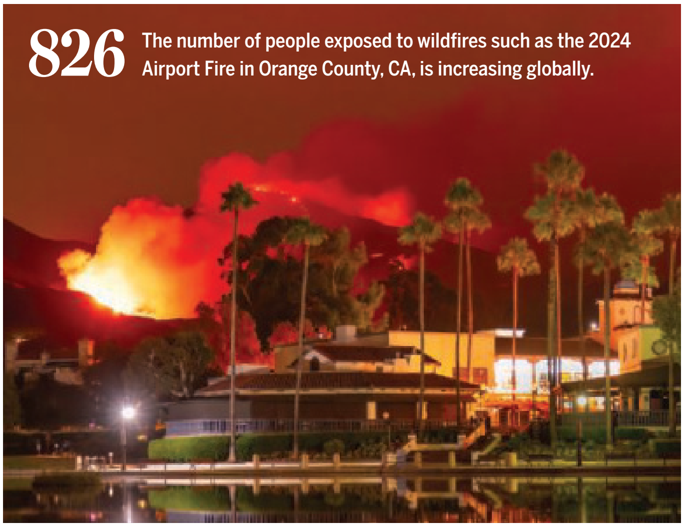

826 The number of people exposed to wildfires such as the 2024 Airport Fire in Orange County, CA, is increasing globally.

RESEARCH ARTICLES

ON THE COVER

Science
RIPPLE BUGS
FAN OUT

A ripple bug gliding on water spreads one of its winglike fan propulsors to execute a rapid turn. The fan's ribbon-shaped microarchitecture passively opens and closes, providing rigidity for propulsion and flexibility for collapse with minimal energy expenditure. These distinctive features were replicated in a bioinspired insect-scale robot with self-morphing fans. See pages 779 and 811. Photo: Víctor M. Ortega-Jiménez/Ornithopterus Lab

ON THE PODCAST

New insights into endometriosis, and mapping dengue in Latin America

WORKING LIFE

PHOTO: AMIR AGHAKOUCHAK

Science serves as a forum for discussion of important issues related to the advancement of science by publishing material on which a consensus has been reached as well as including the presentation of minority or conflicting points of view. Accordingly, all articles published in *Science*—including editorials, news, commentary, and book reviews—are signed and reflect the individual views of the authors and not official points of view adopted by AAAS or the institutions with which the authors are affiliated. *Science* (ISSN 0036-8075) is published weekly on Thursday, except last week in December, by the American Association for the Advancement of Science, 1200 New York Avenue, NW, Washington, DC 20005. Periodicals mail postage (publication No. 484460) paid at Washington, DC, and additional mailing offices. Copyright © 2025 by the American Association for the Advancement of Science. The title *Science* is a registered trademark of the AAAS. Domestic individual membership, including subscription (12 months): $165 ($74 allocated to subscription). Domestic institutional subscription (51 issues): $2865; Foreign postage extra: Air assist delivery: $135. First class, airmail, student, and emeritus rates on request. Canadian rates with GST available upon request, GST #125488122. Publications Mail Agreement Number 1069624. **Printed in the U.S.A. Change of address:** Allow 4 weeks, giving old and new addresses and 8-digit account number. **Postmaster:** Send change of address to AAAS, P.O. Box 96178, Washington, DC 20090–6178. **Single-copy sales:** $15 each plus shipping and handling available from backissues.science.org; bulk rate on request. **Authorization to reproduce** material for internal or personal use under circumstances not falling within the fair use provisions of the Copyright Act can be obtained through the Copyright Clearance Center (CCC), www.copyright.com. The identification code for *Science* is 0036-8075. *Science* is indexed in the *Reader's Guide to Periodical Literature* and in several specialized indexes.

Rewiring science diplomacy

Vaughan C. Turekian and **Peter Gluckman**

Over the past two decades, science diplomacy has been cast in a glow of hopeful optimism, especially by academics. It was framed as the art of bridge building, opening channels between adversaries, a common language across cultures, and a refuge for dialogue in times of political rupture. This aspirational model helped connect scientists across geopolitical divides, built trust, and was a cornerstone of post–Cold War internationalism. In recent years, these ideals have become increasingly affected by the pull of geopolitics. As multilateralism falters and geopolitical rivalries intensify, nations are putting greater emphasis on science and technology as strategic assets. For science diplomacy to remain relevant in this era, it must develop a new mode of engagement—transactional science diplomacy.

Whereas the aspirational model emphasized curiosity and relationship building, its successor, the pragmatic mode, concentrated on shared problem-solving. Of late, there has been a shift to a transactional model, which takes on a more business-like approach with a focus on dealmaking, and near-term returns for the players within broader national strategy. Science's value now is seen as not just a tool of cooperation but also as a currency of negotiation. Agreements are contingent, driven by near-term benefit, and increasingly aimed at advancing national interests.

> **Science's value now is… as a currency of negotiation.**

Consider the conditionality of technology transfer agreements, where access to critical research infrastructure or intellectual property may depend on regulatory concessions, political alignment, or market access guarantees. Countries may trade genomic data for vaccine doses or offer collaboration on artificial intelligence research only in exchange for policy alignment. Scientific cooperation becomes a calculated exchange—often asymmetrical, narrowly scoped, and susceptible to disruption.

This transformation reflects broader shifts. The US CHIPS and Science Act, the European Union's technological sovereignty agenda, and China's state-led innovation strategy all underscore this trend. National science systems are being rewired not only to deliver innovation but to protect and project power.

For all the opportunities this change may bring, there are also substantial risks. It might unlock cost sharing on big-ticket research and development, accelerate collaboration in domains determined as national policy priorities (like semiconductors and synthetic biology), and actively attract private-sector engagement. It also encourages results-focused partnerships. However, transactionalism can erode the scientific commons. When science is seen as a bargaining chip rather than a public good, its legitimacy can be undermined. It also risks entrenching power imbalances. High-income countries may dictate terms that exclude or exploit lower-income partners, particularly in the Global South. And it is focused on only the short term, favoring measurable outputs over enduring partnerships and disincentivizing basic science not tied to immediate gains. It risks shifting the emphasis from issues of the global commons to those more narrowly aligned only with national self-interest. A diplomatic challenge is to develop approaches that act on these risks and their interdependence. Yet transactional diplomacy is not inherently malign. It is a logical, even necessary, response to a more fragmented world where national interests resonate with policy-makers and portions of the public whose taxes fund research. The challenge is to integrate it into a strategic framework.

Today, effective science diplomacy requires a new framework—a trimodal model for science diplomacy that is aspirational, pragmatic, and transactional—leveraging the distinct logics and strengths of each approach. Aspirational diplomacy builds empathy and long-term trust. Pragmatic diplomacy reinforces institutions and solves shared problems. Transactional diplomacy delivers immediate, nationally aligned outcomes.

This is not the first time the style of science diplomacy has changed. The aspirational model gave way to pragmatic diplomacy that reinforces institutions committed to science diplomacy and solves shared problems. Over the past year, diplomacy has started yielding to quid pro quo relationships. But these approaches are not mutually exclusive. Indeed, their integration is essential. Technology diplomacy, for instance, may begin with a transactional agreement—access to quantum research labs in exchange for regulatory alignment—but can evolve into pragmatic infrastructure building or more idealistic collaboration over time. Recognizing which approach is appropriate, and how to move between them, should be central to policy design, the defining role of the science diplomat.

With blurring boundaries between science, policy, and diplomacy, fluency across all three domains will be a prerequisite. A new generation of science diplomats must be trained not only in negotiation and dealmaking but in the ethics of exchange, the value of open science, and the mechanics of multilateral engagement.

The growth of transactional science diplomacy need not mean the end of trust-based collaboration or the fragmentation of scientific cooperation. If managed carefully, it can coexist with and even reinforce other forms of diplomacy. □

Vaughan C. Turekian* is the executive director of Policy and Global Affairs at the US National Academies of Sciences, Engineering and Medicine (NASEM), Washington, DC, USA. vturekian@nas.edu **Sir Peter Gluckman*** is director of the Koi Tū: Centre for Informed Futures, Auckland New Zealand and president of the International Science Council. peter.gluckman@informedfutures.org *Views expressed here do not necessarily reflect those of NASEM or the International Science Council.

10.1126/science.aeb4815

Nadia Barcelona feeds parasite-tainted salmon flesh to juvenile Chinook salmon as part of a study on how fish infections develop under different water temperatures.

NEWS

CONSERVATION BIOLOGY

As salmon in Alaska plummet, scientists suspect a parasite

Chinook in the Yukon River appear to be particularly vulnerable—and warming waters may be abetting the infection

WARREN CORNWALL, in Seattle

When Nadia Barcelona releases a spoonful of orange-colored flesh into the tank, finger-length salmon swarm like little sharks. "You can really see them going crazy," the Alaska Pacific University master's student says.

These juvenile fish at the U.S. Geological Survey's (USGS's) fisheries laboratory here don't realize this is a deadly treat, containing a single-celled fish parasite called *Ichthyophonus*. The meat came from parasite-ridden Chinook salmon pulled from Alaska's Yukon River, where salmon numbers have plummeted in recent years—and *Ichthyophonus* infections, together with rising temperatures, are a prime suspect.

In the coming weeks, the parasite will spread throughout the fish's bodies. White nodules resembling tiny flakes of salt will form on their hearts, disrupting their ability to beat properly. Muscle tissue will wither. Eventually, some will die from the infection.

Barcelona hopes this gruesome fate will help answer crucial questions about what's led to dwindling runs of Yukon Chinook salmon, once a mainstay for communities along North America's fifth largest river system, and how to manage them going forward. Salmon runs have fallen across much of western Alaska, but the Yukon Chinook are hardest hit. The fish are so depleted that Alaskan and Canadian officials last year agreed to a first-ever, 7-year ban on nearly all fishing for Chinook in the river and its tributaries, a Texas-size watershed spanning both countries.

Pinpointing the causes of the decline is "a big egg to crack," says Zachary Liller, a fisheries biologist overseeing commercial fisheries research in western Alaska for the state's Department of Fish and Game (ADFG), which is collaborating with Barcelona. "But if we're successful, it has the potential to be really powerful for the region."

Forty years ago, an average of 375,000 fish returned to the river each year. After falling gradually in the 2010s, returns began to plummet in 2020, down to an average of 44,000 over the past 3 years. Higher water temperatures in both the river and the Bering Sea, where the fish mature, are one likely cause. A record-setting marine heat wave struck the Bering Sea in 2018 and '19. That year, drought and heat drove water temperatures in the Yukon as high as 22°C, well above the 18°C threshold for Chinook to begin suffering heat stress.

Heat revs up fish metabolism, making them hungrier and more likely to starve. Scientists suspect it could also suppress their immune systems, making them more vulnerable to infections. At extremes, high temperatures can exhaust or kill them outright. "The biggest signal we get from [the fish runs] is it's just too warm," USGS aquatic ecologist Vanessa von Biela says.

Ichthyophonus may be compounding the woes. The parasite is

PHOTO: W. CORNWALL/*SCIENCE*

widespread in marine fish around the world, including halibut, herring, and mackerel. It was first noticed in Yukon Chinook in the 1980s, when fishers reported the flesh of infected fish smelled "fruity" and didn't dry properly. In the late 1990s and early 2000s, during a large outbreak, federal and university researchers warned of signs that infected female Chinook were disappearing before reaching spawning grounds. However, state fisheries scientists declared the disease wasn't interfering with overall spawning success.

Richard Kocan, a retired University of Washington microbiologist who led much of the early research, suspects managers did not want to curtail commercial fishing. "There was a really strong effort to not make anything look controversial about Yukon River Chinook salmon, because it was a very lucrative industry," Kocan says.

Infections subsided before resurging in 2020. Now, Liller says he and other state scientists recognize the threat. How much the parasite is harming the run's overall health is still unclear, he says, but "if the fish come back with a heavy enough disease burden, they can die before they reach the spawning grounds." One smoking gun: In 2023 and '24, federal and state scientists found that about three times as many fish had severe infections early in their migration than near spawning grounds upstream, suggesting many of the sickest fish died en route.

Geography and genetics may make the parasite unusually lethal for Yukon Chinook. The fish travel upstream as much as 2700 kilometers in a journey that can last longer than a month, giving the disease more time to spread as their immune system naturally shuts down ahead of spawning, says Jayde Ferguson, a fish pathologist for ADFG.

Experiments have also shown Chinook from the Yukon are more likely to die from the parasite than Chinook from other rivers, including farther south in Alaska. "There's something unique to these Yukon fish that's making them more susceptible," says Paul Hershberger, a disease ecologist at the USGS Western Fisheries Research Center here who first studied the disease in the Yukon in the early 2000s.

In collaboration with Hershberger and the USGS Seattle lab, Barcelona aims to figure out whether high water temperatures also worsen infections. After being fed infected salmon flesh for 10 days, the nearly 1500 juveniles—Yukon stock grown in a hatchery from eggs and sperm harvested from wild salmon—are placed into tanks kept at temperatures ranging from cool (15°C) to abnormally warm (21°C).

"Our hypothesis is that the temperature is the major driver," Hershberger explains over the hum of pumps and gurgle of water at the lab. "When the disease is at its worst, we have really warm temperatures."

There's no prospect of a treatment or cure. But Hershberger hopes the results could inform a new population model that would enable managers to predict, based partly on disease monitoring and temperature data, how many fish are infected, how severe those infections will become, and whether there will be enough fish to allow harvest without harming the population. He hopes the new model could be usable as soon as 2 years from now.

For Indigenous communities along the river, answers can't come soon enough. The decline of salmon runs has been a profound loss, says Rita Painter, an elder in Nulato, a tribal village of fewer than 250 people on the Yukon some 770 kilometers from its mouth. As a child and a young parent, she recalls spending summers at a fish camp where adults would pass along to the next generation knowledge of how to catch and prepare the fish. Those camps have largely vanished. "It seems like today we're lost because we're not teaching our children and we don't have the fish," she says.

Community members in late July held a weeklong educational fish camp for teenagers, to help keep knowledge alive. They received a special permit to put a net in the river for one night and caught three Chinook, or *Ggaal*, as the fish are known in the local Denaakk'e language, as well as chum salmon and whitefish. "We were lucky," says Jasmine Olson, natural resources coordinator for the Nulato Tribal Council.

She also noticed a white, dull quality to the flesh of the Chinook. She hadn't heard of *Ichthyophonus* before, but when she looked it up the description was a match. "That's the first time I've ever seen it," she says. □

TRUMP TRACKER

NIH CHIEF ORDERS NEW REVIEW National Institutes of Health (NIH) Director Jayanta "Jay" Bhattacharya last week released a widely anticipated list of a dozen research priorities as part of "a unified strategy" for his agency. The list spans familiar topics ranging from autism to health disparities. But Bhattacharya sparked concern by ordering a new internal review of the agency's entire funding portfolio. Some scientists worry that effort will further delay NIH's issuing of grant funding. NIH grant officers have already had to scour grants for topics disliked by President Donald Trump's administration, a process that has taken months and helped put NIH at risk of not spending its 2025 budget before the end of the fiscal year. —Jocelyn Kaiser

NSF RESTORES UCLA GRANTS On orders from a federal judge, the National Science Foundation (NSF) last week reinstated 300 grants to the University of California, Los Angeles (UCLA). The agency had suspended them 2 weeks earlier after the Department of Justice found UCLA "had engaged in race discrimination [and] antisemitism." In June, after a class action lawsuit by six UC faculty members, U.S. District Court Judge Rita Lin concluded NSF's termination of an unspecified number of UC grants was illegal. On 12 August, Lin agreed with those plaintiffs that NSF had violated her earlier injunction by suspending the new cohort of UCLA grants. At a 26 August hearing, Lin will consider the plaintiffs' request to extend her injunction to terminated UC grants from the departments of Defense and Transportation. —Jeffrey Mervis

VACCINE PANEL REVIVED Health and Human Services (HHS) Secretary Robert F. Kennedy Jr. last week revived a long-dormant panel, the Task Force on Safer Childhood Vaccines, and named the NIH director as its chair. The group was mandated by a 1986 law to work toward fewer and less serious adverse vaccine reactions but was disbanded in 1998. In May, Children's Health Defense, an antivaccine organization founded by Kennedy, sued him, saying HHS was violating the law by leaving the panel defunct. Kennedy said the group will deliver a first report to Congress in 2 years, followed by reports every 2 years thereafter. —Meredith Wadman

IN OTHER NEWS

GLOBAL PLASTIC TREATY STYMIED AGAIN An international effort to cope with rapidly growing plastic pollution has again failed to reach consensus. The United Nations treaty discussions kicked off several years ago (*Science*, 25 February 2022, p. 801). But in December 2024, in what was supposed to be the final session of negotiations, delegates could not come to an agreement. Roughly 100 countries, including the member nations of the European Union, want to ban toxic chemicals in plastics and cap plastic production, which already surpasses 400 million tons annually. Yet several petroleum-producing countries, including the United States and Saudi Arabia, object and are focused instead on recycling and managing waste. Last week, after 11 days of negotiating in Geneva, representatives went home without a treaty or a timeline for when to reconvene. —Erik Stokstad

A SWIFT SOLUTION? NASA's Neil Gehrels Swift Observatory could be in line for a much needed boost. The orbit of this 21-year-old mission to detect gamma ray bursts—powerful explosions in deep space—and monitor their afterglows has long been decaying but recent solar activity has caused the atmosphere to expand, increasing drag and accelerating the process. The spacecraft could re-enter the atmosphere by the end of 2026 unless lifted to a higher orbit. NASA last week tapped two companies—Cambrian Works of Reston, Virginia, and Katalyst Space Technologies of Flagstaff, Arizona—already working in the area of in-orbit refueling and servicing of satellites to investigate whether their robotic technologies can be exploited to elevate Swift. Each will receive $150,000 for concept design studies. "Swift is the go-to mission many of us rely on to follow up and monitor a wide variety of transients," says Dieter Hartmann of Clemson University, former chair of the Swift Users' Group. "It is exciting to think that Swift could be a … workhorse for another decade, or more." —Daniel Clery

UNIVERSITY LANDS MAJOR CANCER GIFT Nike co-founder Phil Knight and Penny Knight, his wife, last week announced a $2 billion donation for cancer care and research to an institute at Oregon Health & Science University. It's the largest single gift to any U.S. university or health center. —*Science* News staff

HUMAN EVOLUTION

Denisovans, Neanderthals gave Indigenous Americans key mucus gene

Genetic variant might have given the first Americans a sticky shield against new germs

PHOTO: THILO PARG/WIKIMEDIA COMMONS

MICHAEL PRICE

Mucus does more than simply rocket out of our noses when we sneeze. The sticky, viscous secretion that coats many organs also forms our innate immune system's first line of defense, helping trap harmful pathogens. This humble stuff varies around the world, and people Indigenous to the Americas often have a specific variant of a key mucus-producing gene known as *MUC19*. Now, scientists have tracked the winding evolutionary path this variant took from its origins in Denisovans—a mysterious ancient human ancestor—to our close cousins the Neanderthals and finally modern humans.

The work, appearing on p. 798, sheds light on how a critical gene moved between different species or subspecies and the evolutionary forces that might have driven its spread. Examples of such genetic borrowing, or introgression, that wind up having a positive impact are scarce in the modern human genome, says Omer Gokcumen, an evolutionary anthropologist at the University at Buffalo and mucus expert who wasn't involved with the new work. *MUC19* "happens to have traveled a rare path" through our distant ancestors, he says.

A classic example of a genetic variant moving from one group of hominins into another and having a lasting impact is *EPAS1*, a gene that flips hundreds of genetic switches that collectively help people survive in low-oxygen environments. This variant, too, originated in Denisovans and today is prevalent in modern people living at high elevations on the Tibetan Plateau and in the South American Andes. The connection was first discovered as part of a broader investigation into potentially introgressed genes in 2014 by Emilia Huerta-Sanchez, a population geneticist at Brown University who also singled out the mucin gene.

Later that work grabbed the attention of Fernando Villanea, a population geneticist at the University of Colorado Boulder. At the time, he was also looking at another study highlighting genes in Indigenous Americans that natural selection seemed to have favored. "What caught my eye is that both papers had identified the same gene, but for different reasons," he says. "So I

A genome sequenced from a Neanderthal jaw found in Siberia contains the same mucus gene variant found in Denisovans and many Indigenous Americans.

started looking at [that gene] closely from both angles."

The gene in question was *MUC19*. It is one of 22 mucin genes that control the type, thickness, and location of mucus production. A repeated stretch of DNA in the gene, 30 base pairs long, influences how sticky the mucus becomes. Different *MUC19* variants found in people around the world contain anywhere from dozens to several hundred of these repeated sequences.

To better understand *MUC19* diversity, Villanea and colleagues, including Huerta-Sanchez, analyzed thousands of genomes from people around the world, including modern Indigenous Americans sampled through the 1000 Genomes Project and the Simons Genome Diversity Project, as well as from ancient Indigenous individuals. They found that Indigenous people were far more likely than other groups to have a version of *MUC19* with hundreds of repeats. In Mexico and Peru, where people have relatively high amounts of Indigenous ancestry, about one in three people have the variant. (Some have upward of 800 of the DNA repeats, making it the longest known protein in the human genome.)

Then, the researchers ran computer models showing it was unlikely for the *MUC19* variant to have become so prevalent in Indigenous Americans purely by chance. Instead, it must have been advantageous to people who began to migrate into the Americas sometime around 20,000 years ago, Villanea notes.

The researchers knew from previous work that the *MUC19* variant originated in Denisovans and suspected it entered modern humans sometime within the past 40,000 years. As they looked at other archaic genomes, however, they were surprised to see the same version in two different Neanderthal specimens: one from Chagyrskaya Cave in Siberia's Altai Mountains dated to about 55,000 years ago, and another from Vindija Cave in northern Croatia, dated to about 40,000 years ago.

The scientists also noticed that in modern people with the borrowed gene, "there's this sort of Oreo cookie of Neanderthal pieces on the outside and a Denisovan core on the inside," Villanea says. The simplest explanation, he says, is that Denisovans passed this gene to Neanderthals, who then passed it to modern humans.

It's not entirely clear what evolutionary advantage this *MUC19* variant provided. The team's best guess is that it helped protect migrants into the Americas from new pathogens they encountered there. That could explain why it became so prevalent in Indigenous groups yet rare elsewhere.

Gokcumen thinks that explanation is "a little murky," but "I would agree that if you have to speculate, immunity is the likely culprit." *MUC19*'s immune system benefits may also explain why the two Neanderthals also carried the variant, Villanea says. "It strikes me as uncanny that two different Neanderthals from two distinct populations … would carry the Denisovan variant," he says. Although researchers don't know which diseases were in play, this particularly sticky mucus might have been just what Neanderthals and Indigenous Americans alike needed to stay healthy as they colonized new lands. □

IN FOCUS

Smallest cat video ever?

In an advance that could one day help build a quantum computer, researchers have animated a cartoon of Schrödinger's cat—the infamous hypothetical feline that's dead and alive at the same time—using 549 rubidium atoms (fluorescing yellow under laser light), rearranged as often as once every 60 milliseconds. Recently, quantum computer developers have harnessed such neutral atoms as qubits, bits of information that represent 0, 1, or a fragile combination of both states. Computing with the atoms, however, requires rapidly moving them without destroying their state. In the feline demo, reported in *Physical Review Letters*, researchers used artificial intelligence to efficiently calculate how best to position the laser "optical tweezer" that moves the atoms. —Nazeefa Ahmed

IMAGE: RIN *ET AL.*, *PHYSICS* (2025)

SOCIAL SCIENCE

Don't blame the algorithms for online polarization

In tests with virtual social media users, echo chambers and extreme voices always emerged **HANNAH RICHTER**

Following the 2024 U.S. presidential election, millions of aggravated X users flocked to Bluesky to avoid the partisan vitriol that had overtaken the older social media platform. Designed without an algorithm to determine what content users see, Bluesky aimed to avoid X's pitfalls. For a while, it seemed to work: Individuals with lots of followers weren't overamplified, nasty language was less common, and misinformation seemed held at bay. But less than a year later, some of social media's typical ills had emerged on Bluesky. Some complain it, too, has become a bit of an echo chamber, albeit a left-leaning one.

Now, simulations with a scaled-down platform populated with virtual users generated by artificial intelligence (AI) may have revealed why social media tends to become so polarized. The simple platform had no nuanced algorithm feeding users posts that would appeal to them and keep them online the longest. Yet it still split into insular communities, researchers report in a preprint posted to arXiv earlier this month. The results suggest that just the basic functions of social media—posting, reposting, and following—inevitably produce polarization. Others caution, however, that cliquishness may have been baked into the AI-generated users.

The study's "central outcomes are compelling," says Kate Starbird, an information scientist at the University of Washington who studies online rumors and was not involved with the work. "There's a lot of things about it that resonate with hypotheses that I and others have had about online systems."

Experiments studying social media with real participants can be expensive and ethically tricky, and they require reluctant social media companies to cooperate. So, Maik Larooij and Petter Törnberg, computational social scientists at the University of Amsterdam, turned to "generative social simulation," a technique that uses chatbot-style AI programs called large language models (LLMs) to stand in for human subjects. They aimed to strip social media down to its bare bones, then build it back up to determine the root of three negative phenomena: the emergence of partisan echo chambers (like following like), the concentration of influence among a few posters (the rich getting richer), and the amplification of extreme voices (the so-called social media prism).

The network consisted of 500 virtual users, each of whom was assigned characteristics such as age, gender, religion, political leaning, and education, based on real personas from national surveys of voters called the American National Election Studies. In three different trials, the researchers used each of three popular LLMs—ChatGPT, Llama, and DeepSeek—to expand the users into more nuanced personas with hobbies and occupations, and then to make decisions based on those profiles. In the experiments, a randomly selected user would face three choices: Choose a news article from 10 random options (out of 210,000) and write a post about it, repost something, or follow another user based on their profile. The user's choices were influenced by their feed, which consisted of 10 posts. Half were from a user's followers and half were popular posts from people the user didn't follow.

> “This was supposed to be the optimistic paper.
>
> **Petter Törnberg**
> University of Amsterdam

The network ran for 10,000 cycles in each test. But no matter which LLM the researchers used, the platform inevitably developed the negative trifecta of echo chambers, concentrated influence, and extreme voices.

"We were expecting that we would have to work very hard in some way to produce this effect," Törnberg says. But instead, "We get this toxic network that is forming as a result of just these basic actions of reposting and following."

To attempt to fix the toxicity, Törnberg and Larooij tested six simple interventions, including displaying posts solely chronologically, instead of based on engagement. They also tested what amounted to anti-algorithms, routines that showed a user the least engaged posts instead of the most engaged ones, or that showed the user posts expressing political views opposite their own. None of the methods worked completely, and some actually increased the nastiness. "I was a bit disappointed, to be honest," Törnberg says. "Because this was supposed to be the optimistic paper."

Starbird sees the model bringing out "a resonance between human nature and the attention dynamics of social media." Even if you take out the algorithm, as Bluesky did, "the system is still wired in such a way that some of those toxicities remain."

Filippo Menczer, a computer scientist at Indiana University, isn't convinced. AI is a "very huge black box," he says. The LLMs are trained on online human behaviors already reflective of social media toxicity, so the model may be "hard-coded" to devolve into polarization. Even more subtle, he says, problematic algorithms already shape the real online behavior used to train the LLMs, so it's conceivable that they indirectly influenced the outcome of the virtual experiment, making it impossible to rule out their importance.

Jennifer Allen, a computational social scientist at New York University, says the caveats can't be ignored but that "there's a lot of potential with what they found." Though there may never be "easy, straightforward solutions" to social media's ills, she thinks individual users could try tamping down polarization by posting more neutral, bipartisan content.

Understanding how online polarization emerges is vital, Starbird emphasizes. "I don't think you can understand politics in this moment without understanding what's happening on social media." □

Hannah Richter is a science journalist in Washington, D.C.

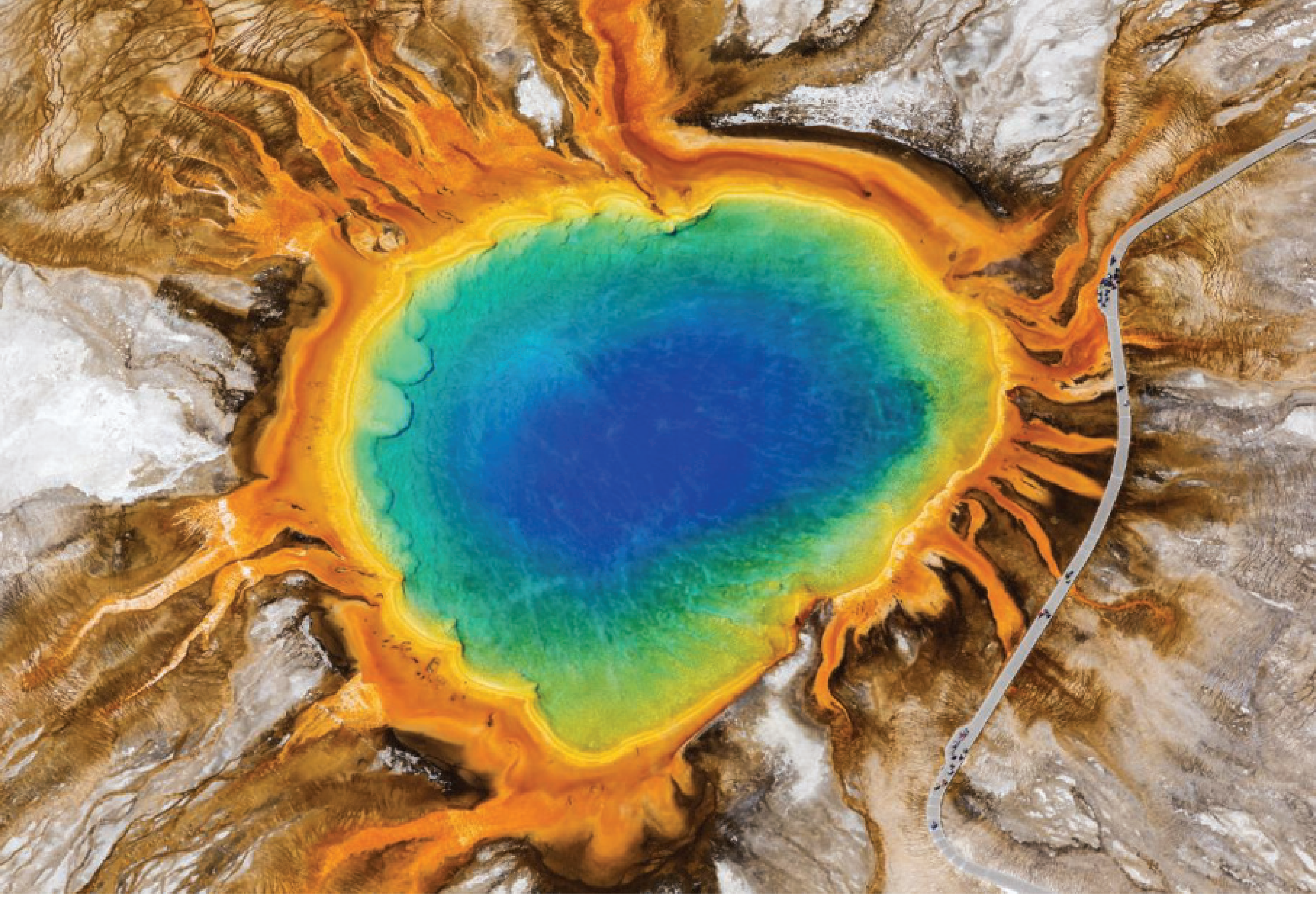

An artificial intelligence screen has identified potential antibiotics in archaea, including in species that thrive in hot springs such as Yellowstone National Park's iconic Grand Prismatic Spring.

PHOTO: PETER ADAMS/AVALON/UNIVERSAL IMAGES GROUP VIA GETTY IMAGES

BIOLOGY

New antibiotics from the third branch of life?

Archaea appear to wield a host of bacteria-killing compounds

ROBERT F. SERVICE

Archaea, microbes that make up the least known branch on the tree of life, are home to a trove of leads for new antibiotics, according to a pair of reports out last week. Renowned for their ability to thrive in extreme environments, such as boiling hot springs and salt flats, archaea also exist alongside bacteria in many environments. Now, two groups suggest that proximity may have prompted hundreds of species of archaea to evolve unique chemical defenses, some of which kill bacteria that can sicken people and are resistant to conventional antibiotics. Although the archaeal compounds remain far from proven medicines, the findings underscore that these microbes may wind up becoming a rich vein for antibiotic explorers to mine.

The papers, published in *Nature Microbiology* and *PLOS Biology*, are "marvelous," says Jim Collins, a bioengineer at the Massachusetts Institute of Technology focused on antibiotic discovery. "I'm surprised we hadn't looked at archaea before."

Most of the best known antibiotics were developed from compounds made by bacteria or fungi. Once thought to be bacteria themselves, archaea are now recognized as a separate domain of life, based on genetic and biochemical differences with bacteria and with eukaryotes, which include fungi and multicellular life. Archaea, for example, do not have the same kind of outer cell wall as bacteria and lack eukaryotes' separate cell nucleus and membrane-bound organelles. Yet, archaea, bacteria, and single-celled eukaryotes all live alongside one another in many environments, such as in the digestive tracts of people, where they help produce methane, and in the hindguts of termites, where they aid in digesting wood. "If they live together in the same niche, chances are they don't always get along," says Tobias Warnecke, a biochemist at the University of Oxford.

To see whether potential conflict has prompted archaea to develop their own antibiotic armamentarium, researchers led by Cesar de la Fuente, a biomolecular engineer at the University of Pennsylvania, trained an artificial intelligence (AI) algorithm to scan their proteomes—the complete amino acid sequence of all an organism's proteins. They searched for protein fragments called encrypted peptides that often have antimicrobial properties and are commonly created when larger proteins are broken down. Scanning the proteomes of 233 archaea species revealed more than 12,600 likely encrypted peptides, de la Fuente and colleagues report in *Nature Microbiology*.

The AI also scored each find for its likelihood of having antimicrobial activity, and de la Fuente's team then synthesized 80 of the most promising peptides. The group found that 93% of these showed antibacterial activity in vitro against dangerous human pathogens such as *Staphylococcus aureus* and *Klebsiella pneumoniae*. Further in vitro studies showed most of these peptides kill bacteria by depolarizing their inner, cytoplasmic membranes.

Collins calls the finding "a very interesting discovery," because the mechanism is very different from that of many known antimicrobial peptides, which more commonly poke holes in bacterial cells' outer membrane. De la Fuente's team showed in mice that one peptide, called archaeasin-73, reduced loads of dangerous wound-infecting bacteria as much as polymyxin B, a last-line antibiotic treatment.

Warnecke and his colleagues came at the antimicrobial hunt in archaea from a different direction. Bacteria, unlike archaea, shroud their cell cytoplasmic membranes with a wall formed from a meshlike assembly of peptides called peptidoglycan. So, they wondered whether archaea harbor peptidoglycan-degrading enzymes called hydrolases to defend themselves against bacterial encroachment on their territory. In *PLOS Biology*, the group reports finding these enzymes in 5% of the more than 3700 archaea species they surveyed.

Studies of the proteins' structure suggest many are secreted outside the cell, and Warnecke's team even uncovered evidence that some archaea have syringelike molecular injectors for delivering these proteins to bacteria. When exposed to bacteria in the lab, some of the hydrolases shredded their peptidoglycan and killed them.

Warnecke and de la Fuente caution that the newly identified enzymes and peptides remain far from actual drugs that could save the lives of patients. Nevertheless, both argue there are almost certainly many more antibiotics in archaea waiting to be discovered. Warnecke says, "This is probably just the tip of the iceberg." □

ASTROPHYSICS

Astronomers set biggest traps ever for messengers from cosmic accelerators

Vast arrays of radio antennas could trace neutrinos back to supernovae and black holes

PHOTO: GRAND

DANIEL CLERY

Neutrinos swarm through the universe like a legion of ghosts. These nearly massless particles are so averse to interacting with other matter that detecting just a few dozen deep-space neutrinos per year has required kilometer-size traps in water or ice. But to capture the rarest neutrinos with the highest energies—messengers from the universe's most powerful particle accelerators—astronomers need something so big they are dubbing their planned facility GRAND.

Last month, at the International Cosmic Ray Conference in Geneva, researchers described initial results from an airport-size detector in China's Gobi Desert that is meant to pave the way for others covering a total area nearly as big as the United Kingdom. The detectors will monitor the air for radio pulses triggered by ultra–high-energy neutrinos whizzing through Earth. "These things are incredibly rare," says astroparticle physicist Naoko Kurahashi Neilson of Drexel University. "If we see one, that's already amazing. If we see one and we know which direction it came from, that's doubly amazing," because it would point back to the powerful cosmic engine that spawned it.

Cosmic rays that bombard Earth with colossal energies already show those accelerators exist. These protons or other small atomic nuclei are believed to come from supernovae, stars being ripped apart by supermassive black holes, or black holes whipping up particles to energies hundreds of times that of the most powerful atom smashers on Earth.

The Giant Radio Array for Neutrino Detection relies on solar-powered radio antennas, deployed in huge numbers across a vast expanse.

But because cosmic rays are charged, magnetic fields in space tug them along twisting paths that can't be traced back to a source. "We still know very little about the origin of ultra–high-energy cosmic rays," says Olga Botner, an astroparticle physicist at Uppsala University. Early in their journey, however, cosmic rays often collide with stray atoms, spawning neutrinos with slightly lower energies that follow straight lines to Earth. "The only way to have almost direct information of what's happening particle-wise inside the sources are neutrinos," says Kumiko Kotera of the Astrophysics Institute of Paris (IAP).

One rare messenger was detected in 2023 by the Cubic Kilometre Neutrino Telescope, a water-based detector at the bottom of the Mediterranean Sea that is still under construction. It spotted a neutrino carrying 220 petaelectronvolts of energy—30 times that of any neutrino previously captured—but wasn't able to trace it back to a source. To catch more of these neutrinos and pinpoint their sources, astronomers need far more than 1 cubic kilometer of water.

> **If we see one and we know which direction it came from, that's doubly amazing.**
>
> **Naoko Kurahashi Neilson**
> Drexel University

GRAND, or the Giant Radio Array for Neutrino Detection, would greatly expand the net. A neutrino skimming through Earth's crust will sometimes hit an atom in the rock and spawn a particle called the tau lepton—like an electron but much more massive. If the collision occurs near the surface, the short-lived tau can emerge into the air and decay, producing a shower of charged particles that generates a radio pulse.

At the cosmic ray conference, the GRAND team, funded with about €2 million from CNRS, France's national research agency, as well as other European institutions and partners in the Chinese Academy of Sciences, said it had installed the first 60 of 300 radio antennas in the Gobi Desert of China's Gansu province. Already, these antennas are detecting telltale radio pulses, although these are sparked not by neutrinos, but by incoming cosmic rays striking air molecules high in the atmosphere.

To capture ultra–high-energy neutrinos, the GRAND team hopes to scale up to two arrays of 10,000 antennas, each covering more than 100 kilometers on a side. Ultimately, they want to build 20 such arrays across the globe. Keeping the detectors—3.5-meter poles with clover leaf–shaped wire antennas and other hardware—as cheap as possible is one challenge. GRAND co-leader Olivier Martineau-Huynh of IAP says mass production could reduce the current cost of €5000 per antenna by a factor of 10.

Another challenge is finding wide-open spaces that are free of radio interference, says Kotera, a GRAND co-leader. "All these areas are either usually national preserves or military regions," she says. "So, one way or the other, you really have to negotiate a lot."

Stephanie Wissel of Pennsylvania State University is working on a more space-efficient approach. She and her colleagues built a tightly packed group of six antennas, known as a phased array, on a mountaintop overlooking a broad valley in California. That prototype, dubbed Beam-forming Elevated Array for Cosmic Neutrinos, is more sensitive to the faint radio signals than GRAND will be, but not as good at tracing neutrino directions. "We're in a position where we would like to get bigger," Wissel says.

In 2023, the two teams worked together to develop a hybrid approach. The result was a proposal for 24 larger phased arrays strung along a ridge in Argentina's San Juan province overlooking a valley floor containing 360 GRAND-style antennas. "It's very exciting because all the pieces are coming together," Kotera says. The European Research Council is considering the €14 million proposal. ☐

ANIMAL RESEARCH

Faced with 'impossible' workload, USDA struggles to oversee lab animal welfare

Shrinking staff and other handicaps threaten enforcement of the Animal Welfare Act

DAVID GRIMM

Employees terrified of being laid off. Shrinking resources combined with unprecedented workloads. The loss of a tool critical to enforcing its mission. Such conditions would strain any organization. But for an already overburdened division of the U.S. Department of Agriculture (USDA) responsible for overseeing the welfare of nearly 800,000 lab animals, they could spell disaster.

In the past several years, the Animal and Plant Health Inspection Service (APHIS) has lost more than one-third of its inspectors, witnessed a doubling in the number of entities it has to oversee, and added an entirely new class of animal to its purview. Now, actions by President Donald Trump's administration threaten to reduce APHIS's workforce even further, and a recent U.S. Supreme Court case has handicapped the agency's ability to punish those who violate the federal Animal Welfare Act, which mandates the humane treatment of animals housed in everything from labs to zoos.

"It's the most challenging time I've ever seen for animal care," says Kevin Shea, a former APHIS administrator who spent more than 4 decades at the agency before retiring in January. If APHIS can't do its job, he says, "animals will suffer."

APHIS has long faced difficult conditions. The organization has a wide range of responsibilities, from regulating genetically engineered crops to managing invasive species. It's also the only federal agency tasked with enforcing the Animal Welfare Act. A small number of inspectors must oversee about 900 research facilities—from universities to private companies—conducting surprise visits at least once a year to ensure that monkeys, rabbits, and other lab animals have proper food, housing, and veterinary care. They also inspect thousands of zoos, breeders, and animal transporters.

Things became more difficult from 2018 to '24, as the number of entities APHIS had to inspect doubled from less than 8000 to more than 17,000—driven largely by a rise in Uber-like services that move animals from, say, breeders to private parties. That same year, USDA lost a lawsuit brought by animal advocacy groups that compelled it to add birds—long excluded from the Animal Welfare Act—to its oversight duties. (Rats and mice are exempt from the act.) The agency must now oversee more than 63,000 research birds, more than dogs and cats combined. "It was a seismic shift," says a current APHIS manager who asked to remain anonymous because they were not authorized to speak to the press.

At the same time, APHIS's workforce is shrinking. In the first few months of this year, the agency lost about a dozen of its inspectors—approximately 15% of its oversight workforce—because of the Trump administration's forced retirements and deferred resignations. It currently only has 77 inspectors—"a ridiculously small number for the job we have to do," the APHIS manager says. "We've given our inspectors an impossible task." The agency is under a hiring freeze, the source notes, so if more inspectors leave, they can't be replaced. In May, the Congressional Research Service warned that "recent efforts to reduce USDA staff may further affect APHIS's ability to carry out its oversight functions."

Trump's proposed budget for the 2026 fiscal year threatens further chaos, with USDA facing billions of dollars in proposed cuts and a massive reorganization, though it's unclear how this will impact APHIS specifically.

APHIS is also grappling with the implications of a Supreme Court decision handed down last year—*SEC* v. *Jarkesy*—which held that federal agencies can't impose civil penalties without jury trials. Animal law experts have interpreted the ruling as prohibiting APHIS from fining violators of the Animal Welfare Act—one of its chief means of enforcement. Indeed, since the court's decision, the agency appears to have only issued a single fine against a research facility. "*Jarkesy* has hamstrung us the most," the APHIS manager says. "We have an inability to do anything, even when we see bad stuff."

Under the Trump administration, federal agencies have moved to phase out animal testing, citing animal welfare as one reason. But at APHIS the administration's antiregulatory push could have the opposite effect. During the president's first term, APHIS inspectors reported far fewer violations than before, and former employees accused the agency of weakening animal welfare guidelines. Shea worries those trends could continue. "I think inspectors will be reluctant to write up anything but the most egregious things," he says. "People will be afraid to do their jobs, at the expense of the animals."

The agency was already under fire for alleged lax enforcement. Audits by USDA's Office of the Inspector General over the years have chastised APHIS for failing to punish violations of the Animal Welfare Act and for not properly investigating repeat offenders. In a recent, high-profile case, the agency faced scathing criticism for taking no action against Envigo—a leading supplier of beagles for biomedical research—despite the documented suffering of thousands of animals at one of its breeding facilities.

> "It's the most challenging time I've ever seen for animal care.
>
> **Kevin Shea**
> formerly of the Animal and Plant Health Inspection Service

"APHIS's current challenges are a recipe for disaster for any agency, even one with the best record of enforcement," says Eric Kleiman, a senior policy adviser at the American Anti-Vivisection Society, an animal rights group. "What we're seeing now is a turbocharging of trends we've be seeing for decades."

In light of these challenges, Kleiman is concerned APHIS will seek to outsource its responsibilities to third-party organizations. A 2021 *Science* investigation (7 May 2021, p. 558) revealed the agency had begun an apparently clandestine policy of conducting more limited inspections of labs accredited by AAALAC International, a private organization of veterinarians and scientists.

Shea thinks "it's inevitable" that APHIS will turn more to AAALAC. "If you're trying to protect as many animals as you can, you have to rely on something beyond your 77 inspectors."

That troubles Kleiman, who recently worked with another animal rights group, Rise for Animals, on an analysis of more than 14,000 USDA inspection reports between 2014 and the middle of this year. They found that although AAALAC-accredited research facilities account for just 42% of all inspected facilities, they received 73% of the two most serious types of USDA citations in that time period and 78% of all fines issued by APHIS from late 2019 to mid-2024. Kleiman also slams AAALAC for giving a clean bill of health to facilities with a history of animal welfare concerns—including Envigo.

AAALAC did not respond to multiple requests for comment. Naomi Charalambakis, director of communications and science policy at Americans for Medical Progress, a biomedical research advocacy group, argues that the Rise for Animals analysis exaggerates the appearance of severe infractions at AAALAC-accredited entities by counting less serious violations in the total and by focusing on percentages instead of raw numbers.

"Labs also often self-report issues to APHIS that they have already corrected," she notes, "yet these issues still show up as citations." Charalambakis acknowledges that AAALAC accreditation is "not a magic guarantee that nothing will ever go wrong," but she says the analysis "paints a misleading picture of how animal research oversight works in practice."

Sally Thompson-Iritani, the assistant vice provost responsible for the University of Washington's animal care program—one of the largest in the United States—says she hasn't noticed a decrease in the quality of APHIS inspections at her university. "We still get inspected, and they're still thorough and thoughtful."

Even if APHIS falters, Thompson-Iritani says universities like hers have long had their own mechanisms to ensure proper animal welfare. Every U.S. institution that receives federal funding for animal research must have an Institutional Animal Care and Use Committee, for example. Still, she says, APHIS provides a valuable service. "I like the idea of holding ourselves accountable *and* getting outside eyes on things."

APHIS can't do that without sufficient resources, however, the APHIS manager says. "We can't protect these animals if we can't enforce the Animal Welfare Act," they say. "Congress wants us to do more. But they don't understand how little we have left in our toolbox." □

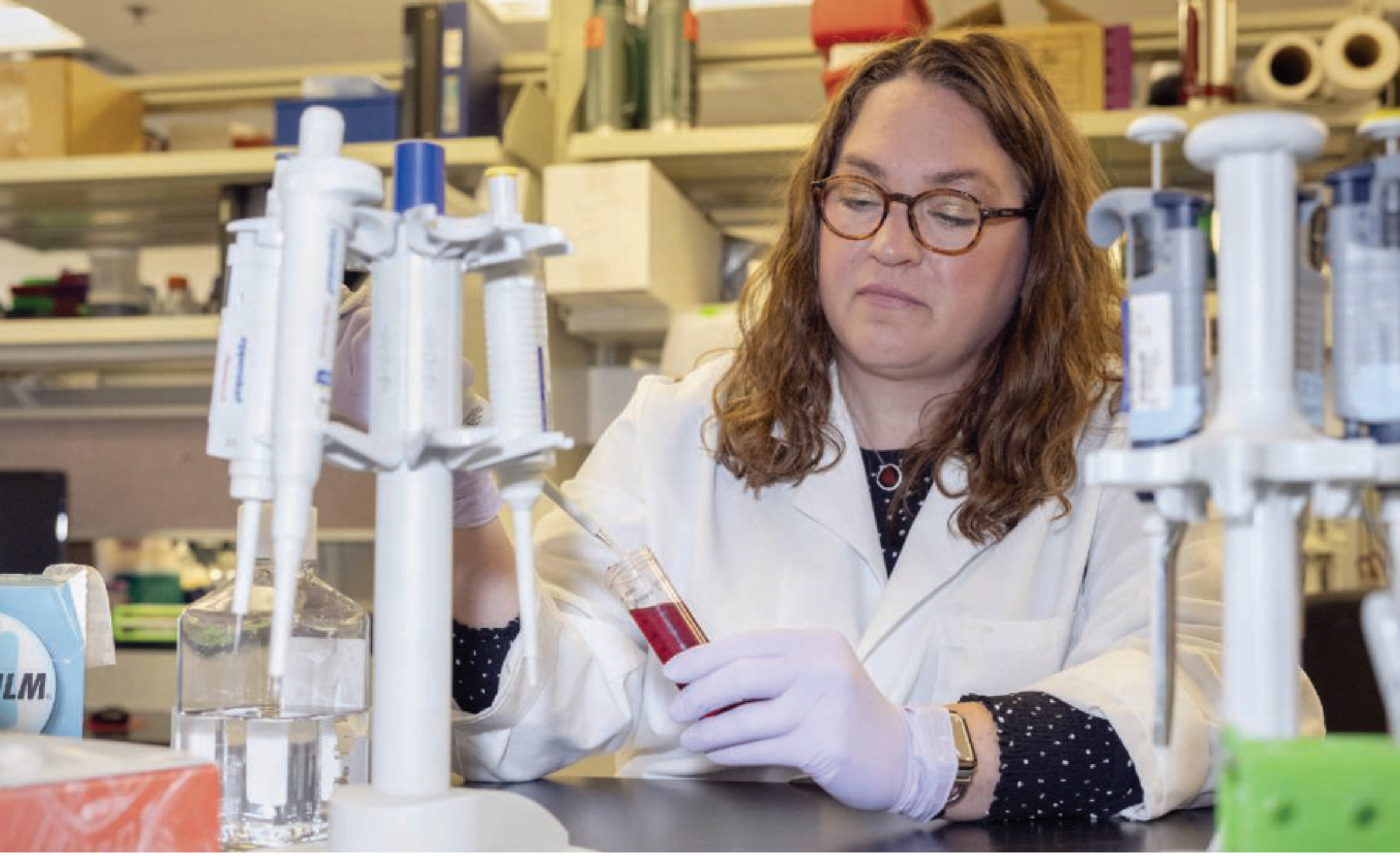
Katie Burns prepares a stain that her University of Cincinnati lab uses to colorize proteins in menstrual fluid for studies of endometriosis.

PHOTO: JOSEPH FUQUA II

FEATURES

PROBING THE PAIN

Katie Burns is helping uncover the role of the immune system in endometriosis—while managing her own disease

MEREDITH WADMAN

When she was a teenager and the pain became agonizing, Katherine "Katie" Burns would crawl under her bed and lie bellydown on the wood floor. She'd clutch a calculator and do "random" math problems to distract herself from the feeling that invisible hands were wringing out her uterus like a washcloth.

In Burns's childhood home in rural Pennsylvania, menstruation, sex, and reproduction weren't welcome topics of conversation, but her parents shuttled her from doctor to doctor searching for the source of her pain—which had visited her occasionally since she was 10 or 11 and became a constant presence once she got her period on the eve of her 13th birthday.

"They said it was growing pains. It was normal. It was nothing," recalls Burns, 47, a pathobiologist and toxicologist at the University of Cincinnati (UC). "They took me out of the room and said to my parents: 'This is psychological. She's seeking help.'"

It wasn't until Burns went away to Gettysburg College that she learned from her roommates that the pain that kept her in her room on Friday nights and that several times sent her to the emergency room wasn't normal. Nor were the periods that soaked a super-plus tampon every hour, or her need to take ibuprofen constantly to be able to function. She went to a gynecologist, who asked whether she had perhaps forgotten to extract a tampon. Eventually, a different gynecologist conducted a thorough physical exam and located a mass sitting under the skin on the right side of her pubic area.

In March 1999, weeks before her 21st birthday, Burns underwent surgery and the mass was extracted. It relieved some of the pain. It also offered validation. Microscopic examination of the mass showed Burns had endometriosis.

"It was a relief," she recalls. "There was actually something that was wrong. I wasn't making this up."

In endometriosis, tissue resembling the endometrium, the lining of the uterus, which is shed each month during menstruation, grows outside of it, mainly in the pelvis. The misplaced tissue can lead to intense pain during periods; chronic pelvic pain; pain with sex, defecation, or urination; and infertility: An estimated 33% of women with the disease are infertile.

But although endometriosis probably affects about one in 10 reproductive-age women—an estimated 190 million worldwide—its origins remain murky and the only treatments target the pain, not the origins of the disease. One reason is that research on endometriosis has been chronically underfunded. Between 2010 and '24, the National Institutes of Health (NIH), the world's largest medical research funder, spent an average of $14.5 million annually—0.039% of its average budget over those years—studying the disease (see graphic, below).

Research on endometriosis "is so far behind because it affects women. And it doesn't kill you," Burns says. Her own search for relief would morph unexpectedly into a life spent in the lab tracking the roots of the disease as part of a cadre of determined scientists, several of them with endometriosis themselves. Researchers have long pursued the role of hormones: Estrogen turbocharges growth of the maverick tissue, which often resists the calming, antigrowth effects of progesterone. But Burns and others have set their sights on the immune system, revealing that it not only fails to clear the errant growths, but seems to be essential to their establishment and flourishing, as lesions become epicenters of chronic, low-grade inflammation that can affect the whole body.

Their work has suggested new, immune-related targets for endometriosis drugs as well as the possibility of diagnostic tests for a disease that still takes, on average, 7 years to identify. Burns herself is pursuing such a test, but in an increasingly tight NIH funding environment, there are no guarantees she will be able to keep the work alive.

The explosion of findings on immune dysfunction is a welcome development, says Stacey Missmer, an epidemiologist at the University of Michigan and president of the World Endometriosis Society, who herself has the condition. "We for so long have been focused on estrogen and progesterone," she says. "We're at this wonderful point of discovery where we are embracing nonhormonal underpinnings that are really holding up in evidence."

AT THE AGE OF 8 OR 9, Burns had informed her mother—who herself had a master's degree in biophysics and supervised her daughter's science experiments growing fungus on petri dishes—that when she grew up, she planned to work with microscopes at NIH. In 2000, 18 months after her diagnosis, she began a Ph.D. program in pathobiology at Pennsylvania State University, with a concentration in toxicology that would lead her into research on liver metabolism.

The lab was male dominated, Burns recalls, and the pain that often incapacitated her "was not really an accepted topic."

One in 10?

The World Health Organization and others put the prevalence of endometriosis at about 10% of reproductive age women and girls. The U.S. government does not produce prevalence figures, and published estimates vary greatly with the population studied. But one rigorous analysis of more than 116,000 U.S. women in the general population indicates a lifetime prevalence of 11.2%.

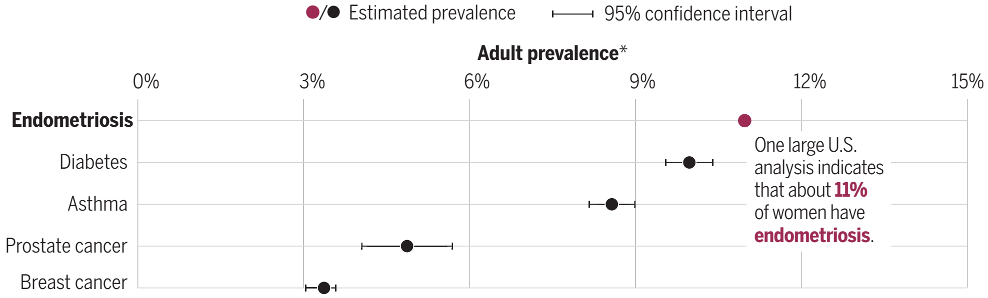

One large U.S. analysis indicates that about **11%** of women have **endometriosis**.

*Prevalence is the proportion of individuals who have a given disease in a population at risk for that disease. In the data above: Endometriosis: lifetime prevalence for women; diabetes and asthma: adults 18 and older; prostate cancer: men 50 and older; breast cancer: women 18 and older.

Deeply discounted

Endometriosis research has received little support from the $48.5 billion National Institutes of Health (NIH), the world's largest medical research funder, compared with conditions that have similar or lower estimated prevalences. NIH is currently funding 54 research project grants with "endometriosis" in their titles and 566 with titles including "breast cancer."

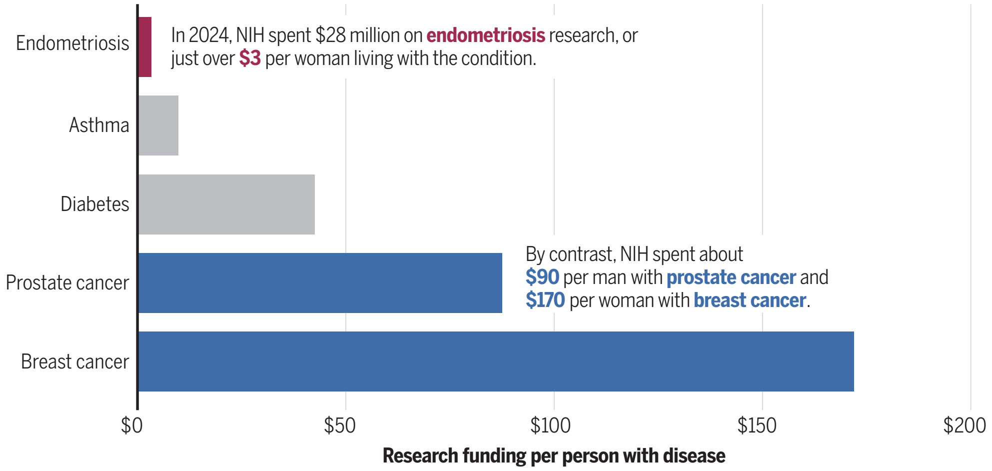

In 2024, NIH spent $28 million on **endometriosis** research, or just over **$3** per woman living with the condition.

By contrast, NIH spent about **$90** per man with **prostate cancer** and **$170** per woman with **breast cancer**.

See https://scim.ag/EndoData for details on the data sources and methodology used in both charts.

CREDITS: (GRAPHICS) V. PENNEY/*SCIENCE*; (DATA) DK SHAH *ET AL.*, *HUMAN REPRODUCTION*, 7, DET120 (2013); CENTERS FOR DISEASE CONTROL AND PREVENTION; U.S. CENSUS BUREAU; NS WAGLE, L NOGUEIRA, TP DEVASIA, ET AL., CA: A CANCER JOURNAL FOR CLINICIANS, 75, 308-340 (2025).

That pain arises from inflammation and scarring in and around endometriosis lesions, and from nerves that infiltrate them. Most lesions are superficial, growing on the peritoneal membrane, which lines the walls of the pelvis, envelops the ovaries and the fallopian tubes, and drapes parts of the ureters, bladder, and bowel. The ovaries are a common site, and here lesions can develop into large cysts called endometriomas (see graphic, p. 774). The aberrant tissue can also reach deep into the muscular walls of the bowel, bladder, and vagina. And it commonly affects certain ligaments that hold the uterus in place. In rare cases, it colonizes the diaphragm, liver, chest cavity, or lungs, which can cause people to cough up blood or become breathless when a lung collapses.

Like many with endometriosis, Burns was disappointed by the few treatment options. Standard birth control pills combining a synthetic version of estrogen with the progesterone analog progestin are a first-line treatment that reduces natural estrogen production to ease pain. But they caused her intolerable, splitting headaches and bloated, painful breasts. (Beyond the potential side effects, such therapy is also a nonstarter for those trying to get pregnant.) Other hormone-based therapies come with their own hazards including hot flashes, night sweats, and, with prolonged use, bone thinning.

Nor was surgery a panacea. Still required for an ironclad diagnosis of endometriosis, it can also ease symptoms by removing lesions, although they can be exceedingly tricky to spot and less practiced surgeons routinely miss them. Even after clean removals, the disease often recurs.

Burns had three surgeries by early 2004, each of which found her pelvis increasingly riddled by endometriosis deposits and adhesions—bands of scar tissue that misshape and tether organs to each other or to the walls of the pelvis. The pain would recur months after each procedure. She would wake at night moaning, nap from exhaustion, then log extra hours in the lab evenings and weekends to try to keep up. She carried petri dishes with two hands because the pain made her hands shake.

That year, in desperation, she enrolled in an NIH-run study to treat endometriosis pain with a drug called raloxifene that, it was hoped, would block estrogen-stimulated lesion growth. Fortunately for Burns, she received a placebo, because the drug worsened pain in those who received it. But the trial changed Burns's life by introducing her to the NIH physician-scientist running it, OB-GYN Pamela Stratton. She understood endometriosis like no other medical professional Burns had met, and her team was doing science in pursuit of a cure. "Just seeing that somebody cared about the disease, that they were trying to understand it, was pivotal in my saying, 'I am done with liver research and I want to try this,'" Burns recalls.

Katie Burns at 13. She soon stopped playing softball because her endometriosis caused pain and heavy periods, which repeatedly bled through her uniform.

PHOTO: LINDA RITCHIE BURNS

Late in her Ph.D., Burns began to look for a postdoctoral position that would let her study endometriosis. Next to no one was doing such research. But in 2007, Kenneth Korach, a reproductive endocrinologist and leading authority on estrogen receptors at NIH's National Institute of Environmental Health Sciences, found her a place in his lab.

WHEN BURNS entered the field, not much more was known about the cause of endometriosis than when American gynecologist John Albertson Sampson in 1927 proposed what became the widely accepted, and still-dominant theory, known as retrograde menstruation: Menstrual blood seeds lesions by flowing backward through the open-ended fallopian tubes and out into the pelvic cavity.

In recent decades, some researchers have questioned whether that theory can explain a disease now understood to have multiple forms—deep, superficial, and endometriomas—with different biology and, plausibly, distinct origins. One alternative theory suggests stem cells that are endometrial progenitors seed the pelvic cavity, in some cases long before puberty. Their possible sources include the adult endometrium, the bone marrow, and retrograde flow during vaginal bleeding that occurs in 5% of female newborns. That would explain why some girls, like Burns, have symptoms before their first period. So would an even older theory than Sampson's, that normal peritoneal tissue, which develops from the same early embryonic cells as the endometrium, transforms into endometriosis lesions. This would also account for patients with lesions far from the uterus, on the diaphragm and in the chest cavity.

Because 90% of women with healthy, unoccluded fallopian tubes have some degree of retrograde menstruation and only a fraction develop the disease, researchers had also long suspected that failures or aberrations of the immune system allow the misplaced cells to survive. Immune cells are known to inundate the peritoneal cavity of people with endometriosis. But these were initially assumed to simply be reacting to the stray tissue. Evidence that the immune system might actively drive inflammation and disease progression, rather than simply failing to clear lesions, was only

Pathways to pain

In endometriosis, tissue resembling the uterine lining takes root outside the uterus, most often in the pelvic cavity. Common sites include the peritoneal membrane that lines the cavity, as well as the ovaries and certain ligaments that hold the uterus in place. Lesions can also affect the fallopian tubes, bowel, bladder, and ureters.

Graphic by **ASHLEY MASTIN**

① Lesions can develop in the **abdominal wall**, often in or near surgical scars like those from cesarean sections.

② The most common lesions are superficial, sitting on the **peritoneal membrane** that lines the pelvic cavity.

③ Endometriotic cysts can grow larger than a typical **ovary** and may cause deep, constant pain.

④ Lesions are common **between the uterus and the rectum**, where gravity likely helps them settle and establish.

⑤ Deep infiltrating endometriosis can invade the muscular walls of the **vagina**, as well as the bowel, bladder, and ureters.

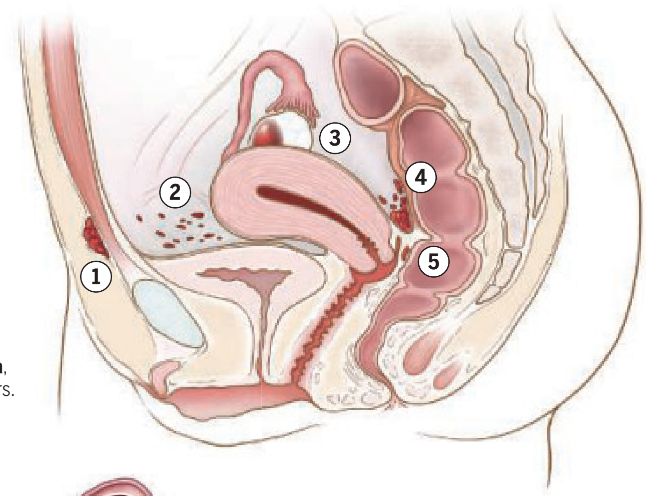

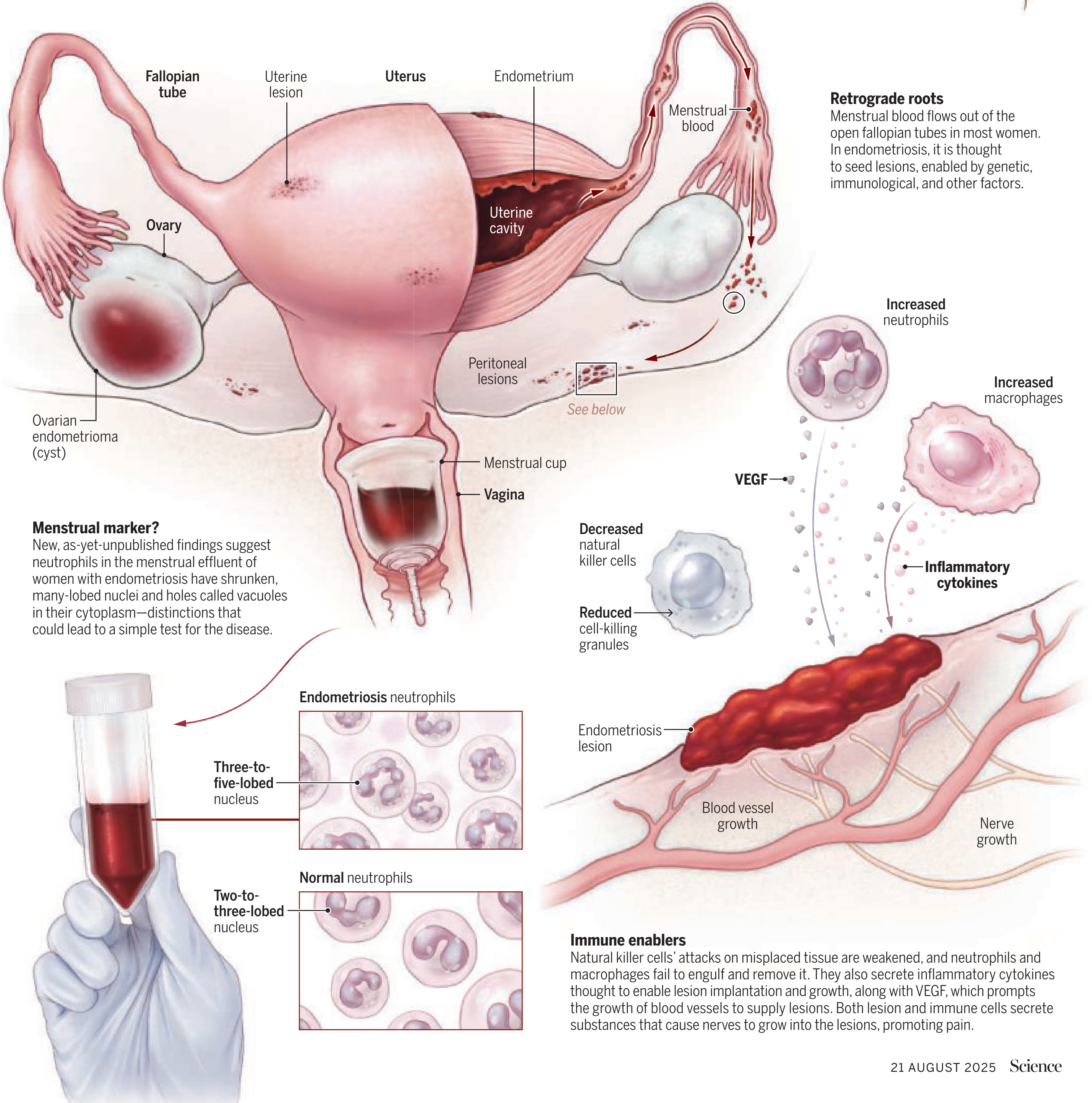

Retrograde roots
Menstrual blood flows out of the open fallopian tubes in most women. In endometriosis, it is thought to seed lesions, enabled by genetic, immunological, and other factors.

Menstrual marker?
New, as-yet-unpublished findings suggest neutrophils in the menstrual effluent of women with endometriosis have shrunken, many-lobed nuclei and holes called vacuoles in their cytoplasm—distinctions that could lead to a simple test for the disease.

Immune enablers
Natural killer cells' attacks on misplaced tissue are weakened, and neutrophils and macrophages fail to engulf and remove it. They also secrete inflammatory cytokines thought to enable lesion implantation and growth, along with VEGF, which prompts the growth of blood vessels to supply lesions. Both lesion and immune cells secrete substances that cause nerves to grow into the lesions, promoting pain.

beginning to attract wider attention as Burns began her research.

In Korach's lab, Burns first set out to develop a mouse model of the disease. Only humans and other primates develop endometriosis naturally, but Burns mimicked the condition in rodents by mincing uterine tissue from one mouse and injecting it into the peritoneal cavity of another—which was genetically identical, to prevent rejection of the foreign tissue. The work, published in *Endocrinology* in 2012, revealed that lesions were fewer, smaller, and less likely to grow in size if either the donor or recipient mice were engineered to lack a key estrogen receptor on their cells, reaffirming the role of this hormone in lesion growth.

But what jumped out at Burns was another finding: Even in recipients that not only lacked the key receptors, but also had their ovaries removed and thus produced almost no estrogen, rudimentary endometriosis lesions developed. These didn't grow and flourish, but something was allowing them to take root. Burns decided to explore what was happening during the first hours and days after injecting the tissue in the mice.

"She was productive. She was creative. She worked extremely hard," Korach recalls. She never mentioned her disease in his presence, he adds. "She was tough. She shouldered it."

But Burns's pain was in fact so bad that she was again considering surgery. By 2009, scarring and inflammation from the disease and five previous operations had left her ureters "like concrete," her surgeon told her. Trying to free them and her other pelvic organs risked more damage that could leave her catheterized for life. "How am I going to live like this?" she remembers asking herself. "Am I going to live with this?"

Luckily, Burns found a physician who helped her persist with a nonsurgical treatment that she found she could tolerate, after getting over the uterine spasms it initially induced: an intrauterine device that releases progestin, which dampens inflammation, suppresses production of disease-driving estrogen, and, in some cases, can inhibit lesion growth. More important, Burns says, she got connected with a pelvic floor therapist whose weekly work began to release muscle tightness and "unstick" her insides.

For the first time since she was 10 or 11 years old, Burns rated her pain a two or three on a scale of 10, instead of the six or seven where it had hovered for years. And for the first time in just as long, she began to socialize, because she wasn't afraid that pain would force a last-minute cancellation of plans. She went to see *Wicked*. She walked with friends. She could now bend over without paralyzing pain, so she planted zucchini and basil and tomatoes and vinca in the garden of her townhouse. And she began to do science without feeling so hamstrung by the disease.

AS BURNS engaged in her studies with new vigor, the field of endometriosis research was becoming more energized, too. In 2014, the same year that advocates launched an annual, worldwide march for endometriosis funding, scientists published the first molecular classification system for the disease and a much-needed set of standards for biobanking endometriosis samples; today, 66 centers in 24 countries have banked more than 10,000 samples. Some scientists began to tease out the roles of multiple genes in the condition. About 50% of disease risk is thought to be inherited, though the genetic loci identified so far make only small contributions. (Environmental triggers including chemicals and diet may also play a causal role, though more research is needed.)

Separately, several teams were beginning to illuminate just how dysfunctional the immune system was in people with endometriosis, using patients' blood and peritoneal fluid, which bathes the pelvic and abdominal organs. Studies had already revealed that the numbers and potency of natural killer cells, an important class of innate immune cells that recognize and destroy errant cells, were reduced in patients. Now, new papers found that these natural killer cells had few activating receptors and many inhibitory ones, and were failing to release key cell-killing chemicals.

Neutrophils, another set of immune cells that are typically the first to flock to foreign tissue, engulf it, and dispose of it, also seemed to be malfunctioning. Lab studies suggested something in patients' peritoneal fluid induced neutrophils to pump out excessive amounts of the growth factor VEGF, which promotes blood vessel growth and could be helping the lesions establish their own blood supplies. And the neutrophils failed to die on schedule, instead secreting chemicals that in the body would draw even more of themselves to a lesion.

Finally, a glut of findings was implicating a third class of innate immune cells, the macrophages that should flock to the scene soon after neutrophils to hoover up errant tissue. In the peritoneal fluid of women with endometriosis, macrophages were not only failing to take up menstrual debris, but they were actively secreting inflammatory molecules that promoted blood vessel growth and sent survival signals to the maverick cells.

Advancing on Burns's mouse model, reproductive biologist Erin Greaves, then at the University of Edinburgh, explored the role of macrophages by giving rodents estrogen and progesterone to prompt artificial menstruation. Greaves, now at the University of Warwick, inserted tissue shed from the "menses" of one mouse into another, tracking its resident macrophages and showing they contributed to lesion formation—the first causal evidence that immune cells from menses were playing a role in establishing lesions.


Amber Seecoomar, clinical research coordinator of the Research OutSmarts Endometriosis study at the Feinstein Institutes for Medical Research, where scientists are trying to develop a diagnostic test for endometriosis using menstrual fluid.

PHOTO: M. WADMAN/*SCIENCE*

Burns, meanwhile, was using her mice to explore the very earliest stages of disease. In the first 24 hours after the animals were injected with minced uterine tissue, before lesions were even established, an army of neutrophils and macrophages had flooded the scene, she found. Within 72 hours, lesions took hold and began developing a blood supply—all in mice lacking almost any estrogen and

Katie Burns around the time she got her first period and her endometriosis symptoms became severe.

PHOTO: LINDA RITCHIE BURNS

> “We really need to recognize how debilitating endometriosis is. How underfunded endometriosis is. And how hard investigators have to fight to be able to study this disease. **Katie Burns**, University of Cincinnati

without key estrogen receptors. Only after 72 hours did the role of estrogen in supporting and maintaining the lesions commence.

The work, published in *Endocrinology* in 2017, suggested that lesion development at first depends on immune cells, before estrogen begins driving it. This two-stage model answered a question born of Burns's own experience: Why are estrogen-manipulating therapies sometimes ineffective?

The results “showed that the immune system was of critical importance for the establishment of peritoneal lesions,” says James Segars, an OB-GYN and endometriosis researcher at the Johns Hopkins University School of Medicine. “That's righteous. That's really important.” (Segars, who describes himself as a “big fan” of Burns's, was on her surgical team during an operation that was part of the NIH raloxifene study in 2004 and has lobbied with Burns for endometriosis funding on Capitol Hill.)

By the time of that paper's publication, Burns had landed a tenure-track job at UC. Although many labs studying the immune system in endometriosis were focused on macrophages, which are hardy and long-lived in the lab, making them easier to study, Burns decided to focus on neutrophils—“a cell type that people have really thrown out,” literally and figuratively, she says, partly because they are famously hard to keep alive.

She also turned toward a new source of biological samples that would allow her to study humans and not just mice: the products of menstruation from people with and without the disease.

Burns wasn't the first to seek insights from menstrual effluent (ME)—so-called because it contains much more than simply blood, including endometrial tissue fragments, and is distinctly different in composition from peripheral blood. Scientists running a project called Research OutSmarts Endometriosis (ROSE) pioneered the study of ME, collected mostly in menstrual cups—small, over-the-counter, reusable silicone cups inserted in the vagina to capture the fluid.

Their results have shown differences between samples from participants with and without the disease that point to potential noninvasive diagnostic tests. Their single-cell sequencing, for example, revealed that natural killer cells were dramatically depleted in the ME of people with endometriosis, reflecting the earlier findings from peritoneal fluid.

When the study launched in 2013, “people literally laughed at us,” recalls Christine Metz, an immunologist at the Feinstein Institutes for Medical Research who co-leads the effort with geneticist Peter Gregersen. Menstrual blood was messy, it was imprecise, it was difficult to collect, OB-GYNs told the pair. Why bother when the disease could be diagnosed with surgery? But the Feinstein team has since enrolled more than 3000 participants and is now one of several pursuing ME tests based on differences in the proteins or RNA expression in the fluid.

“There's something to be discovered here, and we've already shown that in the data,” says the ROSE study's clinical research coordinator, Amber Seecoomar. “If we could really create a screening or a diagnostic tool, we could change thousands of lives.”

In 2020, Burns's team began the painstaking work of studying neutrophils from ME samples. Compared with the neutrophils in peripheral blood, these cells are even more short-lived and fragile, prone to bursting during centrifuging or succumbing to dyes and buffering solutions.

The results, published in *JCI Insight* in January, revealed abnormalities in ME collected from women with endometriosis on day one of menstruation, indicating the aberrations were there from the moment the retrograde flow entered the peritoneal cavity. Endometriosis samples had higher proportions of neutrophils that promote blood vessel growth, and of older neutrophils.

Normally, neutrophils die within hours; those that persist encourage inflammation, a state thought to be conducive to lesion survival.

The paper also described work in mice that bolstered the idea that neutrophil activity in endometriosis represents a healthy process run amok. Examining tissue samples, Burns showed that neutrophil extracellular traps—adhesive meshworks of packed DNA and proteins that the cells normally produce to entrap microbes—were offering the errant cells a foothold, allowing lesions to get established. Perhaps, Burns's team suggested, aged neutrophils are attempting to "rescue" retrograde menstrual tissue, similar to a wound-healing response. The misguided rescue happens with each menstrual cycle, reinforcing the inflammatory environment that caused the previous month's damage.

The immune-related discoveries by Burns and many others haven't led to any approved treatment. But several clinical trials targeting the immune system are edging along. A Chinese company called Hope Medicine last fall reported significant improvements in pain in patients treated during a phase 2 trial of HMI-115, an antibody that locally attacks the prolactin receptor in endometriosis lesions. Prolactin is a hormone that attracts and activates neutrophils, promotes blood vessel growth, and activates nerves in lesions, spurring pain. Another antibody, AMY109, made by Chugai Pharmaceutical, attacks interleukin-8, an inflammatory cytokine pumped out by macrophages and neutrophils drawn to the site of misplaced tissue. It shrank lesions and reduced scarring in monkey studies and was shown to be safe and well tolerated in an initial human trial. The company last year launched a larger, phase 2 trial.

Findings by other researchers not yet in the clinic are pointing to the potential of checkpoint inhibitors, drugs made famous in cancer immunotherapies, in endometriosis—for instance to restore the cell-killing ability of natural killer cells. And a team at the University of Edinburgh is preparing to launch a pilot trial of a compound called nibrozetone that targets macrophages, improving their cell-eating ability and nudging them away from their wound-healing, lesion-supporting tendencies.

All of the activity makes Missmer confident that "the next wave of successful treatments will be in the immunology and inflammation realm."

IN HER OFFICE in Cincinnati, Burns keeps a teal heating pad draped over her desk chair. She lays it in her lap or slaps a lidocaine patch on her lower abdomen to manage her pain, which is less frequent these days.

A not-so-obvious cost of her disease has been a sense of not fitting in, Burns says. Her isolation through her youth and young adulthood has made relationships difficult. She didn't feel she could engage with a prospective partner knowing she was likely infertile. Carrying that knowledge was hard; there were times when she fled church during baptisms. Years of therapy have helped her both grieve and battle her introversion. And her experience has made her a rock for others with her disease, among them her sister, her pelvic floor therapist, and an endless stream of people who reach out to her by email.

People with endometriosis "get desperate and will do almost anything to find answers," she says. "I found it quite shocking that people would send me their medical records, but it happens quite a bit."

Burns's first graduate student, Taylor Wilson, arrived in the lab having lived in silence for years with symptoms of endometriosis. (She has not had diagnostic surgery because, she says, her insurance declines to pay for it.) Wilson says Burns can "look at me and know exactly when I'm not feeling well, and she'll be like, 'OK, what's going on?'"

Wilson, whom Burns draped with a Ph.D. hood earlier this month, was the first author on the January neutrophil paper. In the course of their painstaking experiments, Wilson and Burns also discovered something else in the ME of women with endometriosis, something not yet published and so dramatic that UC's tech transfer office filed patent applications on their behalf.

Under a microscope, the neutrophils from the ME of women without endometriosis had plump, purple-stained nuclei, each with the usual two or three lobes. But in the ME of those with endometriosis, these nuclei had four, five, or even more lobes, yet they were condensed and shrunken. The cytoplasm of these cells was pockmarked with white spaces from storage sacs called vacuoles.

"It shocked us. It's absolutely beautiful," Burns declared as she displayed a slide showing the neutrophils in ME from women with and without the disease at a June meeting at the New York Academy of Sciences.

Linda Griffith, a biological engineer at the Massachusetts Institute of Technology who is developing chip-based devices with endometrial lesion tissue to better study the condition in the lab, and who has the disease herself, says Burns asked a "really great question" about visual differences between cells, and "hit the jackpot" with the finding.

The difference in neutrophils is so "blindingly obvious" that if it plays out in a larger number of people, it could "very quickly," become a diagnostic test, adds another meeting attendee, Michael Rogers, a biologist who is developing endometriosis therapies at Boston Children's Hospital.

Such a test could be less complicated and thus possibly cheaper than other ME tests being developed using measures of RNA expression and proteins. Burns and Wilson now have data supporting the test from more than 30 volunteers; to win funding, potential investors have suggested they'll need closer to 200.

But Burns first has a bigger hill to climb. Her lab, which was flush with cash as recently as 2024, is in danger of closing for lack of funding. Her single NIH grant ran out last year, and bridge funding from her university ran out in June. She has numerous NIH grant applications out.

"The funding situation right now is very—it's very difficult," Burns says. "It's not just my lab. It's everybody studying endometriosis."

At the NIH institutes that have supported Burns's work in the past, fewer than one in 10 grant applications are being funded. The long odds may reflect uncertainty in the face of a 40% NIH funding cut President Donald Trump's administration has requested for 2026, as well as a new NIH policy requiring some multiyear grants to be fully funded immediately.

Burns is now pouring all her energy into keeping her lab alive. "We really need to recognize how debilitating endometriosis is. How underfunded endometriosis is. And how hard investigators have to fight to be able to study this disease." □

NEUROSCIENCE

A shared circuit might link depression and anxiety

Loss of motivation and heightened sensitivity to threat are driven by a network of overlapping brain regions

Michael T. Treadway[1,2]

Anxiety and depression have been described as two distinct reactions to common sources of human suffering, be they loss, pain, or failure. Theoretical models of psychopathology have long speculated on the interplay of these two highly prevalent and comorbid conditions (*1*), yet clear evidence of their shared neural circuitry has remained elusive. On page 840 of this issue, Wood *et al.* (*2*) report a set of elegant experiments conducted in marmosets that reveal a comprehensive circuitry in the brain's prefrontal cortex that may partially underlie two behavioral hallmarks of depression and anxiety in humans: the loss of motivation (anhedonia) and a heightened sensitivity to threat, respectively. The study also identifies potential mechanisms for the fast-acting antidepressant effects of ketamine as well as neuromodulation of the lateral prefrontal cortex, both of which also ameliorate some symptoms of anxiety. Taken together, these data provide crucial knowledge of the neural substrates for key symptoms of anxiety and depression and their comorbidity.

The experiments focused on several prefrontal brain areas previously implicated in depression and its treatment. These were Brodman area 46 in the dorsolateral prefrontal cortex (dlPFC46), area 25 in the subcallosal cingulate cortex (SCC25), and two intervening regions of the anterior cingulate cortex: area 32 (ACC32) and ventral area 32 (ACC32v) (*3*, *4*). These three areas have been previously shown to be anatomically connected, forming a multisynaptic pathway through which lateral prefrontal areas may influence motivational and affective processing in ventromedial cortical and subcortical areas.

Wood *et al.* sequentially deactivated each of these areas in marmosets using designer receptors exclusively activated by designer drugs (DREADDs). In this approach, a viral vector containing DNA encoding a designer inhibitory receptor is infused into the target brain region. The receptor is then activated by exposing the animal to a specific drug, thus inhibiting neural activity in that region. Deactivation of dlPFC46 neurons projecting to the ACC reduced the willingness of animals to work for food rewards and heightened the sensitivity to perceived threat, mimicking behavioral aspects of depression and anxiety, respectively. Moreover, this effect was blocked by pretreatment with a clinically efficacious dose of ketamine injected either systemically or locally within SCC25. Prior work in both marmoset (*5*) and humans (*6*) suggests that hyperactivity within SCC25 may contribute to depression (*3*, *4*). The findings of Wood *et al.* build on these results by implicating SCC25 as a critical region that mediates the rapid antidepressant effect of ketamine. Moreover, the authors show that the effects of inactivating dlPFC46-ACC projections on motivation and threat sensitivity were dependent on indirect connections of dlPFC46 to SCC25 through distinct subregions of ACC32. The targeted inactivation of dlPFC46-ACC32 projections by using DREADDs reduced motivation but did not affect threat sensitivity, whereas inactivation of dlPFC46-ACC32v projections increased sensitivity to threat but did not alter motivation. As such, the authors reveal both shared and distinct circuitry underlying these two behaviors (see the figure).

The findings of Wood *et al.* have several important implications for understanding the biological bases of depression and anxiety and their treatment. The authors demonstrated that although inactivation of dlPFC46-ACC32 projections substantially attenuated the willingness to work for food rewards (reward "wanting"), these effects could not be easily explained by an alteration in the motivation for food (in the absence of work requirements), disruptions to motor function, or cognitive understanding of the task. The authors also used a sucrose preference task to assess whether these deactivations altered reactivity to pleasurable stimuli (hedonic response or reward "liking") and observed no effect. This dissociation of motivational from hedonic responses has long been observed in the context of subcortical dopamine signaling (*7*, *8*) as well as SCC25 activity (*5*), but the role of circuits in the dorsolateral and medial prefrontal cortex has been less clear.

It is also notable that dlPFC46 influences both motivation and threat sensitivity. Why might a common area of dlPFC underlie two seemingly diverse behaviors? In primates, the dlPFC has primarily been associated with cognitive operations such as working memory, abstract reasoning, and cognitive

Two pathways, two symptoms

Deactivation of dorsolateral prefrontal cortex area 46 (dlPFC46) projections to the anterior cingulate cortex in the marmoset reduced willingness to work for a reward (motivational anhedonia) and heightened reactivity to intruders (threat sensitivity). This effect was blocked by delivery of ketamine to subcallosal cingulate cortex area 25 (SCC25). The effect of dlPFC46 on motivation was dependent on its connection with SCC25 through anterior cingulate area 32 (ACC32), whereas the threat sensitivity effect was dependent on ventral ACC32 (ACC32v).

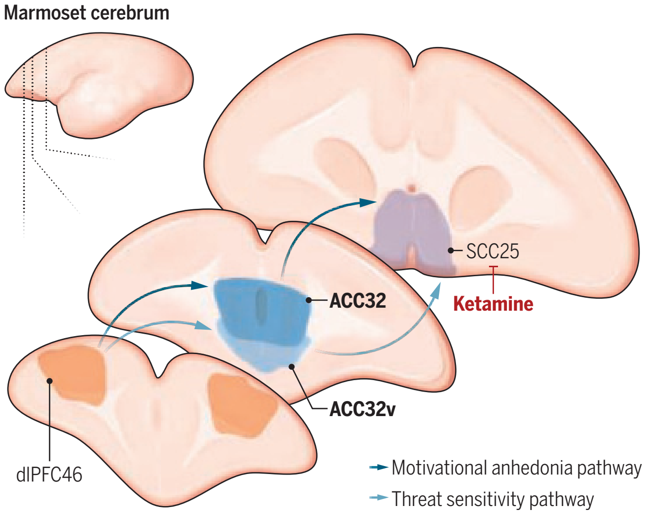

GRAPHIC: A. MASTIN/SCIENCE

control. One possibility is that the dlPFC is needed for the animal to override peripheral signals of muscle fatigue and discomfort to work for food (*9*). A similar cognitive control account could explain the observed increase in threat reactivity, with the loss of dlPFC46 function leading to reduced ability to gate the threat signals coming from subcortical structures. Noninvasive stimulation of dlPFC in humans alters threat processing in other regions, such as the bilateral amygdala (*10*). Further work is needed to resolve these possibilities.

The careful dissection of neural pathways underlying wanting, liking, and threat sensitivity has critical implications for the conceptualization and assessment of psychiatric pathophysiology. For example, standard diagnostic and clinical assessments continue to define anhedonia in major depression using an overly broad "loss of interest or pleasure" definition that treats disruptions to wanting and liking as interchangeable (*11*). This is also reflected in the behavioral assessments used in clinical trials for new potential treatments, which are often not capable of parsing changes in motivation versus pleasure (*12*). Moreover, the question of whether a selective loss of wanting in individuals with depression is specifically associated with comorbid threat sensitivity is not considered under current diagnostic criteria. By contrast, the work by Wood *et al.* suggests that individuals who experience both a selective loss of motivation and heightened reactivity to threat may benefit from treatments that target the dlPFC, such as transcranial magnetic stimulation (TMS) (*13*). Conversely, a clinical presentation of low motivation in the absence of anxiety may point to mechanisms that do not involve dlPFC, such as inflammatory suppression of dopamine release (*12*) or more direct disruption of SCC25 (*4*). Such individuals may be better matches for anti-inflammatory or prodopaminergic interventions, or those that target SCC25—for example, deep brain stimulation or possibly ketamine. Last, individuals experiencing a primary deficit in the loss of pleasure, but without true changes of motivation, may require an entirely different set of interventions (*11*).

A critical next step will be to determine the extent to which parallel circuit functions exist in humans, which may now be possible after the development of noninvasive, deep brain stimulation technologies such as low-frequency focused ultrasound (*14*) and temporal interference stimulation (*15*). These methods allow researchers to focally modulate patterns of activity within deep structures in the brain without disturbing intervening tissue. Nevertheless, the findings of Wood *et al.* represent a substantial advance toward the realization of precision medicine in psychiatry. □

REFERENCES AND NOTES

1. L. A. Clark, D. Watson, *J. Abnorm. Psychol.* **100**, 316 (1991).
2. C. M. Wood *et al.*, *Science* **389**, 840 (2025).
3. D. A. Pizzagalli, A. C. Roberts, *Neuropsychopharmacology* **47**, 225 (2022).
4. S. Alagapan *et al.*, *Nature* **622**, 130 (2023).
5. L. Alexander *et al.*, *Neuron* **101**, 307 (2019).
6. W. C. Drevets *et al.*, *Nature* **386**, 824 (1997).
7. K. C. Berridge, *Psychopharmacology* **191**, 391 (2007).
8. J. D. Salamone, M. Correa, *Behav. Brain Res.* **137**, 3 (2002).
9. M. Pessiglione, B. Blain, A. Wiehler, S. Naik, *Trends Cogn. Sci.* **29**, 730 (2025).
10. M. Ironside *et al.*, *JAMA Psych.* **76**, 71 (2019).
11. M. T. Treadway, D. H. Zald, *Neurosci. Biobehav. Rev.* **35**, 537 (2011).
12. A. H. Miller, *Am. J. Psychiatry* (2025).
13. S. J. H. van Rooij, A. R. Arulpragasam, W. M. McDonald, N. S. Philip, *Neuropsychopharmacology* **49**, 128 (2024).
14. A. R. Arulpragasam *et al.*, *Front. Psychiatry* **13**, 825802 (2022).
15. N. Fani, M. T. Treadway, *Neuropsychopharmacology* **49**, 305 (2024).

ACKNOWLEDGMENTS

The author thanks A. Miller for constructive feedback. In the past 3 years, M.T.T. has been a paid consultant to Boehringer Pharmaceuticals and Ono Pharmaceuticals. M.T.T. acknowledges support by the NIMH (R01MH126083 and R01MH126985).

10.1126/science.aea0913

---

[1]Department of Psychology, Emory University, Atlanta, GA, USA. [2]Department of Psychiatry and Behavioral Sciences, Emory University, Atlanta, GA, USA. Email: mtreadway@emory.edu

---

BIOINSPIRED ROBOTS

Ripple bug robots demonstrate interfacial intelligence

Insect and robot appendages are autonomously controlled by the air-water interface **Cameron A. Aubin**

The ability of a robot to reason, act, and adapt depends on how its sensory, actuation, and control systems; geometry; and materials interact with the physical world (*1*, *2*). This interplay becomes nuanced at small scales, at which forces such as adhesion and surface tension dominate inertial forces. Many small organisms bear structures that exploit the physics of their environments. For example, jellyfish pulse their bell-shaped bodies to create vortex rings that enhance mobility (*3*), and microscopic paramecia propel through water by beating rows of hairlike microstructures (*4*). Increasingly, roboticists view environments as enabling rather than restricting design capabilities. On page 811 of this issue, Ortega-Jimenez *et al.* (*5*) report a water-walking robot inspired by the *Rhagovelia* ripple bug. This insect passively deploys fanlike appendages on its legs as they cross the air-water interface to maneuver in turbulent waters. The bio-inspired design demonstrates a compelling strategy for interfacially mediated autonomous robots.

For small-scale robots and insects alike, motion is inseparable from the surrounding medium. Interfical regimes such as the surface of a body of water are especially dynamic and physically complex. Several insect-inspired robotic systems have been developed to explore locomotion at the air-water interface. Water strider robots, for example, can row across and jump off the water's surface using hydrophobic legs (*6*, *7*). Robots that mimic the rove beetle can rapidly accelerate across the water's surface by leveraging the Marangoni effect—a phenomenon in which surface tension gradients generate fluid flow. (*8*). The robots (and rove beetles) expel surfactants into the water from their distal ends, creating these gradients and producing forward propulsion. Another locomotion strategy is interfacial flight, which is commonly observed in stoneflies and waterlily beetles. These insects produce forward thrust by flapping their wings while their legs remain in contact with the water's surface, allowing them to skim along the interface. Robots that replicate this mode of movement have also been engineered (*9*).

Although these biologically inspired locomotion strategies make use of surface tension forces for support and propulsion, the *Rhagovelia* robot designed by Ortega-Jimenez *et al.* adds a new dimension by using the air-water interface itself as a trigger for the reversible actuation of the fanlike appendages. In ripple bugs, these structures on their middle legs generate impressive propulsive forces and fast turning speeds by maintaining a large surface area, resisting deformation caused by thrust, and rapidly deploying and collapsing during different stroke phases. Ortega-Jimenez *et al.* believed that *Rhagovelia*'s fans could

An environmental interface can trigger a reversible actuation

The *Rhagovelia* ripple bug has fanlike appendages on its middle legs that expand when crossing the air-water interface. Water moves through the barbs and generates capillary forces that control spreading and collapsing of the fan's barbs. This passive process enhances the ripple bug's thrust and maneuverability in turbulent waters. Mimicking the mechanism in a robot demonstrates a new design strategy of using an environmental interface as a trigger to achieve autonomous operation.

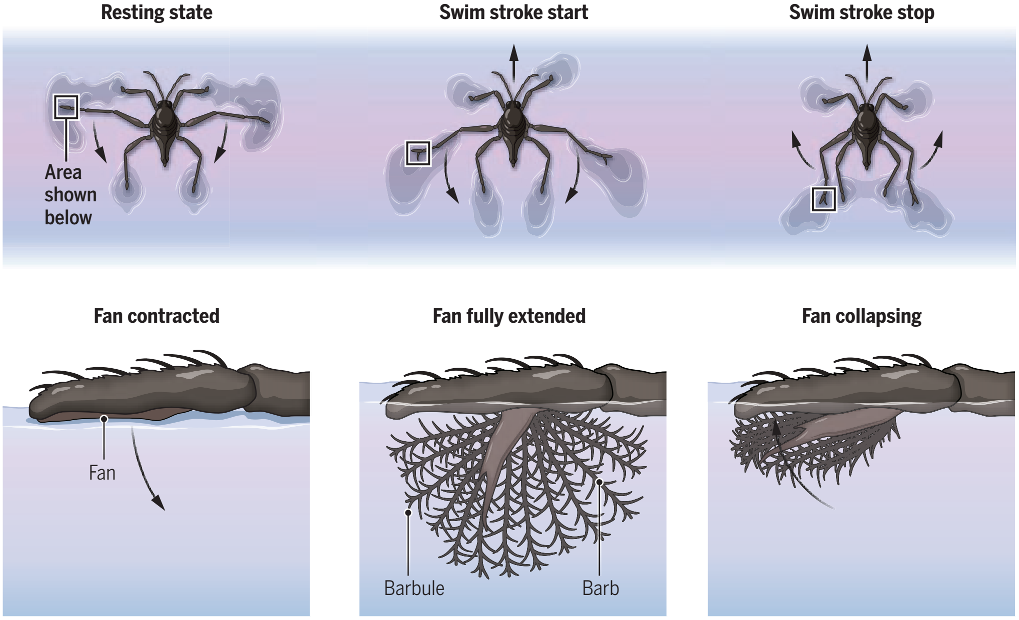

serve as an inspiring template for self-morphing structures, but the fan's mechanism of action had not been fully characterized.

The study by Ortega-Jimenez *et al.* confirmed that capillary forces, which arise from water moving through the barbs of the fanlike appendages, drive the passive spreading and collapsing of *Rhagovelia*'s fans as their legs pierce the water's surface (see the figure). On the basis of this observation, a lightweight (0.23 g) semiaquatic insect robot with synthetic fan appendages was created. These fans improved thrust, braking, and maneuverability of the robot on water. The reversible performance of the propulsor (fan) was controlled entirely through environmental interaction, without active sensing or computational elements. This shift from exploiting surface forces for movement to using the same forces for passive control highlights a subtle but powerful new direction in interfacial robotics, which the authors call "interfacial intelligence."

Designs that can passively change a robot's geometry while traversing an interface would open new avenues for multimodal operation. Which interfaces could be harnessed to influence a robot's morphology, and what physical forces could drive such transitions? Beyond familiar air-water and land-sea boundaries, other environmental changes such as gradients in temperature, salinity, pH, humidity, light, acoustic energy, and electrostatic potential may offer passive control of robotic forms and functions.

Another axis to consider is how control could be achieved by manipulating the material properties of robotic structures through environmental or interfacial means. Stimulus-responsive materials such as shape-memory alloys, liquid crystal elastomers, and piezoelectric composites are frequently implemented in small-scale robots (*10*, *11*). However, in most applications the stimuli originate from programmed signals. It is rare for an environmental impulse, especially one that is triggered by interfacial phenomena, to be used for reversible and repeatable control of robotic movement. Material properties such as stiffness, conductivity, optical characteristics, and permeability could also be tuned through interfacial interactions to allow autonomous operation of a robot.

Ortega-Jimenez *et al.* introduced a strategy for reversible actuation between two mechanical states. This prompts a question of whether combining multiple environmental stimuli could create complex responses. Beyond passive transitions, a hybrid approach that integrates active control with environmentally triggered responses could offer new routes to multifunctionality. Nature often blends these approaches. Ortega-Jimenez *et al.* acknowledged that although *Rhagovelia*'s fan is regulated primarily by passive means, an active claw muscle also exerts some control over fan movement. The closing action of fans relies on the active claw muscle when submerged in water, but capillary forces trigger autonomous closing of the fan when it crosses the water-air interface. In another example, after flying fishes actively generate thrust to breach the water's surface, their postlaunch glide is stabilized by the physical forces of their new air medium (*12*). The air-water interface marks a transition from powered to semipassive motion.

The concept of interfacial intelligence challenges conventional thinking about the origination and definition of robotic control. Future machines may operate autonomously with reduced numbers of sensors and control systems by aligning their physical structure with the physics of the surrounding environment. This approach could potentially improve efficiency by reducing power demands and simplifying control processes, which may also unlock new properties or abilities in complex conditions. Applications may transcend locomotion, enabling capabilities such as sensing, energy harvesting, camouflaging, communication, and environmental sampling. As roboticists continue to draw inspiration from biology, the boundary between organism and environment, which has been considered a restricting factor to an organism's capabilities, could instead be thought of as a template for designing robots with intelligent behavior. □

REFERENCES AND NOTES

1. R. Pfeifer, J. Bongard, S. Grand, *How the Body Shapes the Way We Think: A New View of Intelligence* (MIT Press, 2007).
2. J. Bongard, K. Cho, Y. L. Park, R. Shepherd, *Future directions workshop on embodied intelligence* (US Department of Defense, 2024).
3. B. J. Gemmell, D. R. Troolin, J. H. Costello, S. P. Colin, R. A. Satterlie, *J. R. Soc. Interface* **12**, 20150389 (2015).
4. S. Jana, S. H. Um, S. Jung, *Phys. Fluids* **24**, 041901 (2012).
5. V. M. Ortega-Jimenez *et al.*, *Science* **389**, 811 (2025).
6. J.-S. Koh *et al.*, *Science* **349**, 517 (2015).
7. J. Liu, M. Shen, Z. Ma, X. Zhou, *J. Bionic Eng.* **21**, 635 (2024).
8. X. Ke, H. Yong, F. Xu, H. Ding, Z. Wu, *Nat. Commun.* **15**, 1491 (2024).
9. H. Gao, S. Jung, E. F. Helbling, *IEEE ICRA* **2024**, 6006 (2024).
10. F. M. den Hoed, M. Carlotti, S. Palagi, P. Raffa, V. Mattoli, *Micromachines* **15**, 275 (2024).
11. Z. Shen, F. Chen, X. Zhu, K.-T. Yong, G. Gu, *J. Mater. Chem. B* **8**, 8972 (2020).
12. H. Park, H. Choi, *J. Exp. Biol.* **213**, 3269 (2010).

10.1126/science.aea0926

Robotics Department, University of Michigan, Ann Arbor, MI, USA. Email: caubin@umich.edu

GRAPHIC: A. FISHER/*SCIENCE*

PHYSICS

Outshining molecular disorder with light

Experiments quantify an important criterion for polariton-mediated energy transport

Minjung Son

When molecules interact strongly with light in an optical cavity (an arrangement of mirrors that confine light waves), molecular polaritons—part-photon, part-molecular entities—arise. These hybrid light-matter states can, in principle, carry energy through materials in a wavelike manner. This property has sparked considerable interest in the potential of polaritons to reshape energy transport in materials in ways that could not otherwise be achieved (*1*, *2*). The challenge is that fluctuations in energy levels, ubiquitous in molecular systems, disrupt polariton coherence (long-range correlations of phase and amplitude of waves). This energetic disorder limits a polariton's ability to transport energy effectively. On page 845 of this issue, Yin *et al.* (*3*) report quantitative conditions under which polariton-mediated processes can be sustained against disorder. The finding offers a practical road map for harnessing strong light-matter interactions to achieve robust energy transport and enhanced functionality in molecular materials.

> **The ability to strategically harness disorder…could open new frontiers for polariton-based applications…**

In an ideal model, polaritons are depicted as collective excitations that behave as a single coherent entity because of the strong coupling across many molecules. This allows energy to be distributed over a large spatial area (delocalization) and to move through a material in a wavelike fashion, similar to light. But this ideal situation is often compromised in a real system. Most molecular environments, particularly in soft matter and solutions, exhibit considerable energetic disorder because of thermal motions, solvent interactions, and structural heterogeneity. Such disorder breaks coherence and localizes the polariton to a specific region within a material. These effects also diminish the light component of polaritons and therefore cancel out the effects of light-matter interaction. Consequently, simply achieving strong light-matter interactions is not enough for sustaining polariton delocalization to enable practical applications. The primary challenge is to understand when and how polariton delocalization survives disorder and under which conditions the desired functionalities can be restored. Although theoretical studies have offered important insights and predictions (*4*–*6*), recent findings suggest that the traditionally accepted criteria for sustaining delocalization may need reevaluation for deriving a more stringent requirement (*7*). Furthermore, experimental validation of these fundamental questions remains elusive.

Yin *et al.* performed ultrafast two-dimensional infrared spectroscopy on polaritons that are formed in a well-characterized model molecular system, 2,6-di-*tert*-butylphenol. This technique can investigate photoinduced processes by directly visualizing interactions between polariton states through spectral features and mapping the associated vibrational relaxation pathways in a molecule (*8*). To systematically explore the interplay between energy disorder and light-matter interactions, Yin *et al.* probed the ultrafast dynamics of the same molecule in both solid and liquid media. By comparing the molecule in a disordered liquid medium with that in a more homogeneous solid phase, the authors quantified the extent of polariton delocalization and discovered a sharp contrast between the two regimes. In the liquid phase, substantial energetic disorder, which was evident from the broad spectral width of the vibrational peaks (linewidth), made the photophysical behavior of the molecule insensitive to the presence or strength of light-matter coupling. This indicates that the disorder disrupted coherence and suppressed delocalization of polaritons. By contrast, in the solid medium, in which the molecules adopt an ordered, crystalline arrangement, the reduced inhomogeneity restored delocalization of polaritons and enabled a polariton-mediated vibrational energy transfer between molecules. These observations experimentally validated a simple yet compelling quantitative criterion that was previously proposed from theoretical simulations: Polariton delocalization can be sustained when the collective coupling strength exceeds approximately three times the inhomogeneous linewidth (*7*). This framework offers a practical way to assess and predict polariton behavior in realistic, disordered molecular environments.

The study of Yin *et al.* provides not only an important experimental benchmark but also a broadly applicable conceptual scheme for evaluating the feasibility of polariton-enabled energy transport in molecular materials. This could guide the design of polariton-based devices for applications such as optoelectronics and quantum sensing. Although disorder is often viewed as an intrinsic and unavoidable feature of a molecular system, Yin *et al.* demonstrate that controlling energetic disorder could unlock the full potential of polaritonic systems. Such control can be achieved through rational engineering of molecular structure or optical cavity parameters. By tailoring molecular architectures and the surrounding environment, it may be possible to suppress the inhomogeneity of a molecular system and amplify coherent polariton behavior in a realistic material. Alternatively, the strength of light-matter interaction may be increased by leveraging photonic hotspots (localized areas with enhanced electromagnetic fields) or reducing mode volume (spatial concentration of electromagnetic waves). These strategies could enable robust polariton delocalization even in the presence of moderate disorder.

Insights from the study of Yin *et al.* are likely to extend beyond polariton-mediated vibrational energy transfer to other classes of polaritonic systems (such as electronic or excitonic polaritons) in which energetic disorder similarly undermines coherence and transport (*9*–*11*). In organic semiconductors and photovoltaic materials, the balance between light-matter coupling and inhomogeneity within a material may ultimately determine the feasibility of harnessing polaritonic modes for energy or charge transport. Although further experimental validations will be necessary, the quantitative criterion established by Yin *et al.* may serve as a unifying design rule across a wide class of polariton-enabled technologies.

The ability to strategically harness disorder as a design element could open new frontiers for polariton-based applications in optoelectronic, photonic, and quantum technologies. For example, disorder or defects may be deliberately engineered in a system to direct polariton-mediated processes, enabling reconfigurable or programmable energy transport. The study of Yin *et al.* provides a blueprint for realizing this emerging possibility. □

REFERENCES AND NOTES

1. T. W. Ebbesen, *Acc. Chem. Res.* **49**, 2403 (2016).
2. M. Hertzog, M. Wang, J. Mony, K. Börjesson, *Chem. Soc. Rev.* **48**, 937 (2019).
3. G. Yin *et al.*, *Science* **389**, 845 (2025).
4. J. Cao, *J. Phys. Chem. Lett.* **13**, 10943 (2022).
5. C. Sommer, M. Reitz, F. Mineo, C. Genes, *Phys. Rev. Res.* **3**, 033141 (2021).
6. G. D. Scholes, *Proc. R. Soc. A* **476**, 20200278 (2020).
7. T. Liu, G. Yin, W. Xiong, *Chem. Sci.* **16**, 4676 (2025).
8. B. Xiang *et al.*, *Proc. Natl. Acad. Sci. U.S.A.* **115**, 4845 (2018).
9. T. Khazanov *et al.*, *Chem. Phys. Rev.* **4**, 041305 (2023).
10. S. Dhamija, M. Son, *Chem. Phys. Rev.* **5**, 041309 (2024).
11. A. Dutta *et al.*, *Nat. Commun.* **15**, 6600 (2024).

ACKNOWLEDGMENTS

The author acknowledges support by the American Chemical Society (ACS) Petroleum Research Fund under Doctoral New Investigator Grant 68863-DNI6 awarded to M.S.

10.1126/science.aea1538

Department of Chemistry, Boston University, Boston, MA, USA.
Email: mson@bu.edu

CELL BIOLOGY

A protein tunnel helps stressed lysosomes swell

The endoplasmic reticulum donates lipids through a tunnel-like protein to help lysosomes expand

Jennifer Lippincott-Schwartz

Membrane-bound organelles such as the lysosome, which is involved in cellular waste management, change their surface area to mediate both beneficial and pathological responses. One mechanism that participates in this process is lipid transfer from other organelles to the lysosome, but the details are not well understood. On page 800 of this issue, Yang *et al.* (*1*) report a lipid signaling pathway from the endoplasmic reticulum (ER) that enables lysosomes to swell (vacuolate) to accommodate the increase in their contents under various stress conditions. This pathway results in the recruitment of a tunnel-like lipid transfer protein called PDZ domain-containing protein 8 (PDZD8) to a contact site between the ER and the lysosome, facilitating ER-to-lysosome lipid flow and enabling the expansion of the lysosomal membrane. This mechanism has broad implications for understanding how interorganelle lipid transfer facilitates organelle size regulation.

Roughly 30% of the cytoplasm of eukaryotic cells is occupied by membrane-bound organelles (*2*). These organelles (such as the ER, Golgi, mitochondria, lysosomes, and endosomes) specialize in different important cellular functions, including energy production, waste processing, and protein synthesis. Membrane boundaries allow each organelle to maintain a distinctive internal environment, isolating specific chemical reactions and regulating the exchange of substances between the organelle and the cytoplasm. Organelles regulate their size and activities by vesicle budding and fusion or by direct lipid or metabolite exchange at contact sites with neighboring organelles. This allows organelles to grow or shrink in response to input and outflow of internal components, which is critical for maintaining cell homeostasis.

One organelle that undergoes considerable changes in size is the lysosome, which receives materials taken up from the outside of the cell and breaks them down into usable parts for cell growth and survival. Pathologic conditions such as viral infections, chemotherapy treatment, and lysosomal storage disease lead to the accumulation of undigested solutes inside lysosomes, which causes the organelles to draw in water and swell (*3*). For the lysosome to swell or shrink under different conditions, its membrane boundary's surface area must either increase as the lysosome swells or decrease as it shrinks. This requires the regulation of membrane delivery to or removal from the lysosomal surface. Without such regulation, a lysosome under osmotic pressure may not swell sufficiently to avoid rupture, which can release lysosomal enzymes into the cytoplasm, causing inflammation and, in some cases, cell death. Lysosomal storage diseases such as Niemann-Pick, Gaucher, Fabry, and Tay-Sachs are all characterized by persistent lysosomal swelling (*4*) and ongoing inflammation.

Yang *et al.* set out to dissect the pathways that deliver the extra membrane that is needed for lysosomes to swell under osmotic imbalance. Such delivery could be enabled either through vesicle trafficking pathways to the lysosome or by nonvesicular lipid transfer at contact sites between lysosomes and other organelles (*5*, *6*). The authors induced lysosome swelling in cultured human cell lines using apilimod (an inhibitor of the lipid kinase PIKfyve), which causes lysosomal accumulation of chloride ions (Cl^-) and ammonium, resulting in water influx

Steps enabling lysosomal swelling

PI4K2A is recruited to osmotically stressed lysosomes and generates PI(4)P on these membranes (**1**). ORP binds to PI(4)P on the lysosome and initiates a bidirectional exchange with ER-localized PS and cholesterol (**2**), resulting in a lysosome membrane that is rich in PS and cholesterol (**3**). PS on the lysosome then attracts LYVAC, an ER-associated lipid transfer protein (**4**). Sensing of lysosomal membrane tension and cholesterol enrichment leads LYVAC to mediate directional flow of lipids from the ER to the lysosome, allowing the lysosome to swell (**5**).

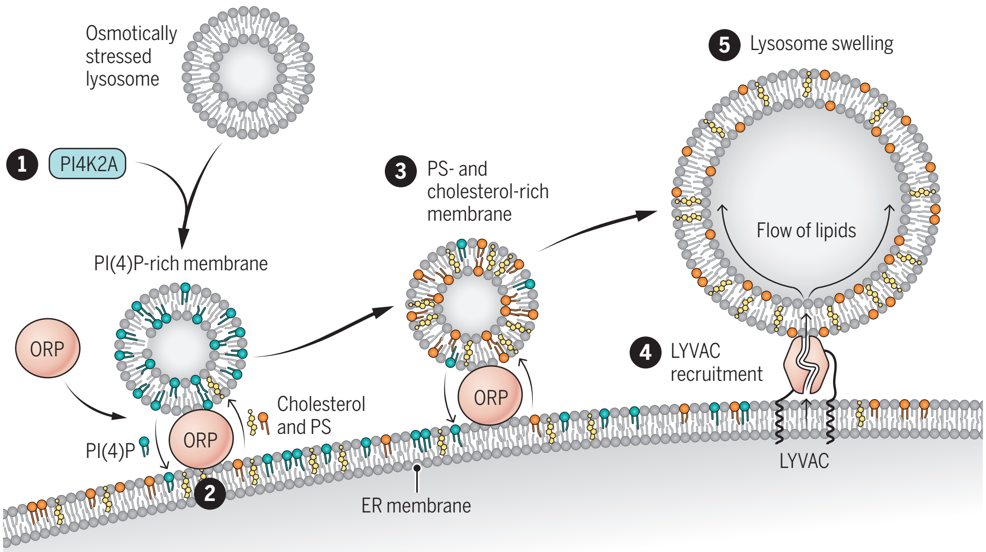

ER, endoplasmic reticulum; LYVAC, lysosome vacuolator; ORP, oxysterol-binding protein–related protein; PI4K2A, phosphatidylinositol 4-kinase type 2 alpha; PI(4)P, phosphatidylinositol 4-phosphate; PS, phosphatidylserine.

and lysosomal swelling. They then used a proximity labeling method to determine what proteins were preferentially recruited to lysosomes. A major hit was PDZD8, a multidomain ER transmembrane protein with a tunnel-like shape capable of tethering the ER to organelles and mediating lipid extraction and transfer (*7*). Yang *et al.* found that recruitment of PDZD8 to stressed lysosomes preceded lysosome vacuolation. In cells lacking the PDZD8 gene, lysosome vacuolation was inhibited and lysosomal osmotic stress was more likely to cause cell death by lysosome rupturing. These observations implicated PDZD8 and nonvesicular lipid transfer in lysosome vacuolation. Therefore, Yang *et al.* renamed PDZD8 as lysosome vacuolator (LYVAC).

Yang *et al.* next analyzed the role of different subdomains of the LYVAC protein in osmotic-induced lysosomal vacuolation using structural and deletion analyses. Negatively charged lipids such as phosphatidylserine on lysosomal membranes were found to recruit LYVAC to the osmotically stressed membrane via LYVAC's C1 domain. Once there, other low-affinity interactions with lysosomal components such as Rab7, a small guanosine triphosphatase involved in regulating membrane traffic, helped establish close contact between the ER-localized LYVAC and lysosome. This enabled lipid transport between the ER and lysosome through LYVAC's lipid tunnel.

How did osmotically stressed lysosomal membranes become enriched in phosphatidylserine in the first place? And what is driving the flow of lipids from the ER to lysosomes once LYVAC is properly positioned? Yang *et al.* addressed these questions by focusing on other lipid transfer proteins, specifically the oxysterol-binding protein (OSBP)–related protein (ORP) family (*8*), that were also enriched on osmotically swollen lysosomes. ORPs are typically recruited to phosphatidylinositol 4-phosphate [PI(4)P]–enriched membranes, where they act as lipid exchangers (*9*). The authors found that apilimod treatment increased the amount of the PI(4)P-producing enzyme PI4K2A on lysosomal membranes, causing recruitment of ORPs to lysosomes. The ORPs then initiated the exchange of PI(4)P on lysosomes with cholesterol and phosphatidylserine on the ER (see the figure). This suggests that ORP-driven increases in phosphatidylserine and cholesterol on osmotically stressed lysosomes set up conditions for recruiting LYVAC. Supporting this possibility, Yang *et al.* found that genetic ablation of the gene encoding PI4K2A abolished both LYVAC recruitment to lysosomes during osmotic stress and lysosomal swelling.

What makes the transfer of lipids from the ER to the lysosome through the LYVAC tunnel unidirectional? The results of liposome transfer assays and molecular dynamic simulations performed by Yang *et al.* suggest that lipid transfer by LYVAC toward phosphatidylserine- and cholesterol-rich lysosomal membranes is chemically favorable because of their finding that lipids move preferentially from cholesterol-poor to cholesterol-rich environments. At the same time, the transfer was energetically favorable because of the membrane tension gradient between the ER and the swelling lysosome, which could help drive lipid movement (*10*). In their model, enhanced membrane tension and increased cholesterol levels in osmotically stressed lysosomes synergize to enable lysosomes to "pull" ER lipids through the LYVAC tunnel to drive lysosomal membrane expansion.

Future work will need to clarify how lysosome swelling under osmotic stress is attenuated. Normally, lysosome swelling is considered helpful to cells because it prevents lysosome rupture, which can trigger cell death by releasing hydrolytic enzymes into the cytoplasm. However, partial, localized, or transient lysosome rupture can be beneficial or even necessary for proper cell function by activating inflammasomes for immune signaling or causing cancer cells to undergo apoptosis or necrosis (*11*). How cells decide to attenuate or continue lysosome swelling to the point of lysosome rupture is thus important to understand. Another avenue for future work is addressing whether LYVAC facilitates the transfer of lipids from the ER to organelles other than lysosomes. For example, LYVAC is found at ER-mitochondria contact sites (*12*). If LYVAC does facilitate transfer of lipids from the ER to mitochondria, it will be important to establish which ORPs are involved and how they are recruited. □

REFERENCES AND NOTES

1. H. Yang *et al.*, *Science* **389**, eadz0972 (2025).
2. A. M. Valm *et al.*, *Nature* **546**, 162 (2017).
3. A. V. Shubin *et al.*, *BMC Cell Biol.* **16**, 4 (2015).
4. A. Ballabio, V. Gieselmann, *Mol. Cell Res.* **1793**, 684 (2009).
5. S. Lev, *Nat. Rev. Mol. Cell Biol.* **11**, 739 (2010).
6. L. Cui *et al.*, *Mol. Biomed.* **3**, 29 (2022).
7. Y. Elbaz-Alon *et al.*, *Nat. Commun.* **11**, 3645 (2020).
8. B. Antonny, J. Bigay, B. Mesmin, *Annu. Rev. Biochem.* **87**, 809 (2018).
9. J. Moser von Filseck *et al.*, *Science* **349**, 432 (2015).
10. Y. Zhang, C. Lin, *Curr. Opin. Cell Biol.* **88**, 102377 (2024).
11. O. Scott, E. Saran, S. A. Freeman, *EMBO Rep.* **26**, 1439 (2025).
12. Y. Hirabayashi *et al.*, *Science* **358**, 623 (2017)

ACKNOWLEDGMENTS

The author thanks members of the Lippincott-Schwartz lab for feedback.

10.1126/science.aea5377

Howard Hughes Medical Institute, Janelia Research Campus, Ashburn, VA, USA.
Email: lippincottschwartzj@hhmi.org

GRAPHIC: K. HOLOSKI/*SCIENCE*

BIOBANKING

Disrupting the biospecimen "treasure trove": Practice, precedent, and future directions

Decentralized biobanking can reconnect individuals to their specimens, democratizing data ownership

Leslie E. Wolf[1, 2], Samantha Kench[3,4], Marielle Gross[5,6,7,8]

Human biospecimens are critical raw materials for biomedical research and development. Biobanks transition donated biospecimens into de-identified research assets, traversing serious ethical and legal challenges for ownership and obligations. Resulting collections are frequently described as "treasure troves" [see, for example, (*1*), p. 83]. The metaphor is evocative of the acquisition process, value generation, and policy framework in which human specimens are "mined" on the quest for scientific discovery. Yet, cases from Henrietta Lacks to 23&Me underscore growing discontent with a system where third parties own and exclusively profit from human specimens, further amplified amid data-hungry artificial intelligence (AI). Existing practice is dehumanizing, erodes public trust, misses opportunities to save lives, and fosters misalignment of incentives that slows scientific progress (*2, 3*). Recent developments in decentralized biobanking disrupt this paradigm by reconnecting individuals to their specimens, restoring trust through transparency, democratizing data ownership, and accelerating collaborative innovation.

> **Decentralized biobanking renders the treasure trove model obsolete.**

By legal definition, a "treasure-trove" is "money or coin, gold, silver, plate or bullion found hidden in the earth or other private place, the owner thereof being unknown" (*4*). Because of its verifiable antiquity and prolonged concealment, a treasure trove's original owner is long-dead. As a result, the finder becomes the treasure's new owner, free to use the treasure as they see fit. By contrast, biospecimen donors are frequently living, with continuing interests in research on their biospecimens, and their identity is known, as biobanks often retain identifiers to collect additional information and biospecimens over time. Nevertheless, the treasure trove's rhetorical appeal appears consistent with US federal regulations governing human subjects research where contributors' identities are unknown to biospecimens' end users and much research proceeds without participant consent. When disputes regarding control or rewards of biospecimen research have arisen, courts have similarly prioritized science over participants, leaving research institutions—and industry—free to exploit and profit from biospecimens. Decentralized biobanking renders the treasure trove model obsolete.

LEGAL PRECEDENT

In cases involving disputes over biospecimens, US courts have perpetuated the biospecimen "treasure trove" by generally rejecting contributors' continuing interests in their biospecimens. Courts' primary concerns when evaluating such disputes has been the potential negative impact on medical research were they to recognize participants' continuing interests in their specimens (see the table).

Despite differences among the cases, there are important commonalities. All but one case were decided on pretrial motions. That is, most courts did not evaluate the merits of the biospecimen contributors' claims at trial. Rather, they considered which, if any, of the biospecimen contributors' claims could proceed. After courts invariably reduced the number of viable claims, settlement—typically, confidential—followed. Notably, the courts also commonly expressed skepticism of the donors' continuing interests in their biospecimens and concern about how their claims could negatively affect medical research. In rejecting contributors' continuing interests in their biospecimens, some courts focused on biospecimens being outside the contributors' body, and the researcher manipulation that made the cells valuable (see the table, *Moore*). Others pointed to contributors' voluntary donation or gift of their biospecimens for research (see the table, *Greenberg, Catalona*). Even a state statute establishing individuals' property right in their DNA analyses did not alter the outcome in biospecimen contributors' favor (see the table, *Greenberg*). In the one case that went to trial (see the table, *Catalona*), the court determined that biospecimen contributors had no continuing interests to direct where their biospecimens were housed, in a dispute between an institution and a researcher changing institutions.

Courts explicitly identified the potentially chilling impact on research in rejecting plaintiffs' claims throughout the cases. According to one court, recognizing a property interest in excised cells would impose a duty on researchers, "which would affect medical research of importance to all of society" and "will hinder research by restricting access to the necessary raw materials" (see the table, *Moore*, p. 144). Another court stated that medical research would be "crippled" if donors retained interests in their samples (see the table, *Greenberg*, p. 1076).

More recent cases have suggested that courts may be more open to recognizing that donors may have some continuing interests in their biospecimens. In *Havasupai Tribe* v. *Ariz. Board of Regents*, despite language in the consent form allowing for future research uses, the court concluded that tribe members could proceed with their privacy-related claims, and the case was settled thereafter. The *Havasupai* case is remarkable for the university taking the unprecedented step of apologizing to the Havasupai for the wrong committed through additional research use of their samples and returning the physical specimens to them, echoing the Native American Graves Protection and Repatriation Act.

More recently, the family of Henrietta Lacks, whose cancer cells were developed into the first immortalized human cell line without her knowledge or consent, sued Thermo Fisher Scientific, which mass-produces the cell line obtained from Lacks to sell for use in commercial research. Although the estate's claims of unjust enrichment were allowed to proceed, the presiding judge expressed skepticism about the estate's legal theory, leading the parties to settle before the case went to trial (*5*). Meanwhile, the Lacks' estate has gone on to file similar claims against other companies, including Ultragenyx, whose motion to dismiss has been denied by a federal judge, Novartis, and Viatris (*6*).

The court decisions described are consistent with how the US federal regulations governing human subjects research, referred to as the Common Rule, treat biospecimen research. Those regulations typically require individuals' informed consent to research participation. But under Office of Human Research Protections guidance, research involving only coded (e.g., de-identified) biospecimens may not even fall within the regulatory definition of human subjects research, if certain conditions are met (*7*). If such research does qualify as human subjects research, it may be deemed exempt under the US code of federal regulations (CFR) [45 C.F.R. 46.101(d)] or may qualify for waiver of consent under 45 C.F.R. 46.116(f) (*7*). Regulators recently contemplated revising the Common Rule to require consent for all biospecimen research, but ultimately rejected such a change, determining it was not "necessary to protect sources' autonomy and privacy interests" (*8*, p. 4). Although consent language may restrict some research uses, collectively, the guidance and regulatory provisions continue to allow substantial amounts of biospecimen research and product development with limited or no consideration of the interests of the individuals who provided the biological materials (*8*).

Consistent with courts' reluctance to recognize continuing interests in biospecimens that could impede medical research is the understanding that, typically, advances require hundreds if not thousands of biospecimens (*9*). The cases of Henrietta Lacks and John Moore, where a single individual's cells themselves become profitable products, are the exception, not the rule. Even in these cases, where the cell lines' names, HeLa and Mo, respectively, reflect the particular contributions of Ms. Lacks and Mr. Moore, transformation of their cells into cell lines required substantial effort and resources. This transformation is essential to the recognition of intellectual property interests, which requires human action and does not extend to things found in nature.

DECENTRALIZED BIOBANKING

What if there were a way to respect biospecimen contributors while also enhancing the research process? Decentralized biobanking is a technology-enabled paradigm for bioethics and biomedical research that keeps donors connected to their biospecimens throughout the research lifecycle (*10*). As a comprehensive solution, decentralized biobanking integrates concepts and components from a wide range of technologies and frameworks advanced to address dynamic consent, privacy protections, return of results, and profit sharing for biospecimen donors. Our approach leverages nonfungible tokens (NFTs), unique digital identifiers recorded on a blockchain, as digital representations of stakeholders, specimens, and protocols, creating an interoperable framework that connects constituents across public and private institutions in a universally accessible biomedical metaverse, or "biomediverse" (*11*). Critically, blockchain, NFTs, and privacy-preserving innovations allow decentralized biobanking software to be integrated with existing biobanking and research platforms, linking donors to their biospecimen records without requiring protocol updates or additional data entry. This new model

Summary of legal cases involving individual interests in biospecimens

Case citation	Brief facts	Specimen collection	Court decision	Case outcome
Moore v. *Regents of the Univ.* of Cal., 51 Cal. 3d 120 (1990)	Moore was a patient whose spleen was removed during surgery, and his surgeon developed a cell line from his tissue.	Clinical	Court rejected 11/13 biospecimen contributors' legal claims.	Settled (pretrial)
Greenberg v. *Miami Children's Hosp. Research Inst., Inc.*, 264 F. Supp. 2d 1064 (S.D. Fla. 2003)	Plaintiffs were a group of parents whose children had Canavan disease, who Defendants, a hospital and research affiliate, took samples from and patented the gene responsible for the disease.	Research	Court rejected 5/6 biospecimen contributors' legal claims.	Settled (pretrial)
Wash. Univ. v. *Catalona*, 490 F.3d 667 (8th Cir. 2007), cert denied, 128 S.Ct. 1122 (2008)	A university sought to establish its ownership of biological materials that a former faculty member collected from donors for research.	Research	Court determined that the university owned the specimens, so donors had no right to direct transfer of specimens to another university.	Court decision in favor of university
Havasupai Tribe v. *Ariz. Bd.* Of Regents, 204 P.3d 1063 (Ariz. Ct. App. 2008)	A Native American tribe gave samples to a university researcher to investigate a genetic link to diabetes but later discovered that the researcher used the samples for nondiabetes research without their consent.	Research	Court found the tribe met procedural requirements allowing them to pursue their claims (reversing lower court ruling against the tribe).	Settled (pretrial)
Lacks v. *Thermo Fisher Scientific, Inc.*, D.C. Md, 1:21-cv-02524	Henrietta Lacks' estate brought an unjust enrichment action against pharmaceutical manufacturer based on its alleged use of the human cell line derived from Lacks' cells.	Clinical	Court found the estate met procedural requirements allowing it to pursue the claim of unjust enrichment.	Settled (pretrial)

allows for transparent yet secure transactions among patients, biobanks, scientists, and physicians (*11*).

Decentralized biobanking has several distinct advantages over the existing model that are consistent with donors' documented preferences and research ethics principles of respect for persons, beneficence, and justice, while responding to issues that have given rise to disputes over biospecimen uses. Many people want to know when they are involved in research, even when human research regulations do not require their consent or ongoing feedback (*12*). Unlike the existing model, decentralized biobanking allows biospecimen contributors to follow their biospecimens and see when and how they are used in research; thus, it is more respectful than the current model (*12*). In addition, engaging biospecimen contributors in the research process conveys the importance of personal and community investments in scientific progress. This communication may serve to reinforce the value of research, restore public trust, and combat misinformation. However, implementing transparency is nontrivial and requires deliberate strategy to manage reputational and financial concerns (*12*).

...decentralized biobanking enables transparency for donors... without imposing undue burdens on scientists...

A recent pilot study supports our theory that recognizing biospecimen contributors' interests using decentralized biobanking may facilitate research, contrary to courts' expressed concerns (*10*). The study implemented decentralized biobanking apps to allow donors to track newly collected and retrospective biospecimens within an existing biobank structure (*10*). Pilot enrollment was robust, and consent for participation in the biobank was significantlyhigher during the pilot than in prior years. Likewise, withdrawal from the biobank was significantly lower than predicted during the pilot study and for 1 year afterward. Pilot participants successfully tracked over 2000 specimens, including allocations to over 40 research protocols, and collectively annotated 760 available specimens (*10*). Empowering donors in this way may align incentives, promote recruitment, foster linkage of multimodal data, and drive specimen utilization, suggesting potential to enhance research.

The blockchain-backed ecosystem allows for more nuanced definition and distribution of stakeholder rights and interests. For example, individuals may retain the right to feedback about their samples' use while delegating decisions about sample distribution to physicians, biobanks, family, patient advocates, or AI agents. Additionally, governance parameters may be designed to account for donors' personal circumstances and context of biospecimen collections. For example, the system may be programmed to recognize emergent health needs and respond by prioritizing deployment of individuals' biospecimens for research with greatest likelihood of directly informing clinical care, i.e., more translational versus basic science. Blockchain architecture can facilitate specimen allocations, translation of findings, enforcement of mutually agreed terms, and system audits.

Notably, this model allows for donor interests in information and greater agency to be supplemented by appropriate compensation if research results in commercialized products (*13*). In other research contexts, there have been calls to compensate participants fairly for their contributions (*14*). The demonstrated feasibility of decentralized biobanking technology for sample tracking creates an urgent need to consider how to value and compensate the contributions of those whose biospecimens are used in research. Different models may be needed when single biospecimen contributors, like Henrietta Lacks, have an outsized impact—a consideration particularly for patient-derived organoids, where potential clinical impact and commercial value of individual contributions may be substantial—compared to where a discrete group's biospecimens lead to discovery or where large numbers of biospecimens are involved. Such a model may have profound implications for the legal standard.

Representing biobank inventories on decentralized ledgers "unhides" assets without compromising donor privacy, permitting specimens to be viewed and accessed by any network participant. Thus, decentralized biobanking enables transparency for donors as a class without imposing undue burdens on scientists, physicians, or institutions. Moreover, NFTs, acting as digital deeds, may reconnect biospecimens to their "original owners" while maintaining de-identification, creating opportunities for inclusion of donors without requiring return of the physical specimens or interfering with ongoing research (*15*). This patient-centered technology generalizes for all physical and digital biospecimens, building on, unlocking, and harmonizing an array of siloed sources. Further development of technical infrastructure, governance frameworks, and incentive mechanisms is essential for a scalable solution.

Decentralized biobanking upends the courts' concerns that recognizing donors' continuing interests in their biospecimens would hinder research. It provides a way forward for governments, institutions, and industry that maximally respects and benefits individuals, while promoting justice and science for the benefit of society. This paradigm shift encounters resistance from entrenched commercial and cultural norms. Rehumanizing and democratizing biospecimen supply chains opens the door for innovative ethical, legal, and economic models whereby individuals and communities may be centered as owners of their native treasures. □

REFERENCES AND NOTES

1. V. G. Koch, K. Todd, *Houst. Law Rev.* **56**, 81 (2018).
2. W. E. Grizzle, M. J. Bledsoe, S. Al Diffalha, D. Otali, K. C. Sexton, *Biopreserv. Biobank.* **17**, 230 (2019).
3. R. J. Cadigan, E. Juengst, A. Davis, G. Henderson, *Genet. Med.* **16**, 738 (2014).
4. *Black's Law Dictionary* (West Publishing, ed. 2, 1910).
5. M. Wadman, *ScienceInsider,* 7 August 2023; https://www.science.org/content/article/what-does-historic-settlement-won-henrietta-lacks-s-family-mean-others.
6. K. Dunleavy, *Fierce Pharma*, 6 August 2024; https://www.fiercepharma.com/pharma/novartis-viatris-sued-estate-woman-whose-cells-were-extracted-research-1951.
7. US Department of Health and Human Services Office for Human Research Protections, *Fed. Reg.* **82**, 7159 (2017).
8. H. F. Lynch, M. N. Meyer, *Hastings Cent. Rep.* **47**, 3 (2017).
9. L. M. Beskow, *Annu. Rev. Genomics Hum. Genet.* **17**, 395 (2016).
10. W. Sanchez *et al*., *JMIR Bioinform. Biotechnol.* **6**, e70463 (2025).
11. M. Gross *et al*., *Front Blockchain* 10.3389/fbloc.2025.1510429 (2025).
12. P. P. O'Rouke *et al*., *Learn. Health Syst.* 10.1002/lrh2.70014 (2025).
13. M. Heller, J. Salzman, *Mine!: How the Hidden Rules of Ownership Control Our Lives* (Anchor Press, 2022).
14. L. E. Wolf, S. Kench, C. J. W. Ledford, *PLOS ONE* **19**, e0303112 (2024).
15. K. Sabharwal, B. Hutler, M. Eifler, M. S. Gross, *J. Health Care Law Policy* (2025); https://digitalcommons.law.umaryland.edu/jhclp/vol28/iss2/5/.

ACKNOWLEDGMENTS

The authors thank R. Faden for helpful insights and feedback. M.G. acknowledges support from Emerson Collective/Yosemite and is the founder and chief executive officer of de-bi, co., a decentralized biobanking company.

10.1126/science.adw8337

---

[1]Georgia State University College of Law and School of Public Health, Atlanta, GA, USA. [2]Medical College of Georgia at Augusta University, Augusta, GA, USA. [3] Georgia State University College of Law, Atlanta, GA, USA. [4]Thomas Horstemeyer, Atlanta, GA, USA. [5]Berman Institute of Bioethics, Johns Hopkins University, Baltimore, MD, USA. [6]de-bi, co., Baltimore, MD, USA. [7]WellSpan Health System, York, PA, USA. [8]Temple University Lewis Katz School of Medicine, Center for Health Justice and Bioethics, Philadelphia, PA, USA.
Email: mariellesophiagross@gmail.com

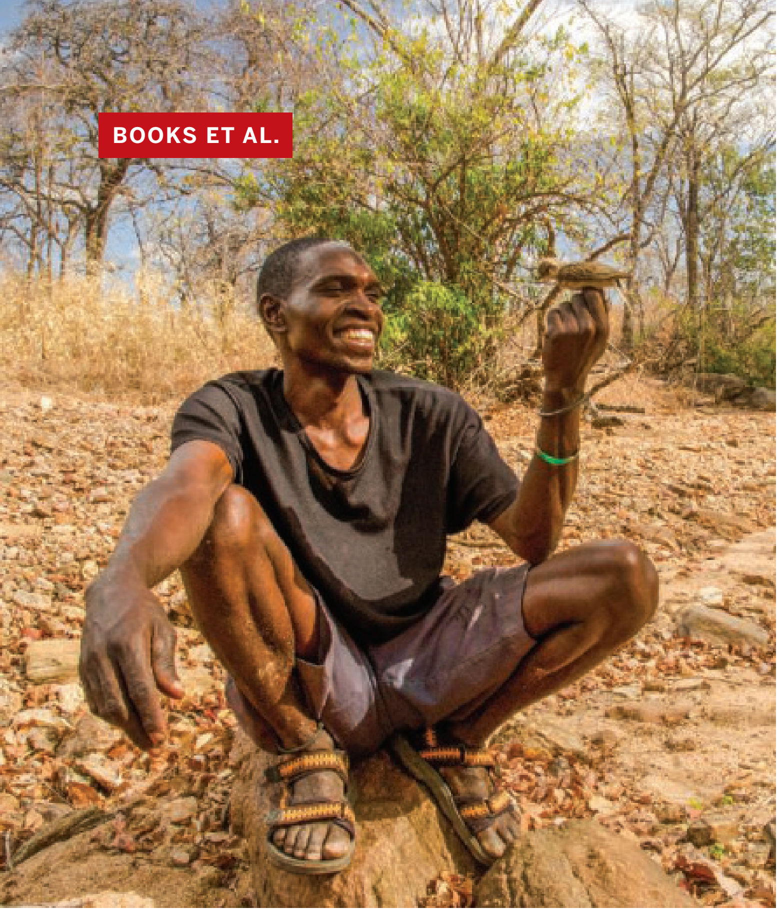

Honey hunter Orlando Yassene and a wild honeyguide work together in the Niassa Special Reserve, Mozambique.

PHOTO: CLAIRE SPOTTISWOODE

BIOLOGY

Mutualism—here, there, and everywhere

A biologist finds wisdom in nature's reciprocal partnerships **Dale Jamieson**

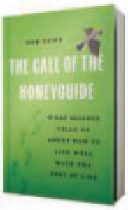

Rob Dunn
Basic Books, 2025.
352 pp.

THE CALL OF THE HONEYGUIDE | If one thing is clear from science studies, it is that we see nature through the eyes of the societies in which we live and we construct these societies in response to our understandings of nature (*1*). The social Darwinism of the late 19th and early 20th centuries, for example, was informed by a (mis)understanding of Darwin's theory of natural selection. Emphasizing the role of competition in the "struggle for existence," it was used to rationalize racism, eugenics, and the extreme inequality of the Gilded Age. After being left for dead mid-century, this misguided framework is making an unfortunate comeback. *The Call of the Honeyguide*, by the distinguished biologist Rob Dunn, can be read as a kind of rejoinder. It is "a call to action for a more mutualistic, less lonely, future."

Mutualism, as understood by biologists, occurs when each member of a symbiotic relationship benefits in virtue of the relationship. As Dunn shows, these relationships have been ubiquitous since the beginning of life on Earth. They exist between large and small animals, large and small plants, and plants and animals of various sizes. Humans live in mutualistic relationships with "many thousands" of partners, including beans in our fields, dogs in our houses, and bacteria in our guts. Mutualism is involved in the construction of our bodies, from cells to organs.

The world, according to Dunn, is profoundly different from how we perceive or imagine it. He introduces compound nouns (e.g., "corn-humans") that he thinks are more descriptively accurate than the language we normally use and implicitly suggests that we should adopt a new ontology, one that is less "delusional" and more reflective of reality.

There is no privileged perspective on a mutualistic relationship. It makes as much sense to talk about our partners domesticating us as ourselves domesticating them. Dunn imagines the yeasts that metabolize sugars into the alcohol in rotting fruit calling out to our ancestors, "come to me." He sees nature as buzzing with conversations with humans, other animals, and plants inviting others to join them in mutualistic relationships. The greater honeyguide (*Indicator indicator*), for example—memorialized in the book's title—is a sub-Saharan African bird that eats wax, which it cannot obtain without help. The bird seeks out human communities (who also seek out the birds) for mutually beneficial partnerships. The birds lead people to beehives, which they break open in order to get honey, thus giving the birds access to wax (*2*).

Our awareness of these relationships is dimming, according to Dunn, and our survival and flourishing rest on increasingly slender threads. In characteristically striking language, he writes that "Together, today, we are 8 billion humans made, like homemade dolls, out of a bit of wheat, some soy, corn, rice, and the animals these crops feed." After the Industrial Revolution, we "partnered with dead plants" (i.e., coal), resulting in massive emissions of greenhouse gases ("the feces of the Industrial Revolution"). We may ultimately do to ourselves with fossil fuels what extinct species of cyanobacteria did to themselves with oxygen more than 2 billion years ago: create planetary conditions that we cannot survive.

According to Dunn, we are at a moment when we must choose which forms of life to live with in mutualistic relations and the terms of those relations. When it comes to making such decisions, however, he provides little help. He writes that "I've come to understand that there are no…simple solutions to the biggest problems." While there is wisdom in this refreshingly modest remark, it is surprising given that Dunn seems to know a lot about almost everything and is generally not afraid to speculate. It is disappointing that he does not guide his readers to the centuries of ethical reflection that might help them in approaching these questions.

The ethical problems come into sharper focus when we reflect on the fact that biologists understand the benefits that mutualism provides as conferring greater fitness, and "a more fit organism is one that produces more offspring" (*3*). As Dunn points out, this leads to the conclusion that humans and factory-farmed animals live in mutualistic relationships, even though the life of an individual factory-farmed animal may be miserable beyond belief. For this reason and others, fitness is an implausible, even reprehensible, guide to how we should choose which forms of life to maintain mutualistic partnerships with and in what ways.

Despite stopping short of systematically addressing the profound questions that he raises, Dunn does an enormous service. Readers will come away from this book with a vivid picture of the incredible, complex, interconnected world in which we live and the tenuousness of our own place within it. These insights, all too rare, are where the search for wisdom must surely begin. ☐

REFERENCES AND NOTES

1. See J. Sapp, *Can. J. Bot.* **82**, 1046 (2004); thanks to A. Tao for the reference.
2. Actually, the story Dunn tells is even more wonderfully complex. For one of the key papers, see C. N. Spottiswoode, K. S. Begg, C. M. Begg, *Science* **353**, 387 (2016).
3. Precisely characterizing fitness involves serious challenges. See E. Sober, *The Philosophy of Evolutionary Theory: Concepts, Inferences, and Probabilities* (Cambridge Univ. Press, 2024), chap. 2.

10.1126/science.adz6497

The reviewer is professor emeritus of environmental studies and founding director of the Center for Environmental and Animal Protection, New York University, New York, NY, USA. Email: dale.jamieson@nyu.edu

PALEOANTHROPOLOGY

Discovering Denisova

A pair of authors invite readers to get to know the elusive archaic human **Brenna R. Hassett**

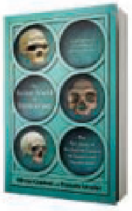

The Secret World of Denisovans
Silvana Condemi and François Savatier
The Experiment, 2025. 272 pp.

The Secret World of Denisovans, the latest collaboration from paleoanthropologist Silvana Condemi and journalist François Savatier, begins with an entirely relatable admission: It can be difficult to accept when old paradigms are obliterated by new. The not-quite-sapiens, not-quite-Neanderthal Denisovan genome was first isolated from a single phalanx epiphysis found in 2008. For paleontologists used to grappling with ambiguous fossil material, the clarity of a Denisova's genetic difference came as a shock. The DNA discovery of Denisova has meant much more than just another species to share the planet with; it gave us an entirely new way to understand the past.

The book's opening five chapters present the history of research in Siberia's Denisova Cave, where the ancient digit was discovered and for which it was named by journalists eager to inaugurate a new human species. The middle third outlines the evolutionary origins of the Denisovans in relation to other hominins, and the latter third reconstructs the environment and physicality of the species. Throughout the book, the authors present a theory of "Denisovation"—a proposed process whereby archaic *Homo* species developed into the species we now call Denisova.

While I may disagree with the authors' assertion that the expansion of Asia's *H. heidelbergensis*—Denisova's predecessor—into the now-submerged Sunda shelf was predicated on the annihilation of *H. erectus* by a meteor event 800,000 years ago, there seems to be good reason to agree with their argument that several of the Middle Pleistocene fossils found in Asia suggest that the species was on a path to becoming Denisova. That the origins of Denisova lie in a recent exegesis of *H. heidelbergensis* from Africa also fits the timeline of events.

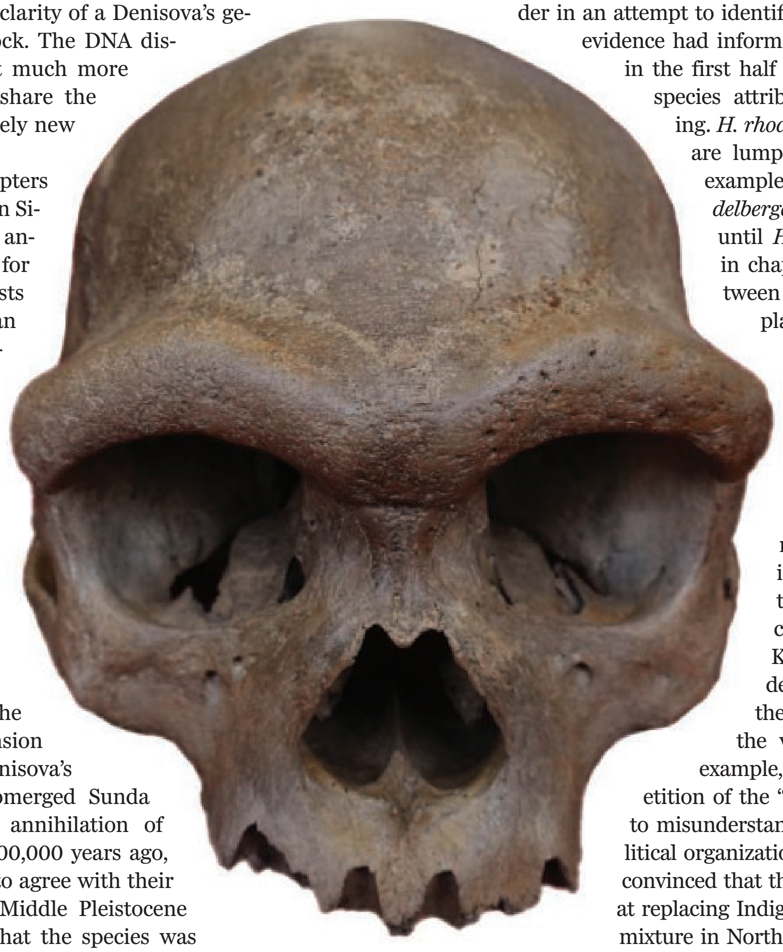

The Harbin, or "Dragon Man," skull, now confirmed as Denisovan, gives a face to the mysterious species.

PHOTO: FU *ET AL.*, *CELL*, 2025

It is something of a triumph to be publishing a book on one of the more mysterious hominins just as the embargo breaks on news that we have finally identified what this species actually looked like (*1*, *2*). With the resolution of the mystery surrounding the so-called "Harbin skull"—now firmly added into the genetic fold of "*Homo denisova*"—we can now put a face to long-extinct inhabitants of our planet who have been defined largely by their genetics for the past 15 years. But even without knowledge of this genomic discovery, the authors have constructed a convincing argument for the inclusion of the myriad Asian Middle Pleistocene species into the Denisova lineage, and it is a rare thing indeed to have a paleoanthropological theory be proven correct.

Despite offering readers a clear overview of Denisova and its immediate antecedents, the book's presentation leaves something to be desired. Large sections, such as the passages describing the discovery of Peking Man, were hard to follow because of the order in which information was presented. Many of the book's arguments begin with a conclusion and are only later supported with data, which made for a very confusing read. (I did, at one point, read through the chapters in reverse order in an attempt to identify what sites, material, or other evidence had informed the broad statements made in the first half of the book.) Meanwhile, dual species attributions appear without warning. *H. rhodesiensis* and *H. heidelbergensis* are lumped together in chapter 4, for example, but then discussion of *H. heidelbergensis* as a monolith holds sway until *H. rhodesiensis* is reintroduced in chapter 8, and the connection between the two is only eventually explained in chapter 9.

There are some other small errors and omissions—there is no acknowledgment of pre-Oldowan tool industries, for instance—but more troubling are the book's cultural mischaracterizations. Statements such as "When Europeans introduced prehistoric science to China in the early twentieth century, scientists in the Middle Kingdom also succumbed to the delicious temptation of believing themselves to be at the center of the world" are unsupportable, for example, and the authors' constant repetition of the "Middle Kingdom" motif seems to misunderstand the recent history of the political organization of China. Likewise, I am not convinced that the French were uniquely skilled at replacing Indigenous populations through admixture in North America, as the authors assert in chapter 8.

I may have had quibbles with small details, certain aspects of presentation, and the implications of an 800,000-year-old meteor, but this book ultimately does provide a reasonable review of what we know about Denisova. The one universal truth, it seems, is that it is impossible to please everyone in the Middle Pleistocene. ☐

REFERENCES AND NOTES

1. Q. Fu *et al.*, *Cell* **188**, 3919 (2025).
2. Q. Fu *et al.*, *Science* **389**, 716 (2025).

10.1126/science.adz6753

The reviewer is at the School of Law and Policing, University of Lancashire, Preston, Lancashire, UK. Email: bhassett@lancashire.ac.uk

LETTERS

Edited by **Jennifer Sills**

The Yarmouk River's recessed water line is visible from Harta, Jordan.

PHOTO: MARCUS YAM/GETTY IMAGES

Yarmouk Treaty could ease Jordan's water crisis

Jordan, one of the world's most water-scarce countries, faces growing stress on its limited resources as a result of aquifer overextraction, unsustainable demand by the agricultural sector, and an inefficient water distribution system (*1*). Jordan's National Water Carrier Project, a plan to desalinate and transport water 300 km inland, aims to increase supply but does so through an energy-intensive infrastructure that does not address the underlying drivers of water insecurity (*2*). Rather than defaulting to man-made supply-side solutions, Jordan should prioritize demand-side solutions and work to unlock natural water sources through regional water diplomacy. Revisiting the 1987 Yarmouk River Agreement (*3*, *4*), which established Jordan's rights to its largest surface water source, could help Jordan achieve water security sustainably.

The Yarmouk River, which originates in Syria, has long been the subject of dispute (*5*, *6*). The Yarmouk agreement, which is still formally in effect, sets terms for shared use but lacks effective enforcement or adaptive provisions (*3*, *4*). The treaty includes no constraints on the use of groundwater, a major driver of diminished river flow. Moreover, it does not account for climate variability or ensure adherence to modern principles of equitable and sustainable use such as those in the 1997 UN Watercourses Convention (*3*).

Recent shifts in regional diplomacy and Syria's gradual reintegration into Arab and international circles create a narrow window to revisit the Yarmouk Agreement (*7*, *8*). Adding joint monitoring mechanisms such as shared hydrological stations and transparent data-sharing protocols would improve trust and increase accountability for river flow and groundwater levels. Groundwater management clauses could establish caps on transboundary aquifer extraction, prohibit unregulated private well drilling, and create a framework for managing surface and groundwater use to prevent depletion. Seasonal allocation mechanisms could set flexible water-sharing schedules that would help to ration usage and meet peak-season demand. Finally, climate resilience clauses could institutionalize adaptive management tools, including basin-level drought plans, early warning systems, and provisions for revisiting quotas based on climate scenarios or environmental thresholds. Together, these reforms would reduce overextraction, discourage inefficient use, and help Jordan access a larger, more sustainable share of its natural surface water resources.

Although only Jordan and Syria are parties to the 1987 Yarmouk Agreement, future revisions should acknowledge the river's place within the wider Jordan River basin. Coordination with all riparian countries in the region, focusing on both water supply and environmental needs, could support efforts to address the ongoing decline of the Dead Sea (*9*) and provide a cost-effective, sustainable path forward for water management.

Hussam Hussein

Department of Politics and International Relations, University of Oxford, Oxford, UK. Email: hh.hussam.hussein@gmail.com

REFERENCES AND NOTES

1. H. Hussein, *Environ. Sci. Policy* **89**, 385 (2018).
2. "National Carrier Project progressing as planned—water minister," *The Jordan Times*, 29 January 2025.
3. M. Zeitoun *et al.*, *Water Alternatives* **12**, 1064 (2019).
4. H. Hussein, *Contemp. Levant*. **2**, 103 (2017).
5. D. Rosenberg, *Arab World Geographer* **9**, 23 (2006).
6. M. Haddadin, *Water Int.* **34**, 420 (2009).
7. R. Hinnebusch, *Glob. Policy* **11**, 113 (2020).
8. H. Elayyan, "Resolving long-standing water dispute with Syria now 'highly urgent', given northern neighbour's new power shift– experts," *The Jordan Times*, 3 February 2025.
9. S. Furnes Bjerkestrand, "Earth Day: Jordan farmers frustrated over shrinking Dead Sea," *Al Jazeera*, 21 April 2022.

10.1126/science.ady5453

Pakistan's reptiles need protection

Pakistan is home to about 195 reptile species (*1*). Reptiles are crucial components of ecological systems, acting as both prey and predators. They contribute to the regulation of pest populations, facilitate nutrient cycling, and support energy transmission across trophic levels, thereby ensuring ecosystem stability (*2*). Globally, reptiles declined 69% between 1970 and 2018 (*3*), but no long-term monitoring data on reptile populations in Pakistan exist (*4*). To conserve its reptile fauna, Pakistan needs to implement targeted studies to assess undocumented declines and to mitigate known threats to their populations and habitats (*1*).

Pakistan's snake, lizard, and turtle species are threatened by hunting and illegal trade to meet the demand for components of traditional medicine (*4*–*6*). The black cobra (*Naja naja*) is used to treat eye infections, and the Bengal monitor lizard (*Varanus bengalensis*), ribbon-sided skink (*Eurylepis taeniolatus*), and Indian fringe-fingered lizard (*Acanthodactylus cantoris*) are used to treat joint pain, cataracts, and cancer, respectively (*6*). The yellow monitor lizard (*Varanus flavescens*), black-spotted pond turtle (*Geoclemys hamiltonii*), Indian softshell turtle (*Nilssonia gangetica*), Indian peacock softshell turtle (*Nilssonia hurum*), and

Indian narrow-headed softshell turtle (*Chitra indica*), all classified as Endangered on the International Union for Conservation of Nature (IUCN) Red List (*7*), are hunted for use in the treatment of paralysis, psoriasis, joint pain, muscle pain, and back pain, respectively (*6*). The olive ridley sea turtle (*Lepidochelys olivacea*), a species once prevalent and breeding in Pakistan, was hunted for religious, medicinal, and spiritual uses (*8*), and there have been no documented instances of the species since 2004 (*9*).

Reptiles in Pakistan are also threatened by substantial habitat loss resulting from unchecked urban expansion, coastal development, and increasing pollution (*1*, *10*, *11*). Turtles are often injured or killed by entanglement in fisherman's nets (*12*). Anthropogenic climate change, such as deforestation and habitat degradation, is among the primary causes of species range declines and population extinctions (*1*).

The Pakistani government, conservation organizations, and local communities should collaborate to mitigate the decline of reptile species. The government should strictly enforce regulations that limit wildlife trade. Public education efforts should aim to prevent deliberate culling. Integrated land-use planning and the expansion of effectively managed protected areas are essential for conserving critical reptile habitats and maintaining the balance of delicate ecosystems. To reduce turtle bycatch, the government should require and subsidize the use of turtle-safe fishing gear in Pakistani gillnet fisheries. To monitor progress, stakeholders should improve data collection on Pakistan's reptiles.

Muhammad Ishfaq

Department of Computer Science and Artificial Intelligence, Huanggang Normal University, Huanggang, Hubei, China. Email: muhammad@hgnu.edu.cn

REFERENCES AND NOTES

1. W. Ali, A. Javid, A. Hussain, S. M. Bukhari, *J. Asia Pac. Biodivers.* **11**, 173 (2018).
2. M. Böhm *et al.*, *Biol. Conserv.* **157**, 372 (2013).
3. J. Westveer *et al.*, "A deep dive into the Living Planet Index: A technical report" (WWF, 2022); https://www.wwf.nl/globalassets/pdf/lpr/lpr-2022-a-deep-dive-into-the-living-planet-index.pdf.
4. M. Z. Khan *et al.*, *Can. J. Pure Appl. Sci.* **9**, 3201 (2015).
5. R. Saleem, M. Altaf, M. Umair, M. S. Amjad, A. M. Abbasi, *J. Wildl. Ecol.* **5**, 13 (2021).
6. S. Adil *et al.*, *Animals* **12**, 2062 (2022).
7. International Union for Conservation of Nature, "The IUCN red list of threatened species" (IUCN, 2025); https://www.iucnredlist.org/.
8. L. Cáceres-Farias *et al.*, *Animals* **12**, 1837 (2022).
9. D. Khan, "Turtle species in Pakistan are about to go extinct," *ProPakistani*, 24 March 2018 .
10. A. Wahab, K. Saeed, M. M. Azam, S. M. Nasir, "Status and distribution of threatened species of freshwater turtles in selected areas of Indus River system," Technical Report (Zooloical Survey Pakistan, 2012); https://doi.org/10.13140/2.1.2057.2489.
11. S. Ahmad, W. Mao, *Science* **382**, 1370 (2023); doi: 10.1126/science.adm7123.
12. U. Shahid *et al.*, "Bycatch analysis of tuna gillnet fisheries of Pakistan: An analysis of bycatch data from 2013-2015" (FAO, 2016); https://www.iotc.org/documents/bycatch-analysis-tuna-gillnet-fisheries-pakistan-analysis-bycatch-data-2013-2015.

10.1126/science.ady3415

Brazilian policy weakens shark conservation

In April, Brazil's Ministries of Fisheries & Aquaculture and Environment enacted Interministerial Ordinance Nº. 30 authorizing targeted fishing of the blue shark (*Prionace glauca*) across national and international waters (*1*). Although presented as a sustainable fisheries measure, the ordinance substantially weakens shark conservation and contradicts Brazil's international commitments under the Convention on International Trade in Endangered Species of Wild Fauna and Flora (CITES) (*2*). The Brazilian government should reevaluate this ordinance through a transparent, science-based process and expedite shark conservation measures.

The blue shark is listed in Appendix II of CITES and is classified as Near Threatened globally and Vulnerable in the South Atlantic (*3*). Yet Ordinance Nº. 30 was endorsed without completing a Non-Detriment Finding (NDF), a scientific risk assessment required for legal trade under CITES. Allowing shark fishing without quantifying the potential negative effects of the policy violates the precautionary principle and diminishes the credibility of national and international conservation frameworks.

Ordinance Nº. 30 falls short of conservation standards. It relies on quotas determined by the International Commission for the Conservation of Atlantic Tunas (ICCAT), but ICCAT assesses data from only a small subset of the tuna fishing fleet, excluding other fleets that also capture blue sharks (*4*), and overlooks the high bycatch rates of juveniles and pregnant females (*5*, *6*). The ordinance also inadequately regulates the use of steel leaders, high-resistance cables that substantially increase shark catches, by permitting them for 10 months of the year. It offers limited capacity for the onboard observers (*4*) who monitor compliance, record bycatch, collect biological data, detect illegal finning, and ensure accurate quota reporting. And it fails to improve enforcement measures that could address the substantial unreported catches linked to illegal fishing and finning (*7*).

Brazil's decision threatens nature-based economies, including ecotourism and diving, which depend on healthy ocean ecosystems (*8*), and exacerbates risks to human health (*9*–*11*). High levels of mercury, arsenic, and other toxic substances have been detected in *P. glauca* (*10*), yet its meat remains widely marketed under the generic label "cação" (*11*). The ordinance increases the volume of potentially hazardous meat entering the market, with no provisions for enhanced labeling, risk communication, or traceability.

Brazil should focus on shark conservation measures instead of allowing more shark fishing. A fin export ban would reduce the economic incentives driving illegal finning and overexploitation, bringing trade practices into compliance with international conservation commitments (*12*). The elimination of steel leaders could decrease catch rates and support population recovery by allowing more individuals, particularly young sharks and pregnant females, to escape capture. Strengthening monitoring systems through traceability, inspections, and DNA barcoding tools would help to curb illegal and unreported catches. An urgent expansion of no-take marine protected areas would help to safeguard key habitats such as nurseries and feeding grounds while fostering ocean resilience and supporting livelihoods.

Gustavo F. de Carvalho-Souza[1] and José Truda Palazzo Júnior[2]

[1]Instituto de Ciencias Marinas de Andalucía, Consejo Superior de Investigaciones Científicas (ICMAN-CSIC), Cádiz, Spain. [2]Instituto Brasileiro de Conservação da Natureza (IBRACON), Canoas, Brazil. Email: gustavo.souza@csic.es

REFERENCES AND NOTES

1. MPA/MMA Inter Ministerial Ordinance Nº 30, de 17 de abril de 2025. Official Gazette of the Union, section 1, Brasília, DF, 75, p. 59 (2025) [in Portuguese].
2. Convention on International Trade in Endangered Species of Wild Fauna and Flora, Appendix II (CITES, 2021); https://www.cites.org/eng/app/appendices.php.
3. International Union for Conservation of Nature, "The IUCN Red List of Threatened Species 2019: Blue shark, Prionace glauca" (IUCN, 2025); https://www.iucnredlist.org/species/39381/2915850.
4. J. P. Torres-Florez *et al.*, "Technical note, Letter No. 20250428/1, Brasilia April 26, 2025" (2025); https://crbio07.gov.br/wp-content/uploads/2025/04/EN-Oficio-20250428_1-Analise-Tecnica-pela-URGENTE-revogacao-da-Portaria-Interministerial-MPA_MMA-no-30_2025EA-SHEPHERD-BRASIL.pdf.
5. F. Mas *et al.*, *Mar. Biol.* **171**, 106 (2024).
6. PROTUNA, "Chamada MCTI/MPA/CNPq 22/2015: Ordenamento da Pesca Brasileira" [in Portuguese] (2022); https://www.gov.br/mpa/pt-br/assuntos/cadastro-registro-e-monitoramento/pesquisa/projetos-de-pesquisa/2022/protuna-1-_compressed.pdf.
7. T. E. F. da Silva *et al.*, *Neotrop. Biol. Conserv.* **16**, 71 (2021).
8. A. C. Siddiqi *et al.*, *Mar. Pol.* **161**, 105995 (2024).
9. M. Alvarenga *et al.*, *Biol. Conserv.* **292**, 110543 (2024).
10. R. A. Hauser-Davis *et al.*, *Ecotoxicol. Environ. Saf.* **288**, 117358 (2024).
11. H. Bornatowski *et al.*, *Science* **340**, 923 (2013).
12. F. Ferretti *et al.*, *Conserv. Lett.* **13**, 12708 (2020).

COMPETING INTERESTS

G.F.d.C.-S. is supported by a fellowship from the Junta de Andalucía.

10.1126/science.adz3632

CALL FOR PAPERS

SPJ
SCIENCE PARTNER JOURNALS

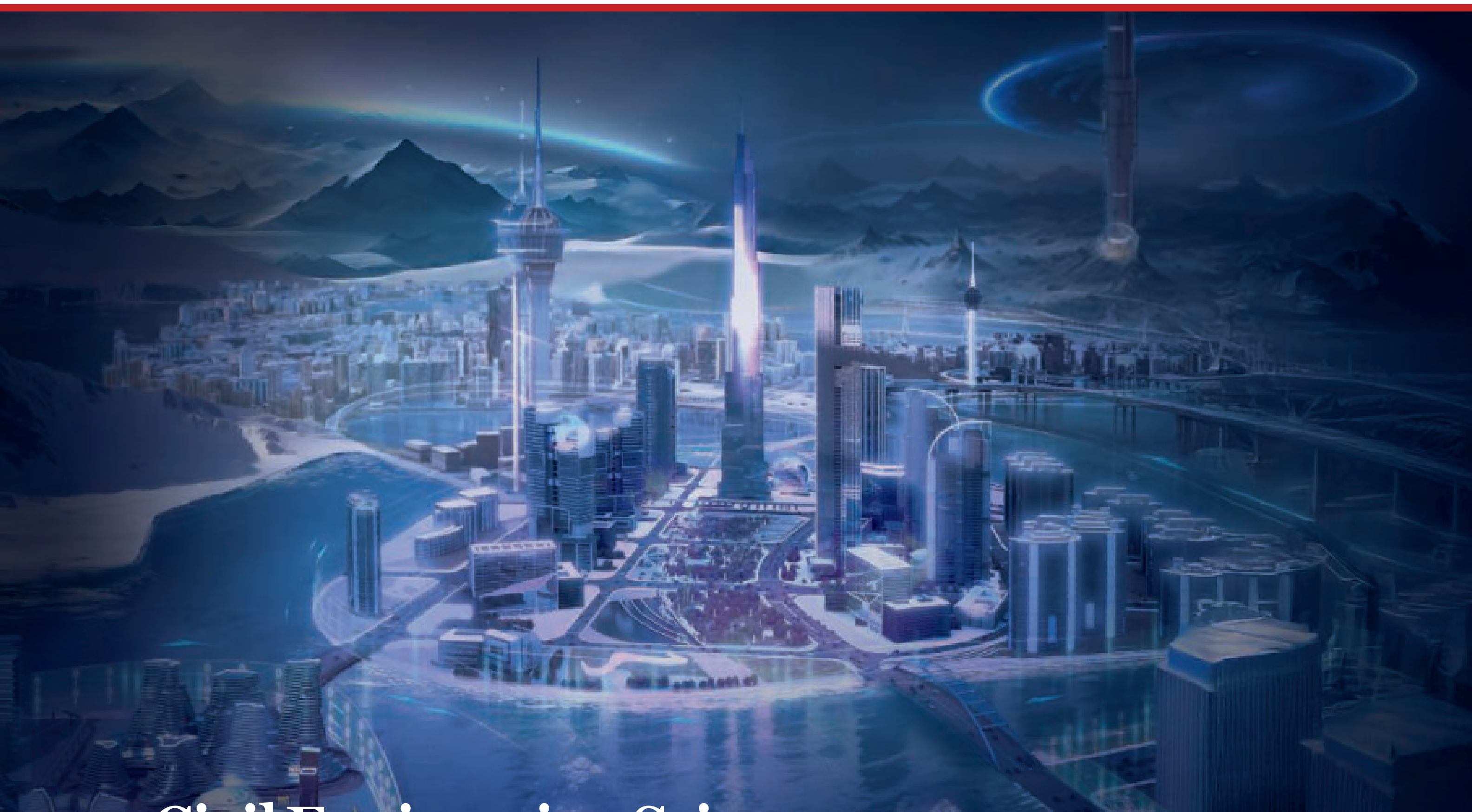

Civil Engineering Sciences

OPEN ACCESS

Civil Engineering Sciences is an Open Access journal published in affiliation with the China Civil Engineering Society (CCES) and Tsinghua University (THU) and distributed by the American Association for the Advancement of Science (AAAS). The journal aims to publish cutting-edge research on scientific discoveries and technological innovations driven by major civil engineering needs, as well as breakthroughs in civil engineering technology resulting from new scientific discoveries.

The Science Partner Journals (SPJ) program was established by the American Association for the Advancement of Science (AAAS), the nonprofit publisher of the *Science* family of journals. The SPJ program features high-quality, online-only, open access publications produced in collaboration with international research institutions, foundations, funders and societies. Through these collaborations, AAAS expands its efforts to communicate science broadly and for the benefit of all people by providing top-tier international research organizations with the technology, visibility and publishing expertise that AAAS is uniquely positioned to offer as the world's largest general science membership society.

Submit your research to *Civil Engineering Sciences* today!
Learn more at: **spj.science.org/journal/cesci**

@SPJournals **@SPJournals** **@SPJournals**

ARTICLE PROCESSING FEES WAIVED THROUGH DECEMBER 2028

REVIEW SUMMARY

DRUG DEVELOPMENT

Load and lock: An emerging class of therapeutics that influence macromolecular dissociation

Raymond J. Deshaies* and Patrick Ryan Potts*

Full article and list of author affiliations:
https://doi.org/10.1126/science.adx3595

BACKGROUND: Cells rely on many dynamic, rapidly reversible interactions between macromolecules. Each interaction has an on-rate (k_{on}, how quickly partners bind) and an off-rate (k_{off}, how quickly a complex falls apart), and their ratio defines the binding affinity (K_D). Many complexes are transient by design—i.e., have a fast k_{off}—and if k_{off} is slowed, downstream events may be disrupted; an example of such a complex is a kinesin head domain dissociating from tubulin as kinesin walks along a microtubule. Conversely, extending the lifetime of a complex can amplify its signal output, as is the case for some ligand-receptor engagements.

Modulating how long molecules stay bound to each other is thus a promising way to influence physiology and treat disease. Traditional drugs often work by reducing the formation of molecular complexes (i.e., reducing apparent k_{on}) through competitive inhibition, such as inhibitors of protein kinases that block binding to adenosine triphosphate. This approach can be limited to readily druggable enzymes but has proven to be difficult for more challenging targets, such as transcription factors. In this Review, we discuss a different approach to drug discovery that may enable drugging of unconventional targets through stabilization of macromolecular complexes with molecules we refer to as “LOCKTACs.”

ADVANCES: We define LOCKTACs as compounds that reduce the k_{off} of naturally interacting molecules, effectively “locking” a dynamic complex in place. Like proteolysis-targeting molecular chimeras (PROTACs) or molecular glues, a LOCKTAC has two binding surfaces that tether two partners together. However, instead of forging a new protein-protein interaction, LOCKTACs stabilize a preexisting, functionally relevant interaction to make it last longer. These can be small or large molecules that bind at, adjacent to, or even at a distance from the interface of the target complex to form a more persistent assembly.

LOCKTACs can either enhance or inhibit a biological function, depending on which interaction is stabilized. Activator LOCKTACs stabilize transient or inefficient complexes that promote a process, thereby boosting that process. For example, risdiplam is used in the treatment of spinal muscular atrophy and works by altering splicing of the *SMN2* mRNA through stabilizing its binding to U1 small nuclear ribonucleoprotein. By contrast, inhibitory LOCKTACs hold together interactions that normally need to fall apart, thereby blocking a process. For example, sovilnesib can stop the kinesin KIF18A molecular motor from moving along microtubules by preventing the necessary bind-and-release catalytic cycle. In both cases, the drug forces a normally short-lived interaction to persist, which can either enhance or disrupt the targeted pathway, depending on the biological context.

OUTLOOK: LOCKTACs are promising because they open new avenues to modulate disease mechanisms. By reinforcing an existing interaction rather than blocking one, a LOCKTAC can target less-conserved surfaces and avoid competing with high-affinity natural ligands. This may provoke fewer off-target effects and enable drugging of targets once considered out of reach.

The discovery of LOCKTACs poses challenges. Because locking an interaction can result in agonism or antagonism depending upon context, targets will need to be selected judiciously. Moreover, screening for slow dissociation requires time-resolved kinetic assays that are more difficult than standard binding tests. Nevertheless, LOCKTACs represent a promising, largely untapped opportunity to develop drugs against difficult targets. By drawing attention to a diverse set of existing and emerging drugs that work through a LOCKTAC-like mechanism, we seek to inspire deliberate efforts to unlock a new chapter in pharmacology through the pursuit of “sustained proximity.” □

---

*Corresponding author. Email: rdii2003@gmail.com (R.J.D.); ryan.potts@amgen.com (P.R.P.) Cite this article as R. J. Deshaies, P. R. Potts, *Science* **389**, eadx3595 (2025). DOI: 10.1126/science.adx3595

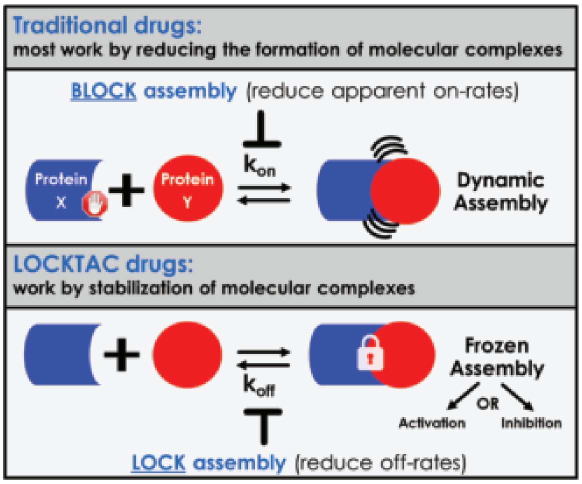

LOCKTACs promote sustained proximity to expand the druggable target space. Most traditional drugs (represented as blocking symbol) work by reducing the formation of molecular complexes. LOCKTACs are small or large molecules (represented as lock symbol) that bind protein assemblies to convert dynamic native complexes into stable frozen assemblies. LOCKTACs can activate or inhibit the output of these interactions, leading to altered downstream signaling.

RESEARCH

IN *SCIENCE* JOURNALS

Edited by **Michael Funk**

LIGHT POLLUTION

Extending the day

Light pollution has become ubiquitous across much of the planet. This situation has the potential to widely affect a variety of species because most living organisms have evolved to respond, in one way or another, to the circadian light-dark cycle. Pease *et al.* looked at the influence of light pollution on activity patterns in more than 500 species of birds globally. They found that birds were generally vocal for nearly an hour longer in the presence of light pollution. Furthermore, birds that are more exposed, or entrained, to light were more affected, such as those with large eyes and open nests. —Sacha Vignieri *Science* p. 818, 10.1126/science.adv9472

QUANTUM SIMULATION

A coarsening gas

Ordering that is characterized by a growing length scale is referred to as coarsening. In an isolated system, the dynamics of coarsening become complex. Gazo *et al*. studied this process in a homogeneous two-dimensional Bose gas of potassium atoms. The researchers found universal long-time scaling in their data and measured a dynamical exponent consistent with theoretical expectations. —Jelena Stajic

Science p. 802, 10.1126/science.ado3487

QUANTUM MATTER

Measuring quantum geometry

The quantum geometric tensor of a material provides insight into the topology and geometry of its electronic states. The real part of this tensor, the quantum metric, has so far been measured only in a limited number of materials. Sala *et al.* broadened this range of materialsby predicting that spin-momentum locking of electronic states is associated with a finite quantum metric. The researchers experimentally verified this prediction by using 111-oriented lanthanum aluminate–strontium titanate ($LaAlO_3/SrTiO_3$) interfaces as a model system. —Jelena Stajic

Science p. 822, 10.1126/science.adq3255

GEOGRAPHY

In the way of wildfires

Wildfires are increasingly destructive to people and property globally as a result of both increased fire activity and human development at the urban-wildland interface. Seydi *et al*. quantified the number of people exposed to fires (i.e., those living within areas that have burned) at the global scale between 2002 and 2021. Over that

PHOTO: PAUL HOBSON/MINDEN PICTURES

Birds in areas with high light pollution, such the flock of starlings here, tend to be active earlier in the morning and later into the evening.

period, fire exposure increased by 40% even as burned area declined globally. Almost all of the increase in exposure was in Africa, which accounted for more than 85% of all people directly exposed to wildland fires over the study period. —Bianca Lopez

Science p. 826 10.1126/science.adu6408

SPINTRONICS

Driving fast

Antiferromagnetic spintronics hold the promise of high speed and high efficiency unachievable with ferromagnets. However, reaching these goals in experiments has proven tricky. Takeuchi *et al*. realized all-electrical driving of an antiferromagnetic Mn_3Sn (manganese-tin) nanodot. The researchers used electric-current pulses as short as 0.1 nanoseconds at current densities insensitive to pulse width. —Jelena Stajic

Science p. 830, 10.1126/science.ado1611

CONSERVATION GENETICS

Genetic trade-offs

As habitats become increasingly fragmented and populations continue to decline, more and more species face genetic threats associated with small population sizes. Although introduction of individuals from related populations can introduce genetic variability and thus “rescue” populations with low heterozygosity and high inbreeding, such introductions can also lead to outbreeding depression. Looking at populations of endangered pocket mice, Wilder *et al*. found that breeding of individuals with different karyotypes did lead to lower fitness; however, their fitness was still higher than those breeding with closely related individuals. —Sacha Vignieri

Science p. 835, 10.1126/science.adn4666

ARCHAEOLOGY

Victims of Neolithic violence

The presence of people in atypical burials and with skeletal signs of violent injuries in Neolithic archaeological sites in France (dating to about 4300 to 4150 BCE) raises questions about how their lives and identities differed from people who were not victims of violence. Fernández-Crespo *et al.* used isotopes informative about diet and migration in a comparison of victims and nonvictims. Their findings suggest that the victims were members of invading groups, and the excessive violence that they experienced at the time of death was related to celebrations of warfare victories by local people. —Sharon N. DeWitte

Sci. Adv. (2025)
10.1126/sciadv.adv3162

EPIDEMIOLOGY

Dengue beyond borders

Dengue is a serious health concern in Latin America, which has experienced a surge in recent outbreaks. Quandelacy *et al*. used historical surveillance data going back decades to analyze seasonal and multiannual patterns of dengue incidence at a regional scale across a swathe of Latin America. The authors report that more than half of all provinces or islands studied had dengue outbreaks about every 12 months, with strong synchrony observed. Additionally, increased dengue incidence was associated with strong seasonality of occurrence. Changes in temperature and precipitation (including El Niño weather patterns) often occurred months before changes in case incidence. This study provides a comprehensive view of regional dengue incidence across Latin America and could potentially aid in forecasting or intervention efforts. —Catherine Charneski

Sci. Transl. Med. (2025)
10.1126/scitranslmed.adq4326

PHOTONICS

Active spectral synthesis

Spectroscopy requires knowing precisely the input spectrum used to probe the sample. At present, most photonic components, such as blazed gratings or metasurfaces, have fixed functionalities and static spectral properties, providing only limited spectral tunability that is often restricted to narrowband adjustments or broad, nonselective shifts. Liu *et al*. introduce a nano-opto-electro-mechanical grating based on a pixelated array of coupled resonators to dynamically control the spectral output. Their on-chip approach provides access to real-time optical spectrum control in an ultracompact footprint, offering agility and spectral flexibility for integrated photonics. —Ian S. Osborne

Science p. 806, 10.1126/science.adu8492

IN OTHER JOURNALS

Edited by **Corinne Simonti** and **Jesse Smith**

PLANT GENETICS

MSH1 suppresses organelle mutation

Seed plants have very low mitochondrial mutation rates compared with most eukaryotes. Broz *et al.* investigated the function of MSH1, which prevents inappropriate recombination between small repeat sequences. After seven or eight generations, the authors found no changes at all in wild-type organelle genomes but substantial sequence variation in *msh1* mitochondrial and plastid DNA. In *msh1* plants, nucleotide substitution rates rocketed to 10 to 100 times greater than that in nematodes and arthropods. This individual DNA repair protein has a profound effect in suppressing organelle mutation in *Arabidopsis*. Given that *MSH1* homologs are widespread, it is possible that variation in their function may explain differences in mutation rates between species. —Madeleine Seale

PLOS Genet. (2025)
10.1371/journal.pgen.1011764

CELL BIOLOGY

Mitochondrial depletion

In addition to generating ATP, mitochondria play key roles in regulating cell death and in signal transduction, cell differentiation, and developmental timing. However, the extent to which eukaryotic development depends on mitochondria remains unclear. Schmitz *et al.* developed a transgenic enforced mitophagy strategy to remove mitochondria from human and mouse pluripotent stem cells (PSCs) and mouse embryos. Mitochondria-depleted PSCs surprisingly retained pluripotency and mitochondrial gene expression, whereas embryos showed delayed preimplantation development. By fusing human PSCs, with or without mitochondria, with ape PSCs, the authors created interspecies hybrid PSCs containing species-specific mitochondrial DNA, uncovering species-specific transcriptional and metabolic differences. —Stella M. Hurtley

Cell (2025)
10.1016/j.cell.2025.05.020

FUNGAL BIOLOGY

The feast of us

Parasites often manipulate host behavior to benefit their own survival and reproduction. Zhao *et al.* investigated how the fungus *Cordyceps militaris* affects feeding in its caterpillar hosts. They found that infection by *C. militaris* triggers a starvation-like state in silkworms by reducing their blood sugar levels, leading to increased feeding and weight gain. The fungus achieves this by expressing a host-like trehalase enzyme that breaks down insect trehalose and by inducing the orexigenic peptide HemaP in caterpillars. This manipulation results in larger, fatter hosts that support better fungal growth and reproduction, revealing a novel strategy of parasite-host interaction. —Di Jiang

Curr. Biol. (2025)
10.1016/j.cub.2025.06.002

NEUROIMMUNOLOGY

Mast cells help plug permeable areas

As part of their role in host defense, mast cells release an array of mediators that promote inflammation. Mamuladze *et al.* found that mast cells accumulated in the outer membranes that surround and protect the brain near spaces that form around veins punctuating a barrier of epithelial cells. In mice, histamine released by mast cells promoted vasodilation, closing the spaces between the veins and the surrounding epithelial cells. The ability of mast cells to secure these gaps and recruit neutrophils to the area helped to prevent the spread of bacteria into the brain. This mast cell–mediated defense mechanism did have a consequence: It temporarily decreased the circulation of cerebrospinal fluid, which could affect the clearance of metabolic waste from the brain. —Sarah H. Ross

Cell (2025)
10.1016/j.cell.2025.06.046

ORGANOMETALLICS

Getting sodium into solution

Organolithium compounds are widely used in molecular synthesis as exceptionally strong bases. By contrast, sodium analogs tend to suffer from poor solubility, which limits their application. Anderson *et al*. report the synthesis and isolation of neopentyl sodium through an exchange reaction between sodium tert-butoxide and neopentyl lithium. They determined the solid-state structure, in which sodium cations and neopentyl anions occupy opposite vertices of a cube and also took advantage of the compound's solubility in hydrocarbons to deprotonate arenes for carboxylations and borylations. —Jake S. Yeston

Angew. Chem. Int. Ed. (2025)
10.1002/anie.202511492

FIRE HISTORY

Rise in human fires by 50,000 years ago

Through most of the Pleistocene, fires fluctuated with seasonal and longer bioclimatic cycles. Precisely when humans began to play a significant role is being resolved by studying archeological sites and looking at pyrogenic carbon in marine sediments. Sampling cores from International Ocean Drilling Site U1429, Jiang *et al.* measured pyrogenic carbon content and flux for northern East Asia over the past 300,000 years. Their data, combined with records from Europe, Southeast Asia, and the Papua New Guinea-Australia region, suggest a major shift in human fire use about 50,000 years ago, well before the Last Glacial Maximum. —Angela Hessler

Proc. Natl. Acad. Sci. U.S.A. (2025)
10.1073/pnas.2500042122

ROBOTICS

Freedom to move around

Human hands can grasp and reorient an object through a twisting of the wrist that does not require reorientation of the entire arm. Robotic arms that use simple grippers and wrists with three degrees of freedom cannot achieve this because of the separation between the gripper and the wrist. Patel and Dollar designed a robot hand mechanism starting from a 3-RRS wrist, where the R refers to revolute joints that allow hinge-like motion and the S is a spherical joint similar to a ball and socket, to which they added actuation to the two revolute axes on each finger. This design allows for pure spherical rotations of a grasped object around a fixed point near to the object, and this point is independent of object shape or initial grasp. Grasped objects can be rotated over large angles with simple open-loop control. —Marc S. Lavine

Nat. Mach. Intell. (2025)
10.1038/s42256-025-01039-1

RESEARCH ARTICLE SUMMARY

SINGLE-CELL ANALYSIS

Stereo-cell: Spatial enhanced-resolution single-cell sequencing with high-density DNA nanoball–patterned arrays

Sha Liao†, Xiaoxi Zhou†, Chuanyu Liu†, Chang Liu†, Shijie Hao†, Hongyu Luo†, *et al.*

Full article and list of author affiliations:
https://doi.org/10.1126/science.adr0475

INTRODUCTION: Single-cell sequencing has transformed our ability to study cellular diversity and molecular function. However, most existing methods require trade-offs between throughput, sensitivity, and compatibility with diverse cell types. Limitations in capture uniformity and compatibility with different cell sizes or experimental modalities restrict their utility in applications such as unbiased cell detection, analysis of in situ microenvironments or cell-cell interactions, and integration with spatial or multimodal assays.

RATIONALE: We hypothesized that high-density DNA nanoball (DNB)–patterned arrays, with their planar architecture and nanometer-scale resolution, could enable a single-cell sequencing strategy based on in situ transcript capture without the need for compartmentalized encapsulation. This design would support direct profiling of small to large cells, extracellular vesicles, and microstructures. To this end, we developed Stereo-cell, a spatially resolved, high-throughput single-cell transcriptomic platform built on DNB arrays. This system enables scalable, unbiased capture of cells across a wide input range and supports high-fidelity transcriptome profiling while also allowing integration with multiplexed imaging and multiomics workflows.

RESULTS: Stereo-cell accurately and efficiently captured transcriptomes from a broad range of cell types, with input sizes spanning from as few as 200 to nearly 1 million cells per chip. The platform demonstrated high reproducibility and robust performance across different cell loading densities, with consistent transcript detection and minimal doublet rates, supported by deep learning–based cell segmentation and imaging-based doublet elimination. In benchmarking studies that used human peripheral blood mononuclear cells (PBMCs), Stereo-cell generated gene expression profiles closely matching those obtained from established droplet-based methods while recovering cell-type proportions that aligned more faithfully with flow cytometry reference data. Notably, Stereo-cell identified rare immune populations, such as hematopoietic stem and progenitor cells, from large-scale samples. Integration with multiplex immunofluorescence and oligo-barcoded antibodies enabled concurrent profiling of mRNA and protein markers, revealing distinct immune activation states and uncovering phenotypic diversity not apparent from RNA alone. Stereo-cell further enabled in situ profiling of cultured fibroblasts, capturing microenvironmental cues, extracellular vesicle–like structures based on distinct gene signatures and imaging data, and fibroblast responses to stimulation. Stereo-cell succeeded in sequencing structurally complex and oversized samples, including mouse oocytes and multinucleated skeletal myofibers, while preserving transcript localization at subcellular resolution. RNA staining validation and spatial gene module analysis confirmed Stereo-cell's capability to resolve intracellular transcript architecture and microenvironmental organization.

CONCLUSION: Stereo-cell establishes an integrative framework for high-throughput single-cell transcriptomics with spatial and multimodal capabilities. This platform overcomes key limitations of existing methods, improving scalability, flexibility, and precision in profiling cell-cell interactions, microenvironments, and subcellular gene expression. These improvements underscore the expansive potential of Stereo-cell across a spectrum of applications. □

Corresponding author. Longqi Liu (liulongqi@genomics.cn); Ao Chen (chenao@genomics.cn); Xun Xu (xuxun@genomics.cn) †These authors contributed equally to this work.
Cite this article as S. Liao *et al*., *Science* 389, eadr0475 (2025). DOI: 10.1126/science.adr0475

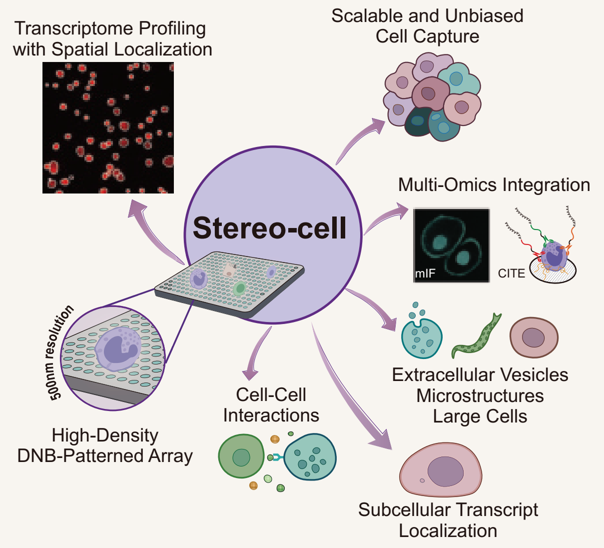

Stereo- cell: A single-cell multimodal platform. Stereo-cell leverages high-density DNB-patterned arrays for scalable and unbiased cell capture, enabling single-cell transcriptome profiling, integration with multiomics workflows as well as in situ analysis of cell-cell interactions, structurally complex and oversized samples, and subcellular transcript localization. mIF, multiplex immunofluorescence. CITE, cellular indexing of transcriptomes and epitopes.

RESEARCH ARTICLE SUMMARY

ARCHAIC HOMININS

The *MUC19* gene: An evolutionary history of recurrent introgression and natural selection

Fernando A. Villanea†, David Peede†, Eli J. Kaufman, Valeria Añorve-Garibay, Elizabeth T. Chevy, Viridiana Villa-Islas, Kelsey E. Witt, Roberta Zeloni, Davide Marnetto, Priya Moorjani, Flora Jay, Paul N. Valdmanis, María C. Ávila-Arcos, Emilia Huerta-Sánchez*

Full article and list of author affiliations:
https://doi.org/10.1126/science.adl0882

INTRODUCTION: Modern human genomes contain a small number of archaic variants, the legacy of past interbreeding events with Neanderthals and Denisovans. Most of these variants are putatively neutral, but some archaic variants found in modern humans have been targets of positive natural selection and may have been pivotal for adapting to new environments as humans populated the world. American populations encountered a myriad of novel environments, providing the opportunity for natural selection to favor archaic variants in these new environmental contexts. Indigenous and admixed American populations have been understudied in this regard but present great potential for studying the underlying evolutionary processes of local adaptation.

RATIONALE: Previous studies identified the gene *MUC19*—which codes for a mucin involved in immunity—as a candidate for introgression from Denisovans as well as a candidate for positive natural selection in present-day Indigenous and admixed American populations. Therefore, we sought to confirm and further characterize signatures of both archaic introgression and positive selection at *MUC19*, with particular interest in modern and ancient American populations.

RESULTS: We identify an archaic haplotype segregating at high frequency in most admixed American populations, and among ancient genomes from 23 ancient Indigenous American individuals who predate admixture with Europeans and Africans. We conclude that the archaic haplotype has undergone positive natural selection in these populations, which is tied to their Indigenous components of ancestry. We also find that modern admixed American individuals exhibit an elevated number of variable number tandem repeats (VNTRs) at *MUC19*, which codes for the functional domain of the MUC19 protein, where it binds to oligosaccharides to form a glycoprotein, a characteristic of the mucins. Remarkably, we find an association between the number of VNTRs and the number of introgressed haplotypes; individuals harboring introgressed haplotypes tend to have a higher number of VNTRs. In addition to the differences in VNTRs, we find that the archaic *MUC19* haplotype contains nine Denisovan-specific, nonsynonymous variants found at high frequencies in American populations. Finally, we observed that the Denisovan-specific variants are contained in a 72-kb region of the *MUC19* gene, but that region is embedded in a larger 742-kb region that contains Neanderthal-specific variants. When we studied *MUC19* in three high-coverage Neanderthal individuals, we found that the Chagyrskaya and Vindija Neanderthals carry the Denisovan-like haplotype in its heterozygous form. These two Neanderthals also carry another haplotype that is shared with the Altai Neanderthals.

CONCLUSION: Our study identifies several aspects of the gene *MUC19* that highlight its importance for studying adaptive introgression: One of the haplotypes that span this gene in modern humans is of archaic origin, and modern humans inherited this haplotype from Neanderthals who likely inherited it from Denisovans. Then, as modern human populations expanded into the Americas, our results suggest that they experienced a massive coding VNTR expansion, which occurred on an archaic haplotype background in *MUC19*. The functional impact of the variation at this gene may help explain how mainland Indigenous Americans adapted to their environments, which remains underexplored. Our results point to a complex pattern of multiple introgression events, from Denisovans to Neanderthals and Neanderthals to modern humans, which may have later played a distinct role in the evolutionary history of Indigenous American populations. ☐

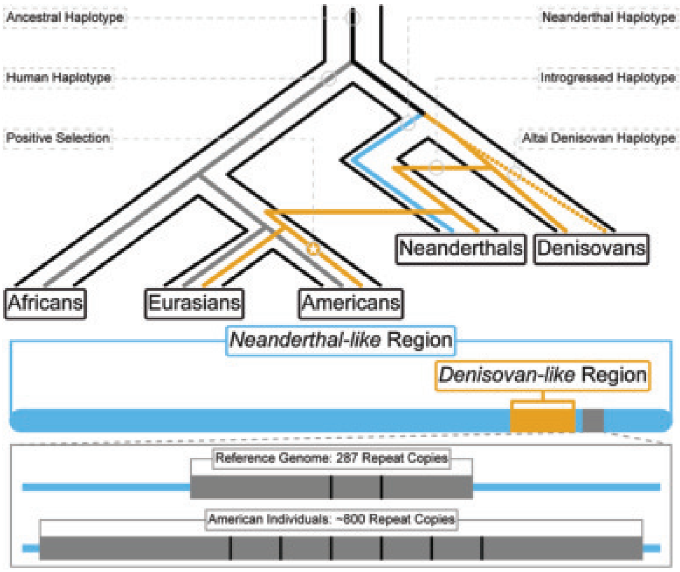

The proposed evolutionary history of *MUC19*. The Denisovan-like haplotype (in orange) was first introgressed from Denisovans into Neanderthals and then introgressed into modern humans. The introgressed haplotype later experienced positive selection in populations from the Americas. The introgressed *MUC19* haplotype is composed of a 742-kb region that contains Neanderthal-specific variants (blue). Embedded within this Neanderthal-like region is a 72-kb region containing a high density of Denisovan-specific variants (orange), and an exonic variable number tandem repeat (VNTR) region (gray). The box below the 742-kb region depicts zooming into the *MUC19* VNTR region, in which admixed American individuals carry an elevated number of tandem repeat copies.

---

*Corresponding author. Email: emilia_huerta-sanchez@brown.edu †These authors contributed equally to this work.

Cite this article as F. Villanea *et al*., *Science* 389, eadl0882 (2025). DOI:10.1126/science.adl0882

BACTERIAL IMMUNITY

Disassembly activates Retron-Septu for antiphage defense

Chen Wang†, Anthony D. Rish†, Emily G. Armbruster, Jiale Xie, Anna B. Loveland, Zhangfei Shen, Bradley Gu, Andrei A. Korostelev, Joe Pogliano, Tian-Min Fu*

Full article and list of author affiliations: https://doi.org/10.1126/science.adv3344

INTRODUCTION: The Retron-Septu system represents a fusion of two bacterial antiphage defense modules: a retron (composed of a reverse transcriptase and multicopy single-stranded DNA, or msDNA) and the Septu adenosine triphosphatase (ATPase)–HNH nuclease complex (PtuAB). Although retrons are gaining attention as promising genome-editing tools, the molecular principles governing their assembly and activation remain poorly understood.

RATIONALE: Despite the widespread distribution and biotechnological potential of retron systems, their mechanisms of activation are largely unexplored. Leveraging the hybrid Retron-Septu system as a model, we sought to uncover core mechanistic principles that may be generalizable to other retrons.

RESULTS: We reconstituted two *Escherichia coli* Retron-Septu systems, Ec83 and Ec78 (also known as Eco4 and Eco7, respectively), and found that the reverse transcriptase (RT), msDNA, and the PtuAB subcomplex form a large, asymmetric nucleoprotein complex. Notably, some PtuAB subcomplexes remain dissociated in solution, suggesting a dynamic assembly-disassembly equilibrium that may regulate activity.

Cryo–electron microscopy structures of the retron Ec83-Septu and retron Ec78-Septu complexes revealed that msDNA plays a central architectural role: It binds both the RT and PtuAB, effectively “gluing” these components together into an asymmetric complex.

To test the functional consequence of this architecture, we conducted in vitro biochemical assays. We found that the intact Retron-Septu complex is catalytically inactive, whereas the dissociated PtuAB subcomplex develops strong nuclease activity specifically toward single-stranded DNA (ssDNA), but not tRNA, single-stranded RNA (ssRNA), or double-stranded DNA (dsDNA). Further, electrophoretic mobility shift assays showed that PtuA binds to DNA, positioning PtuB for efficient cleavage. Structural analysis of the dissociated PtuAB subcomplex, reconstituted PtuAB complex, and PtuA dimer confirmed conformational rearrangements that accompany activation.

To directly test whether complex disassembly is essential for activation, we engineered disulfide–cross-linked retron Ec83-Septu complex. Locking the complex in its intact state abolished Ec83 antiphage defense, confirming that disassembly is essential for function.

Finally, time-course imaging of T5n phage infection in *E. coli* showed that the retron Ec83-Septu system restricts phage replication, linking the molecular activation mechanism to a physiological immune response.

CONCLUSION: Our study uncovers a disassembly-driven mechanism in which msDNA acts as a molecular glue to maintain the Retron-Septu system in an autoinhibited state. Phage-induced degradation of msDNA triggers complex disassembly, liberating the PtuAB subcomplex to cleave ssDNA and restrict phage replication. This contrasts sharply with classical immune activation paradigms based on oligomerization and instead highlights disassembly as a previously unknown regulatory strategy in bacterial immunity. These findings provide a conceptual framework for understanding and engineering retron systems for genome engineering. ☐

---

*Corresponding author. Email: tianmin.fu@umassmed.edu †These authors contributed equally to this work. Cite this article as C. Wang *et al*., *Science* **389**, eadv3344 (2025). DOI: 10.1126/science.adv3344

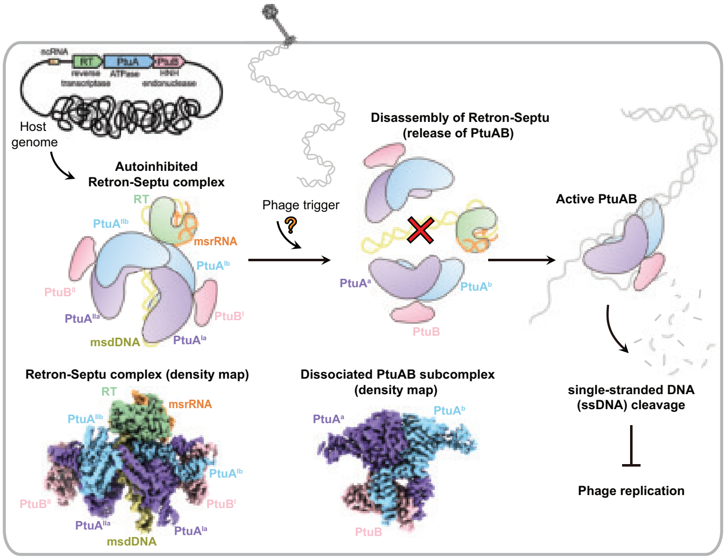

Mechanism of Retron-Septu assembly and activation. RT, msDNA, and PtuAB assemble into an autoinhibited complex, in which msDNA acts as a molecular glue bridging RT and PtuAB. Upon phage infection, degradation of msDNA triggers complex disassembly, releasing PtuAB to cleave single-stranded DNA and restrict phage replication.

RESEARCH ARTICLE SUMMARY

CELL BIOLOGY

LYVAC/PDZD8 is a lysosomal vacuolator

Haoxiang Yang†, Jinrui Xun†, Yajuan Li, Awishi Mondal, Bo Lv, Simon C. Watkins, Lingyan Shi, Jay Xiaojun Tan*

Full article and list of author affiliations:
https://doi.org/10.1126/science.adz0972

INTRODUCTION: Lysosomes degrade a wide range of macromolecules, supporting cellular growth, metabolism, and stress resilience. Under various pathophysiological conditions, including lysosomal storage disorders, aging, infection, and neurodegeneration, lysosomes can form large vacuoles associated with lysosomal dysfunction. Although lysosomal vacuolation has been observed for decades and is presumed to be an adaptive stress response, its underlying mechanisms and physiological functions remain poorly understood.

RATIONALE: Lysosomal vacuolation could potentially result from lysosomal osmotic stress owing to increased luminal solute load, which would drive water influx and membrane swelling. Lysosomal osmotic stress can be induced by diverse stimuli, including lysosomotropic weak bases, storage substrates such as sucrose, or a hypotonic extracellular environment. In several disease models, including prion diseases and cadmium toxicity, lysosomal vacuolation is linked to loss of function of the lipid kinase PIKfyve, which in turn causes lysosomal osmotic stress by triggering ion storage. We used PIKfyve inhibition in human cell lines as a model of lysosomal vacuolation to explore the molecular mechanisms underlying vacuole formation.

RESULTS: Our proteomics analysis identified PDZD8 (PDZ domain–containing 8), which we propose to be renamed as LYVAC (lysosomal vacuolator), as the top hit selectively enriched on vacuolating lysosomes after PIKfyve inhibition. LYVAC is an endoplasmic reticulum (ER)–anchored lipid transfer protein, suggesting its potential role in mediating vacuole formation by transferring lipids from the ER to lysosomes.

Genetic deletion of LYVAC strongly suppressed lysosomal vacuolation caused by either inhibition or genetic deletion of PIKfyve. LYVAC was also essential for lysosomal vacuolation triggered by a variety of unrelated stressors, including weak base compounds, sucrose storage, and hypotonic stress. These findings establish LYVAC as a general mediator of lysosomal vacuole formation.

LYVAC was recruited to lysosomes under all tested vacuolating conditions, each of which induced lysosomal osmotic stress. LYVAC and another lipid transfer protein, ATG2, selectively responded to lysosomal osmotic stress and membrane damage, respectively.

Domain analysis revealed that LYVAC was recruited through multivalent weak interactions mediated by two distinct domains: one that binds to RAB7, a marker of late endosomes and lysosomes, and another that binds to negatively charged lipids, particularly phosphatidylserine (PS). Lysosomal osmotic stress triggered phosphoinositide signaling that drove the ER-to-lysosome transfer of PS and cholesterol, both of which were required for lysosomal vacuolation.

PS and cholesterol not only promoted LYVAC recruitment but also activated its lipid transfer function. The lipid transfer domain of LYVAC directly binds to PS- and cholesterol-enriched membranes through conserved motifs recognizing the presence of both PS and cholesterol. In cells, label-free chemical imaging revealed LYVAC-dependent large-scale, ER-to-lysosome lipid movement after vacuole induction. In vitro reconstitution assays and molecular dynamics simulations supported the idea that this directional lipid movement was driven by lysosomal osmotic membrane tension and lipid composition differences between the ER and lysosomes.

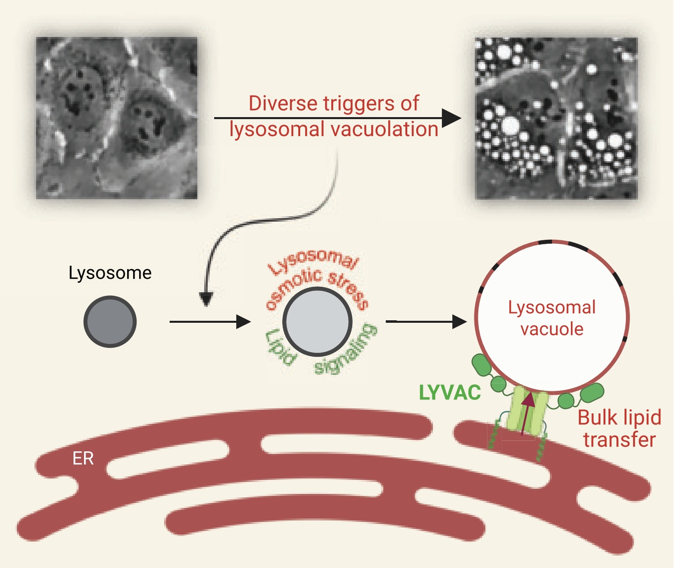

LYVAC/PDZD8 mediates lysosomal vacuolation through ER-to-lysosome lipid transfer. Diverse lysosomal vacuolation inducers trigger lysosomal osmotic stress and lipid signaling, which in turn recruits and activates LYVAC to mediate bulk lipid transfer from the ER to lysosomes, leading to vacuole formation. LYVAC-dependent lysosomal vacuolation may help manage cellular responses to a wide range of pathophysiological conditions involving lysosomal osmotic imbalance. [Figure created with BioRender.com]

CONCLUSION: Our study identifies LYVAC-mediated, directional ER-to-lysosome lipid transfer as an essential mechanism for lysosomal vacuolation. Diverse vacuolating stimuli converged on a common pathway involving lysosomal osmotic stress, lipid signaling, and regulation of LYVAC recruitment and lipid transfer. By linking lysosomal osmotic imbalance to vacuole formation, LYVAC underlies a robust cellular response with broad implications for lysosomal adaptation, osmoresilience, lysosomal storage pathology, and neurodegeneration. □

---

*Corresponding author. Email: jay.tan@pitt.edu †These authors contributed equally to this work. Cite this article as H. Yang *et al.*, *Science* **389**, eadz0972 (2025). DOI: 10.1126/science.adz0972

EVOLUTION

Recent evolution of the developing human intestine affects metabolic and barrier functions

Qianhui Yu†, Umut Kilik†, Stefano Secchia†, *et al.*

Full article and list of author affiliations:
https://doi.org/10.1126/science.adr8628

INTRODUCTION: The innovation of cooking and the transition from hunter-gatherer to agricultural societies created a distinctly human gut environment compared with that of our great ape relatives. The modern human intestine exhibits distinct morphological, metabolic, and immunological adaptations, including an increase in the allometric relationship between the small and large intestines. Intestinal epithelial cells directly interface with the luminal environment, facilitating nutrient absorption while forming a barrier against microbiota. Prenatal gene regulatory mechanisms orchestrate intestinal development and function; however, the species-specific molecular adaptations of epithelial cells remain poorly understood.

RATIONALE: Cross-species comparisons of genomic sequences, gene expression, and chromatin accessibility can link evolutionary changes to cellular function at the molecular level. Pluripotent stem cell–derived intestinal organoids model intestinal development, which enables the study of otherwise inaccessible developing chimpanzee tissues and functional assays in physiologically relevant contexts. We integrated single-cell sequencing data from developing human and mouse intestinal tissues with data from great ape intestinal organoids and used comparative genomics to characterize the evolutionary dynamics of intestinal cell types and their molecular machinery. We then performed functional assays in human organoids to examine how human-specific selection on gene regulatory regions affects gene expression.

RESULTS: Assessment of nonsynonymous-to-synonymous substitution ratios of expressed genes and deepest ancestry analysis of accessible regulatory regions revealed that enterocytes of the developing human intestinal epithelium are rapidly evolving. We identified genes with human-specific expression profiles and associated open chromatin regions with differential accessibility between humans and chimpanzees in epithelial cells. These findings, combined with evolutionary rate analysis, indicate recent evolutionary changes in the human intestinal epithelium, particularly in barrier function and metabolism. We cataloged and ranked epithelial regulatory regions by composite evolutionary selection signatures and then conducted functional assays on top candidates in human small intestinal organoids. We validated a cis-regulatory region in the *MCM6* gene as a functional enhancer for the *LCT* gene, suggesting how a positively selected polymorphism associated with lactose tolerance in adulthood disrupts a repressor-binding site. We functionally highlight several other recent gene regulatory changes in regions associated with *PDX1*, *RBP2*, and *IGFPB2*. Notably, *IGFBP2* has two enhancers overlapping human accelerated regions and exhibiting higher chromatin accessibility in developing human intestinal epithelial cells compared with chimpanzee counterparts. In silico mutagenesis predictions and variant-resolved enhancer assays confirmed elevated enhancer activity of selected loci compared with the ancestral sequence. CRISPR-Cas9 deletion of each enhancer reduced *IGFBP2* gene expression in small intestinal organoids.

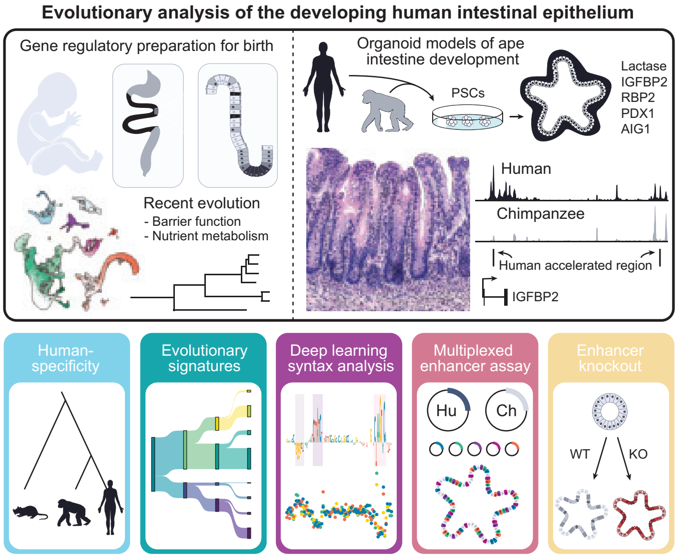

Recent evolution affects the developing human intestine epithelium. Comparative genomic analysis of expressed genes and accessible regulatory regions in developing human intestinal epithelium revealed recent evolutionary changes affecting metabolism and barrier function. Human and chimpanzee pluripotent stem cell (PSC)–derived organoids, combined with primary developing human and mouse intestinal tissues, identified regulatory regions selected in human controlling cell type–dependent gene expression. Enhancer assays and loss-of-function experiments in organoids provided functional validation. WT, wild-type; KO, knockout.

CONCLUSION: Our work highlights the interface between humans and our external environment during developmental stages, when metabolic and barrier functions are being established. We characterized recent evolutionary dynamics in the developing human intestine, identified human-specific molecular features, and functionally evaluated regulatory regions in a complex human model system. The human selection signatures and the elevated chromatin accessibility of two functionally validated enhancers of *IGFBP2* in humans suggest that recent evolutionary modifications within the insulin and insulin-like signaling pathways affect human small intestine development. This research advances our understanding of human intestinal gene regulatory mechanisms in an evolutionary context and reveals the functional effects of human-specific selection that may contribute to modern disease risks. □

Corresponding authors: Craig B. Lowe (craig.lowe@duke.edu); Jason R. Spence (spencejr@umich.edu); J. Gray Camp (jarrettgrayson.camp@unibas.ch) †These authors contributed equally to this work. **Cite this article as Q. Yu *et al.*, *Science* 389, eadr8628 (2025). DOI: 10.1126/science.adr8628**

QUANTUM SIMULATION

Universal coarsening in a homogeneous two-dimensional Bose gas

Martin Gazo[1]*, Andrey Karailiev[1], Tanish Satoor[1], Christoph Eigen[1], Maciej Gałka[1,2], Zoran Hadzibabic[1]

Coarsening of an isolated far-from-equilibrium quantum system is a paradigmatic many-body phenomenon, relevant from subnuclear to cosmological length scales and predicted to feature universal dynamic scaling. Here, we observed universal scaling in the coarsening of a homogeneous two-dimensional Bose gas, with exponents that match analytical predictions. For different initial states, we reveal universal scaling in the experimentally accessible finite-time dynamics by elucidating and accounting for the initial-state-dependent prescaling effects. The methods we introduce allow direct comparison between cold-atom experiments and nonequilibrium field theory and are applicable to any study of universality far from equilibrium.

Understanding the dynamics of order formation in many-body systems is a long-standing problem in contexts that include critical phenomena (*1*), driven systems (*2*), and active matter (*3*, *4*). Of particular interest are general ordering principles that are independent of the microscopic details of a system. A prime example of this is coarsening, the emergence of order characterized by a single length scale that grows in time (*5*, *6*). In systems that can exchange energy with the environment, coarsening is intuitively linked with cooling, most notably through a phase transition. However, the problem is more intricate if a far-from-equilibrium system is isolated and relaxes toward equilibrium only under the influence of internal interactions (*7*–*10*). In this case, coarsening commonly involves bidirectional dynamics in momentum space, with most excitations flowing toward lower wave numbers k, but the conserved energy flowing to high k.

The framework of nonthermal fixed points (*8*, *10*, *11*) aims to provide a unifying picture of relaxation in isolated far-from-equilibrium systems, including the early universe undergoing reheating (*12*), quark-gluon plasma in heavy-ion collisions (*13*), quantum magnets (*14*), and ultracold atomic gases (*15*–*22*). In all these cases, relaxation is expected to feature self-similar dynamic scaling; this spatiotemporal analog of the spatial scale-invariance in equilibrium systems near critical points (*23*) could allow formulation of universality classes for far-from-equilibrium dynamics.

In experiments with highly controllable Bose gases, self-similar dynamics akin to the nonthermal fixed point predictions have been observed in a range of scenarios, including different dimensionalities and relaxation of both particle and spin distributions (*24*–*29*). However, many experimental and theoretical questions regarding the values of the scaling exponents remain open. A key challenge is that, for a generic initial state, universal scaling can be directly observed only for very long evolution times (*30*–*33*, *10*), which are difficult to access experimentally.

Here, we studied coarsening in a homogeneous two-dimensional (2D) Bose gas (*34*, *35*) by engineering different far-from-equilibrium initial states and measuring the momentum distributions $n_k(k)$ by matter-wave focusing (*36*, *37*). Crucially, by elucidating and accounting for the nonuniversal effects of initial conditions, we reveal the universal long-time scaling in finite-range experimental data, introducing methods applicable to any quantitative study of universality far from equilibrium. We found that the low-k [infrared (IR)] coarsening is characterized by the theoretically predicted dynamical exponent $z = 2$ (*19*, *22*) [see also (*5*, *7*, *18*, *21*, *38*)] and that the form of the self-similarly evolving n_k matches an analytical field-theory prediction (*19*); the high-k [ultraviolet (UV)] energy dynamics corresponds to weak four-wave turbulence (*39*).

The experiment: Bidirectional relaxation

We started with an interacting 2D condensate of $N = 7 \times 10^4$ atoms of ^{39}K in the lowest hyperfine state, confined in a square box trap (*40*) of size $L = 50$ μm. In equilibrium, a 2D gas undergoes the Berezinskii-Kosterlitz-Thouless (BKT) transition to a superfluid state (*40*, *41*), which, for an infinite system, is associated with quasi-condensation and no true long-range order; however, far below the critical temperature T_{BKT}, our finite-size gas is experimentally indistinguishable from a pure condensate (*41*, *42*). We prepared essentially pure condensates by evaporative cooling to $T \approx 20$ nK $\ll T_{\mathrm{BKT}} \approx 240$ nK, at which point we could not discern any thermal excitations (*43*); note that because most particles were in the condensate, the average thermal energy per particle was much smaller than $k_{\mathrm{B}}T$ (where k_{B} is the Boltzmann constant). After the cooling stage, we set the trap depth to approximately 800 nK for the preparation of our far-from-equilibrium states and the subsequent relaxation of the gas.

The interparticle interactions in our gas, characterized by the scattering length a, are tuneable by the magnetic Feshbach resonance at 402.7 G (*44*). To prepare our far-from-equilibrium initial states, we turned off the interactions ($a \rightarrow 0$) and shook the gas with a spatially uniform oscillating force F (see Fig. 1A). This destroyed the condensate

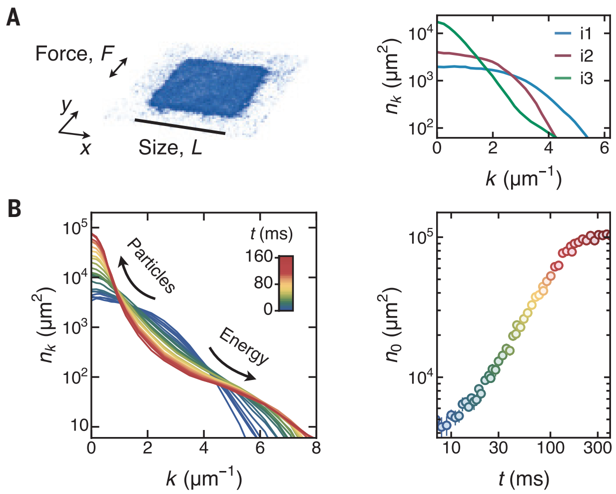

Fig. 1. Bidirectional relaxation in a box-trapped 2D Bose gas. (**A**) Starting with a quasi-pure condensate in a box of size $L = 50$ μm, we temporarily turned off the interatomic interactions and drove the gas with an oscillating force F to engineer different far-from-equilibrium momentum distributions i1 to i3. (**B**) After we stopped the driving and turned on interactions (at $t = 0$), the gas exhibited bidirectional relaxation, shown here for i2: Most particles flowed to the IR (low-k modes), whereas the net energy flow was to the UV (high k). The right panel shows $n_0(t) = n_k(k = 0, t)$, which characterizes the growth of the condensate; for $t \gtrsim 150$ ms, the observed growth of n_0 is limited by our k-space resolution. All measurements were repeated about 30 times and the error bars show the standard error of the mean (*62*).

---

[1]Cavendish Laboratory, University of Cambridge, Cambridge, UK. [2]Physikalisches Institut der Universität Heidelberg, Heidelberg, Germany. ***Corresponding author. Email: mg816@cam.ac.uk**

and, as previously studied in 3D (*45*, *46*), resulted in an isotropic highly nonthermal momentum distribution. After preparing one of the three different initial states, i1 to i3, shown in Fig. 1A, we stopped the shaking, reinstated the interactions, and let the gas relax; we set $a \to 30\ a_0$ (where a_0 is the Bohr radius), which for our gas corresponds to the dimensionless 2D coupling strength $\tilde{g} \approx 0.03$ and the inverse healing length $k_\xi = \sqrt{N\tilde{g}/L^2} \approx 1\ \mu\text{m}^{-1}$ (*41*).

The states i1 to i3 do not have a defined temperature, but $E = \int \varepsilon(k)\mathrm{d}k$, where $\varepsilon = \pi\hbar^2 k^3 n_k/m$, $\hbar$ is the reduced Planck constant and m is the atom mass, gives the total kinetic energy; we get $E/k_B = 4.1(3)$, 2.2(3), and 1.0(3) mK, for i1 to i3, respectively. Per particle, this approximately corresponds to values between 60 and 15 nK. Crucially, for all three initial states, E is sufficiently low for a condensate to reemerge during relaxation.

In Fig. 1B, we show for i2 the bidirectional dynamics of the full n_k distribution (left panel) and the growth of $n_0 = n_k(k = 0)$, which characterizes the growth of the condensate (right panel). Here, $t = 0$ corresponds to the time when the interactions are switched on and the relaxation starts.

Dynamic scaling theory

According to the dynamic scaling hypothesis, the evolution of n_k is given by

$$n_k(k,t) = \left(\frac{t}{t_0}\right)^{\alpha} \ell_0^d\, f\left[\left(\frac{t}{t_0}\right)^{\beta} k\ell_0\right] \tag{1}$$

where α and β are the scaling exponents, d is the system dimensionality, f is a dimensionless scaling function, and ℓ_0 is the characteristic length scale at an arbitrary reference time t_0. For bidirectional dynamics, such scaling should apply separately in the IR (with $\alpha, \beta > 0$) and the UV (with $\alpha, \beta < 0$), with the normalization of f depending on the value of the transport-conserved quantity.

In our experiments, the IR dynamics were at $k \lesssim k_\xi$ (see Fig. 1B) and could, in principle, be dominated by either wave or vortex excitations (*47*). In both scenarios, theory predicts $\alpha/\beta = d = 2$, reflecting particle-conserving transport, and coarsening is then captured by the scaling

$$\ell(t) = \left(t/t_0\right)^{\beta} \ell_0 \tag{2}$$

Considering only wave excitations, analytical theory (*10*, *19*) predicts $\beta = 1/z = 1/2$, and for generic vortex-rich initial states, numerical simulations (*18*) give essentially the same β (*48*). However, the expected scaling functions are different depending on what dominates the dynamics. For waves, simulations (*22*, *49*) are captured by $f \propto 1/\left[1+\left(k/k_0\right)^{\kappa}\right]$, with $k_0 = 2\pi/\ell_0$ and analytically predicted exponent $\kappa = 3$ (*19*); by contrast, for vortices, $\kappa = 4$ is analytically predicted (*5*, *15*).

For our UV dynamics, at $k > k_\xi$, the prediction based on the theory of weak four-wave turbulence (*39*, *50*) is $\beta = -1/6$ and $\alpha = (d + 2)\beta = -2/3$ (*51*), with $\alpha/\beta = 4$ reflecting energy-conserving transport. In this case, the theory does not predict the scaling function f.

Crucially, this universal scaling should not depend on the initial conditions. Hence, a far-from-equilibrium system can exhibit such scaling only after it "forgets" its specific initial state.

Stages of relaxation: From nonuniversal to universal

To explain the different stages of relaxation, we focus on the IR dynamics, specifically on the growth of n_0, for which Eq. 1 reduces to

$$n_0(t) = At^{\alpha} \propto \ell^{d}(t) \tag{3}$$

with time-independent $A = \left(\ell_0^d/t_0^{\alpha}\right)f(0)$.

For a generic initial state, it first takes some nonuniversal time t_1 for n_k to acquire the scaling form f. At t_1, the system joins the scaling trajectory depicted in red in Fig. 2A, which follows Eq. 1. However, even for $t > t_1$, this equation does not directly give the system dynamics. Specifically, because the evolution is not universal for $t < t_1$, in general $n_0(t_1)$ differs from At_1^{α}. Rather, writing $n_0(t_1) = At_2^{\alpha}$ gives some $t_2 \neq t_1$, so the state of the system at t_1 is as if it had always followed the scaling trajectory but evolved for t_2. Then, defining $t^* = t_1 - t_2$, time-invariance of the Hamiltonian dictates that on the scaling trajectory, for $t > t_1$

$$n_0(t) = A(t - t^*)^{\alpha} \tag{4}$$

The system thus exhibits scaling with respect to $t_{\text{uni}} = t - t^*$, the "universal clock time" that is offset from t by a constant t^* that depends on the initial state (*52*). With respect to t, the system exhibits "prescaling" (*31*–*33*), with the flowing exponent $\mathrm{d}[\ln(n_0)]/\mathrm{d}[\ln(t)] = \alpha/(1 - t^*/t)$ (see Fig. 2B).

This flowing exponent coincides with the true α for $t \gg |t^*|$, but in practice, this regime may not be accessible or even exist; for example,

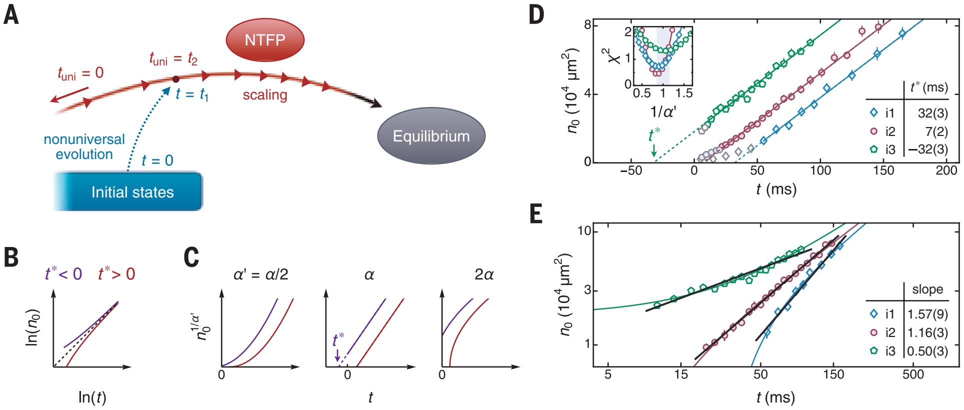

Fig. 2. Nonuniversal dynamics, prescaling, and the universal-scaling exponents. (**A**) A system starting in a generic initial state takes some nonuniversal time t_1 to join the scaling trajectory (red) associated with a nonthermal fixed point (NTFP). At t_1, its state is the same as if it had always been on this trajectory and evolved for some $t_2 \neq t_1$. At $t > t_1$, it exhibits scaling with respect to the universal-clock time $t_{\text{uni}} = t - t^*$, where $t^* = t_1 - t_2$ can be positive or negative. (**B**) $n_0 \propto (t - t^*)^{\alpha}$ shows "prescaling," with a flowing exponent $\mathrm{d}[\ln(n_0)]/\mathrm{d}[\ln(t)] = \alpha/(1 - t^*/t)$ that asymptotically approaches α. (**C**) One can deduce α from finite-t data using the fact that $n_0^{1/\alpha'}(t)$ is linear only for $\alpha' = \alpha$. (**D**) Analysis of our i1 to i3 data (*62*). The main panel shows that the predicted $\alpha = 1$ gives straight lines that differ just in the intercepts t^*, and the inset shows $\chi^2(\alpha')$ for linear fits of $n_0^{1/\alpha'}$. The gray symbols indicate early times excluded from the analysis, and the shading in the inset indicates $1/\alpha' = 1.00 \pm 0.15$. (**E**) Log-log plots of $n_0(t)$ show different prescaling for each initial state. The converging colored lines, with slopes 1 for $t \gg |t^*|$, are the same as the straight ones in (D), whereas the naïve power-law fits shown in black have slopes that vary between 0.5 and 1.6.

(pre)scaling breaks down if a system approaches equilibrium, which in any finite-size system happens in finite time (*53*). However, one can deduce α from the prescaling data ($t > t_1$, but not necessarily $t \gg |t^*|$), as we show in Fig. 2C for two different t^* values: plotting $n_0^{1/\alpha'}(t)$ for various α′ gives a linear plot (with intercept t^*) only for $\alpha' = \alpha$.

In Fig. 2D, we show the results of such analysis for our data taken with initial states i1 to i3. The predicted $\alpha = 1$ gives three parallel straight lines, with the differences between the initial states fully captured by the intercepts t^*. In the inset, we show that requiring the linearity of $n_0^{1/\alpha}$ for i1 to i3 separately gives consistent α values (*54*).

For comparison, $n_0(t)$ plots in Fig. 2E show different prescaling for each initial state. Here, the slopes of naïve power-law fits (black), which approximate the instantaneous values of the flowing prescaling exponents, have values that vary between 0.5 and 1.6. Moreover, for the same data, these nonuniversal values also depend on how one defines $t = 0$; this choice is arbitrary, because any state during evolution can be treated as the initial one for further evolution. By contrast, our extraction of α is independent of this choice, because any arbitrary shift of t is simply absorbed by t^* (see fig. S2).

Universal coarsening

We now turn to the dynamics of the full IR distributions, leveraging the fact that we have deduced the nonuniversal t^* values for i1 to i3 from the n_0 data. In Fig. 3A, we show five n_k curves, for different initial states and evolution times, which illustrate that distributions corresponding to the same $t_{\text{uni}} = t - t^*$ are the same, irrespective of the initial conditions.

In Fig. 3B, we present all three datasets color-coded according to t_{uni} and show that they all collapse onto the same universal curve when scaled according to Eq. 1 with $t \to t_{\text{uni}}$, $\alpha = 1$, $\beta = 1/2$, and no free parameters (see also fig. S3). The collapsed data are fitted well by $C/[1 + (k/k_0)^\kappa]$ with $\kappa = 3$, in agreement with the analytical prediction for wave dynamics (*19*), and $k_0 = 2\pi/\ell_0 \approx 0.5\,\mu\text{m}^{-1}$ for the arbitrarily chosen $t_0 = 80$ ms; treating κ as a free parameter gives $\kappa = 2.9(2)$.

Note that this observation does not exclude the presence of some vortices in the gas but implies a bound on how many there are. Vortices do not observably affect n_k as long as their typical separation is much larger than $\ell(t)$, which in Fig. 3B grows approximately from $L/10$ to $L/3$ (see Eq. 2). This implies that at the end of the observed scaling, there are no more than a few (≪ 10) vortices present, whereas at the start there could be up to 10 times more.

Also note that universality requires only the exponents α, β, and κ to be the same for different initial states; we, however, observed that the IR dynamics for i1 to i3, measured with respect to t_{uni}, are essentially identical, even though the three states have very different energies (*55*). This "superuniversality" is restricted to states that have the same value of the transport-conserving quantity, which in the IR is the atom number.

UV dynamics

Finally, we discuss the complementary UV dynamics, for which the ideas from Fig. 2 also apply. For an arbitrary initial n_k, there is no reason for t_1 or t^* to be the same as in the IR. Moreover, in the UV, there is no fixed k at which $n_k \propto (t - t^*)^\alpha$ for $t > t_1$. However, the peaks of our energy spectra, $\varepsilon(k) \propto k^3 n_k$, provide a characteristic wave number $k_\varepsilon(t)$ (fig. S4A), for which Eq. 1 gives the asymptotic behavior $k_\varepsilon \propto t^{-\beta}$, and more generally, for $t > t_1$, one expects

$$k_\varepsilon^{-1/\beta} \propto t - t^* \tag{5}$$

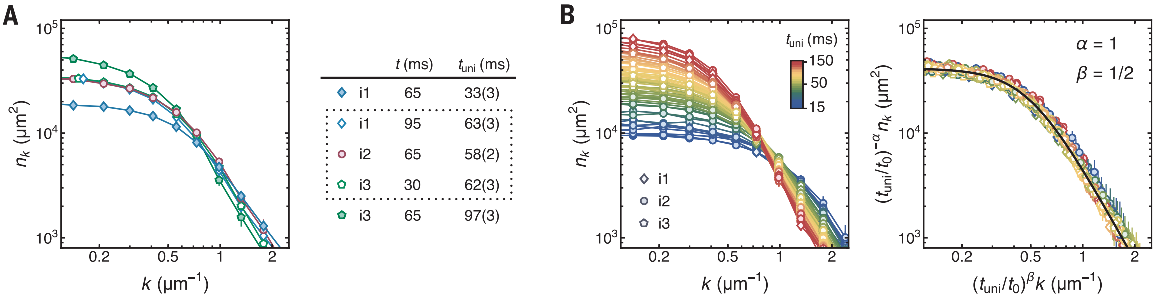

		t (ms)	t_{uni} (ms)
◆	i1	65	33(3)
◇	i1	95	63(3)
○	i2	65	58(2)
⬠	i3	30	62(3)
⬟	i3	65	97(3)

Fig. 3. Universal coarsening. (**A**) For i1 to i3, the IR distributions after the same evolution time t (here 65 ms) are different, but n_k at the same universal-clock time $t_{\text{uni}} = t - t^*$ (here ≈60 ms) are the same; the t^* values for i1 to i3 are those independently determined in Fig. 2D. (**B**) The n_k curves for all three initial states collapse onto a universal curve (right panel) according to Eq. 1 with $t \to t_{\text{uni}}$, $\alpha = 1$, and $\beta = 1/2$, without any free parameters (*62*); $t_0 = 80$ ms is an arbitrary reference time. The solid black line shows a fit to the collapsed data with $C/[1 + (k/k_0)^3]$.

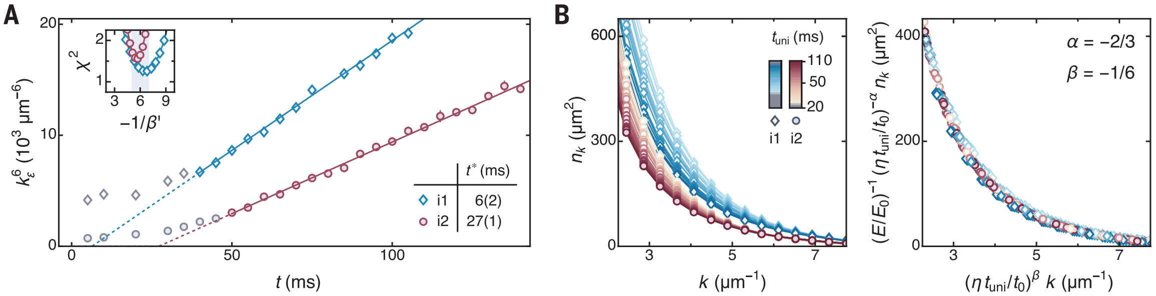

	t^* (ms)
◇ i1	6(2)
○ i2	27(1)

Fig. 4. UV dynamics, for i1 and i2. (**A**) Evolution of k_ε, the position of the peak of the energy spectrum, $\varepsilon \propto k^3 n_k$ (fig. S4). For the predicted $\beta = -1/6$, plotting $k_\varepsilon^{-1/\beta}(t)$ gives straight lines with intercepts t^*; the gray symbols indicate early times excluded from the analysis. The inset shows $\chi^2(\beta')$ for linear fits of $k_\varepsilon^{-1/\beta'}(t)$, with the shading indicating $-1/\beta' = 6 \pm 1$. (**B**) Dynamic scaling of the UV momentum distributions. The i1 and i2 curves labeled by $t_{\text{uni}} = t - t^*$ (left panel) collapse onto a single universal curve (right panel) when we (i) set $\alpha = -2/3$, $\beta = -1/6$, and the arbitrary $t_0 = 80$ ms; (ii) account for the different (energy-dependent) clock speeds by setting $\eta(\text{i2}) = 1$ and $\eta(\text{i1}) = 1.53$, the ratio of the dk_ε^6/dt slopes observed in (A); and (iii) normalize n_k by E, with E_0 arbitrarily set to $E(\text{i2}) = k_B \times 2.2$ mK (*62*).

One can thus use the ideas from Fig. 2C to determine β and t^*.

In Fig. 4, we show our results for initial states i1 and i2; for i3, with the lowest energy E, our high-k signal is too weak for a quantitative study. In Fig. 4A, we present the linearity of $k_\varepsilon^{-1/\beta}$ (with t^* intercepts) for the predicted $\beta = -1/6$ and show that treating β as a free parameter gives consistent values for both states (inset). Here, the transport-conserved quantity is E, which is not the same for i1 and i2, and we do not observe the superuniversality seen in the IR; whereas β is the same, $\mathrm{d}k_\varepsilon^6 / \mathrm{d}t$ is larger for the higher-energy i1, corresponding to a faster-running t_{uni} (faster evolution along a scaling trajectory).

In Fig. 4B, we show the dynamic scaling of the UV distributions. Simply setting $t \to t_{\mathrm{uni}}$, $\alpha = -2/3$, and $\beta = -1/6$ in Eq. 1 collapses the n_k curves shown in the left panel onto two separate curves, with normalizations set by E(i1) and E(i2) (fig. S4B). In the right panel of Fig. 4B, we normalize n_k by E, and the clock speeds by the observed $\mathrm{d}k_\varepsilon^6 / \mathrm{d}t$ slopes, which collapses all the data onto a single universal curve.

Discussion and outlook

Our experiments provide a comprehensive picture of universal coarsening dominated by wave excitations in a 2D Bose gas. More broadly, we establish methods for direct quantitative comparisons of experiments and analytical field theories of far-from-equilibrium phenomena. Specifically, we show how to extract the theoretically relevant asymptotic long-time evolution from the experimentally accessible finite-time dynamics.

Our analysis methods are equally applicable to studies of wave- and vortex-dominated dynamics (*47*), and in the future, one could look for vortex-dominated coarsening, with different dynamic-scaling exponents (*5*, *15*, *48*), by creating many vortices in an otherwise coherent condensate (*56*, *57*). It would also be interesting to extend our work to (miscible) two-component gases, with one component acting as a bath for the other, which would allow studies of the effects of a tunable openness of the system (*21*). Finally, studies in gases with a supersolid ground state (*58*) could reveal a fascinating interplay of coarsening and pattern-formation dynamics.

REFERENCES AND NOTES

1. P. C. Hohenberg, B. I. Halperin, *Rev. Mod. Phys.* **49**, 435–479 (1977).
2. M. C. Cross, P. C. Hohenberg, *Rev. Mod. Phys.* **65**, 851–1112 (1993).
3. S. Ramaswamy, *Annu. Rev. Condens. Matter Phys.* **1**, 323–345 (2010).
4. M. J. Bowick, N. Fakhri, M. C. Marchetti, S. Ramaswamy, *Phys. Rev. X* **12**, 010501 (2022).
5. A. J. Bray, *Adv. Phys.* **51**, 481–587 (2002).
6. L. F. Cugliandolo, *C. R. Phys.* **16**, 257–266 (2015).
7. K. Damle, S. N. Majumdar, S. Sachdev, *Phys. Rev. A* **54**, 5037–5041 (1996).
8. J. Berges, A. Rothkopf, J. Schmidt, *Phys. Rev. Lett.* **101**, 041603 (2008).
9. A. Polkovnikov, K. Sengupta, A. Silva, M. Vengalattore, *Rev. Mod. Phys.* **83**, 863–883 (2011).
10. A. N. Mikheev, I. Siovitz, T. Gasenzer, *Eur. Phys. J. Spec. Top.* **232**, 3393–3415 (2023).
11. J. Berges, G. Hoffmeister, *Nucl. Phys. B* **813**, 383–407 (2009).
12. R. Micha, I. I. Tkachev, *Phys. Rev. D* **70**, 043538 (2004).
13. J. Berges, K. Boguslavski, S. Schlichting, R. Venugopalan, *Phys. Rev. D* **89**, 074011 (2014).
14. S. Bhattacharyya, J. F. Rodriguez-Nieva, E. Demler, *Phys. Rev. Lett.* **125**, 230601 (2020).
15. B. Nowak, J. Schole, D. Sexty, T. Gasenzer, *Phys. Rev. A* **85**, 043627 (2012).
16. A. Piñeiro Orioli, K. Boguslavski, J. Berges, *Phys. Rev. D* **92**, 025041 (2015).
17. J. Berges, K. Boguslavski, S. Schlichting, R. Venugopalan, *Phys. Rev. Lett.* **114**, 061601 (2015).
18. M. Karl, T. Gasenzer, *New J. Phys.* **19**, 093014 (2017).
19. I. Chantesana, A. Piñeiro Orioli, T. Gasenzer, *Phys. Rev. A* **99**, 043620 (2019).
20. A. Chatrchyan, K. T. Geier, M. K. Oberthaler, J. Berges, P. Hauke, *Phys. Rev. A* **104**, 023302 (2021).
21. A. J. Groszek, P. Comaron, N. P. Proukakis, T. P. Billam, *Phys. Rev. Res.* **3**, 013212 (2021).
22. L. Gresista, T. V. Zache, J. Berges, *Phys. Rev. A* **105**, 013320 (2022).
23. P. M. Chaikin, T. C. Lubensky, *Principles of Condensed Matter Physics* (Cambridge Univ. Press, 1995).
24. M. Prüfer *et al.*, *Nature* **563**, 217–220 (2018).
25. S. Erne, R. Bücker, T. Gasenzer, J. Berges, J. Schmiedmayer, *Nature* **563**, 225–229 (2018).
26. J. A. P. Glidden *et al.*, *Nat. Phys.* **17**, 457–461 (2021).
27. A. D. García-Orozco *et al.*, *Phys. Rev. A* **106**, 023314 (2022).
28. S. Lannig *et al.*, arXiv:2306.16497 [cond-mat.quant-gas] (2023).
29. S. Huh *et al.*, *Nat. Phys.* **20**, 402–408 (2024).
30. V. M. Kendon, M. E. Cates, I. Pagonabarraga, J. C. Desplat, P. Bladon, *J. Fluid Mech.* **440**, 147–203 (2001).
31. A. Mazeliauskas, J. Berges, *Phys. Rev. Lett.* **122**, 122301 (2019).
32. C.-M. Schmied, A. N. Mikheev, T. Gasenzer, *Phys. Rev. Lett.* **122**, 170404 (2019).
33. M. P. Heller, A. Mazeliauskas, T. Preis, *Phys. Rev. Lett.* **132**, 071602 (2024).
34. L. Chomaz *et al.*, *Nat. Commun.* **6**, 6162 (2015).
35. N. Navon, R. P. Smith, Z. Hadzibabic, *Nat. Phys.* **17**, 1334–1341 (2021).
36. S. Tung, G. Lamporesi, D. Lobser, L. Xia, E. A. Cornell, *Phys. Rev. Lett.* **105**, 230408 (2010).
37. See supplementary materials.
38. N. P. Proukakis, *Encyclopedia of Condensed Matter Physics*, T. Chakraborty, Ed. (Academic Press, ed. 2, 2024), pp. 84–123.
39. S. Dyachenko, A. C. Newell, A. Pushkarev, V. E. Zakharov, *Physica D* **57**, 96–160 (1992).
40. P. Christodoulou *et al.*, *Nature* **594**, 191–194 (2021).
41. Z. Hadzibabic, J. Dalibard, *Riv. Nuovo Cim.* **34**, 389–434 (2011).
42. N. V. Prokof'ev, B. V. Svistunov, *Phys. Rev. A* **66**, 043608 (2002).
43. $T \approx 20$ nK is an estimate based on the fact that during evaporation, we lowered the trap depth to 100 nK, and at earlier stages of evaporation, the temperature was about one-fifth of the trap depth.
44. J. Etrych *et al.*, *Phys. Rev. Res.* **5**, 013174 (2023).
45. G. Martirosyan *et al.*, *Phys. Rev. Lett.* **132**, 113401 (2024).
46. Y. Zhang *et al.*, *C. R. Phys.* **24S3**, 153–171 (2023).
47. The large-scale forcing (*45*, *59*, *60*) we used to prepare our far-from-equilibrium initial states a priori favors wave over vortex excitations, but our analysis does not presume the dominance of waves during coarsening; it is the observed exponent κ that reveals which excitations are dominant.
48. Note that numerical simulations for some specific initial vortex configurations found an "anomalous" $\beta \approx 0.2$ (*18*, *61*).
49. R. Walz, K. Boguslavski, J. Berges, *Phys. Rev. D* **97**, 116011 (2018).
50. S. Nazarenko, *Wave Turbulence* (Springer, 2011).
51. The corresponding prediction for weak three-wave turbulence, $\beta = -1/4$ and $\alpha = -1$, assumes a time-independent n_0 and is not applicable here. If the UV dynamics in our experiments were dominated by three-wave interactions, they would have to be even "faster" (with larger $|\beta|$), owing to the growing n_0.
52. Note that a similar mathematical structure appears in the analysis of finite-capacity turbulent cascades (*50*), but with $t \to t^* - t$; in that case, t^* denotes the time at which the scaling ends.
53. In our case, n_0 saturates at long times because of our k-space resolution, rather than because the gas approaches equilibrium, so the (pre)scaling might extend further in time than we observed.
54. In additional experiments, we also changed the scattering length to 45 a_0 and still found α consistent with 1 (fig. S1).
55. This is also hinted at by the fact that the three lines in Fig. 2D are parallel.
56. G. Gauthier *et al.*, *Science* **364**, 1264–1267 (2019).
57. S. P. Johnstone *et al.*, *Science* **364**, 1267–1271 (2019).
58. T. Bland *et al.*, *Phys. Rev. Lett.* **128**, 195302 (2022).
59. N. Navon, A. L. Gaunt, R. P. Smith, Z. Hadzibabic, *Nature* **539**, 72–75 (2016).
60. M. Gałka *et al.*, *Phys. Rev. Lett.* **129**, 190402 (2022).
61. A. J. Groszek, M. J. Davis, T. P. Simula, *SciPost Phys.* **8**, 039 (2020).
62. M. Gazo *et al.*, Research data supporting "Universal coarsening in a homogeneous two-dimensional Bose gas." Apollo - University of Cambridge Repository (2025); https://doi.org/10.17863/CAM.116865.

ACKNOWLEDGMENTS

We thank G. Martirosyan, J. Etrych, C. Ho, Y. Zhang, N. Dogra, P. Christodoulou, R. Smith, T. Gasenzer, M. Oberthaler, and A. Mazeliauskas for discussions and comments on the manuscript. **Funding:** This work was funded by Engineering and Physical Sciences Research Council grant no. EP/P009565/1, the European Research Council (UniFlat), Science and Technology Facilities Council grant nos. ST/T006056/1 and ST/Y004469/1, Germany's Excellence Strategy EXC2181/1-390900948 (Heidelberg Excellence Cluster; STRUCTURES) (to M.Gał.), and a Royal Society Wolfson Fellowship (Z.H.). **Author contributions:** M.Gaz. led the data collection and analysis. All authors contributed to the interpretation of the results, with the most significant contributions from M.Gaz., M.Gał., and Z.H. All authors contributed to the preparation of the manuscript. Z.H. supervised the project. **Competing interests:** The authors declare that they have no competing interests. **Data and materials availability:** The data that support the findings of this study are available in Apollo - University of Cambridge Repository (*62*). **License information:** Copyright © 2025 the authors, some rights reserved; exclusive licensee American Association for the Advancement of Science. No claim to original US government works. https://www.science.org/about/science-licenses-journal-article-reuse. This research was funded in whole or in part by the European Research Council (UniFlat) (ERC 101019302); as required the author will make the Author Accepted Manuscript (AAM) version available under a CC BY public copyright license.

SUPPLEMENTARY MATERIALS

science.org/doi/10.1126/science.ado3487
Materials and Methods; Supplementary Text; Figs. S1 to S4; References

Submitted 1 February 2024; accepted 16 June 2025

10.1126/science.ado3487

PHOTONICS

Ultracompact on-chip spectral shaping using pixelated nano-opto-electro-mechanical gratings

Weixin Liu[1,2,3], Siyu Xu[1,2], Chengkuo Lee[1,2,3,4]*

The ability to shape light spectra dynamically and arbitrarily would revolutionize many photonic systems by offering unparalleled spectral efficiency and network flexibility. However, most existing optical components have rigid spectral functionalities with limited tunability, hindering compact and fast optical spectral shaping. We introduce a pixelated nano-opto-electro-mechanical (NOEM) grating that exploits electromechanically induced symmetry breaking for precise, pixel-level control of grating coupling strength, yielding a miniaturized (~0.007 square millimeters) on-chip spectral shaper. We demonstrate the synthesis of grating pixels for arbitrary spectral responses, and we achieved rapid (<10 nanoseconds), high-contrast (>100 decibels), wavelength-selective switching through collective, nanometer-scale electrostatic perturbations. Our pixelated NOEM grating delivers exceptional spectral manipulation capabilities in an ultracompact, on-chip manner, offering prospects for next-generation optical information networks, computing architectures, and beyond.

Photonics has long been pursued as a game changer in high-speed communications and high-performance computing, offering far greater data throughput than conventional electronics through massive spectral bandwidth and parallelism (*1*, *2*). Yet fully exploiting these spectral resources requires precise control over a broad optical spectrum. In particular, wavelength-selective switching and dynamic spectral shaping empower real-time, high-speed customization of different wavelength channels in an optical signal. Such capabilities would revolutionize optical networks and computing architectures through frequency-parallel data processing (*3*, *4*), flexible bandwidth allocation (*5*), and adaptive system reconfiguration (*6*). Beyond communications and computing, compact and rapid spectral shaping also opens new avenues in fields such as microwave photonic signal processing (*7*), ultrafast spectroscopy (*8*), and integrated quantum photonics (*9*).

However, most current spectral shaping techniques still rely on bulky, free-space "disperse-and-modulate" configurations, where light is first spatially dispersed by prisms or diffraction gratings and then parallel-modulated using large arrays of liquid crystal or micromirror-based spatial light modulators (*10*, *11*). Though conceptually versatile, these systems are typically slow with kilohertz refresh rates and unsuitable for chip-scale integration. Integrating on-chip wavelength (de)multiplexers (e.g., arrayed waveguide gratings) with waveguide modulator arrays offers a path toward chip-scale spectral shaping (*12*), but these solutions still occupy substantial footprints (tens of square millimeters) and face limited channel counts owing to crosstalk and phase errors (*13*). Programmable waveguide meshes provide another approach to generating various spectral responses (*14*, *15*), yet they have inherent constraints on the transfer functions that can be realized.

Alternatively, waveguide Bragg gratings—one-dimensional periodic structures created by modulating a waveguide's refractive index—provide a more compact route for on-chip spectral shaping, delivering strong wavelength selectivity and high spectral flexibility without the need for dispersive optics. By apodizing the index modulation profile, Bragg gratings can, in principle, produce arbitrary user-defined spectral responses (*16*). This versatility has provided many opportunities for Bragg gratings in optical signal processing and telecommunications (*17*, *18*). Yet in most implementations, these index modulations are statically "baked in," affording minimal postfabrication tunability (*19*). The resulting mismatch between theoretical flexibility and practical rigidity has long impeded dynamic, on-demand spectral shaping using grating structures.

In this work, we introduce a miniaturized (~0.007 mm^2), pixelated nano-opto-electro-mechanical (NOEM) grating that overcomes this rigidity by enabling submicrometer-scale, electromechanical tunability, yielding an on-chip programmable spectral shaper (Fig. 1A). Our design discretizes the grating into individual "pixels," each featuring an independently tunable coupling coefficient κ (the grating strength that governs energy transfer between counterpropagating light) controlled by localized electrostatic forces (*19*). This pixel-level tunability arises from a new mechanism—electromechanically induced symmetry breaking—that switches the grating between subwavelength and Bragg regimes. We demonstrate dynamic spectral shaping through per-pixel control of κ, successfully synthesizing various complex spectral filters, such as Fabry-Pérot (FP), comb, and multilayer moiré configurations. By further introducing the layer-peeling algorithm (LPA) as a universal grating synthesis method (Fig. 1B), we can readily produce nearly arbitrary user-defined spectra. Additionally, by exploiting collective nanometer-scale electrostatic perturbations of low-mass nanobeams to produce coherent buildup, our NOEM grating enables wavelength-selective, bandwidth-tunable switching with ultrafast operation speeds (<10 ns), high switching contrasts (>100 dB), and low reconfiguration energy (~1 pJ).

Device concept and design

In our NOEM devices, suspended gratings are organized in a periodic arrangement, with the lattice constant Λ specifically set to half the period typical of a Bragg grating (Fig. 1, C and D). The supporting beams of several micrometers in length, designed to be thinner, perform three critical functions: They act as metamaterial claddings for lateral light confinement, provide mechanical stability, and establish electrical connectivity. Each pair of adjacent gratings (colored in red or blue) is interconnected and doubly end anchored, forming discrete, robust units that are electrically isolated by etched trenches. Under zero-bias equilibrium (Applied voltage $V_d = 0$ V; Fig. 1D, left, grating gap $g_1 = g_2$), our NOEM gratings operate within the subwavelength regime, optically equivalent to homogeneous anisotropic materials with negligible diffraction or reflection (*20*). Upon applying biases ($V_d > 0$ V; Fig. 1D, right), we harness electrostatic forces of a few tens of nanonewtons to attract gratings with opposite charge signs, closing gap g_1 between them. These periodic nanometer-scale perturbations break the original Λ translational symmetry and induce a new 2Λ periodicity that satisfies the first-order Bragg condition, thus transitioning the structure from a subwavelength to a Bragg grating. In the band structure, this period doubling folds the Brillouin zone at $k = \pi/(2\Lambda)$ (where k is the wavenumber; Fig. 1E), and the resulting even-odd mode divergence at this new boundary (Fig. 1F, inset) leads to a band splitting. Consequently, the biased NOEM grating will reflect all (and only) light within this emerging bandgap (Fig. 1F). The refractive-index contrast Δn between two band-edge modes scales with the grating-core displacement d, which in turn determines the bandgap width $\Delta\lambda$ and κ (*19*).

Notably, this zone-folding-induced bandgap exhibits a topological nature, as evidenced by the distinct geometric (Zak) phases (*21*) of gratings with $\Delta g < 0$ and $\Delta g > 0$, where $\Delta g = (g_2 - g_1)/2$ (fig. S1A) (*19*). Tuning Δg through zero induces a band inversion at $\Delta g = 0$, marking

---

[1]Department of Electrical and Computer Engineering, National University of Singapore, Singapore. [2]Center for Intelligent Sensors and MEMS (CISM), National University of Singapore, Singapore. [3]National Centre for Advanced Integrated Photonics (NCAIP), Singapore. [4]NUS Graduate School - Integrative Sciences and Engineering Programme (ISEP), National University of Singapore, Singapore. ***Corresponding author. Email: elelc@nus.edu.sg**

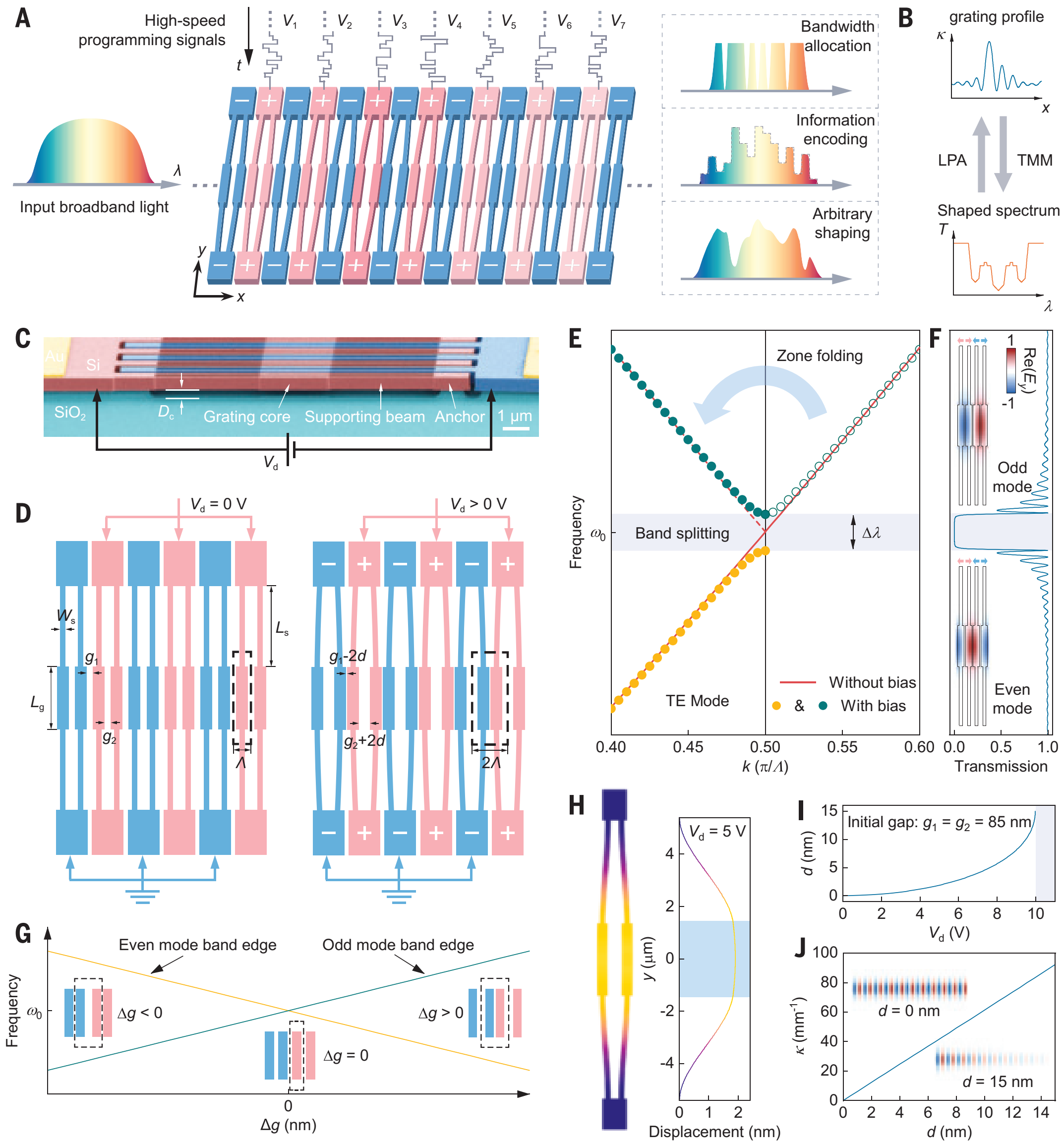

Fig. 1. Design of the NOEM grating. (**A**) Schematic of the pixelated NOEM grating for optical spectral shaping. Each grating pixel is individually controlled by distinct electrical biases, allowing programmable coupling strengths. (**B**) The shaped spectrum is derived from the κ profile using the TMM. Conversely, the κ profile is synthesized from a target spectrum using the LPA. (**C**) Oblique-view false-color scanning electron microscopy (SEM) of the NOEM grating. (**D**) Periodicity doubling of the grating after electrical biasing. The grating core length $L_g = 2.8$ μm. (**E**) Photonic band structures without (solid line) and with (solid dots) electrical bias. (**F**) Simulated transmission of a biased NOEM grating. (Inset) Mode profiles (E_y) of even and odd quasi–transverse electric (TE) modes at the Brillouin zone boundary. (**G**) Band edge evolution as a function of Δg. Only grating cores are shown for clarity. (**H**) Mechanical deformation (left) and corresponding displacement (right) of the NOEM grating. Displacement is exaggerated and color-coded for clarity. (**I**) Simulated displacement d versus V_d. The shaded area indicates pull-in instability. (**J**) Simulated κ versus d. (Inset) E_y distributions of the quasi-TE mode at Bragg resonance.

the topological transition (Fig. 1G). Consequently, light traversing gratings of opposite Δg will undergo a π-phase shift, indicating a sign change in κ (*19*). We define κ as negative for gratings with $\Delta g < 0$ and positive for those with $\Delta g > 0$. By introducing a negative spatial pre-offset ($\Delta g < 0$ at zero bias; fig. S1B), increasing V_d drives Δg from negative through zero to positive, thus enabling κ to tune continuously from its negative minimum to positive maximum.

We prototyped our NOEM gratings on a midinfrared silicon-on-insulator platform with a typical Bragg period of approximately 1 μm (*19*). By precisely controlling the undercut time of SiO_2 beneath, we secured the anchors to the substrate while fully suspending the grating structure (Fig. 1C, cavity depth $D_c \approx 500$ nm). This resulted in a robust double-clamped beam structure, achieving a fabrication yield exceeding 99.5%. Figure 1H shows the deformation of a discrete grating unit ($\Delta g = 0$) under a 5-V bias, revealing a nearly uniform nanometer-scale core displacement (where light is predominantly localized) that ensures an almost linear κ–displacement relationship. The small g_1 allows V_d of only several volts to induce over 10 nm of core displacement (Fig. 1I and fig. S2). Consequently, we can precisely manipulate κ up to 90 mm^{-1} before pull-in instability (Fig. 1J). This high κ can sufficiently attenuate light within the bandgap over only tens of wavelengths (Fig. 1J, inset).

Spectral-specific switching dynamics

First, we characterized our NOEM grating under uniform bias conditions, wherein gratings are alternately connected to only two electrodes (Fig. 2A) (*19*). In the unbiased state, its subwavelength geometry ($\Delta g = 0$)

yielded minimal insertion loss (0.24 dB for a device length $L = 300$ μm). Applying a bias transformed the NOEM grating into a high-contrast spectral filter with tunable rejection depth and bandwidth, demonstrating its fundamental wavelength-selective switching capabilities (Fig. 2, B and C). At Bragg resonance, we observed a switching contrast of 25 dB at 4 V and of >40 dB at 5 V, whereas off-resonance wavelengths (e.g., 4.05 μm) remain largely unaffected (<0.5 dB modulation even at 9 V). Theoretically, our NOEM grating can achieve a switching contrast exceeding 100 dB at 9 V (fig. S3), though our current detection is limited to ~53 dB by detector noise. The bandgap width Δλ is tunable from 25 to >100 nm with >30 dB maximum contrast (Fig. 2C). Increasing the device length can further narrow Δλ (down to 8 nm at $L = 1$ mm and 4 nm at $L = 2$ mm) while also reducing the required bias (fig. S4).

The low effective mass ($m_{\mathrm{eff}} \approx 1.4$ pg) and high stiffness ($k_{\mathrm{g}} \approx 13$ N/m) of the double-clamped beam structure endow our NOEM grating with a high resonance frequency of approximately 16 MHz (Fig. 2D) (*19*). This supports ultrafast switching dynamics, achieving complete light switching at Bragg resonance in tens of nanoseconds (fig. S5). Moreover, its wavelength-selective and bandwidth-tunable nature concentrates most of the optical power switching for detuned wavelengths within a short, intermediate segment of the mechanical displacement, further reducing the effective response time to just a few nanoseconds (fig. S6) (*19*). For example, at a wavelength red-detuned by 10 nm from Bragg resonance, the NOEM grating switches from “OFF” to “ON” in just 7 ns and from “ON” to “OFF” in 10 ns when driven by step voltages between 2 and 6 V (Fig. 2E). These ultrafast time dynamics—two to three orders of magnitude faster than conventional opto-electro-mechanical devices (*22*–*25*) (table S1)—underscore the potential of our NOEM grating as an ideal candidate for high-speed optical switching fabrics in both data center networking and photonic computing (*26*). To assess reliability, we operated our device with a 12 MHz sinusoidal signal for more than 2 trillion cycles (~48 hours) without noticeable performance degradation. The estimated power consumption is 13.2 μW, with a switching energy of only 1.1 pJ per operation (*19*).

Pixelated operation and active spectral shaping

Next, we demonstrated the pixelated operation of our NOEM grating ($\Delta g = -8$ nm) by segmenting a 490-μm-long device into 80 individually programmable pixels through isolation trenches (Fig. 3A). Each grating pixel is connected to its own biasing electrode (V_1 to V_{80}) while sharing a common ground electrode. Figure S7 illustrates how Bragg resonance transmission and Δλ evolved under uniform bias sweeps, from which we extracted the voltage-κ relationship for subsequent spectral synthesis (*19*). The tuning range of κ spans from approximately -22 mm^{-1} to over 40 mm^{-1}.

In Fig. 3B, by constructing two Bragg grating sections with opposite signs of κ, we formed a π phase shifted FP cavity that acts as a narrow bandpass filter at the bandgap center. By extending the phase-shifted section ΔL, we can accommodate multiple spectral resonances with controllable free spectral range (FSR), extinction ratio, and quality factor (Fig. 3C and fig. S8) (*19*). Moreover, a comb filter can be produced by embedding phase-shifted sections periodically into a uniform Bragg grating, i.e., sampling it with a long-periodic rectangular function of period P_{c} and window width L_{c} (Fig. 3, D and E; see fig. S9 for more results). In this configuration, the intrinsic Bragg resonance couples to a series of side peaks with an FSR of $\lambda^2/(2n_{\mathrm{g}}P_{\mathrm{c}})$, where n_{g} is the group index (*27*).

We further exploited the interplay of multiple periodicities within a single NOEM grating by superposing bilayer or multilayer artificial subgratings to induce moiré effects, thereby enabling unparalleled spectral control. Although often studied in twisted systems (*28*, *29*), moiré superlattices can also arise from superposing periodic patterns with slightly different periods (*30*), as shown in our moiré grating (Fig. 3F). In a bilayer moiré grating, owing to the interference between two subgratings with periods Λ_1 and Λ_2, the superposed profile naturally forms a slowly varying sinusoidal envelope with a large moiré period $\Lambda_{\mathrm{M}} = 2\Lambda_1\Lambda_2/|\Lambda_1 - \Lambda_2|$, modulating over a much smaller, underlying grating period $\Lambda_{\mathrm{s}} = 2\Lambda_1\Lambda_2/(\Lambda_1 + \Lambda_2)$. To harness this moiré effect in our NOEM grating with a given Bragg period of $\Lambda_{\mathrm{s}} = 2\Lambda$, we instead modulated κ along its length to match a sinusoidal moiré profile of

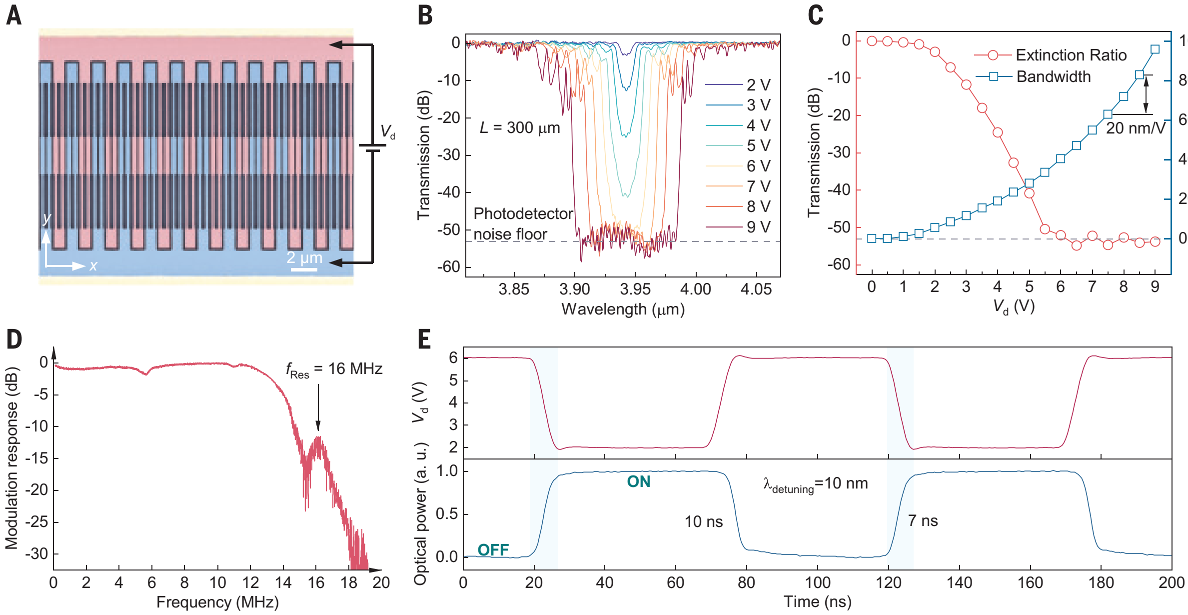

Fig. 2. Wavelength-selective switching and ultrafast temporal dynamics. (**A**) False-color SEM of the NOEM grating in two-electrode configuration. The supporting beam length $L_{\mathrm{s}} = 4$ μm. (**B**) Optical transmission spectra at different V_{d}, normalized to the zero-bias baseline. The dashed line indicates the noise floor. (**C**) Bragg resonance transmission and Δλ versus V_{d}. The nonlinear voltage response enables a bandwidth tuning efficiency ($d\Delta\lambda/dV_{\mathrm{d}}$) of ~20 nm/V at 8 V. (**D**) Frequency-dependent modulation response. f_{Res}, mechanical resonance frequency. (**E**) Square wave driving signal and corresponding optical response at $\lambda_{\mathrm{detuning}} = 10$ nm. The steady-state optical switching contrast between “ON” and “OFF” already exceeds 99% (fig. S6). a.u., arbitrary units.

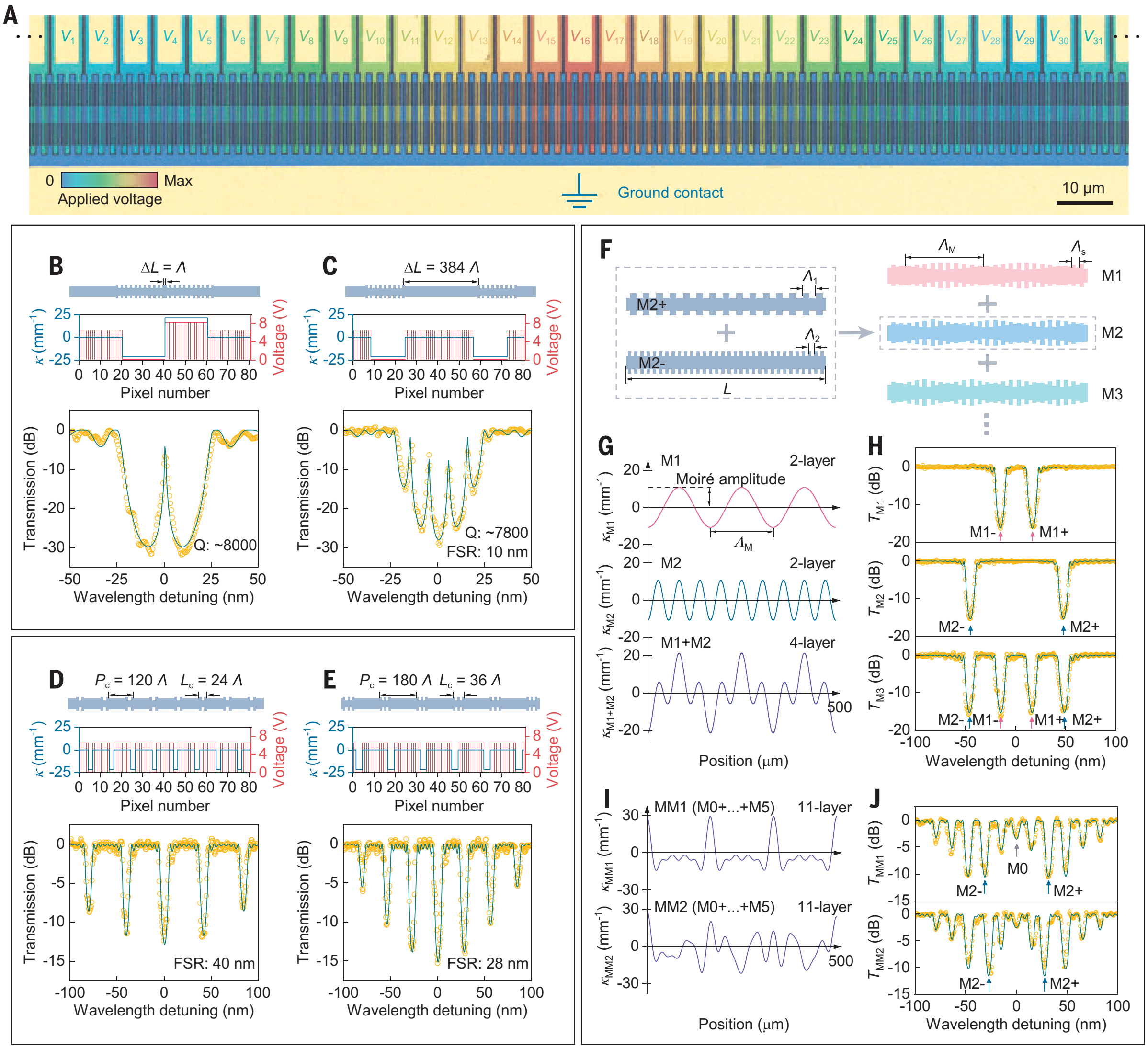

Fig. 3. Active spectral shaping as complex spectral filters. (**A**) False-color SEM of the pixelated NOEM grating with 80 pixels. (**B** to **E**) Each panel consists of three tiers: (Top) Schematic of the programmed NOEM grating. The grating width indicates its effective index. (Middle) Designed κ profiles (line) and programmed drive voltage per pixel (bar). (Bottom) Simulated (line) and measured (dot) transmission spectra. ΔL denotes phase-shifted sections. (**F**) Superposing two subgratings with periods Λ_1 and Λ_2 forms a bilayer moiré grating with Bragg period Λ_s and moiré period Λ_M. Superposing multiple bilayer moiré gratings (M1, M2, M3…) with the same Λ_s but different Λ_M forms a multilayer moiré grating. (**G**) κ profiles and (**H**) transmission (T) spectra of bilayer moiré gratings M1 ($\Lambda_M = L/3$, $\kappa_{max} = 11\ \text{mm}^{-1}$) and M2 ($\Lambda_M = L/9$, $\kappa_{max} = 11\ \text{mm}^{-1}$) as well as their superposition as a four-layer moiré grating. (**I**) κ profiles and (**J**) transmission spectra of 11-layer moiré gratings. Translational symmetry in MM2 is broken by setting $\Lambda_{M2} = L/3\sqrt{3}$ (fig. S14).

period Λ_M [Fig. 3G, M1 and M2 (top and middle)]. This modulation effectively mimics the superposition of two artificial subgratings with periods $\Lambda_1 = \Lambda_M\Lambda_s/(\Lambda_M + \Lambda_s)$ and $\Lambda_2 = \Lambda_M\Lambda_s/(\Lambda_M - \Lambda_s)$, respectively. With a moderate moiré period ($\Lambda_s \ll \Lambda_M < L/2$), the wavenumbers of subgratings ($2\pi/\Lambda_1$ and $2\pi/\Lambda_2$) are sufficiently spaced to produce two distinct resonance peaks. These peaks lie symmetrically around the intrinsic Bragg resonance, with their wavelength separation given by $\lambda^2/(n_g\Lambda_M)$ (Fig. 3H, M1 and M2). Varying Λ_M thus allows fine-tuning the wavelengths of two bandstop filters, with their extinction ratios determined by the moiré amplitude (i.e., the maximum κ) (fig. S10).

Furthermore, by stacking multiple bilayer moiré gratings (M1, M2, M3…), we can form a reconfigurable multilayer moiré grating that produces multiple pairs of resonance peaks, each independently controllable (Fig. 3F, right). For example, superposing the κ profiles of M1 and M2 creates a four-layer moiré grating (Fig. 3, G and H, bottom), where each moiré envelope retains its resonance pair and allows independent tuning of peak positions and extinction ratios (fig. S11). Notably, the intrinsic Bragg resonance can be reintroduced as a constant-κ subgrating by adding a DC component (M0) to the overall κ profiles (fig. S12). In Fig. 3, I and J, we further demonstrated 11-layer moiré gratings by stacking five sinusoidal envelopes (M1 to M5) and one DC component (M0) (see figs. S13 and S14 for moiré compositions and more results). This yielded five controllable resonance pairs and a tunable intrinsic Bragg resonance. Notably, although MM1 (Fig. 3I, top) preserves translational symmetry through carefully chosen commensurate moiré periods, this symmetry can be broken by incommensurate periods or insufficient grating length to exhibit symmetry (*31*, *32*), as demonstrated in MM2 (Fig. 3I, bottom) and fig. S14B. This flexibility enables seamless tuning of peak wavelengths in multilayer moiré gratings.

Inverse scattering synthesis for arbitrary spectral shaping

Lastly, we introduced the LPA as a universal inverse-scattering method to synthesize arbitrary user-defined spectra (*16*). LPA begins with a target reflection spectrum $r(\lambda)$ and models each grating unit as a discrete reflector (ρ_i) spaced by 2Λ (Fig. 4A). These reflectors collectively provide distributed optical feedback (v_1 to v_M) and produce a temporal impulse response $h(t)$, which is the inverse discrete Fourier transform of $r(\lambda)$. By causality, at time $t = 0$, only the first reflector contributes to $h(t)$ (there is insufficient time for light to reach subsequent reflectors), so ρ_1 can be extracted from $h(0)$ as if only the first reflector existed. The light field is then advanced to the next layer using the transfer matrix method (TMM), allowing each layer to be "peeled off" sequentially until the full grating profile is reconstructed (*19*). We first applied LPA to synthesize a "W"-shaped spectrum (Fig. 4B). Because its initial temporal impulse is infinite and extends into negative time, we truncated and shifted $h(t)$ into the positive domain to ensure physical realizability (fig. S15) (*19*). We then used LPA to determine the κ profile for this modified response (Fig. 4B, top). Furthermore, we synthesized a spectrum to emulate the contour of a simple-drawing castle, as shown in Fig. 4C.

Conclusions and outlook

Our pixelated NOEM grating combines exceptional compactness with nanosecond response times, delivering fully reconfigurable, on-chip spectral shaping. The electromechanically induced symmetry breaking at its core is inherently adaptable across broad spectral regimes, extending the applicability of our design methodology from the near infrared to the terahertz (*19*). Our approach is poised to reshape integrated photonics by fully harnessing spectral bandwidth and parallelism. For example, by supporting tens or even hundreds of independently tunable spectral channels within a single, compact device, it invites a new generation of photonic computing architectures that operate in the frequency domain rather than (or alongside) conventional spatial dimensions (*3*). This capacity for massive spectral parallelism—especially when paired with broadband sources, such as optical frequency combs (*33*)—allows computational tasks, such as large-scale multiply-accumulate operations, to be executed in a single clock cycle with minimal hardware overhead. Additionally, the multilayer moiré superlattices within the NOEM grating offer a distinct opportunity to dynamically explore wave phenomena typical of moiré systems, such as flat band formation (*34*) and wavepacket localization (*31*, *35*), which are typically observed in more complex two-dimensional material or photonic platforms (*29*, *36*). With dynamic, layer-by-layer tunability, one can emulate, explore, and potentially harness these phenomena in real time, promising to bridge fundamental moiré physics and next-generation photonics within a miniaturized device.

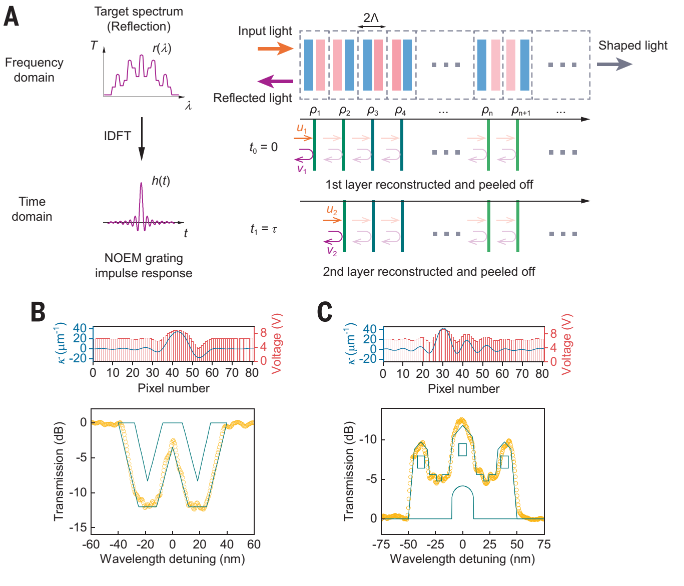

Fig. 4. Arbitrary spectral shaping based on inverse scattering transform. (**A**) Layer-peeling approach for synthesizing user-defined spectra. τ represents the round-trip time to the second reflector. IDFT, inverse discrete Fourier transform. (**B** and **C**) (Top) κ profiles (line) and corresponding biasing voltages (bar) along the grating to emulate (B) the outline of the letter "W" and (C) a simple drawing of a castle. (Bottom) Measured spectra (dot) well reproduced the spectral targets (line).

REFERENCES AND NOTES

1. A. Singh *et al.*, *Comput. Commun. Rev.* **45**, 183–197 (2015).
2. G. Wetzstein *et al.*, *Nature* **588**, 39–47 (2020).
3. P. L. McMahon, *Nat. Rev. Phys.* **5**, 717–734 (2023).
4. X. Xu *et al.*, *Nature* **589**, 44–51 (2021).
5. P. J. Winzer, D. T. Neilson, A. R. Chraplyvy, *Opt. Express* **26**, 24190–24239 (2018).
6. Q. Cheng, M. Bahadori, M. Glick, S. Rumley, K. Bergman, *Optica* **5**, 1354–1370 (2018).
7. D. Marpaung, J. Yao, J. Capmany, *Nat. Photonics* **13**, 80–90 (2019).
8. M. Maiuri, M. Garavelli, G. Cerullo, *J. Am. Chem. Soc.* **142**, 3–15 (2020).
9. J. Wang, F. Sciarrino, A. Laing, M. G. Thompson, *Nat. Photonics* **14**, 273–284 (2020).
10. A. M. Weiner, *Rev. Sci. Instrum.* **71**, 1929–1960 (2000).
11. S. Ngcobo, I. Litvin, L. Burger, A. Forbes, *Nat. Commun.* **4**, 2289 (2013).
12. S. T. Cundiff, A. M. Weiner, *Nat. Photonics* **4**, 760–766 (2010).
13. M. L. Calvo, L. Vasudevan, *Optical Waveguides: From Theory to Applied Technologies* (CRC Press, 2018).
14. W. Bogaerts *et al.*, *Nature* **586**, 207–216 (2020).
15. D. Pérez *et al.*, *Nat. Commun.* **8**, 636 (2017).
16. J. Skaar, L. Wang, T. Erdogan, *IEEE J. Quantum Electron.* **37**, 165–173 (2001).
17. K. O. Hill, G. Meltz, *J. Lightwave Technol.* **15**, 1263–1276 (1997).
18. S. Kaushal *et al.*, *Front Optoelectron.* **11**, 163–188 (2018) review.
19. See the supplementary materials.
20. P. Cheben, R. Halir, J. H. Schmid, H. A. Atwater, D. R. Smith, *Nature* **560**, 565–572 (2018).
21. J. Zak, *Phys. Rev. Lett.* **62**, 2747–2750 (1989).
22. D. U. Kim *et al.*, *Nat. Photonics* **17**, 1089–1096 (2023).
23. N. Quack *et al.*, *Microsyst. Nanoeng.* **9**, 27 (2023).
24. H. Sun, Q. Qiao, Q. Guan, G. Zhou, *Micromachines* **13**, 1509 (2022).
25. S. Gyger *et al.*, *Nat. Commun.* **12**, 1408 (2021).
26. L. Midolo, A. Schliesser, A. Fiore, *Nat. Nanotechnol.* **13**, 11–18 (2018).
27. B. J. Eggleton, F. Ouellette, L. Poladian, P. A. Krug, *Electron. Lett.* **30**, 1620–1622 (1994).
28. F. He *et al.*, *ACS Nano* **15**, 5944–5958 (2021).
29. L. Du *et al.*, *Science* **379**, eadg0014 (2023).
30. T. H. Talukdar, A. L. Hardison, J. D. Ryckman, *ACS Photonics* **9**, 1286–1294 (2022).
31. P. Wang *et al.*, *Nature* **577**, 42–46 (2020).
32. F. Alpeggiani, L. C. Andreani, D. Gerace, *Appl. Phys. Lett.* **107**, 261110 (2015).
33. J. Feldmann *et al.*, *Nature* **589**, 52–58 (2021).
34. D. X. Nguyen *et al.*, *Phys. Rev. Res.* **4**, L032031 (2022).
35. C. Saadi *et al.*, *Optica* **11**, 245–250 (2024).
36. Y. Cao *et al.*, *Nature* **583**, 215–220 (2020).
37. W. Liu, S. Xu, C. Lee, Data for: "Ultracompact on-chip spectral shaping using pixelated nano-opto-electro-mechanical gratings," Dryad (2025); https://doi.org/10.5061/dryad.2v6wwq014.

ACKNOWLEDGMENTS

We thank B. Dong for the helpful discussions. Device fabrication was performed at the Center for Advanced 2D Materials at National University of Singapore. **Funding:** This work is supported by the Ministry of Education (MOE) Singapore Tier Two project (MOE-T2EP50220-0014). We acknowledge funding support from the National Semiconductor Translation and Innovation Centre (M24W1NS005) and the National Centre for Advanced Integrated Photonics (NRF-MSG-2023-0002) in Singapore. **Author contributions:** W.L. and C.L. conceived the project. W.L. designed structures, fabricated devices, and performed simulations and measurements. W.L. and S.X. analyzed the data. W.L. wrote the manuscript. All authors discussed the results and commented on the manuscript. C.L. supervised the project. **Competing interests:** W.L. and C.L. are inventors on a patent application to be submitted by National University of Singapore that covers the design methodologies of NOEM gratings and the spectral shaping technology based on pixelated NOEM gratings. S.X. declares no competing interests. **Data and materials availability:** All data are available in the main text, the supplementary materials, or deposited in Dryad (*37*).

SUPPLEMENTARY MATERIALS

science.org/doi/10.1126/science.adu8492
Materials and Methods; Supplementary Text; Figs. S1 to S17; Table S1; References (*38*–*73*)

Submitted 10 March 2025; accepted 18 June 2025

10.1126/science.adu8492

BIOMIMICRY

Ultrafast elastocapillary fans control agile maneuvering in ripple bugs and robots

Victor M. Ortega-Jimenez[1,2,3]*†, Dongjin Kim[4]†, Sunny Kumar[3], Changhwan Kim[4], Je-Sung Koh[4]*, Saad Bhamla[3]*

Rhagovelia ripple bugs use specialized middle-leg fans with a flat-ribbon architecture to navigate the surfaces of fast-moving streams. We show that the fan's directional stiffness enables fast, passive elastocapillary morphing, independent of muscle input. This flat-ribbon fan balances collapsibility during leg recovery with rigidity during drag-based propulsion, enabling full-body 96° turns in 50 milliseconds, with forward speeds of up to 120 body lengths per second—on par with fruit fly saccades in air. Drawing from this morphofunctional architecture, we engineered a 1-milligram elastocapillary fan integrated into an insect-scale robot. Experiments with both insects and robots confirmed that self-morphing fans improve thrust, braking, and maneuverability. Our findings link fan microstructure to controlled interfacial propulsion and establish design principles for compact, elastocapillary actuators in agile aquatic microrobots.

Ripple bugs exhibit remarkable diversity around the globe (*1*–*3*) and are distinguished by their millimeter size and agility in navigating turbulent waters. This locomotory proficiency stems from a feathery fanlike structure at the distal end of their middle legs (Fig. 1A). This fan, regulated by two taxon-restricted genes, enhances maneuverability in an ecologically challenging niche by increasing turning angles and facilitating movement upstream in rapid flows (*4*). *Rhagovelia* can also rapidly immerse, open, and close the barbs and barbules of their fan. Although it has been suggested that only the claw muscle drives this spreading and collapsing (*3*), it remains unclear whether capillary forces also contribute to the rapid fan deployment. Such a capillary-driven mechanism could be crucial for quick locomotive responses to unpredictable disturbances, such as sudden flow perturbations or approaching predators and prey.

Other aquatic insects such as water beetles (*5*), backswimmers (*5*), and water striders (*6*, *7*) propel movements using specialized swimming hair. *Rhagovelia*'s fan generates high propulsion by maintaining a large surface area and resisting deformation caused by thrust. Conversely, this fan can flexibly collapse from ~180° to 0° (and vice versa) as it enters or exits water. The fan's biomechanical property, which combines flexibility for rapid deployment and rigidity for high thrust, presents an intriguing functional duality.

Rhagovelia's fan serves as an inspiring template for developing self-morphing artificial propellers, providing insights into their biological form and function. Such configurations are largely unexplored in semiaquatic robots (*8*, *9*). Current semiaquatic robots rely on three size-dependent propulsion mechanisms. Large-scale robots (>50 g) typically row using bulky, rigid, hydrophilic pads (mimicking oars) to generate drag-based thrust (*10*). By contrast, small-scale robots (<50 g) often adopt thin, hydrophobic legs (*11*, *12*), mimicking Gerridae water striders (*13*). Although thin, hydrophobic legs reduce surface tension that impedes leg rowing, they inherently limit the momentum generated.

Another type of small-scale robot uses hydrophilic pads, which passively bend back and forth only underwater to circumvent surface tension effects (*14*). However, recovering the pad underwater for the next stroke reduces overall stroke efficiency. *Rhagovelia* overcomes these limitations by using hydrophilic, reversibly actuating oars, even at smaller scales than that of robots. These fans provide effective drag-based propulsion without losing considerable momentum during leg recovery. Thus, designing artificial morphing fans inspired by *Rhagovelia* could address the limitations of small-scale robots, improving locomotion performance in turbulent waters.

A self-morphing propulsor

Scanning electron microscopy (SEM) images revealed that *Rhagovelia*'s fan comprises numerous flat, ribbon-like barbules and barbs (Fig. 1, A to C). The barbs interconnect and branch, whereas the barbules are uniformly distributed along both sides of each barb (Fig. 1C). *Rhagovelia*'s claw, smooth and flat, resembles a seam ripper tool (Fig. 1B). Both the fan and the claw attach to the tip of the leg. We observed that the fan of an isolated leg fully spreads underwater only when the claw is unfolded (fig. S1). Upon removal from the water, the fan collapses and adheres to the claw, forming a sharp tip, with no noticeable water dripping (movie S1).

To demonstrate that *Rhagovelia*'s fan spreads because of capillary forces independent of muscle or claw, we isolated a fan from a specimen. Using a single human hair, we placed and removed the isolated fan from a water droplet (Fig. 1D). The fan fully spread in ~10 ms upon contact with water, with barbules spreading even faster, at just 1 ms after water contact (Fig. 1E and movie S1). In agreement, we found that the theoretical spreading time (τ) for barbules has a similar order of magnitude to that of *Rhagovelia*'s fan, on the basis of the relation $\tau \sim \mu L^6/\gamma p^3 lb^2$, where lb is the capillary bending length, p is the interbarbule (or interbarb) space, L is the characteristic length for barbules (or barb), μ is viscosity of water, and γ is surface tension (fig. S2 and table S1). The fan rapidly collapsed upon removal from the water, also within ~10 ms (Fig. 1F). Experiments with a fixed leg and fan, gradually raising the water level, showed that the fan fully spreads only when completely submerged (fig. S3 and movie S1). Additionally, a wet fan in a droplet remains spread after drying (fig. S1). These experiments confirmed that the isolated fan acts as an ultrafast capillary self-actuator without claw mediation, requiring full submersion or removal from water for complete spreading or collapse.

Fan spreading during rowing and swimming

We analyzed *Rhagovelia*'s rowing performance to understand fan spreading rates. Individuals initiate a leg stroke by reducing the gap between their hydrophobic leg and the water surface (Fig. 1G and movie S1). This triggers the fan to open, reaching full spread in ~10 ms (Fig. 1H) and staying open for most of the stroke (~50 ms). At the stroke's end, they remove the fan from the water, closing it in ~10 ms (Fig. 1I). The claw's movements synchronize with the fan's opening and closing. During the power stroke, the leg maintains contact at the tip throughout the interstroke period. These observations indicate that the fan spreading and closing dynamics during rowing mirror the passive behavior of an isolated fan.

We assessed the claw's role during *Rhagovelia*'s underwater swimming. Folding a submerged self-spread fan with the claw is more challenging than opening because the claw must actively force the fan to fold. Consequently, the fan remains partially spread rather than fully closed during swimming (Fig. 1, J to L, and movie S1). These findings reveal that *Rhagovelia* exerts both active and passive control over fan dynamics. Fan closing relies on passive elastocapillary forces when removed from the water or active forces through claw-muscle action when fully submerged. Fan opening is predominantly passive, but the claw can act as a gate, controlling the release of the fan underwater.

---

[1]Department of Integrative Biology, University of California, Berkeley, CA, USA. [2]School of Biology and Ecology, University of Maine, Orono, ME, USA. [3]School of Chemical and Biomolecular Engineering, Georgia Institute of Technology, Atlanta, GA, USA. [4]Department of Mechanical Engineering, Ajou University, Gyeonggi-do, Republic of Korea. ***Corresponding author. Email: vortex@berkeley.edu (V.M.O.-J.); jskoh@ajou.ac.kr (J.-S.K.); saadb@chbe.gatech.edu (S.B.)** †These authors contributed equally to this work.

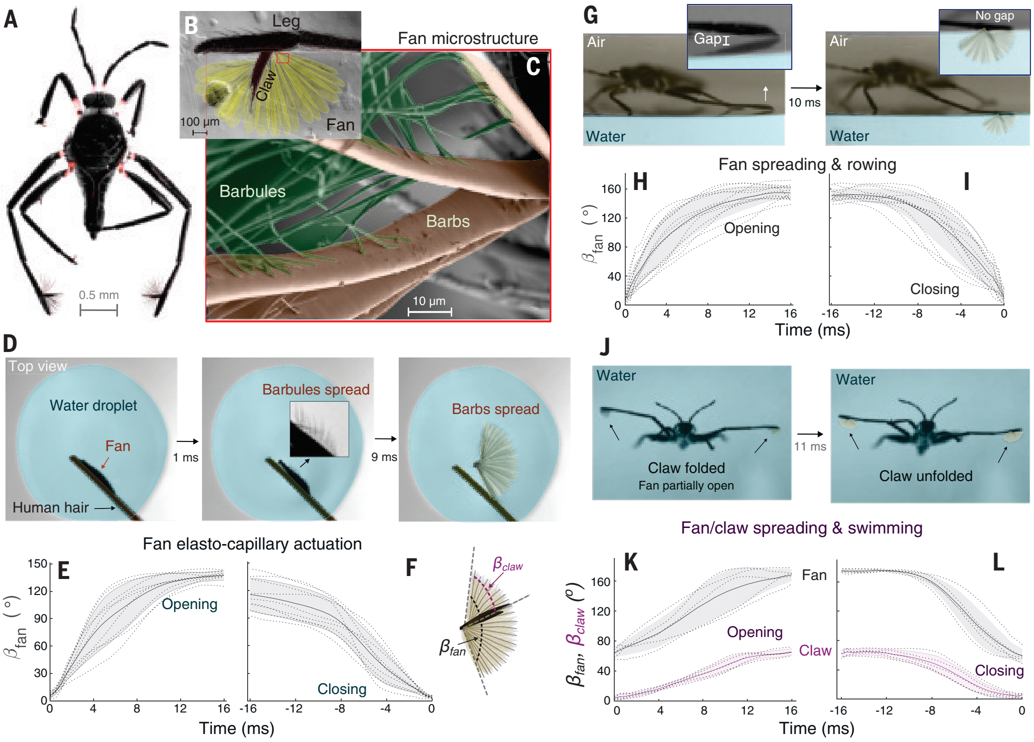

Fig. 1. *Rhagovelia* fan microstructure and spreading performance. (**A**) *Rhagovelia obesa* showing fans and claws at the tip of the middle legs. (**B**) Image of fan and claw. (**C**) SEM image of flat-ribbon microstructure of barbs and barbules. (**D**) Video frames showing a top view of an isolated fan (left) before and while placed on a water droplet. (Middle) Barbules spread after 1 ms. (Right) Barbs spread after 10 ms. (**E** and **F**) Time series of the spreading angle (β_{fan}) of the isolated fan during (E) opening and (F) closing. (**G**) Video frames of a rowing individual (left) before and (right) when the fan is fully open in the water. (**H** and **I**) Time series of fan's spreading angle (β_{fan}) during (H) opening and (I) closing while rowing. (**J**) Video frames of a swimming individual (left) before and (right) when the fan is fully open. The fan remains partially spread before the claw starts to open while swimming. (**K** and **L**) Time series of the fan's and claw's spreading angle (β_{fan} and β_{claw}, respectively) during (K) opening and (L) closing. Lines, shadows, and dashed lines in plots indicate the mean value, 1 SD, and individual data, respectively.

Robotic fan design and passive operation

We developed an artificial fan to investigate the mechanical advantages of a flat-ribbon structure, focusing on elastocapillary self-morphing and drag-force production. This fan, attached to a bio-inspired insect robot called "Rhagobot," is placed at the tip of each rowing middle leg (Fig. 2A). Measuring 10 by 5 mm and weighing ~1 mg, the fan folds and spreads passively through elastocapillarity. It consists of 21 flat ribbon–shaped barbs with a claw-like structure (5 mm in length), and its size is ~20 times larger than that of *Rhagovelia*'s fan (Fig. 2B). Each barb is made from 16 µm thickness of polyimide (PI) film, processed with an ultraviolet laser (Fig. 2, C and D, and fig. S4).

Rapid closing and spreading occur when the fans are removed from or introduced to water, respectively (Fig. 2E). The artificial claw at the fan's base enables the barbs to collapse under surface tension in the desired direction. This capillary-driven passive operation allows the fan to function during the Rhagobot's stroke cycle without needing an actuator. This elastocapillary morphing offers two advantages: First, the fan's collapsibility reduces surface area, minimizing surface tension during the recovery stroke (Fig. 2F), and second, the fan's spreading facilitates drag-based propulsion during the power stroke by retaining its shape (Fig. 2G).

Optimizing elastocapillary and drag forces

We designed artificial barbs with a flat ribbon shape to optimize the fan for elastocapillary collapse and drag resistance by ensuring different stiffness levels in two orthogonal directions (Fig. 2H). For effective elastocapillary folding, the barb must bend around the y axis because of surface tension (Fig. 2F). To achieve this, the surface energy ($E_{\text{surface}} \sim 2A\gamma$, where A is barb area and γ is surface tension) needs to exceed the bending energy for elastocapillary folding. The bending energy depends on the second moment of inertia around the y axis, which is given as $E_{\text{bending}} \sim EI_yL/2R^2$, where E is Young's modulus, I_y is the moment of inertia, L is the length of the curved barb, and R is the radius of curvature. Because a flat ribbon–shaped barb's moment of inertia around the y axis is a function of t^3($I_y = wt^3/12$) (where w is barb width and t is barb thickness), we could effectively reduce the bending energy below the surface energy by adjusting the thickness of barb (t).

To maximize drag-based propulsion, the barb deformation must be minimized during the power stroke. Drag-induced deformation centers around the z axis, with the moment of inertia around the z axis being a function of w^3 (Fig. 2G). By optimizing both thickness (t) and width (w) through modeling, the flat ribbon shape achieved both elastocapillary-driven morphing and maximum drag force (fig. S5).

We quantified the mechanical advantages of the flat-ribbon shape over a cylindrical-shaped barb (Fig. 2H). By comparing the bending and surface energies of the barbs at the ends (B1 and B21) when unfolded and folded, we determined the maximum thickness for elastocapillary bending to be $t_{\text{EC}} = 16.3$ µm (Fig. 2I, fig. S5, and table S2). For a cylindrical barb, the maximum radius for collapse is $r_{\text{EC}} = 11.1$ µm (Fig. 2J). Although the thickness of the flat ribbon shape remains fixed at t_{EC}, adjusting the width (w) minimizes deformation due to drag while maintaining collapsibility. Increasing w up to 0.3 mm results in negligible deformation (Δ), maximizing drag utilization (Fig. 2K). By contrast, a cylindrical barb with $r = 11.1$ µm undergoes 70% deformation (Δ), reducing the drag-receiving surface area and thus propulsion force. Increasing r_{EC} to minimize deformation increases the moment of inertia around both the z axis and y axis, compromising collapsibility. The energy balance indicates that not only the artificial fan but also the *Rhagovelia* fan is collapsible because the surface energy is three orders of magnitude greater than the bending energy of the biological fan (tables S3 and S4 and fig. S6).

Observations of the artificial fan, lifted and lowered by the Rhagobot, show that it opens in ~120 ms and collapses in ~80 ms in water (Fig. 2, L and M, and movie S2). This finding agrees with the theoretical spreading time (τ ~ 300 ms) for the artificial fan (fig. S2G and tables S1 and S5).

Controlled maneuvers and vortex hydrodynamics

Rhagovelia exhibits an average turning angle of 96°, a peak angular speed of 4200, and a turning duration of 50 ms, similar to those of a

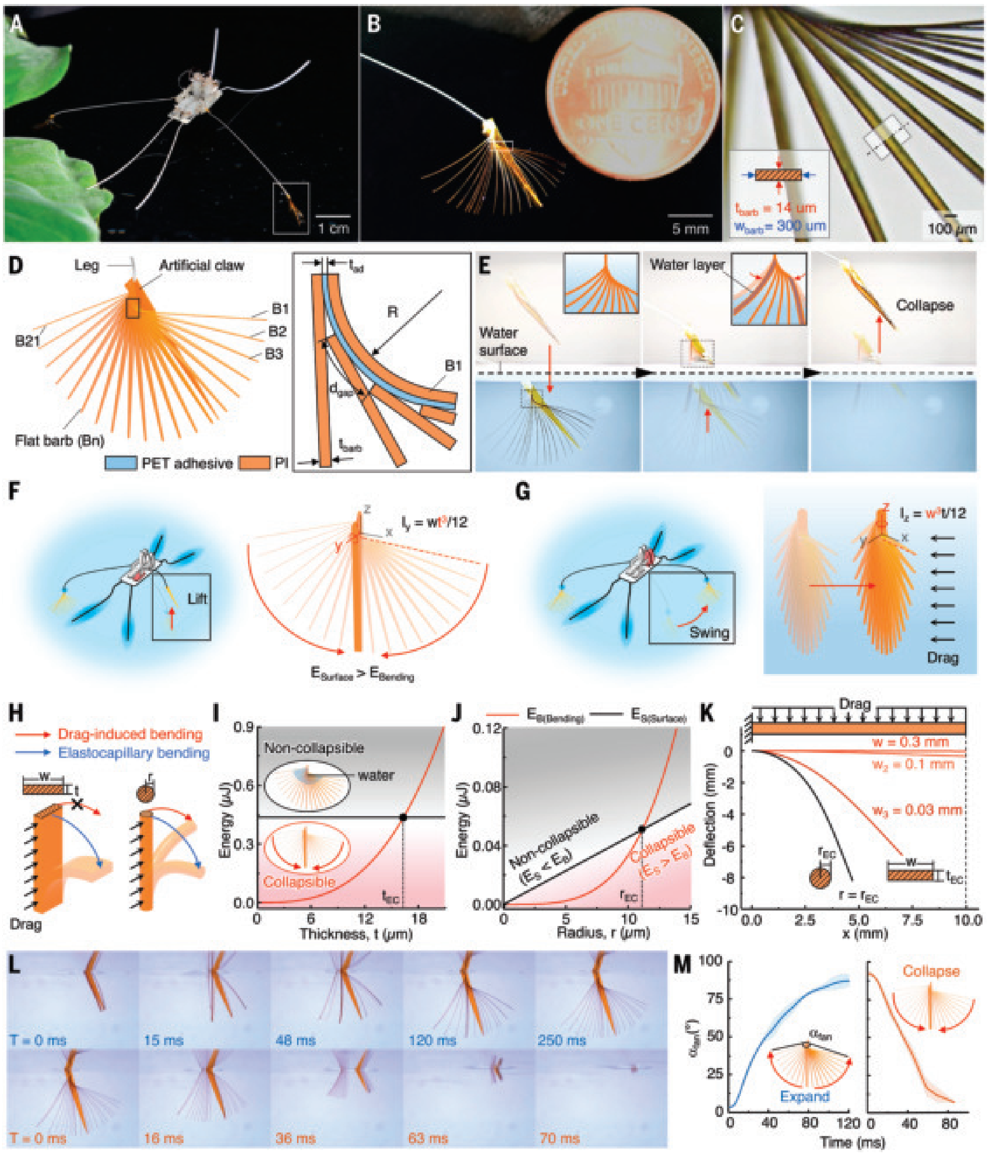

Fig. 2. Design and mechanism of robotic fan driven by elastocapillarity. (**A**) The 0.23-g semiaquatic robot, Rhagobot, with self-morphing fans at the ends of its middle legs. (**B**) The 1-mg robotic fan expanded underwater. (**C**) Close-up view of the fan showing flat-ribbon barbs that mimic the structure of the biological counterpart. (**D**) Schematic of the fan consisting of 21 barbs (B1 to B21) and an artificial claw. (**E**) Image sequence of fan expansion and collapse. (Left) Expanded underwater. (Middle) Collapsing at the air–water interface. (Right) Fully collapsed in air. (**F** and **G**) Schematic of the robot lifting its leg from the water and swinging its leg underwater, demonstrating (F) low bending stiffness around the *y* axis for capillary-driven collapse and (G) high bending stiffness around the *z* axis to prevent bending due to drag. (**H**) Schematic illustration of two barb geometries—flat ribbon–shaped (lamella) with a rectangular cross section, and cylindrical with a circular cross section—under the influence of drag or capillary forces. (**I** and **J**) Bending (red line) and surface (black line) energy as a function of thickness and radius (t_{barb}, r_{barb}) of barb with (I) rectangular cross section and (J) circular cross section. (**K**) Comparison of drag-induced deformation in circular and rectangular cross-section barbs, all capable of collapsing through elastocapillarity. (**L**) Image sequence of the fan (top) expanding upon water entry and (bottom) collapsing when exiting. (**M**) Angle (α_{fan}) profile of a fan during expansion and collapse as it (left) enters and (right) exits the water.

fly (Fig. 3, A to F, and fig. S7). A turn begins when an individual moves both legs forward in a reverse stroke, with only one leg and its fan interacting with the water. This asymmetric braking turns the body toward the dragging leg. During the subsequent power stroke, both legs and fans engage synchronously, producing symmetric vortical wake and capillary waves (Fig. 3, D and H). *Rhagovelia* achieves greater turning angles with fast braking control. In a reverse stroke using both legs and fans, this action induces a complex wake of interconnected dipolar vortices that resemble a Kármán vortex street (Fig. 3F). This sudden change in direction may facilitate obstacle avoidance in fast, unsteady streams; evade predators; or escape unwanted mates. We calculated that adult *Rhagovelia*, with a mass of 2.1 ± 0.4 mg, traveling with a speed and acceleration of ~0.2 m/s and ~12 m/s^2, respectively, exerts a force of 26 μN and a momentum of 4.5×10^{-7} kg m/s during propulsion.

When turning, *Rhagovelia* induces a wake of dipolar vortices with the fan in contact with the water. These vortices have vorticities of up to ~100 s^{-1} and flow velocities of up to ~2 cm/s. By contrast, during propulsion, the vortices show similar vorticity to those observed during turning, but the flow velocity doubles (Fig. 3, K and L, and fig. S8). This suggests that individuals need to exert less momentum to the bulk fluid during turning. Tip vortices are shed and remain connected to the fan during a propulsion stroke (Fig. 3, G, I, and J). Capillary waves form during propulsion, along with bow waves at the front of the body (Fig. 3H and movie S1). Constructive interference occurs when waves from each leg converge at the back (Fig. 3H and movie S1).

Active and inactive fans

To understand the role of fans in *Rhagovelia* during the propulsive stroke, we filmed four adults with intact fans rowing on the water surface using a high-speed camera. We inactivated one fan on each individual with Loctite super glue and dusted the leg tip with lycopodium particles to maintain hydrophobicity (fig. S9). We then filmed these individuals rowing with one inactivated fan and one intact fan. Last, we inactivated the remaining fan on each individual and filmed them rowing again.

Legs with intact fans consistently showed lower tip accelerations and speeds than those of legs with inactivated fans, regardless of the treatment stage (control, one fan inactivated, or two fans inactivated) (Fig. 3M, fig. S10, and table S6). The reduced leg speed indicates a greater reaction force from the water acting on the leg, which is transferred to the body momentum. Thus, intact fans significantly enhance momentum transfer to the water through drag, resulting in high body speed (fig. S10). Particle image velocimetry (PIV) analysis supports these findings, showing that legs with intact fans during a propulsive stroke double the maximal flow speed compared with legs with inactivated fans (Fig. 3N).

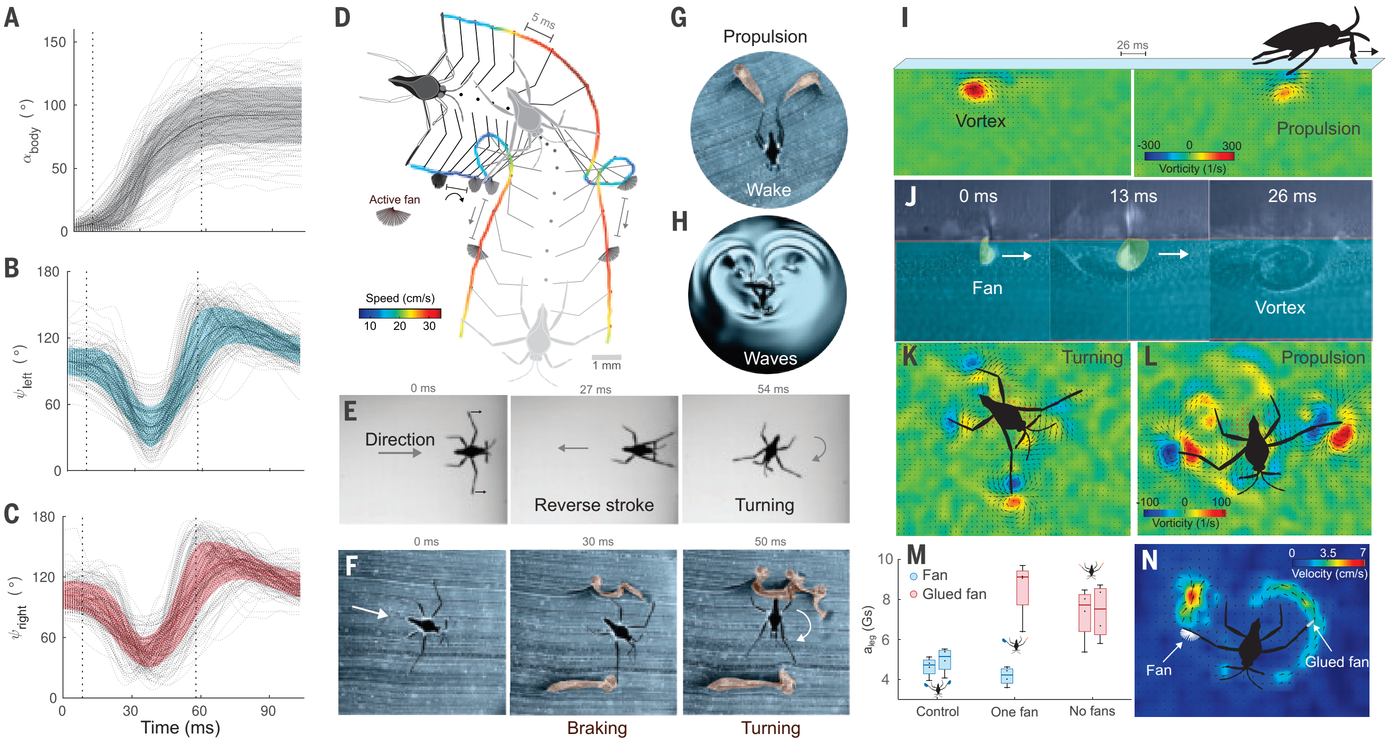

Fig. 3. *Rhagovelia*'s kinematics and hydrodynamics. (**A** to **C**) Time series of the (A) body angle, (B) left leg, and (C) right leg during turning maneuvering and propulsion. Dashed lines indicate each trial ($n = 159$). The colored line and shaded region indicate the mean and 1 SD. (**D**) Detailed illustration of turning and propulsion of an individual showing when the fan is spread. The time lapse between points is 5 ms, and the color bar indicates speed. (**E**) Braking maneuver using a symmetric reverse stroke and turning. (**F**) Vortical wake produced during braking and turning. (**G**) Vortical wake and (**H**) capillary waves produced during propulsion. (**I** and **J**) Side view of vortex produced by *Rhagovelia* during propulsion showing the (I) vorticity field and (J) flow visualization. The spread fan orientation is shown in (J). (**K** and **L**) Top view of (K) turning and (L) propulsion showing the vorticity field. (**M**) Leg acceleration during propulsion for individuals ($n = 4$) with both fans intact (control), one fan inactivated (one fan), and both fans inactivated (no fans). Box plots indicate median (line), 25th to 75th percentile (box), and extreme values (whiskers). (**N**) Velocity field using PIV of an individual with one fan inactivated. The intact fan induces higher flow speed than does the inactivated fan.

Rhagobot's actuation and control

For controlled leg movement in small-scale robotics, the Rhagobot uses four lightweight shape memory alloy (SMA) actuators (17 mg) (Fig. 4A and fig. S11). Actuators R1 and L1 manage the swing input, and R2 and L2 control the lift input, enabling robust horizontal and vertical leg movements (Fig. 4B and fig. S12A). The actuators can swing the open fan underwater without the fan bending and lift it from the water, achieving passive elastocapillary collapse (Fig. 4B). We applied 3 V of high voltage (V_2) to a single actuator to achieve fast full actuation and 0.75 V of low voltage (V_1) to maintain actuator position without overheating the SMA. Sequenced actuator signals enabled various leg motions—power, recovery, reverse strokes, liftoff, and touchdown—facilitating forward motion, braking, rotation while advancing, and rotation in place (Fig. 4C and fig. S12B).

Rhagobot performance with and without fan

To assess the impact of the artificial fan on locomotion, we constructed two types of robots. The first robot has driving legs coated with a superhydrophobic material for surface tension–based propulsion, similar to those of Gerridae water striders (*12*, *13*). The second robot has our hydrophilic artificial fan on the driving legs for drag-based propulsion in water, mimicking *Rhagovelia*. We applied identical input voltage signals to both robots, resulting in forward and turning motions.

Robots with fans traveled farther and made sharper turns as compared with those without fans (Fig. 4, D and E, and movie S2). Despite receiving the same input energy, the fan-equipped robot gains more momentum in water. PIV analysis showed that the fan increases maximum flow speed by 33% and vorticity by 24% during propulsion (Fig. 4F and fig. S13).

Leg speed during a stroke confirms that the fan generates stronger momentum. Comparing three configurations—both legs with fans, one leg with a fan, and neither leg with a fan—the legs without fans consistently show high speed (indicating less resistance in water and consequently less thrust) (Fig. 4G). This aligns with experiments on *Rhagovelia* with and without fans (Fig. 3, M and N). Fan-equipped robots achieved greater momentum, enhancing distance traveled and turning angle (Fig. 4H). The fan increased the forward acceleration and speed of the robot by 60 and 41%, respectively (Fig. 4, I and J). The average and maximum speeds of the robot with fan were 12.14 cm/s [1.47 body lengths (BL)/s] and 16.16 cm/s (1.96 BL/s), respectively.

Fan-assisted robot maneuverability

The fan-induced thrust increased forward speed and allowed rapid braking as well (Fig. 4K and movie S2). Without the fan, lowering both legs during forward motion did not sharply reduce speed owing to low shear force on the superhydrophobic legs. Lowering one leg into the water while moving forward enabled yaw turns centered on the fan. For faster rotation, swinging both legs in opposite directions induced rapid on-the-spot yaw rotation. The robot's average and maximum rotation speed for on-the-spot rotation were 87.1°/s and 206°/s, respectively, with the fan (Fig. 4L).

The collapsibility of the fan also notably reduced the energy required for the robot to lift the leg from the water. The artificial fan undergoes elastocapillary deformation when lifted from the water

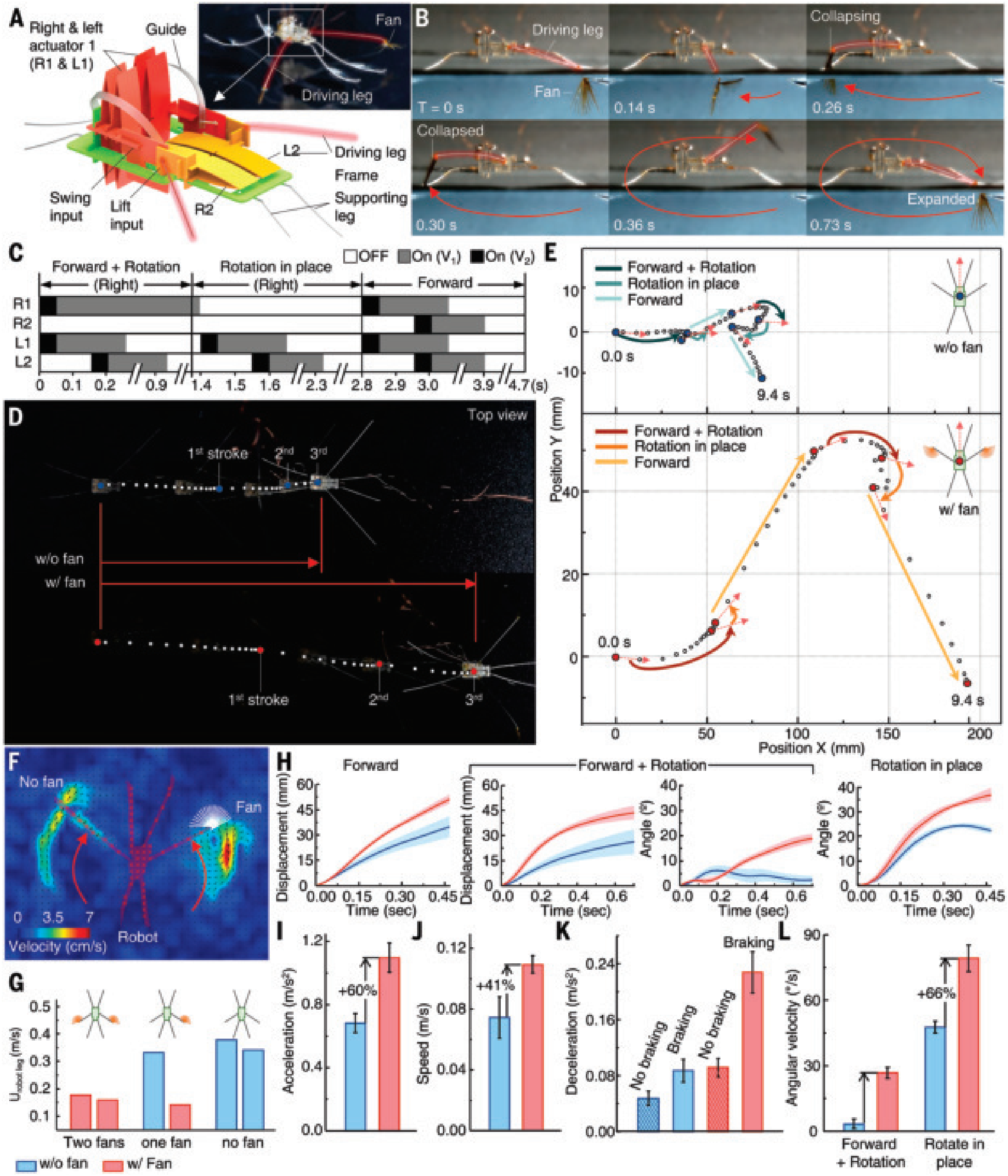

Fig. 4. Rhagobot control, performance, and agility. (**A**) Computer-aided design (CAD) model of a rhagobot driven by four SMA-based actuators. (**B**) Sequence of images showing the right side of the robot performing a rowing motion with a self-morphing artificial fan. (**C**) Driving voltage sequence of the four actuators (R1, R2, L1, and L2) to achieve three distinct motions: rotation while advancing, rotation in place, and forward motion. A high voltage (V_2) induces full actuator stroke within 50 ms, and a lower voltage (V_1) maintains the actuator's extended state without overheating the SMA. (**D**) Comparison of three sequential forward motions on the water surface with and without a fan. (**E**) Trajectory of the robot with and without fan performing three motions: rotation while advancing, rotation in place, and forward motion on the right and left sides. (**F**) Velocity field by using PIV to compare a swinging leg with a fan and a superhydrophobic coated leg. (**G**) Leg speed comparison for three robot configurations: both legs equipped with fans, only one leg with a fan, and neither leg with a fan. (**H**) Distance and body angle profiles of robots with and without fans. (**I** to **L**), Comparative analysis of (I) acceleration, (J) speed, (K) deceleration, and (L) angular velocity, demonstrating the superior performance of the robot equipped with fans.

surface, minimizing its surface area compared with that of noncollapsible structures, which are rigid solid pad and high-stiffness fan (Fig. 5A). The collapsible fan reduced the required energy for a leg to exit the water to less than 1/10 of that for a leg with noncollapsible structures (Fig. 5, B and C), which is critical for efficient interfacial locomotion. The Rhagobot cannot lift noncollapsible structures from water surface because of high surface tension acting on them (movie S2). Despite operating under the same input energy, the fan-equipped robot generated 3.01 μJ of kinetic energy, whereas the robot without a fan generated only 1.91 μJ (Fig. 5D).

The Rhagobot exhibited agile turning and faster speed as compared with those of previously reported semiaquatic robots. Rowing with a large hydrophilic pad has traditionally been feasible only in large-scale robots (*10*, *15*–*18*), which possess sufficient power output to overcome surface tension (Fig. 5, E and F). By contrast, small-scale robots typically rely on surface tension–based propulsion (*11*, *12*, *19*–*24*), which is limited until the water surface is broken. The other small-scale robot propulsion method involves the back-and-forth movement of passive flaps underwater (*14*, *25*–*29*), which leads to a reduction in overall stroke during recovery phase. The self-morphing elastocapillary fan enables the Rhagobot to generate greater momentum by maintaining its large surface area underwater and avoiding speed reduction in the recovery phase by retracting the collapsible fan from the water (Fig. 5F and table S7).

Discussion

Adaptations for unsteady aquatic niches

Natural streams are characterized by unsteady dynamics and abundant prey (*30*). These habitats pose substantial challenges for terrestrial insects, being difficult, dangerous, and energetically costly to transit. In situ field PIV analysis revealed that *Rhagovelia* moves in waters with flow speeds up to 1.6 m/s and turbulence levels of 65% (fig. S14). Long-term laboratory time-lapse observations uncovered that *Rhagovelia* rows continuously, day and night, stopping only briefly for feeding, cleaning, or molting (movie S1). At an average speed of 0.14 m/s, *Rhagovelia* can travel per day ~13 km, which is similar to the long-distance flights exhibited by fruit flies (*31*).

Fan structure and function

The anisotropic barbs and barbules of *Rhagovelia*'s fan promote rapid passive spreading and collapse, akin to a paintbrush interacting with liquid (fig. S15). Synthetic fan experiments show that this flat-ribbon geometry provides divergent stiffness in orthogonal directions, balancing elastocapillary spreading and drag-based thrust. The fan's minimal water retention aligns with observations in paintbrushes with flexible fibers and dandelion seeds (*32*). *Rhagovelia* keeps the tip of its leg on the water to avoid the extra load of a wet fan (fig. S3), contrasting with Gerridae water striders, which elevate their hydrophobic legs during recovery strokes (*13*).

Active and passive control mechanisms

Rhagovelia exhibits both passive (elastocapillarity) and active (claw-muscle) control over fan movement. The duration of fan spreading and collapse is similar in both cases. However, muscle-driven fan closing during swimming often leaves the fan partially spread, increasing drag during recovery strokes. Nonetheless, active control mechanisms allow precise locomotive control during unexpected challenges. Other water bugs, such as *Ptilomera sp.* (*7*) and *Halobates spp.* (*6*), have specialized hair brushes on their middle legs, which may also self-spread underwater through elastocapillary action. Comparative studies of these structures could provide insights into the evolutionary trends and locomotive functions of hair-like structures in water striders.

Turning like a fly

Rhagovelia's locomotion on the water surface mirrors the acrobatics of flying fruit flies during banking maneuvers. *Rhagovelia* can turn 96° at a peak angular speed of 4200°/s, in 50 ms (fig. S7), metrics that are similar to the fruit fly's quick body saccades of 93° turns at rate of 5000°/s in 49 ms (*33*, *34*). Whereas flies rely on continuous wing flapping for sharp yaw rotations (*35*), *Rhagovelia* achieves these maneuvers with a single reverse stroke (fig. S16). Compared with those of

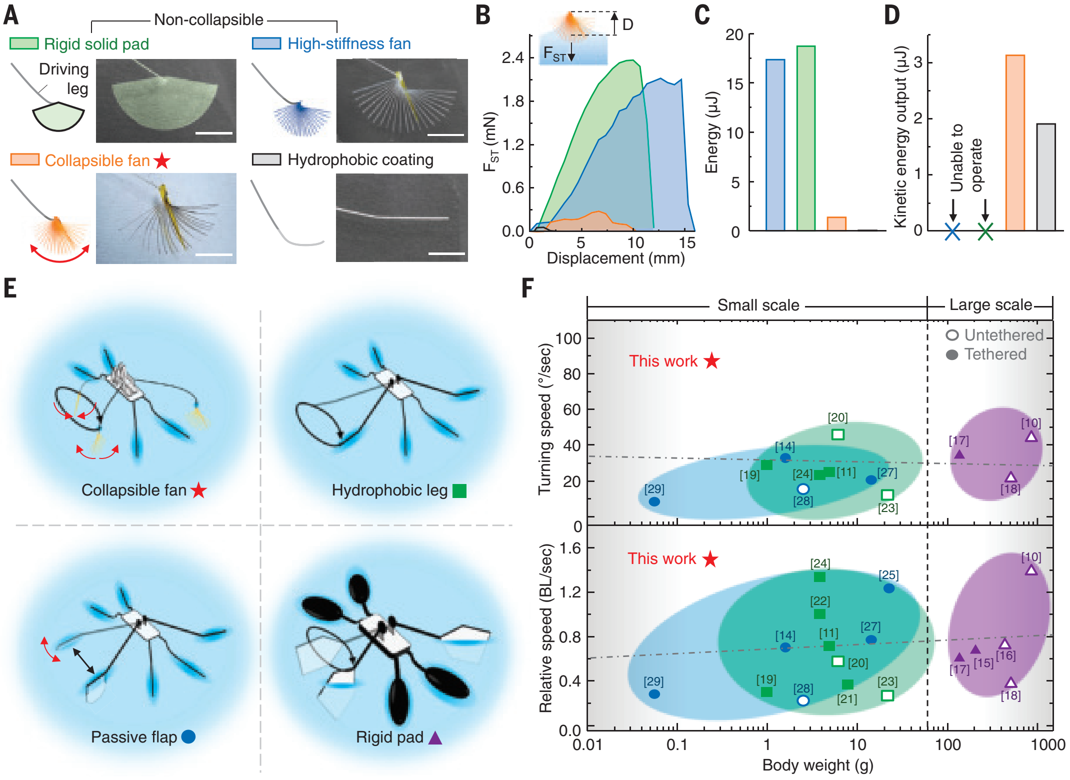

Fig. 5. Energy comparison of different types of driving legs and semi-aquatic robot comparison. (**A**) Schematics and images of the four different types of driving legs. (Top left) Rigid solid fan. (Top right) High-stiffness fan. (Bottom left) Collapsible fan. (Bottom right) Hydrophobic leg. Scale bar, 1 cm. (**B**) Pulling force (F_{ST}) acting on each leg as a function of its displacement. (**C**) Energy required to lift each leg completely out of the water. (**D**) Output kinetic energy of the robot equipped with each type of driving leg. (**E**) Schematics showing four different propulsion mechanisms of semiaquatic robots. (Top left) Rowing with a collapsible fan. (Top right) Rowing with a thin hydrophobic leg (Bottom left) Swinging a passive flap back and forth. (Bottom right) Rowing with a large rigid pad. Details of the robots are provided in table S7. (**F**) Turning speed and relative speeds comparison of semiaquatic robots relative to body weight. Dashed line indicates a linear fit of the robot performance data.

semiaquatic whirligig beetles, *Rhagovelia*'s turning rates are 50% faster (fig. S17 and table S8), and its stroke frequency (~20 Hz) is 2.5 times less (*36*, *37*). Whirligig beetles are limited to curved circular trajectories in slow, low-turbulence waters, whereas *Rhagovelia* performs sharp turns at high rates with low stroke frequencies in unsteady flow conditions.

Vortices and waves

Aquatic paddling birds generate thrust through lift using their feet as inverted delta wings (*38*), suggesting a similar lift-based thrust mechanism in *Rhagovelia* fan-based propulsion. Moreover, *Rhagovelia*'s wake during rowing comprises multiple vortices that resemble tip vortices on flying wings during propulsion (Fig. 3, G and F, and movie S1), warranting further hydrodynamic investigations. *Rhagovelia* also produces capillary waves during leg strokes, similar to those by Gerridae species and whirligig beetles (*13*, *39*). Recent evidence based on kinematic differences between the body and legs suggests that whirligig beetles during straight-path swimming may produce lift-based thrust (*40*). These capillary waves might serve locomotion, communication, or sensing functions, both in individuals and collectives.

Fan-assisted robotic maneuvers

The Rhagobot uses four compact, lightweight (~17 mg), SMA-based actuators (*41*), allowing each leg to be controlled with two degrees of freedom. These actuators enable the Rhagobot's various leg motions—power, recovery, reverse strokes, liftoff, and touchdown—allowing controlled rapid maneuverability up to ~1.96 BL/s and 206°/s.

Simple and lightweight passive actuation structures are essential for microrobots, eliminating the need for active actuators. Strategies such as passive wings (*42*), flaps (*25*), and alignments (*43*) have been widely used to interact with the environment. This concept, known as embodied intelligence (*44*), is exemplified by *Rhagovelia*'s fan. Inspired by this biological structure, we developed an ultralightweight, 21-layer robotic fan (~1 mg) that enables passive self-deployment for agile interfacial locomotion at small scales. This efficient, drag-dominant rowing at small scales offers new insights into locomotion strategies for both microrobots (*45*) and semiaquatic organisms (*46*) in surface tension–dominated regimes (*47*).

This work frames a physical basis for "interfacial intelligence": fast, reversible actuation governed by elastocapillarity and structural anisotropy. These mechanisms may generalize across systems in which geometry mediates fluid-structure interactions and in which contact, wetting, or immersion trigger deployment.

REFERENCES AND NOTES

1. J. T. Polhemus, D. A. Polhemus, *Hydrobiologia* **595**, 379–391 (2008).
2. D. Armisén *et al.*, *Mol. Biol. Evol.* **39**, msac229 (2022).
3. N. M. Andersen, *The Semiaquatic Bugs (Hemiptera, Gerromorpha): Phylogeny, Adaptations, Biogeography and Classification* (Scandinavian Science Press, 1982).
4. M. E. Santos, A. Le Bouquin, A. J. J. Crumière, A. Khila, *Science* **358**, 386–390 (2017).
5. W. Nachtigall, in *The Physiology of Insecta*, M. Rockstein, Ed. (Academic Press, ed. 2, 1974), pp. 381–432.
6. G. A. Mahadik *et al.*, *Sci. Rep.* **10**, 7785 (2020).
7. W. Kim *et al.*, *J. Ethol.* **40**, 211–221 (2022).
8. D. Kim, C. J. Park, J.-S. Koh, J. Ha, *MRS Bull.* **49**, 148–158 (2024).
9. B. Kwak, J. Bae, *Bioinspir. Biomim.* **13**, 041002 (2018).
10. X. Zhang, J. Yan, K. Yang, J. Zhao, S. Tang, *IEEE Robot. Autom. Lett.* **7**, 2463–2470 (2022).
11. J. Yan, K. Yang, G. Liu, J. Zhao, *IEEE Access* **8**, 89643–89654 (2020).
12. D. Kim *et al.*, *Micromachines* **13**, 627 (2022).
13. D. L. Hu, J. W. M. Bush, *J. Fluid Mech.* **644**, 5–33 (2010).
14. Y. Chen, N. Doshi, B. Goldberg, H. Wang, R. J. Wood, *Nat. Commun.* **9**, 2495 (2018).
15. H. Kim, D. Lee, K. Jeong, T. Seo, *IEEE/ASME Trans. Mechatron.* **21**, 175–183 (2016).
16. Z. Shihao *et al.*, in *2016 6th IEEE International Conference on Biomedical Robotics and Biomechatronics (BioRob)* (2016), pp. 145–150.
17. J. Yan, X. Zhang, K. Yang, J. Zhao, in *2019 IEEE International Conference on Robotics and Biomimetics (ROBIO)* (2019), pp. 142–147.
18. H. Huang, C. Sheng, G. Wu, Y. Shen, H. Wang, *Appl. Sci.* **10**, 6300 (2020).
19. Y. S. Song, M. Sitti, *IEEE Trans. Robot.* **23**, 578–589 (2007).
20. Y. S. Song, M. Sitti, in *Proceedings 2007 IEEE International Conference on Robotics and Automation* (2007), pp. 980–984.
21. K. Suzuki, H. Takanobu, K. Noya, H. Koike, H. Miura, in *2007 IEEE/RSJ International Conference on Intelligent Robots and Systems* (2007), pp. 590–595.
22. X. Zhang *et al.*, *ACS Appl. Mater. Interfaces* **3**, 2630–2636 (2011).
23. O. Ozcan, H. Wang, J. D. Taylor, M. Sitti, *Int. J. Adv. Robot. Syst.* **11**, 85 (2014).
24. J. H. Yan *et al.*, *Bioinspir. Biomim.* **10**, 046016 (2015).
25. B. Kwak, J. Bae, *J. Bionic Eng.* **14**, 260–271 (2017).
26. B. Kwak, J. Bae, *Bioinspir. Biomim.* **12**, 036014 (2017).
27. S. Wang *et al.*, *Smart Mater. Struct.* **28**, 045006 (2019).
28. J. Ko *et al.*, *Sci. Robot.* **7**, eabo6463 (2022).
29. C. K. Trygstad, X. T. Nguyen, N. O. Pérez-Arancibia, in *2023 IEEE/RSJ International Conference on Intelligent Robots and Systems (IROS)* (2023), pp. 2693–2700.
30. T. L. Ramey, J. S. Richardson, *Bioscience* **67**, 808–819 (2017).
31. K. J. Leitch, F. V. Ponce, W. B. Dickson, F. van Breugel, M. H. Dickinson, *Proc. Natl. Acad. Sci. U.S.A.* **118**, e2013342118 (2021).
32. T. Yamamoto *et al.*, *NPG Asia Mater.* **8**, e241–e241 (2016).
33. F. T. Muijres, M. J. Elzinga, J. M. Melis, M. H. Dickinson, *Science* **344**, 172–177 (2014).
34. F. T. Muijres, M. J. Elzinga, N. A. Iwasaki, M. H. Dickinson, *J. Exp. Biol.* **218**, 864–875 (2015).
35. A. J. Bergou, L. Ristroph, J. Guckenheimer, I. Cohen, Z. J. Wang, *Phys. Rev. Lett.* **104**, 148101 (2010).
36. J. H. Thorp, D. C. Rogers, *Thorp and Covich's Freshwater Invertebrates: Ecology and General Biology* (Elsevier Science, 2014).
37. F. E. Fish, A. J. Nicastro, *J. Exp. Biol.* **206**, 1649–1656 (2003).
38. L. C. Johansson, R. Å. Norberg, *Nature* **424**, 65–68 (2003).
39. T. Steinmann, A. Cribellier, J. Casas, *J. Fluid Mech.* **915**, A118 (2021).
40. Y. Sun, J. Shields, C. Roh, *Curr. Biol.* **34**, R12–R13 (2024).
41. D. Kim *et al.*, *Nat. Commun.* **13**, 4155 (2022).
42. H.-V. Phan, H. C. Park, D. Floreano, *Nature* **632**, 1067–1072 (2024).
43. M. A. Graule *et al.*, *Science* **352**, 978–982 (2016).
44. G. Mengaldo *et al.*, *Nat. Rev. Phys.* **4**, 595–610 (2022).
45. J.-S. Koh *et al.*, *Science* **349**, 517–521 (2015).
46. W. Kim *et al.*, *Proc. Natl. Acad. Sci. U.S.A.* **120**, e2219972120 (2023).
47. M. Gwon *et al.*, *Nat. Commun.* **14**, 1473 (2023).

ACKNOWLEDGMENTS

V.M.O.-J. thanks C. Sanford and KSU for their support during his postdoctoral research, particularly in the initial observations, as well as some of the experiments, data collection, and fluid visualizations of *Rhagovelia* included in this paper. J.-S.K. acknowledges J. Ha for validating the energy equations related to elastocapillarity. We thank F. E. Fish for the helpful comments on turning rates in fig. S17. We thank E. Perry and S. Lee for SEM imaging support. We thank D. He and Y. Hu for help with atomic force microscopy measurements. **Funding:** V.M.O.-J. acknowledges the internal funding support from the University of Maine and the University of California, Berkeley. S.B. acknowledges funding support from NIH MIRA grant R35GM142588; NSF grants PHY-2310691, CMMI-2218382, and CAREER iOS-1941933; the Open Philanthropy Project; and Schmidt Sciences. J.-S.K. acknowledges funding support from the National Research Foundation of Korea grants funded by the Korean government (grants RS-2021-NR061649 and RS-2024-00411660) and the internal funding from Ajou University. **Author contributions:** V.M.O.-J., D.K., J.-S.K., and S.B. conceptualized the research. V.M.O.-J. designed the animals' experimental framework. D.K. and J.-S.K. contributed to the design of the artificial fan and semiaquatic robot. D.K., C.K., and J.-S.K. developed the robot's experimental design. V.M.O.-J., D.K., J.-S.K., and S.B. contributed to the research methodology. D.K., C.K., and J.-S.K. conceived the theoretical model of the robotic fan. S.K. and S.B. analyzed the fan's physical properties. V.M.O.-J. conducted fieldwork and fluid dynamics analysis. S.B. and J.-S.K. provided funding for the project and supervised the research. V.M.O.-J., D.K., J.-S.K., S.K., and S.B. contributed to writing, reviewing, and editing the manuscript. **Competing interests:** The authors declare no competing interests. **Data and materials availability:** All data are available in the manuscript or the supplementary materials.

SUPPLEMENTARY MATERIALS

science.org/doi/10.1126/science.adv2792
Materials and Methods; Figs. S1 to S17; Tables S1 to S8; References (*48*–*71*); Movies S1 and S2; Data S1 to S6

Submitted 13 January 2025; accepted 20 June 2025

10.1126/science.adv2792

LIGHT POLLUTION

Light pollution prolongs avian activity

Brent S. Pease[1]*† and Neil A. Gilbert[2]*†

Light pollution disrupts light–dark cues that organisms use as timetables for life. Although studies—typically focusing on individual species—have documented earlier morning onset of bird vocalization in light-polluted landscapes, a synthesis of light pollution effects across species, space, and season is lacking. We used a global acoustic dataset of more than 60 million detections, representing 583 diurnal bird species, to synthesize effects of light pollution on avian vocalization. On average, light pollution prolonged vocal activity by 50 min. Light pollution responses were strongest for species with large eyes, open nests, migratory habits, and large ranges and during the breeding season. Prolonged activity may confer negative, neutral, or positive fitness effects; documenting these fitness effects and curbing light pollution are challenges for 21st-century conservation.

In many parts of the world, the night is no longer dark. Light pollution affects 23% of Earth's surface (*1*) and is rapidly growing in both extent and intensity (*2*). Beyond detrimental effects on human health (*3*), many wildlife taxa are affected by light pollution, with negative consequences including die-offs of insects (*4*), disorientation of nocturnally migrating birds (*5*), and disruptions of seasonal hormonal rhythms (*6*).

One of the most insidious effects of light pollution is the disruption of the biological timings that organisms have evolved in response to the light–dark cycles of day and night (*7*). Diurnal species may misinterpret artificial light as daylight and be active earlier in the morning and later in the evening than they would be in dark landscapes (Fig. 1A) (*7*). In birds, several studies have documented earlier onset of morning vocalization in light-polluted sites (*8*–*11*); however, other studies have reported weak or no influence of light pollution (*12*–*14*). This heterogeneity in the literature likely arises from data limitations, as most studies focus on one or a few species for a small number of locations and a single season (*9*, *12*). We leverage a global dataset (Fig. 1B) of millions of observations of morning onset and evening cessation of vocalization for hundreds of bird species to provide a synthesis of light pollution's effects on bird behavior across species, space, and seasons.

We hypothesized that species traits (eye size, nest structure, migratory habit, range size, and habitat structure) and context (latitude, biotic community, and season) mediate light pollution responses. Our data come from BirdWeather, an emerging project that represents a three-way intersection of volunteer science, automated biodiversity monitoring, and machine learning (Fig. 1C). Volunteers deploy acoustic sensors linked to the BirdNET algorithm, which identifies vocalizations for ~6000 bird species (*15*) (Fig. 1C). We downloaded BirdWeather observations for March 2023 to March 2024 (181 million detections prior to filtering; Fig. 1D) and calculated the time of first vocalization (relative to sunrise; hereafter "onset") and last vocalization (relative to sunset; hereafter "cessation"). To characterize light pollution, we extracted the average radiance (nanowatts/sr/cm^2) from the Visible Infrared Imaging Radiometer Suite (VIIRS) satellite product at sensor coordinates for the month corresponding to each observation of onset or cessation (*16*) (Fig. 1B). In summary, for onset we had 2.6 million observations for 583 species (94 families) from 7824 locations, whereas for cessation we had 1.8 million observations for 493 species (76 families) from 7658 locations (Fig. 1, B and D).

Vocal activity prolonged by nearly an hour

Avian vocal activity was prolonged by an average of 50 min in the brightest landscapes (Fig. 2A). Averaged across species, space, and seasons, there was moderate evidence that birds began vocalizing earlier in the morning as light pollution increased [effect size: −0.05 ± 0.03 (standard error); $P = 0.06$] such that vocalization onset occurred 18 min earlier in the brightest landscapes compared with the darkest landscapes (Fig. 2, A and B). Similarly, there was strong evidence that evening cessation of vocalization shifted later with increasing light pollution (effect size: 0.09 ± 0.04, $P = 0.03$) such that cessation occurred 32 min later in the brightest compared with the darkest landscapes (Fig. 2, A and C). The stronger effect for cessation compared with onset contradicts a recent meta-analysis that found stronger effects of light pollution on onset relative to cessation for diurnal species (*17*). We suspect our result arises because the species in the cessation analysis (493 versus 583 for onset) are disproportionately sensitive to light pollution. To test this, we fit an additional onset model for the 493 species represented in the cessation analysis and did indeed find stronger effects: The effect of light pollution on morning onset was −0.07 ± 0.03 ($P = 0.02$), representing an advance of 25 min. A supplemental analysis revealed similar light pollution effects for a model that also included distance to road, a proxy for noise pollution, which also affects bird vocal behavior (*9*) [supplementary materials (SM), fig. S2]. Finally, as a corollary to our finding that diurnal species show prolonged activity in response to light pollution, we expected that nocturnal species would show truncated activity in light-polluted areas; a supplemental analysis produced weak support of this hypothesis (SM, fig. S3).

Eye size, nest type, migration, and range size linked to light pollution responses

Species with large eyes showed stronger responses to light pollution than species with small eyes for both onset ($P = 0.005$) and cessation ($P < 0.001$; Fig. 3A). Comparing the brightest versus darkest landscapes, species with the largest eyes began vocalizing 35 min earlier in the morning, contrasting with only a 3-min advance for the smallest-eyed species (Fig. 3A). Similarly, in the evening, species with the largest eyes ceased vocalizing 56 min later in the brightest landscapes, contrasting with only an 8-min delay for the smallest-eyed species (Fig. 3A). Large-eyed species, which tend to live in dark habitats such as forest understory (*18*, *19*), may be particularly capable of perceiving photic cues, including light pollution, compared with small-eyed species, driving the stronger response we observed. Alternatively, large-eyed species may be disproportionately exposed to light pollution because they are active under dimmer conditions (e.g., earlier in the morning) relative to small-eyed species (*20*), leading to the strong effects observed. Sensory traits such as eye size—which are phylogenetically conserved (*19*)—likely explain why closely related families often showed similar baseline vocalization and light pollution responses (Fig. 3B). For example, five out of six of the families in the order Charadriiformes began vocalization prior to sunrise and showed earlier vocalization onset with increasing light pollution (Fig. 3B). Moreover, sensory traits likely underpin the analogous family-level results between morning and evening; for example, 76% of families showed baseline vocalization times after sunrise and before sunset (i.e., both during the daylight; Fig. 3B).

Species with open nests showed stronger light pollution responses compared with cavity nesters for onset ($P < 0.001$) and cessation ($P = 0.02$; Fig. 3A). Comparing the brightest and darkest landscapes, open-nesters began vocalizing 22 min earlier in the morning and ceased

---

[1]School of Forestry and Horticulture, Southern Illinois University, Carbondale, IL, USA. [2]Department of Biology, Oklahoma State University, Stillwater, OK, USA. ***Corresponding author. Email: bpease1@siu.edu (B.S.P.); neil.gilbert@okstate.edu (N.A.G.)** †These authors contributed equally to this work.

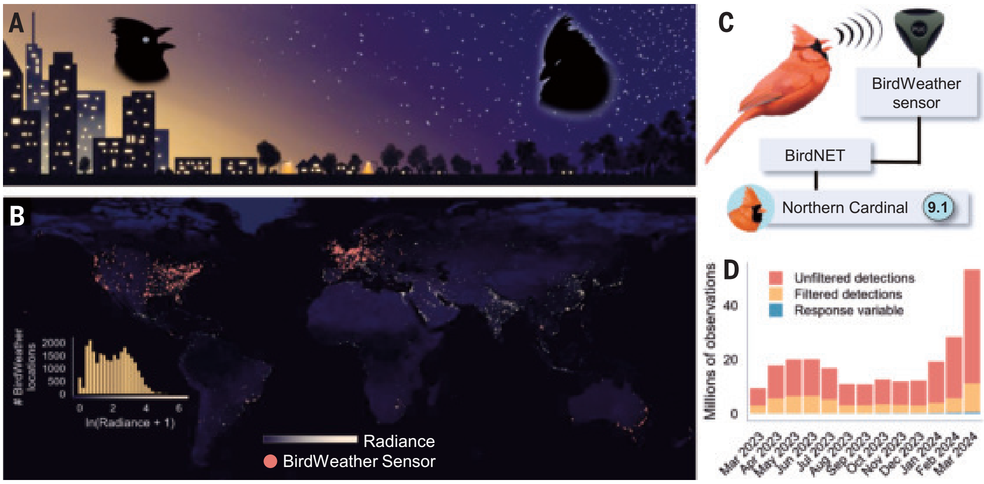

Fig. 1. Big data reveal the global impact of light pollution on avian activity. (**A**) Light pollution causes birds to vocalize earlier in the morning and later in the evening compared with dark landscapes. (**B**) We obtained bird vocalization data from 7824 BirdWeather locations (red dots; see fig. S1 for a larger map) and extracted light pollution data from the VIIRS nighttime lights product (basemap). The histogram (inset) shows the distribution of light pollution values for all BirdWeather sensors. (**C**) BirdWeather is a network of acoustic sensors maintained by volunteers that are linked to the BirdNET machine learning algorithm, which classifies vocalizations to species. (**D**) Number (in millions) of BirdWeather observations per month; red represents unfiltered detections, yellow represents detections filtered with BirdNET confidence and sample size thresholds, and blue represents one of the response variables (morning onset).

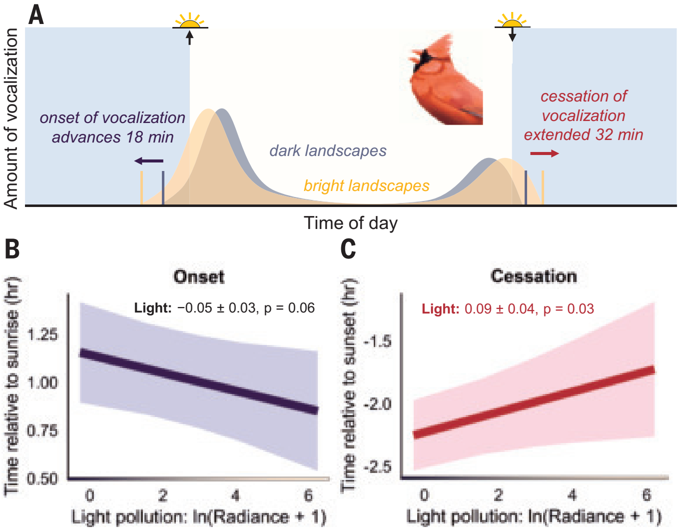

Fig. 2. Light pollution prolongs avian vocal activity by nearly an hour. (**A**) Most diurnal bird species show bimodal vocalization patterns with peaks in the morning and evening; in light-polluted landscapes (yellow shading), the first vocalizations occur earlier in the morning and the last vocalizations occur later in the evening. (**B**) Globally—averaged across species, space, and season—onset of morning vocalization shifted 18 min earlier in the brightest landscapes versus the darkest landscapes. (**C**) Similarly, evening cessation was delayed by an average of 32 min. In (B) and (C), lines are means and shaded regions are 95% confidence intervals (CI) of model predictions.

vocalizing 35 min later in the evening, contrasting with a 0.9-min earlier onset and a 19-min later cessation for cavity-nesters (Fig. 3A). These results support the idea that nest structure can shield birds from light pollution (*21*). The asymmetry in the strength of nest effect between morning and evening likely arises because a bird that nests or roosts in a cavity must enter its chamber to be shielded from photic cues.

Migrant species showed stronger light pollution responses compared with sedentary ones for onset and cessation ($P < 0.001$; Fig. 3A). Comparing the brightest versus darkest landscapes, migratory species began vocalizing 27 min earlier in the morning and ceased vocalizing 51 min later in the evening, contrasting with a 14-min earlier onset and a 20-min later cessation for sedentary species (Fig. 3A). Partial migrants (i.e., species for which only a minority of the population migrates long distances) did not show different light pollution responses from sedentary species ($P = 0.93$ and 0.87 for onset and cessation, respectively). Many migratory species migrate at night—despite being otherwise diurnal—and may thus have more circadian flexibility compared with sedentary species (*22*). Alternatively, migration rapidly exposes birds to latitudinal differences in day length and may prime migratory species to respond to light pollution cues (*23*).

Species with large ranges exhibited stronger responses to light pollution than species with small ranges for both onset ($P < 0.001$) and cessation ($P < 0.001$; Fig. 3A). For example, comparing the brightest versus darkest landscapes, this result implies that a species with a range size of 65,500,000 km^2 (~13% of Earth's land area) would show a 29-min earlier onset while a species with a range size of 163,000 km^2 (~0.03% of Earth's land area) would show a 1.4-min later onset. Previous work indicates that species with larger ranges have broader diets, habitat preferences, and thermal tolerances (*24*); our result may indicate that species with large ranges may also be "time generalists" with a broader or more flexible temporal niche than species with small ranges (*23*).

Limited evidence for effects of habitat density, latitude, and species richness

We found contradictory results between morning and evening for habitat density, as birds associated with open habitats showed stronger light pollution responses for onset ($P = 0.02$) but weaker light pollution responses for cessation ($P < 0.001$) relative to species associated with dense habitats. Although the results for onset support the hypothesis that habitat structure, such as nest structure, nests may shield birds from artificial light, the opposing results for cessation indicate that this result is perhaps best interpreted with caution.

We did not find statistically significant effects of latitude on light pollution responses (Fig. 3A). Latitude could influence light pollution responses through its association with photoperiod seasonality; if high-latitude species are adapted to seasonal variation in photoperiod and low-latitude taxa have more fixed temporal niches, stronger light pollution responses may be apparent for high-latitude species (*23*). Alternatively, because low-latitude birds can perceive even minor variation in day length near the equator (*25*, *26*), light pollution may represent a more novel cue and motivate stronger responses in low-latitude species. Because only ~0.2% of our dataset came from latitudes between −20° and 20° (Fig. 1B), we are hesitant to interpret our results as conclusive that light pollution responses do not vary by latitude (*23*).

High species richness was associated with stronger light pollution effects for cessation ($P = 0.03$) but not for onset ($P = 0.22$; Fig. 3A). Although conspecific vocalizations can entrain circadian rhythms (*27*) and induce earlier onset of vocalization (*28*), previous work has

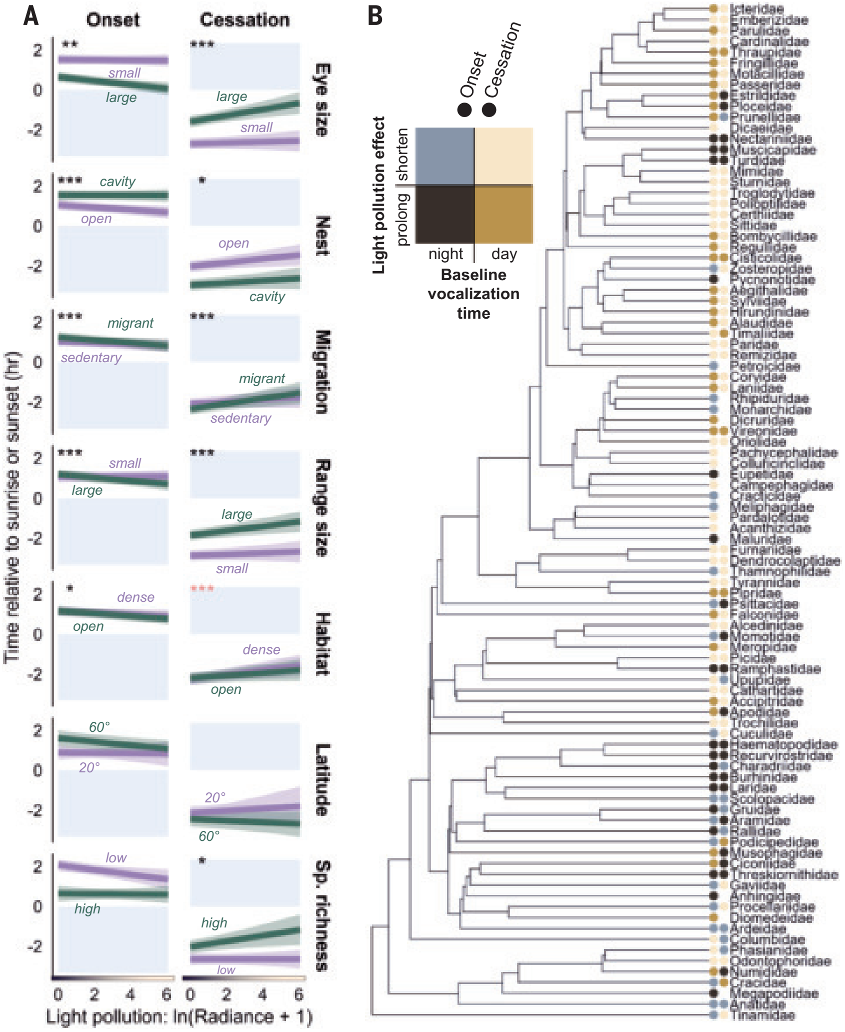

Fig. 3. Variation in light pollution responses by traits, context, and phylogeny. (**A**) Effects of traits and context on light pollution responses; lines are means and shaded regions are 95% CI of model predictions. Shaded rectangles in the background indicate whether the time is during the day (yellow, after sunrise or before sunset) or night (gray, before sunrise or after sunset). The asterisks indicate the degree of significance for the interaction between light pollution and the covariate (***, $P < 0.001$; **, $P < 0.01$; *, $P < 0.05$). Asterisk color indicates whether the effect of the covariate supports (black) or opposes (red) the hypotheses. (**B**) Family-level summary of baseline onset and cessation timing (cool colors, before sunrise and after sunset; warm colors, after sunrise and before sunset) and light pollution response (darker colors, prolonged activity; paler colors, shortened activity).

reported mixed evidence that birds initiate activity in response to heterospecific vocalizations (*28*, *29*). If birds use heterospecific cues to time activity, birds in more diverse locations may show stronger light pollution responses because richer communities likely contain species that exhibit strong light pollution responses and whose vocalizations reinforce photic cues. Our results might indicate an "inertia" effect such that heterospecific cues are not sufficient to initiate vocalizations from inactive birds but are enough to motivate continued activity of already-active birds. However, the discrepancy between morning and evening results is perhaps best interpreted as only weak evidence of effects of interspecific cues on light pollution responses.

Strongest effects of light pollution during the breeding season

Light pollution effects showed substantial seasonal variation and were generally strongest during the breeding season, particularly for onset (Fig. 4). This result likely arises because birds naturally vocalize earlier in the morning during the breeding season relative to the nonbreeding season (*8*), heightening exposure to light pollution. For example, the Northern Cardinal (*Cardinalis cardinalis*, a North American species), showed the largest onset advances during the week of 29 May (a 60-min earlier onset in the brightest landscapes compared to the darkest) but the weakest effects during the week of 11 September (a 48-min later onset in the brightest landscapes; Fig. 4A). Of the Northern Hemisphere species that were detected throughout the year ($n = 75$ for onset, $n = 61$ for cessation), 50% of species showed their strongest light pollution effects between the weeks of 1 April and 15 July (i.e., 28.8% of the year) for onset and the weeks of 4 March and 23 September (i.e., 55.8% of the year) for cessation (Fig. 4B). The highest proportions of species with prolonged vocalization in bright landscapes occurred May to June in the Northern Hemisphere but December to January in the Southern Hemisphere (Fig. 4C). Seasonality likely explains the considerable species-level variation in light pollution effects, which often eclipsed family-level variation; the standard deviation among family-level light pollution slopes was 0.22, compared with 0.47 for a nested grouping by species, 5° grid cell, and week.

Outstanding question: Fitness effects of prolonged days

Our analyses suggest that, on average, light pollution prolongs vocal activity of diurnal birds by nearly an hour. This prolonged activity could have negative, neutral, or positive fitness effects. On the one hand, 50 min of prolonged activity may represent a substantial loss of resting time, particularly during the breeding season, which is an already demanding period for birds (*30*). In humans, sleep debt is associated with adverse health outcomes such as inflammatory disease (*31*). In nonhuman vertebrates, loss of rest from light pollution has been linked with increased levels of stress hormones (*32*, *33*), and for two species of mice, reduced fecundity and survival (*33*). For birds, however, prolonged activity may not translate to sleep debt and the detrimental effects thereof if birds can rest during the day, sleep more intensely during periods of nonactivity (*34*, *35*), or sleep with one brain hemisphere during activity (*36*). Indeed, light pollution–related changes to activity may lead to positive fitness effects if they facilitate increased foraging time (*37*, *38*) or reproductive output (*39*–*41*). Regarding reproductive output, earlier onset of activity is linked to higher numbers of extra-pair copulations for males (*42*) and larger numbers of chicks fledged for females (*43*). Moreover, studies have documented parents of diurnal bird species feeding their young during the night in light-polluted environments (*39*, *40*), and one of these studies linked the increased foraging time to increased fledging success (*39*). Resolving the fitness impacts, if any, of light-polluted prolonged days requires rigorous field experiments to facilitate meta-analyses (*44*) in conjunction with creative analysis of macro-demography databases (*45*).

Accumulation of global acoustic data and nighttime conservation

We leveraged an emerging global dataset to synthesize light pollution responses of hundreds of bird species over multiple seasons. Although our dataset has global coverage, the BirdWeather database demonstrates a pattern prevalent in ecological studies: the United States, western

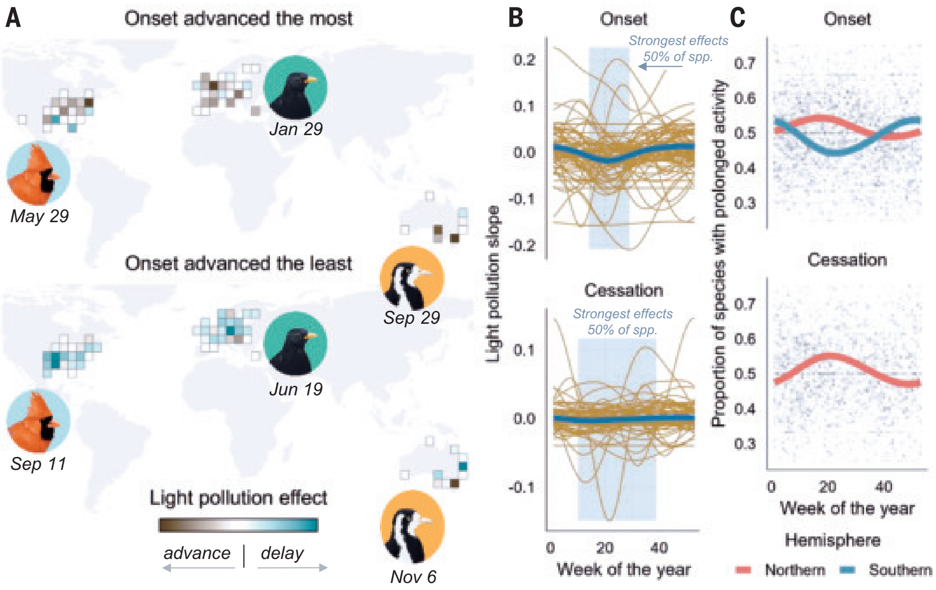

Fig. 4. Light pollution effects are strongest during the breeding season. (**A**) Relative strength of light pollution effects on vocalization onset during the two weeks with the strongest and weakest advances for three species: Northern Cardinal (*Cardinalis cardinalis*, North America), Eurasian Blackbird (*Turdus merula*, Europe), and Magpie-lark (*Grallina cyanoleuca*, Australia). (**B**) Seasonal trends in light pollution slopes for northern hemisphere species that were detected throughout the year ($n = 75$ for onset, $n = 61$ for cessation). Brown lines are trends for individual species; the blue line is the trend across species. Shaded boxes indicate the weeks containing the strongest light pollution responses for at least 50% of species. (**C**) Proportion of species (by 5° grid cell and week) that show prolonged vocal activity in response to light pollution. The highest proportions of species with prolonged activity occur May to June in the northern hemisphere (red) but December to January in the southern hemisphere (blue; insufficient data for cessation).

Europe, and Australia are overrepresented, with less data coming from the Global South. However, user-friendly software such as BirdNET promises to expand participation and, over time, ameliorate the sampling imbalances between regions (*46*). Expansion of data in the Global South and in high-latitude regions will clarify latitudinal patterns of light pollution responses (*47*). Moreover, behavioral differences between temperate and tropical birds—for example, year-round territory defense in some tropical species (*48*)—might give rise to different seasonal effects of light pollution (e.g., more consistent effects through the year) than those we identified. Further accumulation of global data may also motivate development of intergovernmental policy—akin to climate change efforts—to counteract light pollution. Restoring the darkness of our nights is a preeminent challenge for 21st-century conservation and demands global cooperation (*49*).

REFERENCES AND NOTES

1. F. Falchi *et al.*, *Sci. Adv.* **2**, e1600377 (2016).
2. C. C. M. Kyba, Y. Ö. Altıntaş, C. E. Walker, M. Newhouse, *Science* **379**, 265–268 (2023).
3. M. D. C. Cupertino *et al.*, *Biol. Rhythm Res.* **54**, 263–275 (2023).
4. A. C. S. Owens *et al.*, *Biol. Conserv.* **241**, 108259 (2020).
5. B. M. Van Doren *et al.*, *Proc. Natl. Acad. Sci. U.S.A.* **118**, e2101666118 (2021).
6. D. Dominoni, M. Quetting, J. Partecke, *Proc. Biol. Sci.* **280**, 20123017 (2013).
7. K. J. Gaston, T. W. Davies, S. L. Nedelec, L. A. Holt, *Annu. Rev. Ecol. Evol. Syst.* **48**, 49–68 (2017).
8. C. A. Staicer, D. A. Spector, A. G. Horn, in *Ecology and Evolution of Acoustic Communication in Birds*, in D. E. Kroodsma, E. H. Miller, Eds. (Cornell University Press, 1996), pp. 426–453.
9. O. H. Marín-Gómez, I. MacGregor-Fors, *Ibis* **163**, 1133–1154 (2021).
10. A. Da Silva, B. Kempenaers, *J. Anim. Ecol.* **86**, 1286–1297 (2017).
11. A. Da Silva, M. Valcu, B. Kempenaers, *Philos. Trans. R. Soc. B* **370**, 20140126 (2015).
12. A. L. Dickerson, M. L. Hall, T. M. Jones, *Anim. Behav.* **198**, 93–105 (2023).
13. R. A. Fuller, P. H. Warren, K. J. Gaston, *Biol. Lett.* **3**, 368–370 (2007).
14. A. M. Dorado-Correa, M. Rodríguez-Rocha, H. Brumm, *R. Soc. Open Sci.* **3**, 160231 (2016).
15. S. Kahl, C. M. Wood, M. Eibl, H. Klinck, *Ecol. Inform.* **61**, 101236 (2021).
16. C. D. Elvidge, K. Baugh, M. Zhizhin, F. C. Hsu, T. Ghosh, *Int. J. Remote Sens.* **38**, 5860–5879 (2017).
17. D. Sanders, E. Frago, R. Kehoe, C. Patterson, K. J. Gaston, *Nat. Ecol. Evol.* **5**, 74–81 (2021).
18. V. Jirinec, P. F. Rodrigues, B. R. Amaral, P. C. Stouffer, *Ecology* **103**, e3645 (2022).
19. I. J. Ausprey, *Proc. Biol. Sci.* **288**, 20210853 (2021).
20. R. J. Thomas *et al.*, *Proc. Biol. Sci.* **269**, 831–837 (2002).
21. T. Raap, R. Pinxten, M. Eens, *J. Exp. Zool. A Ecol. Integr. Physiol.* **329**, 449–456 (2018).
22. D. Zúñiga *et al.*, *Sci. Rep.* **6**, 34207 (2016).
23. N. A. Gilbert *et al.*, *Trends Ecol. Evol.* **38**, 324–336 (2023).
24. R. A. Slatyer, M. Hirst, J. P. Sexton, *Ecol. Lett.* **16**, 1104–1114 (2013).
25. R. Quispe, J. M. B. Protazio, M. Gahr, *Sci. Rep.* **7**, 9140 (2017).
26. M. Hau, M. Wikelski, J. C. Wingfield, *Proc. Biol. Sci.* **265**, 89–95 (1998).
27. M. Menaker, A. Eskin, *Science* **154**, 1579–1581 (1966).
28. L. Hodgson, J. R. Waas, J. R. Foote, *J. Avian Biol.* **49**, e01749 (2018).
29. C. Xia, H. Lloyd, J. Shi, C. Wei, Y. Zhang, *Ethology* **124**, 400–409 (2018).
30. S. Daan, C. Deerenberg, C. Dijkstra, *J. Anim. Ecol.* **65**, 539–544 (1996).
31. M. R. Irwin, *Annu. Rev. Psychol.* **66**, 143–172 (2015).
32. V. J. Alaasam *et al.*, *J. Exp. Zool. A Ecol. Integr. Physiol.* **329**, 465–472 (2018).
33. H. Vardi-Naim, A. Benjamin, T. Sagiv, N. Kronfeld-Schor, *Sci. Rep.* **12**, 16486 (2022).
34. J. A. Lesku, A. L. Vyssotski, D. Martinez-Gonzalez, C. Wilzeck, N. C. Rattenborg, *Proc. Biol. Sci.* **278**, 2419–2428 (2011).
35. F. Connelly *et al.*, *Environ. Pollut.* **267**, 115484 (2020).
36. N. C. Rattenborg *et al.*, *Nat. Commun.* **7**, 12468 (2016).
37. R. G. Dwyer, S. Bearhop, H. A. Campbell, D. M. Bryant, *J. Anim. Ecol.* **82**, 478–485 (2013).
38. E. Amichai, N. Kronfeld-Schor, *Sci. Rep.* **9**, 11052 (2019).
39. J.-S. Wang, M.-N. Tuanmu, C.-M. Hung, *Environ. Pollut.* **288**, 117805 (2021).
40. S. A. Rush, T. R. Rovery, A. Naveda-Rodríguez, *J. Ornithol.* **166**, 303–305 (2025).
41. A. P. Rose, B. E. Lyon, *Ecology* **94**, 1327–1337 (2013).
42. B. Kempenaers, P. Borgström, P. Loës, E. Schlicht, M. Valcu, *Curr. Biol.* **20**, 1735–1739 (2010).
43. R. J. Womack, P. Capilla-Lasheras, C. L. McGlade, D. M. Dominoni, B. Helm, *Anim. Behav.* **205**, 65–78 (2023).
44. T. Raap, R. Pinxten, M. Eens, *Glob. Change Biol.* **23**, 5024–5026 (2017).
45. M. Senzaki *et al.*, *Nature* **587**, 605–609 (2020).
46. C. M. Wood, S. Kahl, A. Rahaman, H. Klinck, *PLOS Biol.* **20**, e3001670 (2022).
47. S. A. Keith, J. P. Drury, B. J. McGill, G. F. Grether, *Trends Ecol. Evol.* **38**, 1177–1188 (2023).
48. E. S. Morton, in *Ecology and Evolution of Acoustic Communication in Birds*, in D. E. Kroodsma, E. H. Miller, Eds. (Cornell University Press, 1996), pp. 258–268.
49. A. Alva, E. Brown, A. Evans, D. Morris, K. Dunning, *J. Environ. Plann. Manage.* **68**, 907–934 (2025).
50. N. Gilbert, B. Pease, BrentPease1/alan: v1.21, Version revisionv21 (Zenodo, 2025); https://doi.org/10.5281/zenodo.15635107.

ACKNOWLEDGMENTS

We thank J. Popp for scientific illustration services, the BirdWeather team (T. Clark, V. Parashchak, and S. Pohlenz) for developing the BirdWeather program, and the thousands of volunteers who deployed listening devices for BirdWeather. We thank the three anonymous reviewers for constructive feedback that improved the manuscript. **Funding:** This work was in part supported by the McIntire-Stennis Formula Grant through the National Institute of Food and Agriculture and McIntire-Stennis Formula Grant ILLZ 22-R002 (to B.S.P.) **Author contributions:** Conceptualization: B.S.P. and N.A.G. Methodology: B.S.P. and N.A.G. Investigation: B.S.P. and N.A.G. Visualization: B.S.P. and N.A.G. Writing – original draft: BSP, NAG; Writing – review & editing: B.S.P. and N.A.G. **Competing interests:** The authors declare that they have no competing interests. **Data and materials availability:** Data and code are available at Zenodo (*50*).

SUPPLEMENTARY MATERIALS

science.org/doi/10.1126/science.adv9472
Materials and Methods; Supplemental Analysis: Influence of noise pollution; Supplemental Analysis: Effect of light pollution on nocturnal species; Figs. S1 to S3; Table S1; References (*51*–*76*); MDAR Reproducibility Checklist

Submitted 15 January 2025; resubmitted 15 April 2025; accepted 23 June 2025

10.1126/science.adv9472

QUANTUM MATTER

The quantum metric of electrons with spin-momentum locking

Giacomo Sala[1]*, Maria Teresa Mercaldo[2], Klevis Domi[1], Stefano Gariglio[1], Mario Cuoco[3], Carmine Ortix[2]*, Andrea D. Caviglia[1]*

Quantum materials are characterized by electromagnetic responses intrinsically linked to the geometry and topology of electronic wavefunctions that are encoded in the quantum metric and Berry curvature. Whereas Berry curvature–mediated transport effects have been identified in several magnetic and nonmagnetic systems, quantum metric–induced transport phenomena remain limited to topological antiferromagnets. Here, we show that spin-momentum locking, a general characteristic of the electronic states at surfaces and interfaces of spin-orbit–coupled materials, leads to a finite quantum metric. This metric activates a nonlinear in-plane magnetoresistance that we measured and electrically controlled in 111-oriented $LaAlO_3/SrTiO_3$ interfaces. These findings demonstrate the existence of quantum metric effects in a vast class of materials and enable previously unexplored strategies to design functionalities based on quantum geometry.

Nonlinear electronic responses can reveal physical properties that are out of the reach of linear probes (*1*). For example, the anomalous Hall effect senses the Berry curvature of magnetic materials (*2*, *3*). By comparison, its nonlinear, second-order counterpart can exist even in the presence of time-reversal symmetry in noncentrosymmetric and nonmagnetic materials and provides information on closely related geometric quantities: the Berry curvature dipole (*4*–*8*) and the Berry curvature triple (*9*).

Nonlinear electronic responses can manifest themselves as a nonreciprocal magnetoresistance, which was conventionally associated with disorder (*1*). However, recent works have identified an intrinsic nonlinear magnetoresistance driven by the quantum metric of electronic wavefunctions (*10*, *11*). The quantum metric $g = \Re(G)$ corresponds to the real part of the quantum geometric tensor G and, together with the Berry curvature $\Omega = -2\mathcal{J}(G)$, defines the geometrical and topological characteristics of quantum systems (*12*–*14*). Despite the profound implications of the quantum metric for several physical phenomena (*14*–*18*), experimental observations of it remain scarce (*19*–*25*) and in metallic systems are limited to topological antiferromagnets (*26*–*28*).

Here, we theoretically predicted and experimentally demonstrated that a condensed-matter phenomenon as fundamental (*29*, *30*) and technologically relevant (*31*, *32*) as the spin-momentum locking of electronic states at surfaces and interfaces of spin-orbit–coupled materials is endowed with a finite quantum metric. This intrinsic geometrical feature activates a nonlinear in-plane magnetoresistance that we used to provide evidence of the quantum metric at 111-oriented $LaAlO_3/SrTiO_3$ interfaces. Our findings and the abundance of materials with spin-momentum–locked electronic bands broaden the significance of the quantum metric in condensed matter and open up a whole line of possibilities to explore quantum geometry in a variety of systems (*14*).

Quantum metric of spin-momentum–locked electronic bands

The direct relation between the spin-momentum locking and the quantum metric can be found by considering the general case of a single pair of Kramers–related bands with parabolic dispersion that are shifted in momentum space by a Rashba-like linear term $\alpha_R(\mathbf{z}\times\mathbf{k})\cdot\sigma$ (*30*), where $\mathbf{z}$ is the direction normal to the surface or interface of interest and α_R is the Rashba parameter. The linear coupling between the crystalline momentum $\mathbf{k}$ and the electron spin σ leads to helical spin textures (Fig. 1A) that are characterized by the complete absence of the Berry curvature (*6*). Nevertheless, we found here that the quantum metric of spin-locked electronic bands is generally finite. As shown in Fig. 1B, the metric diagonal components g_{xx} and g_{yy} vanish only along the $k_y = 0$ and $k_x = 0$ lines, respectively, and have a singular point at the time-reversal invariant momentum $k = 0$. The band-energy normalized quantum metrics (BNQM, also known as Berry connection polarizabilities) of the spin-split bands cancel each other at the same crystal momentum. However, in the region of momenta populated by a single spin band, the BNQM is finite. This implies that the dipole density components Λ_{xxx} and Λ_{yyy} of the BNQM governing the longitudinal nonlinear conductivities feature alternating positive and negative hotspots with a characteristic quadrupolar profile in momentum space [Fig. 1C and (*33*)]. In the absence of magnetic fields, i.e., in time-reversal invariant conditions, the integrated dipole components vanish and so does the nonlinear response associated with the quantum metric (*10*).

We considered next the effect of a planar magnetic field B, which, without loss of generality, we set along the y direction. The Kramers doublet at $k \neq 0$ is now split, but a mirror symmetry–protected double degeneracy still occurs on the residual mirror-symmetric line $k_y = 0$. The ensuing distortion of the spin-split bands is accompanied by an analogous change of the spin textures, which still preserve a mirror-symmetric arrangement. Thus, the only effect of the magnetic field on the quantum metric is a simple shift of its singular point and lines of zeros. However, the consequences for the dipole of the BNQM are completely different. In the distorted annulus between the two Fermi lines of the spin-split bands, the BNQM dipoles lose their quadrupolar profile. As a result, the integrated dipole component Λ_{xxx} governing the nonlinear response perpendicular to the magnetic field becomes finite. Its magnitude increases linearly with B for small magnetic fields and diverges at the critical field B_c at which the Fermi lines of the two split-spin bands intersect each other on the band degeneracy point (*33*). For magnetic fields much larger than B_c, the nonlinear response again becomes vanishingly small.

The spin-momentum locking is therefore endowed with a quantum metric that only requires broken inversion symmetry and exists in time-reversal symmetric conditions. However, electronic transport associated with the quantum metric becomes possible only upon lifting the time-reversal symmetry (*10*, *11*). This can be accomplished by applying a planar magnetic field, which activates a nonlinear in-plane magnetoresistance that can be thus used as a probe of the quantum metric. We call this effect quantum metric magnetoresistance (QMMR). Unlike topological antiferromagnets (*26*, *27*), the QMMR is allowed in materials lacking $\mathcal{PT}$ symmetry. The BNQM dipole component Λ_{yyy} regulating the nonlinear conductivity parallel to the applied magnetic field remains overall zero, which implies the absence of a nonlinear magnetoresistance in the direction of B. This features makes the QMMR similar to the semiclassical Drude-like bilinear magnetoelectric resistance (BMER) first unveiled at the surfaces of three-dimensional (3D) topological insulators (*34*) but with one important difference. The BMER of the Rashba spin-split bands is strictly zero for magnetic fields smaller than B_c (*33*, *35*), thus making the nonlinear in-plane magnetoresistance at small fields completely determined by the BNQM.

Nonlinear magnetotransport

To study this quantum magnetotransport effect, we considered the 2D electron gas at the 111-oriented $LaAlO_3/SrTiO_3$ interface (Fig. 2A). The heterostructures are synthesized by pulsed laser deposition and lithographically patterned into Hall bars oriented along the two principal in-plane crystallographic directions: the $[\bar{1}10]$ (x) and the $[\bar{1}\bar{1}2]$ (y) axis (Fig. 2B) (*33*). The sheet conductivity of the electron gas is

---

[1]Department of Quantum Matter Physics, University of Geneva, Geneva, Switzerland. [2]Dipartimento di Fisica E. R. Caianiello, Università di Salerno, Fisciano, Italy. [3]CNR-SPIN c/o Università di Salerno, Fisciano, Italy. ***Corresponding author. Email: giacomo.sala@unige.ch (G.S.); cortix@unisa.it (C.O.); andrea.caviglia@unige.ch (A.D.C.)**

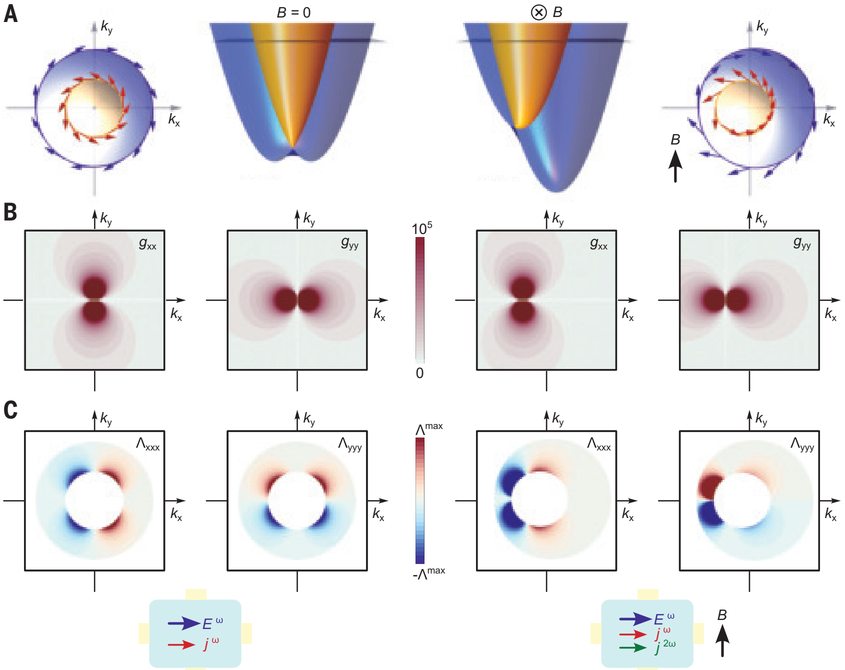

Fig. 1. Quantum geometry of 2D Rashba bands. (**A**) Spin-locked electronic bands induced by the 2D Rashba effect in the absence (left) and presence (right) of a planar magnetic field $B = 0.1E_0$, where E_0 is a reference energy (*33*). (**B**) Reciprocal space maps of the diagonal components g_{xx} and g_{yy} of the quantum metric tensor of the Rashba bands at zero and nonzero planar magnetic field. The maps were calculated assuming a Rashba parameter $\alpha_R = 0.4\varepsilon_F/k_F$, where ε_F and k_F are the Fermi energy and Fermi wavevector, respectively. (**C**) Contour plots of the dipole density components Λ_{xxx} and Λ_{yyy} of the band-normalized quantum metric in the exclusion region between the two Fermi lines. In response to an electric field E^ω, the planar magnetic field activates a nonlinear longitudinal current $j^{2\omega}$ driven by the band-normalized quantum metric.

controlled by an electrostatic field effect in a back-gate geometry that tunes the carrier density and mobility (Fig. 2C) (*36*, *37*). The combination of spin-orbit coupling and orbital degrees of freedom associated with the t_{2g} electrons of titanium atoms leads to three Kramers-related pairs of Rashba bands, enabling a gate-induced Lifshitz transition from one- to multicarrier transport (Fig. 2D) (*38*–*40*). The Rashba effect endows all three band pairs with the quantum metric and BNQM dipoles discussed above. However, the nonlinear magnetotransport driven by the quantum metric is expected to be always dominated by one pair of bands only. This is because the critical magnetic field B_c depends strongly on the band filling and is on the order of a few Teslas when the chemical potential is close to the band bottom of one of the Kramers pairs (*33*). Stated differently, at intermediate fields, only low-filled Rashba bands yield a sizable QMMR.

Figure 3 showcases the electronic response of the 2D electron gas as a function of the planar magnetic field oriented along the $[\bar{1}10]$ direction. At fields well below 3 T, the first harmonic transverse resistance R^ω_{xy} increases linearly with the magnetic field strength, which is compatible with a small out-of-plane misalignment of the field (Fig. 3A). However, R^ω_{xy} increases sharply above a magnetic field threshold modulated by the back gate. This sudden onset can be attributed to the anomalous planar Hall effect appearing in systems without mirror symmetries (*41*, *42*). Although the magnetic field along the $[\bar{1}10]$ direction leaves a residual mirror symmetry on the triangular titanium atoms net, the antiferrodistortive octahedron rotations of the oxygen atoms and the formation of domain patterns at the cubic-to-tetragonal transition of $SrTiO_3$ make our system mirror free independently of the magnetic field direction. This then leads to the emergence of Berry curvature hotspots when the avoided level crossing at B_c enters the Fermi surface annulus (*6*). The appearance of the anomalous planar Hall effect at fields of a few Teslas thus confirms that the critical magnetic field B_c is experimentally accessible and that the chemical potential lies close to the bottom of one of the Kramers pairs.

At magnetic field strengths $B \geq 2$T, we also observed a nonlinear and field-antisymmetric in-plane magnetoresistance $R^{2\omega,\text{asym}}_{yyy}$ (Fig. 3B) that is strongly suppressed when the magnetic field is collinear with the current (Fig. 3C). Sweeping the gate voltage allows us to tune $R^{2\omega,\text{asym}}_{yyy}$ and explore its dependence on the band filling. As shown in Fig. 3E, the nonlinear magnetoconductivity $\sigma^{2\omega}_{yyy} = J^{2\omega}_y / (E^\omega_y)^2$ associated with $R^{2\omega,\text{asym}}_{yyy}$ vanishes in the low-conductivity region and sharply emerges at a threshold $\sigma_{yy} = J^\omega_y / E^\omega_y \simeq 6$ mS, similar to the anomalous planar Hall conductivity $\sigma^\omega_{xy} = J^\omega_x / E^\omega_y$ (Fig. 3D). Measurements of the ordinary Hall effect revealed that a transition from one to two-carrier transport occurs at this threshold conductivity (Fig. 3F) (*33*, *37*, *39*). This finding indicates that the enhancement of the nonlinear response practically coincides with the filling of the second pair of Kramers bands. Together, these observations demonstrate the existence of a nonlinear longitudinal electronic response that fulfills the requirements of the BNQM-driven magnetotransport. The field-symmetric counterpart of $R^{2\omega,\text{asym}}_{yyy}$ cannot originate from the quantum metric, but rather derives from nonlinear skew scattering and side-jump contributions that also exist in the presence of time-reversal symmetry (*8*, *33*, *43*).

Quantum metric nonlinear magnetoresistance

Our experimental observations cannot be attributed to thermal effects, nonohmic contacts, capacitive or inductive coupling, or the AC modulation of the gate voltage (*33*). Instead, the nonlinear in-plane magnetoresistance is compatible with the QMMR of Rashba spin-split bands and the BMER. Because of hexagonal warping effects in 111-oriented heterostructures, the BMER can be finite, not only for magnetic field strengths larger than the critical magnetic field, but also for $B < B_c$ (*35*). The observation of a quantum metric–induced nonlinear transport, therefore, requires disentangling the QMMR from the BMER. To this aim, we exploited the fact that the QMMR and BMER contributions to the total nonlinear magnetoresistance can be parsed because of their different dependence on the electronic scattering time τ (*10*). The latter can be controlled through the gate tunability of the sheet conductance or by varying temperature. Whereas the QMMR contribution σ_{qm} is intrinsic in origin and scales as τ^0, the BMER grows with the square of the scattering time, i.e., as $\sim\tau^2$. Because the mobility is linear in the band-resolved relaxation time, we could equivalently consider the dependence of the nonlinear conductivity on the mobility μ_2 of the second Kramers pair of bands. As shown in Fig. 4B, this scaling analysis allowed us to disentangle the two effects in the conductivity region in which the carrier density n_2 is constant (*27*). The nonideal linear fit at intermediate magnetic fields may be attributed to the variation of the spin-orbit coupling and effective mass with the gate voltage, which is not captured by the mobility-scaling analysis. We found that both the QMMR and the BMER conductivities change nonmonotonically with the magnetic field (Fig. 4C), in agreement with our theory calculations based on a Rashba 2D electron gas with an additional trigonal warping (Fig. 4D) (*33*). The opposite sign for the QMMR and BMER predicted by the theoretical analysis also matches our experimental observation. We can thus conclude that the Rashba electron gas at the 111-oriented $LaAlO_3/SrTiO_3$ interface features a nonlinear magnetoresistance driven by a quantum metric contribution that is three orders of magnitude larger than that reported for 2D topological antiferromagnets at a similar temperature (*27*).

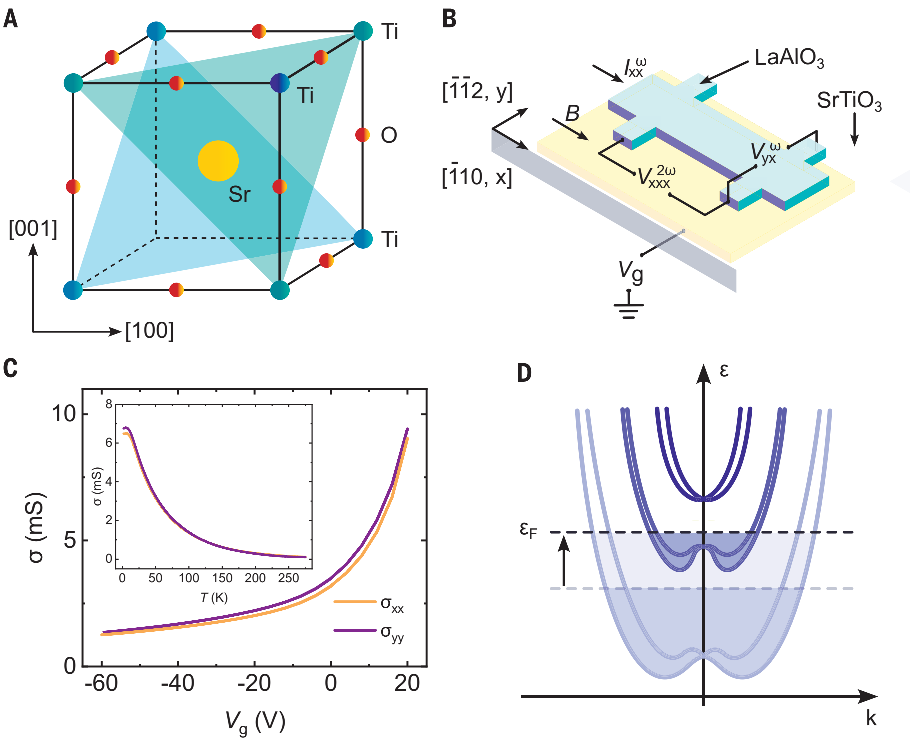

Fig. 2. 2D electron gas at the 111-oriented LaAlO$_3$/SrTiO$_3$ interface. (**A**) Crystal structure of SrTiO$_3$. The shaded triangles identify the {111} planes of titanium atoms. (**B**) Sketch of the magnetotransport measurements. The transverse and longitudinal first and second harmonic voltages are measured in a Hall bar device while sweeping the magnetic field along the [$\bar{1}$10] (*x*) or [$\bar{1}\bar{1}$2] (*y*) direction. Two devices with the current path oriented along *x* and *y* were measured simultaneously. A variable gate voltage V_g is applied at the back of the sample. (**C**) Gate voltage and temperature (inset) dependence of the sheet conductivity. (**D**) Schematic representation of the (exaggerated) Rashba-split electronic bands at the 111-oriented LaAlO$_3$/SrTiO$_3$ interface. The arrow shows the direction of band filling upon application of a positive gate voltage.

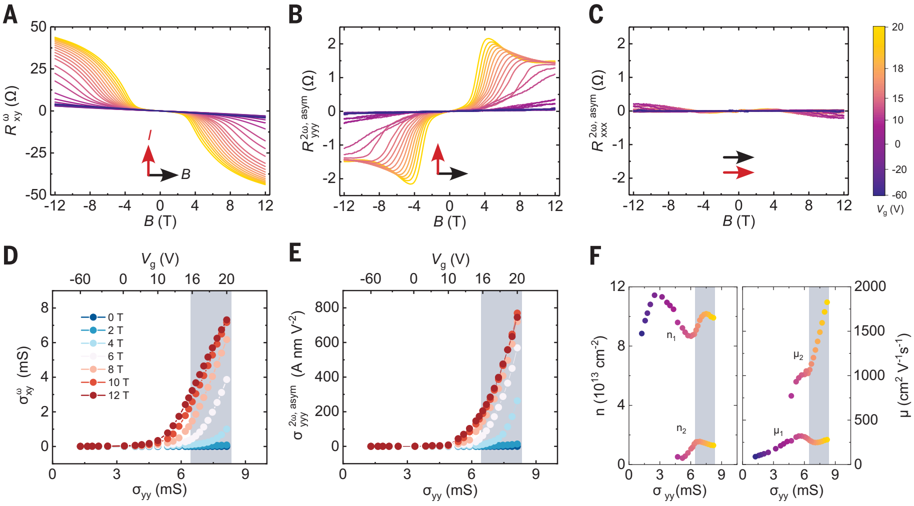

Fig. 3. Linear and nonlinear magnetotransport. (**A** to **C**) First harmonic transverse and second harmonic longitudinal resistances as a function of the in-plane magnetic field *B* and gate voltage V_g at a temperature *T* = 3 K. The black and red arrows indicate the direction of *B* and the electric current *I*, respectively. The current is applied along the $\bar{1}\bar{1}$2 (*y*) crystallographic direction in (A) and (B) and along $\bar{1}$10 (*x*) in (C). (**D**) Transverse linear conductivity calculated from (A) at different magnetic fields as a function of the zero-field longitudinal linear conductivity. (**E**) As in (D) but for the longitudinal nonlinear conductivity calculated from (B). (**F**) Two-band electron densities *n* and mobilities μ at variable V_g and *T* = 3 K. The shaded areas define the conductivity regions considered in Fig. 4.

Finally, we performed a similar scaling analysis of the anomalous planar Hall resistance to account for the presence of disorder-mediated effects in addition to the intrinsic Berry curvature-induced contribution. The linear dependence of the anomalous planar Hall conductivity on the mobility μ_2 (Fig. 4A) demonstrates the existence of a skew-scattering contribution σ_{sk} that is absent in a rotational symmetric Rashba 2D electron system (*44*) but is activated by the nonvanishing Berry curvature triple because of hexagonal warping effects (*9*). In addition, due to the combined action of side-jump and intrinsic Berry curvature, the τ^0 term varies nonmonotonically as the magnetic field is increased. This behavior is correctly captured by a theory calculation of the Berry curvature–mediated anomalous planar Hall response (Fig. 4D), which indicates that the intrinsic contribution dominates the τ-independent anomalous planar Hall conductivity. Therefore, the intrinsic contributions to the anomalous planar Hall effect and nonlinear in-plane magnetoresistance provided us with direct access to the Berry curvature and the quantum metric of the 111-oriented LaAlO$_3$/SrTiO$_3$ interface and allowed us to study the electronic dynamics associated with its full quantum geometric tensor. This unique property marks the difference of 111-oriented LaAlO$_3$/SrTiO$_3$ with respect to $\mathcal{PT}$-symmetric materials such as topological antiferromagnets (*26*, *27*), for which the quantum geometric tensor is purely real and accessible only through the nonlinear response.

Discussion and outlook

Our analysis of the conductivity dependence on scattering time allowed us to identify the intrinsic contribution of the quantum metric and Berry curvature to the electronic magnetotransport. Whereas the Berry curvature is enabled by the trigonal symmetry of the 111-oriented interface, the quantum metric is rotationally invariant and is not contingent on specific symmetry requirements in addition to the broken inversion symmetry. This property makes quantum metric effects potentially observable in a vast class of nonmagnetic materials. Moreover, the common origin of the QMMR and BMER suggests that all platforms in which the BMER was previously reported also host the quantum metric. The QMMR is thus not limited to oxide heterostructures (*45*, *46*), but is expected for all materials with spin-locked electronic bands such as semiconductors (*29*, *47*–*49*), surface states of heavy metals (*50*), magnetic and nonmagnetic interfaces (*29*, *30*, *51*), and even policrystalline samples. Therefore, our findings not only demonstrate the existence of a quantum metric associated with the spin-momentum locking, but also suggest new directions for investigating and functionalizing the quantum

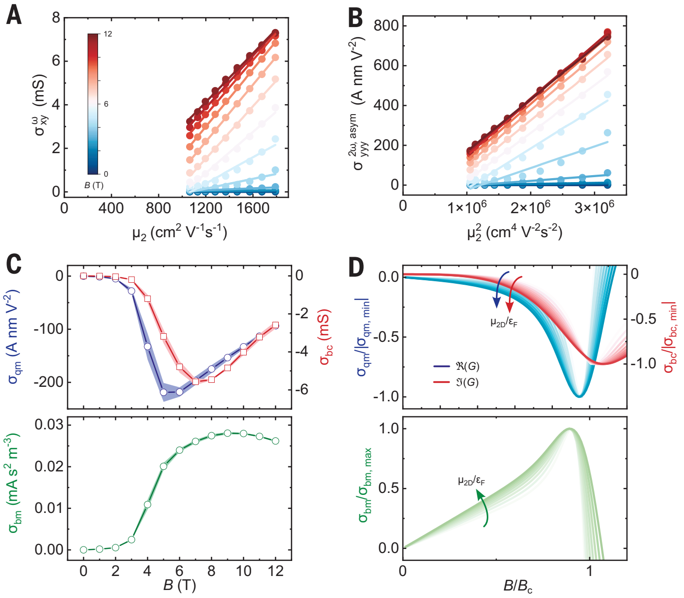

Fig. 4. Electronic transport driven by the full quantum geometric tensor. (**A**) Linear transverse conductivity at different magnetic fields as a function of the electronic mobility of the second Kramers pair. The lines are linear fits to the data. (**B**) Nonlinear longitudinal conductivity as a function of the square of the electronic mobility of the second Kramers pair. (**C**) Quantum metric (σ_{qm}), Berry curvature (σ_{bc}), and bilinear magnetoeletric (σ_{bm}) conductivities extracted from the fits in (A) and (B) as a function of the magnetic field. The shaded areas define the uncertainty of the fits. (**D**) Magnetic field dependence of the normalized σ_{qm}, σ_{bc}, and σ_{bm} calculated from $\sigma_{qm} = \frac{e^3}{\hbar}\sum_n \int_{\mathbf{k}} f_n(\mathbf{k})\Lambda^{(n)}_{xxx}(\mathbf{k})$, $\sigma_{bc} = -\frac{e^2}{\hbar}\sum_n \int_{\mathbf{k}} f_n(\mathbf{k})\Omega(\mathbf{k})$, and $\sigma_{bm} = -\tau^2\frac{e^3}{\hbar^3}\sum_n \int_{\mathbf{k}} f_n(\mathbf{k})\,\partial^3\varepsilon_n(\mathbf{k})/\partial k_x^3$, respectively, where n is the band index and $f_n(\mathbf{k})$ the Fermi distribution function (*33*). The color intensity codes the ratio $\mu_{2D}/\varepsilon_F = 0.2$ to 0.6 between the chemical potential of the 2D electron gas and the Fermi energy ε_F. The magnetic field is normalized to the critical field B_c.

geometry. In addition to magnetotransport, the quantum metric of the spin-momentum locking is, in principle, accessible to terahertz photocurrents and spectroscopic tools in time-reversal symmetric conditions (*52*, *53*). From a technological perspective, integrating the spin-momentum locking with magnetic and ferroelectric thin films could lead to the on-demand, reversible, and nonvolatile control of the physical effects emerging from the quantum metric. Moreover, combining spintronics with the quantum metric may reveal unforeseen disorder-free mechanisms to interconvert charge and spin-orbital currents (*29*, *30*, *54*). Therefore, the results of our study could enable a range of possibilities to harness quantum metric effects in condensed matter and may ultimately inspire technologies based on the geometry of the electronic wavefunctions.

REFERENCES AND NOTES

1. Y. Tokura, N. Nagaosa, *Nat. Commun.* **9**, 3740 (2018).
2. D. Xiao, M.-C. Chang, Q. Niu, *Rev. Mod. Phys.* **82**, 1959–2007 (2010).
3. N. Nagaosa, J. Sinova, S. Onoda, A. H. MacDonald, N. P. Ong, *Rev. Mod. Phys.* **82**, 1539–1592 (2010).
4. I. Sodemann, L. Fu, *Phys. Rev. Lett.* **115**, 216806 (2015).
5. Q. Ma *et al.*, *Nature* **565**, 337–342 (2019).
6. E. Lesne *et al.*, *Nat. Mater.* **22**, 576–582 (2023).
7. Z. Z. Du, H.-Z. Lu, X. C. Xie, *Nat. Rev. Phys.* **3**, 744–752 (2021).
8. C. Ortix, *Adv. Quantum Technol.* **4**, 2100056 (2021).
9. P. Makushko *et al.*, *Nat. Electron.* **7**, 207–215 (2024).
10. D. Kaplan, T. Holder, B. Yan, *Phys. Rev. Lett.* **132**, 026301 (2024).
11. K. Das, S. Lahiri, R. B. Atencia, D. Culcer, A. Agarwal, *Phys. Rev. B* **108**, L201405 (2023).
12. J. P. Provost, G. Vallee, *Commun. Math. Phys.* **76**, 289–301 (1980).
13. R. Cheng, arXiv:1012.1337 [quant-ph] (2010).
14. P. Törmä, *Phys. Rev. Lett.* **131**, 240001 (2023).
15. R. Resta, *Eur. Phys. J. B* **79**, 121–137 (2011).
16. S. Peotta, P. Törmä, *Nat. Commun.* **6**, 8944 (2015).
17. E. Rossi, *Curr. Opin. Solid State Mater. Sci.* **25**, 100952 (2021).
18. K.-E. Huhtinen, J. Herzog-Arbeitman, A. Chew, B. A. Bernevig, P. Törmä, *Phys. Rev. B* **106**, 014518 (2022).
19. X. Tan *et al.*, *Phys. Rev. Lett.* **122**, 210401 (2019).
20. A. Gianfrate *et al.*, *Nature* **578**, 381–385 (2020).
21. M. Yu *et al.*, *Natl. Sci. Rev.* **7**, 254–260 (2020).
22. J. Ren *et al.*, *Nat. Commun.* **12**, 689 (2021).
23. Q. Liao *et al.*, *Phys. Rev. Lett.* **127**, 107402 (2021).
24. H. Tian *et al.*, *Nature* **614**, 440–444 (2023).
25. C.-R. Yi *et al.*, *Phys. Rev. Res.* **5**, L032016 (2023).
26. A. Gao *et al.*, *Science* **381**, 181–186 (2023).
27. N. Wang *et al.*, *Nature* **621**, 487–492 (2023).
28. J. Han *et al.*, *Nat. Phys.* **20**, 1110–1117 (2024).
29. C. H. Li *et al.*, *Nat. Nanotechnol.* **9**, 218–224 (2014).
30. G. Bihlmayer, P. Noël, D. V. Vyalikh, E. V. Chulkov, A. Manchon, *Nat. Rev. Phys.* **4**, 642–659 (2022).
31. S. Manipatruni *et al.*, *Nature* **565**, 35–42 (2019).
32. P. Noël *et al.*, *Nature* **580**, 483–486 (2020).
33. Additional data and analyses are available as supplementary materials.
34. P. He *et al.*, *Nat. Phys.* **14**, 495–499 (2018).
35. G. Tuvia *et al.*, *Phys. Rev. Lett.* **132**, 146301 (2024).
36. A. D. Caviglia *et al.*, *Nature* **456**, 624–627 (2008).
37. A. M. Monteiro *et al.*, *Phys. Rev. B* **99**, 201102 (2019).
38. T. C. Rödel *et al.*, *Phys. Rev. Appl.* **1**, 1 (2014).
39. U. Khanna *et al.*, *Phys. Rev. Lett.* **123**, 036805 (2019).
40. M. Diez *et al.*, *Phys. Rev. Lett.* **115**, 016803 (2015).
41. R. Battilomo, N. Scopigno, C. Ortix, *Phys. Rev. Res.* **3**, L012006 (2021).
42. M. Trama, V. Cataudella, C. A. Perroni, F. Romeo, R. Citro, *Phys. Rev. B* **106**, 075430 (2022).
43. Z. Z. Du, C. M. Wang, S. Li, H.-Z. Lu, X. C. Xie, *Nat. Commun.* **10**, 3047 (2019).
44. M. Borunda *et al.*, *Phys. Rev. Lett.* **99**, 066604 (2007).
45. A. Ohtomo, H. Y. Hwang, *Nature* **427**, 423–426 (2004).
46. L. M. Vicente-Arche *et al.*, *Adv. Mater.* **33**, e2102102 (2021).
47. J. Nitta, T. Akazaki, H. Takayanagi, T. Enoki, *Phys. Rev. Lett.* **78**, 1335–1338 (1997).
48. T. Ideue *et al.*, *Nat. Phys.* **13**, 578–583 (2017).
49. Y. Li *et al.*, *Nat. Commun.* **12**, 540 (2021).
50. C. R. Ast *et al.*, *Phys. Rev. Lett.* **98**, 186807 (2007).
51. J. C. R. Sánchez *et al.*, *Nat. Commun.* **4**, 2944 (2013).
52. J. Ahn, G.-Y. Guo, N. Nagaosa, *Phys. Rev. X* **10**, 041041 (2020).
53. Q. Ma, R. Krishna Kumar, S.-Y. Xu, F. H. L. Koppens, J. C. W. Song, *Nat. Rev. Phys.* **5**, 170–184 (2023).
54. X. Feng *et al.*, *Mater. Today Quantum* **6**, 100040 (2025).
55. G. Sala *et al.*, Data for: The quantum metric of electrons with spin-momentum locking, Zenodo (2024); https://doi.org/10.5281/zenodo.10692339.

ACKNOWLEDGMENTS

We thank J.-M. Triscone, M. Gabay, A. Srivastava, E. Lesne, and G. Kimbell for fruitful discussions; M. Lopes and J.-L. Lorenzoni for technical support; and A. Morpurgo and I. Gutiérrez for contributing to the sample fabrication. **Funding:** This work was supported by the Swiss State Secretariat for Education, Research and Innovation (SERI) under contract MB22.00071; the Gordon and Betty Moore Foundation (grant 332 GBMF10451 to A.D.C.); the European Research Council (ERC); and the Dutch Research Council (NWO) as part of the VIDI (project 016.Vidi.189.061 to A.D.C.). G.S. acknowledges support from the Swiss National Science Foundation (grant PZ00P2_223542). A.D.C., M.T.M., and M.C. acknowledge support from the EU Horizon 2020 research and innovation program (grant 964398, SUPERGATE). M.T.M. and C.O. acknowledge support from the MAECI project "ULTRAQMAT" and the PNRR MUR project PE0000023-NQSTI (TOPQIN). M.C. acknowledges financial support from PNRR MUR project PE0000023-NQSTI. **Author contributions:** G.S. fabricated the oxide heterostructures and the transport devices. G.S. and K.D. performed the measurements and analyzed the data with the support of S.G. M.T.M., M.C., and C.O. developed the theoretical model. A.D.C. supervised the experimental work. C.O. supervised the theoretical work. All authors contributed to writing the manuscript. **Competing interests:** The authors declare no competing financial interests. **Data and materials availability:** The data and code that support the findings of this study are available on Zenodo (*55*).

SUPPLEMENTARY MATERIALS

science.org/doi/10.1126/science.adq3255
Materials and Methods; Supplementary Text; Figs. S1 to S13; References (*56*–*59*)

Submitted 8 May 2024; accepted 17 June 2025

10.1126/science.adq3255

GEOGRAPHY

Increasing global human exposure to wildland fires despite declining burned area

Seyd Teymoor Seydi[1], John T. Abatzoglou[2], Matthew W. Jones[3], Crystal A. Kolden[2], Gabriel Filippelli[4], Matthew D. Hurteau[5], Amir AghaKouchak[6,7,8], Charles H. Luce[9], Chiyuan Miao[10], Mojtaba Sadegh[1,8]*

Although half of Earth's population resides in the wildland-urban interface, human exposure to wildland fires remains unquantified. We show that the population directly exposed to wildland fires increased 40% globally from 2002 to 2021 despite a 26% decline in burned area. Increased exposure was mainly driven by enhanced colocation of wildland fires and human settlements, doubling the exposure per unit burned area. We show that population dynamics accounted for 25% of the 440 million human exposures to wildland fires. Although wildfire disasters in North America, Europe, and Oceania have garnered the most attention, 85% of global exposures occurred in Africa. The top 0.01% of fires by intensity accounted for 0.6 and 5% of global exposures and burned area, respectively, warranting enhanced efforts to increase fire resilience in disaster-prone regions.

Wildland fires, defined here as fires in vegetated land excluding commercial agriculture areas, have increasingly affected social and environmental systems in various regions across the globe in recent years (*1*, *2*), directly accounting for at least 2500 human deaths and 10,500 injuries from 1990 to 2021 (*3*). Indirect impacts of wildland fires are several times larger and extend for years after the burn (*4*). For example, an annual 1.53 million deaths around the globe are attributable to landscape-fire–induced air pollution (*5*). Fire activity is directly linked with climate and weather (*6*), and climate change has increased the number of days conducive to extreme fire behavior over many fire-prone regions, culminating in a >54% increase in extreme fire weather from 1979 to 2022 globally (*3*), longer fire-weather seasons (*7*), and increased nighttime flammability (*8*).

Human activities can compound or confound the climate change impacts on fire activity (*3*, *9*, *10*). Human ignitions, both intentional and accidental, account for 84% of all wildfires in the contiguous United States (*11*) and for >90% in Mediterranean Europe (*12*). Although lightning ignitions can dominate in more remote regions (*13*, *14*), human activity strongly modifies the timing and locations of fires (*11*, *15*), as well as the vegetation type, structure, density, and continuity, which in turn change regional fire regimes (*16*). For example, the introduction of invasive species in deserts of North America resulted in more frequent and larger wildfires (*17*), whereas agriculturally induced land fragmentation in African savannas reduced burned areas (*18*). Outside of the tropics, humans commonly seek to limit burned area by suppressing fire, but as settlement expands into previously wildland areas, causing the wildland-urban interface (WUI) to grow (*19*), human exposure to fire also grows (*20*). Although the WUI covers only 4.7% of the global land surface, nearly half of Earth's population resides in WUI areas (*21*), and regional and global WUIs have been expanding (*22*, *23*).

The confluence of changing social and environmental controls of fires resulted in a 26% decline in global burned area in the past two decades driven by trends in African savannas (*24*) despite the increased fire extent in temperate and boreal forests (*25*) and the increased occurrence of intense fire events (*26*). Here, we examine the global and regional patterns and trends of human exposure to wildland fires. We further probe the characteristics of wildland fires that affect humans and investigate the role of population dynamics in the overall exposure patterns and trends. Additionally, we investigate patterns, trends, and drivers of population exposure to intense fire events because exposure to such fires has been tied to fire disasters (*2*). We used 18.6 million individual fire records from 2002 to 2021 from the MODIS-based Global Fire Atlas (*18*, *27*) and gridded population data from WorldPop (*28*). We also used MODIS-based land cover and use data (*29*), active fire records (*30*), and vegetation indices (*31*) to exclude nonwildland fires in the Global Fire Atlas (*27*). Our approach does not exclude deforestation and other vegetation-clearing fires, so it does not differentiate between intentional fire use and wildfires. We define human exposure to wildland fire as the number of persons who resided within the burned perimeters, noting that (i) burned perimeters include unburned patches, (ii) consequential human impacts from fires extend well beyond burn perimeters, and (iii) human and societal impacts of exposures to less frequent but more intense fires (e.g., in Western North America) are different from those in the case of frequent low intensity fires (e.g., in African savannas). Exposure to wildland fires can be harmful and devastating, resulting in loss of lives and damage to infrastructure, but not all instances of exposure lead to negative outcomes.

Patterns of global exposure to wildland fire

A total of 440.2 million persons were directly exposed to wildland fires globally from 2002 to 2021 (Fig. 1A), and 85.6% of these exposures occurred in Africa. Although major wildfire disasters occurred in Oceania, Europe, and North America in recent years, these three continents cumulatively accounted for <2.5% of global exposures (Fig. 1B). Cumulative burned area in these wildland fires from 2002 to 2021 was 49.2 million km^2 (Fig. 1C), of which Africa accounted for 64.3% (Fig. 1D). Europe had the highest human exposure per unit burned area, hereafter referred to as exposure density (17.7 persons/km^2), followed by Africa (11.9 persons/km^2). The global exposure density was 8.9 persons/km^2 (fig. S1B).

Spatial patterns of cumulative human exposure to wildland fire, cumulative burned area, and per capita human exposure illustrate the variability in human relationships to fire across latitudes and continents (Fig. 1, A, C, and E). The highest levels of per capita exposure to wildland fire occurred in the tropical savannas of Africa (Fig. 1E and figs. S2 and S3), areas characterized by frequent human- and lightning-started low-intensity fires where populations regularly use fire for land management and agricultural purposes (*16*). From 2002 to 2021, 1.8% of Africa's population was exposed to wildland fire, more than an order of magnitude larger than the per capita exposure on any other continent. Similarly, cumulative exposure to fire was highest in regions such as tropical Africa (*16*), with five tropical African countries accounting for half of the global exposures (Fig. 1A). The high cumulative burned area in tropical Australia and Brazil (Fig. 1C) reflects both naturally started fires and widespread intentional use of fire for regenerative and deforestation practices in sparsely populated to unpopulated areas, whereas moderate cumulative

---

[1]Department of Civil Engineering, Boise State University, Boise, ID, USA. [2]Management of Complex Systems Department, University of California, Merced, Merced, CA, USA. [3]Tyndall Centre for Climate Change Research, School of Environmental Sciences, University of East Anglia (UEA), Norwich, UK. [4]Department of Earth Science, Indiana University, Indianapolis, IN, USA. [5]Biology Department, University of New Mexico, Albuquerque, NM, USA. [6]Department of Civil and Environmental Engineering, University of California, Irvine, CA, USA. [7]Department of Earth System Science, University of California, Irvine, CA, USA. [8]United Nations University Institute for Water, Environment and Health, Richmond Hill, Ontario, Canada. [9]USDA Forest Service Rocky Mountain Research Station, Boise, ID, USA. [10]State Key Laboratory of Earth Surface Processes and Disaster Risk Reduction, Faculty of Geographical Science, Beijing Normal University, Beijing, China. ***Corresponding author. Email: mojtabasadegh@boisestate.edu**

burned area in sparsely populated regions of northern Russia and North America reflects increasing wildfire area burned associated with climate change.

Top-quintile events in terms of size, perimeter, duration, speed, and spread rate accounted for the largest fraction of wildland fire exposures (see the supplementary materials, section S1, and figs. S4 to S9).

Trends of global exposure to wildland fire

Global annual exposure to wildland fire increased by 7.7 million persons (+39.6%) from 2002 to 2021 (382,700 persons/year; $P < 10^{-5}$; fig. S1A). Africa accounted for nearly all of the increase (373,000 persons/year; $P < 10^{-7}$; +46.3%). South America (+33.8%), North America (+15.7%), and Asia (+2.8%) experienced nonsignificant increases in exposure to wildland fire from 2002 to 2021, whereas Oceania (–47.3%) and Europe (–17.3%) observed nonsignificant declines (fig. S1A). Interannual variability of exposure to wildland fire and age distribution of the exposed populations are discussed in the supplementary materials, sections S2 and S3 (fig. S10), respectively.

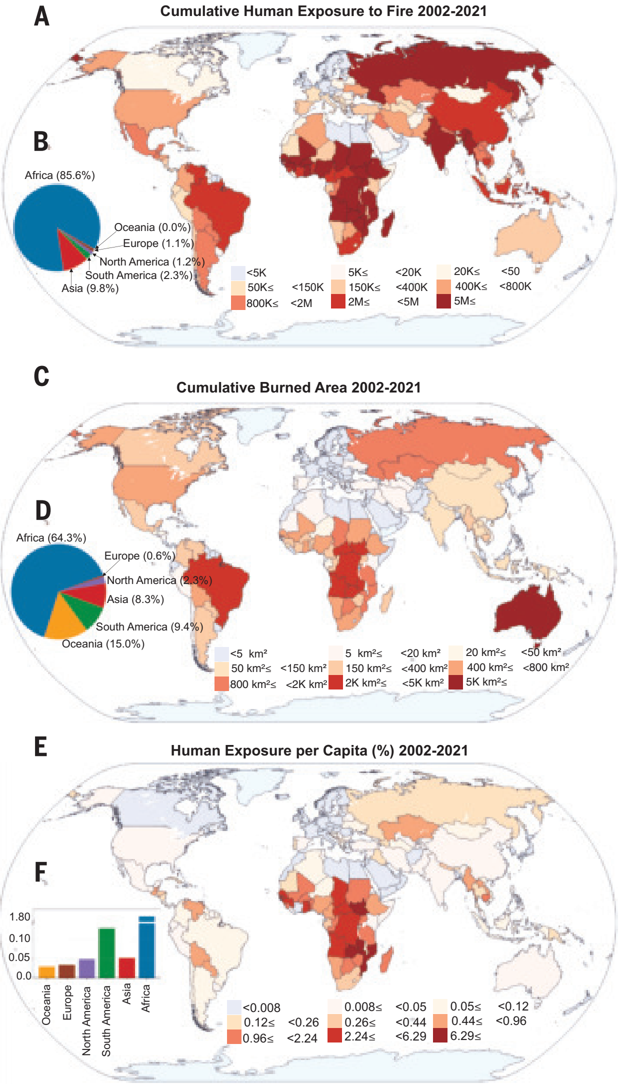

Fig. 1. Human exposure to wildland fires from 2002 to 2021. (**A** and **C**) Cumulative human exposure to wildland fires (A) and cumulative burned area (C) from 2002 to 2021 at the country level. (**B** and **D**) Share of continents in wildland fire exposure (B) and burned areas (D). (**E** and **F**) Percentage of population exposed to wildland fire from 2002 to 2021 in each country (E) and continent (F). K, one thousand; M, one million.

Exposure density also increased globally from 2002 to 2021, exposing an additional 6.2 (+93.4%) persons/km^2 of burned area in these two decades ($P < 10^{-6}$; fig. S1B). All continents experienced rising exposure density, with Africa and Europe showing the largest increases, exposing an additional 7.9 (+90.4%) and 6.8 (+42.3%) persons/km^2 of burned area, respectively, in two decades ($P < 10^{-7}$ and $P = 0.2$, respectively; fig. S1B).

Role of population dynamics in exposure to wildland fire

By applying fixed 2002 population patterns, we developed a counterfactual model to account for the role of population dynamics versus fire dynamics in driving the observed exposure trends. Population dynamics, i.e., population growth and migration, from 2002 to 2021 accounted for 111.3 million exposures to wildland fire in the past two decades globally (25.3% of all global exposures; Fig. 2A). Without the effects of population dynamics, cumulative exposure to wildland fire from 2002 to 2021 would have been between 10.0 and 27.9% lower in Africa, Asia, North America, and South America but 5.0 and 2.3% higher in Europe and Oceania, respectively (Fig. 2). Counterfactual trends in Europe and Oceania were driven by the marginal shrinking of the fire and human settlement overlap from 2002 to 2021 due to a variety of factors, including migration from rural to urban areas.

In the absence of population dynamics, the global exposure to wildland fire would have decreased at a rate of 278,000 persons/year ($P < 10^{-4}$; 27.7% decline in two decades), commensurate with the decline in burned area (Fig. 2A), with counterfactual trends primarily driven by

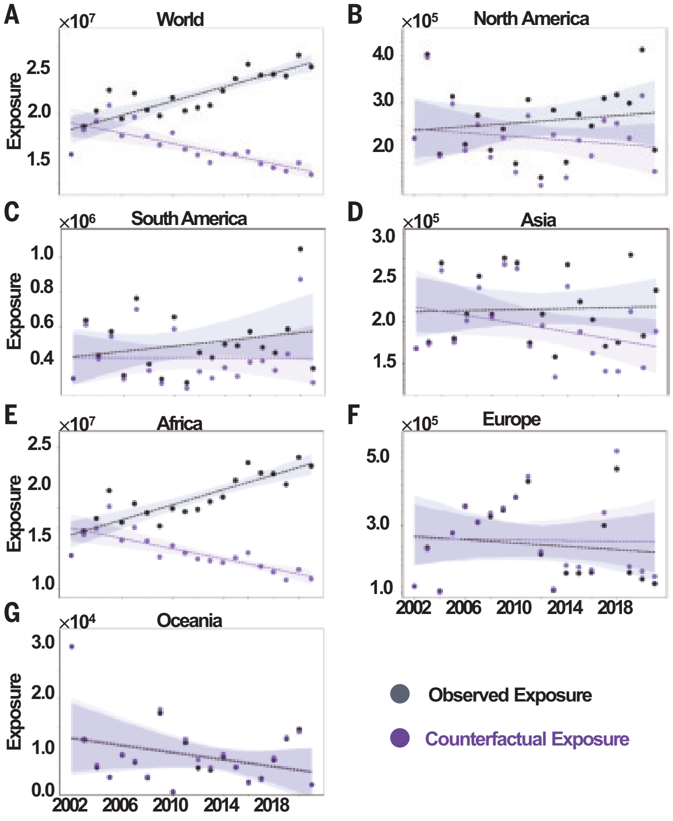

Fig. 2. Contribution of population dynamics to wildland fire exposure. (**A** to **G**) Observed (black) and counterfactual constant-population scenario (purple) exposures to wildland fire from 2002 to 2021 across the globe (A) and in each continent [(B) to (G)]. In observed exposures, both population and burned area data are dynamic, whereas in counterfactual exposures, population is fixed at year 2002 but the burned area is dynamic.

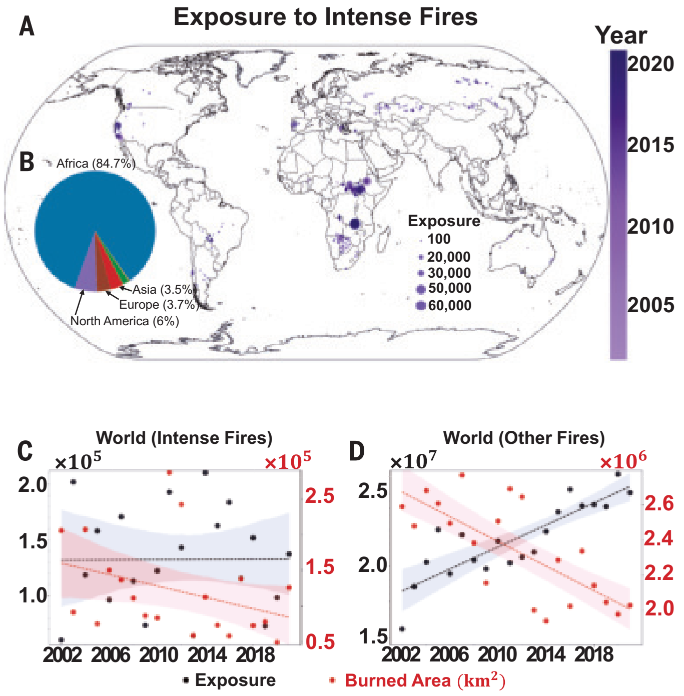

Fig. 3. Population exposure to intense wildland fires. (**A** and **B**) Location, occurrence year, and exposure to individual intense fires that exposed >100 persons from 2002 to 2021 (A) and share of continents in global population exposure to intense fires (B). (**C** and **D**) Trends in annual exposure to and burned area by intense fires globally.

declines in Africa of –250,000 persons/year ($P < 10^{-4}$; –29.8% decline in two decades; Fig. 2E).

Without the population changes since 2002, exposure per unit burned area would have been rather stable globally (1.8% decline in two decades; –0.006 persons/km^2/year; $P = 0.83$), indicating that human influences, including population increase in and migration to fire-prone areas, were the main driver of increasing exposures to wildland fires in the past two decades.

Population exposure to intense wildland fires

Following Cunningham *et al.* (*26*), we define “intense” fires as events with cumulative fire radiative power exceeding the 99.99th percentile of all wildland fires globally (Fig. 3A). Intense fires had a disproportionately large impact, representing just 0.01% of all wildland fires yet accounting for 0.6% of total population exposures (2.7 million persons) and 5.0% of the cumulative burned area (2.4 million km^2) globally. Similar to all wildland fires, 84.7% of global exposures to intense wildland fires occurred in Africa, whereas a significantly higher proportion was observed in North America (6.0% for intense fires compared with 1.2% for all wildland fires). Regional impacts of intense fires were pronounced in North America, Oceania, and Europe, accounting for 3.1% (14.1%), 2.7% (15.2%), and 2.0% (4.1%) of all population exposures to wildland fire (burned area) in each continent, respectively (fig. S11). See fig. S12 for the contribution of population dynamics to exposure to intense fires.

Population exposure to intense fires remained stable globally from 2002 to 2021 (Fig. 3B), with mixed nonsignificant trends in different continents (fig. S11). Global burned area declined both for intense fires (–47.2%; $P = 0.12$) and other fires (–24.9%, $P < 0.01$) (Fig. 3, B and C) in the past two decades. Regional trends, however, showed nuanced differences; for example, burned area by intense fires increased significantly in North America and South America from 2002 to 2021 (fig. S11).

In the wildfire disaster–prone regions (*2*) of Western North America, the Mediterranean, and Southern Australia, where loss of life and property to wildfires has occurred several times, 253,400 persons were exposed to intense fires from 2002 to 2021, accounting for 32.0, 4.1, and 2.8% of all exposures to wildland fire in each region, respectively (fig. S13), far in excess of the 0.6% of global exposures to intense fires. Population exposure to intense fires showed nonsignificant increases in Western North America and Southern Australia from 2002 to 2021 (fig. S13).

Discussion

Fires are complex social-ecological phenomena, and using burned area alone, often a common indicator of fire activity, fails to capture their full impact (*20*). The contrasting trends of burned area and exposure to wildland fire indicate multidimensional relationships among fire, humans, and landscapes (*9*, *10*, *25*, *32*, *33*). Specifically, land fragmentation (*24*) induced by increasing human presence and expanding commercial agriculture in Africa reduced regional burned area but colocated more humans with wildland fires, including intentional fires, and increased their exposure (*3*). Increasing human exposure to wildland fire in North America is due to both expansion of the WUI (*19*) and increasing burned area (*14*), and declining exposures in Europe are due to depopulation of rural areas (*34*), although climatic trends promoted more extreme potential fire behavior in both regions (*35*–*37*). In South America and Asia, population dynamics increased human exposure to wildland fire despite a decline in burned areas from 2002 to 2021.

We found an increasing colocation of wildland fire and human settlements globally and in every continent. Global exposure density roughly doubled in the past two decades, mostly driven by trends in Africa. These trends are consistent with the expansion of the global WUI (*22*, *23*). WUI expansion not only places humans at a higher risk for the negative effects of fire (*19*), it also increases the number of anthropogenic ignitions of fire (*38*).

Effects of intense fires were particularly significant in North America, Oceania, and Europe, coinciding with global hotspots in fire disasters (*2*). Various wildfire mitigation strategies can be implemented in disaster-prone regions to reduce human impacts from fire exposure (*39*), as well as to limit human-caused fires (*40*). In wildfire-prone WUI areas, home hardening, i.e., incorporating structural and landscaping modifications to enhance fire resistance, is essential. There is also a need for increased intentional fire use as a vegetation management tool to mitigate wildfire disasters (*41*–*43*).

Our wildland fire exposure estimates focus solely on direct human exposure and do not account for indirect impacts such as exposure to smoke and postfire debris flow and flood (*44*). As a result, these figures are conservative, and the total number of persons affected by wildland fires directly or indirectly is likely much higher. Extreme fire weather and fire behavior are expected to intensify in a warming climate (*45*), and fires are projected to increasingly affect humans, especially given the population increases and WUI expansions (*23*).

Finally, our analysis indicates that the geography of wildfire disasters is distinctly different from the geography of major human exposures to wildland fires globally (*2*). Most wildfire disasters with the highest fatalities and societal losses have occurred in areas with Mediterranean climates in Australia, Southern Europe, South Africa, Western North America, and the west coast of South America (*2*, *26*, *46*). These wildfire disaster regions are not global hotspots in human exposure to wildland fire. By contrast, our analysis found the highest cumulative area burned and the highest human exposure to wildland fire, both cumulative exposure and exposure density, in regions that have had relatively few wildfire disasters, such as tropical Africa (*2*).

REFERENCES AND NOTES

1. C. E. Synolakis, G. M. Karagiannis, *PNAS Nexus* **3**, pgae151 (2024).
2. D. M. J. S. Bowman *et al.*, *Nat. Ecol. Evol.* **1**, 0058 (2017).
3. M. W. Jones *et al.*, *Rev. Geophys.* **60**, e2020RG000726 (2022).
4. C. A. Kolden, J. T. Abatzoglou, M. W. Jones, P. Jain, *Nat. Rev. Earth Environ.* **5**, 238–240 (2024).
5. R. Xu *et al.*, *Lancet* **404**, 2447–2459 (2024).
6. J. T. Abatzoglou, A. P. Williams, L. Boschetti, M. Zubkova, C. A. Kolden, *Glob. Chang. Biol.* **24**, 5164–5175 (2018).
7. W. M. Jolly *et al.*, *Nat. Commun.* **6**, 7537 (2015).
8. J. K. Balch *et al.*, *Nature* **602**, 442–448 (2022).
9. D. I. Kelley *et al.*, *Nat. Clim. Chang.* **9**, 690–696 (2019).
10. M. Forkel *et al.*, *Biogeosciences* **16**, 57–76 (2019).
11. J. K. Balch *et al.*, *Proc. Natl. Acad. Sci. U.S.A.* **114**, 2946–2951 (2017).
12. A. Ganteaume *et al.*, *Environ. Manage.* **51**, 651–662 (2013).
13. T. A. J. Janssen *et al.*, *Nat. Geosci.* **16**, 1136–1144 (2023).
14. J. T. Abatzoglou, C. A. Kolden, J. K. Balch, B. A. Bradley, *Environ. Res. Lett.* **11**, 045005 (2016).
15. A. D. Syphard, K. C. Clarke, J. Franklin, *Landsc. Ecol.* **22**, 431–445 (2007).
16. D. M. J. S. Bowman *et al.*, *J. Biogeogr.* **38**, 2223–2236 (2011).
17. C. J. McDonald, G. R. McPherson, *Fire Ecol.* **9**, 26–39 (2013).
18. N. Andela, G. R. Van Der Werf, *Nat. Clim. Chang.* **4**, 791–795 (2014).
19. V. C. Radeloff *et al.*, *Proc. Natl. Acad. Sci. U.S.A.* **115**, 3314–3319 (2018).
20. A. Modaresi Rad *et al.*, *Nat. Sustain.* **6**, 1343–1351 (2023).
21. F. Schug *et al.*, *Nature* **621**, 94–99 (2023).
22. B. Chen *et al.*, *Nat. Sustain.* **7**, 474–484 (2024).
23. W. Tang, C. He, L. Emmons, J. Zhang, *Environ. Res. Lett.* **19**, 044028 (2024).
24. N. Andela *et al.*, *Science* **356**, 1356–1362 (2017).
25. M. W. Jones *et al.*, *Science* **386**, eadl5889 (2024).
26. C. X. Cunningham, G. J. Williamson, D. M. J. S. Bowman, *Nat. Ecol. Evol.* **8**, 1420–1425 (2024).
27. N. Andela *et al.*, *Earth Syst. Sci. Data* **11**, 529–552 (2019).
28. A. J. Tatem, *Sci. Data* **4**, 170004 (2017).
29. M. Friedl, D. Sulla-Menashe, "MCD12Q1 MODIS/Terra+Aqua Land Cover Type yearly L3 global 500m SIN grid V006" (NASA, 2019); https://doi.org/10.5067/modis/mcd12q1.006.
30. L. Giglio, L. Boschetti, D. P. Roy, M. L. Humber, C. O. Justice, *Remote Sens. Environ.* **217**, 72–85 (2018).
31. E. Vermote, R. Wolfe, "MODIS/aqua surface reflectance daily L2G global 1km and 500m SIN grid V061" (NASA, 2021); https://doi.org/10.5067/MODIS/MYD09GA.061.
32. W. Knorr, A. Arneth, L. Jiang, *Nat. Clim. Chang.* **6**, 781–785 (2016).
33. C. Wu *et al.*, *One Earth* **4**, 517–530 (2021).
34. F. Seijo, R. Gray, *Hum. Ecol. Rev.* **19**, 58–69 (2012).
35. P. Jain *et al.*, *Nat. Commun.* **15**, 6764 (2024).
36. M. Turco *et al.*, *Sci. Rep.* **9**, 13886 (2019).
37. C. S. Juang *et al.*, *Geophys. Res. Lett.* **49**, GL097131 (2022).
38. A. D. Syphard, V. C. Radeloff, T. J. Hawbaker, S. I. Stewart, *Conserv. Biol.* **23**, 758–769 (2009).
39. T. Schoennagel *et al.*, *Proc. Natl. Acad. Sci. U.S.A.* **114**, 4582–4590 (2017).
40. M. Kumar, A. AghaKouchak, J. T. Abatzoglou, M. Sadegh, *Npj Nat. Hazards* **2**, 17 (2025).
41. P. M. Fernandes, H. S. Botelho, *Int. J. Wildland Fire* **12**, 117–128 (2003).
42. P. M. Fernandes *et al.*, *Front. Ecol. Environ.* **11**, e4–e14 (2013).
43. C. A. Kolden, *Fire* **2**, 30 (2019).
44. R. Xu *et al.*, *Nature* **621**, 521–529 (2023).
45. M. Turco *et al.*, *Proc. Natl. Acad. Sci. U.S.A.* **120**, e2213815120 (2023).
46. D. M. J. S. Bowman *et al.*, *Ambio* **48**, 350–362 (2019).
47. S. T. Seydi, J. Abatzoglou, M. Sadegh, M. Jones, Global human exposure to wildland fires dataset: 2002–2021, Zenodo (2025); https://doi.org/10.5281/zenodo.15549088

ACKNOWLEDGMENTS

Funding: This work was supported by the Joint Fire Science Program (grant L21AC10247 to M.S. and J.T.A.), the National Science Foundation (grants OAI-2019762 to J.T.A. and 2429021 to M.S.), Boise State University Healthy Idaho Initiative (M.S.), and the Natural Environment Research Council (NERC grant NE/V01417X/1 to M.W.J.). Any use of trade, firm or product names is for descriptive purposes only and does not imply endorsement by the US government. **Author contributions:** Conceptualization: M.S., J.T.A.; Funding acquisition: M.S., J.T.A.; Investigation: S.T.S., J.T.A., M.S., M.W.J., C.A.K., G.F., M.D.H., A.A., C.H.L., C.M.; Methodology: M.S., J.T.A., S.T.S., M.W.J.; Project administration: M.S.; Supervision: M.S., J.T.A.; Visualization: S.T.S.; Writing – original draft: S.T.S., J.T.A., M.S., M.W.J., C.A.K., G.F., M.D.H., A.A., C.H.L., C.M.; Writing – review & editing: S.T.S., J.T.A., M.S., M.W.J., C.A.K., G.F., M.D.H., A.A., C.H.L., C.M. **Competing interests:** The authors declare no competing interests. **Data and materials availability:** All data and materials used in this study are available on Zenodo (*47*).

SUPPLEMENTARY MATERIALS

science.org/doi/10.1126/science.adu6408

Materials and Methods; Supplementary Text; Figs. S1 to S20; Table S1; References (*48*–*61*)

Submitted 14 November 2024; resubmitted 6 March 2025; accepted 23 June 2025

10.1126/science.adu6408

SPINTRONICS

Electrical coherent driving of chiral antiferromagnet

Yutaro Takeuchi[1,2,3]*, Yuma Sato[4,5], Yuta Yamane[4,6]*,
Ju-Young Yoon[4,5], Yukinori Kanno[4,5], Tomohiro Uchimura[4,5],
K. Vihanga De Zoysa[4,5], Jiahao Han[1,4], Shun Kanai[1,4,5,7,8,9],
Jun'ichi Ieda[10], Hideo Ohno[1,4,7,11], Shunsuke Fukami[1,4,5,7,11,12]*

Electric current driving of antiferromagnetic states at radio or higher frequencies remains challenging to achieve. In this study, we report all-electrical, gigahertz-range coherent driving of chiral antiferromagnet manganese-tin (Mn_3Sn) nanodot samples. High coherence in multiple trials and threshold current insensitive to pulse width, in contrast to results observed with ferromagnets, were achieved in subnanosecond range, allowing 1000/1000 switching by 0.1-nanosecond pulses at zero field. These features are attributed to the inertial nature of antiferromagnetic excitations. Our study highlights the potential of antiferromagnetic spintronics to combine high speed and high efficiency in magnetic device operations.

Electrical manipulation of collective spin states is a central subject of magnetics and spintronics, and various physical schemes have been demonstrated mostly with ferromagnetic systems (*1*–*3*). The spin-orbit torque (SOT) (*4*–*6*), a relativistic phenomenon originating from the spin Hall effect (*7*) and/or Rashba-Edelstein effect (*8*) in magnetic heterostructures, has been recently applied to antiferromagnets (*9*–*11*). One of the prospective advantages of antiferromagnets over ferromagnets is their potential for faster driving with higher efficiency, due to the exchange-enhanced intrinsic frequency (*12*) and the inertia in their dynamics (*13*). Ultrafast switching of ferromagnets has been recently reported; however, it required relatively large current densities and the assistance of external fields and thermal effects (*14*, *15*). For antiferromagnets, an electrical control was achieved by the staggered SOT (*16*), which emerges in locally noncentrosymmetric crystals (*16*–*20*). Later, the standard SOT in antiferromagnet/nonmagnet heterostructures was demonstrated to be capable of switching (*21*–*27*) and continuously rotating (*28*, *29*) antiferromagnetic spin states. In pursuit of revealing the high-speed dynamics of antiferromagnets, earlier works reported switching of antiferromagnets by picosecond laser pulses (*30*, *31*) and an efficient excitation and ultrafast propagation of antiferromagnetic magnons (*32*–*34*). However, all-electrical switching of an antiferromagnet, required for electronic devices, has been limited in timescales longer than nanoseconds, where the results can be understood by an extrapolation from the dc-regime experiments. Despite the promising prospect for all-electrical switching of antiferromagnets with a combination of high speed and high efficiency that cannot be reached with ferromagnets, experimental exploration of this area remains challenging.

Here, we show all-electrical driving of a chiral antiferromagnetic manganese-tin (Mn_3Sn) nanodot by single electric pulses in the gigahertz range, through coherent spin excitations in a single antiferromagnetic domain. In contrast to ferromagnets, in which fast electrical control at the timescale of 0.1 ns and beyond is challenging because of sizable increase in the threshold current (*35*–*39*), we show that it is not the case for antiferromagnets. The markedly suppressed increase in the driving current in subnanosecond range, combined with a high coherence of the system used, allows us to achieve 1000/1000 switching by 0.1-ns pulses at zero magnetic field. The observed advantage of antiferromagnets over ferromagnets can be attributed to the universal inertial nature of antiferromagnetic dynamics, as indicated by our theoretical modeling.

Sample structure and measurement layout for control of coherent rotation in chiral antiferromagnet Mn_3Sn nanodot

To realize a coherent control of the antiferromagnetic order, we fabricate Mn_3Sn/heavy metal heterostructure–based nanodot samples. The stack structure consists of W (2 nm)/Ta (3 nm)/Mn_3Sn (20 nm)/MgO (1.3 nm)/Ru (1 nm), which is deposited on a MgO(110) substrate by sputtering [materials and methods (*40*)]. We confirm $(1\bar{1}00)$-plane (M-plane) oriented, epitaxial Mn_3Sn films where the kagome plane is perpendicular to the film plane (fig. S1) (*28*, *41*). The films are processed into Hall-bar devices, where a Mn_3Sn nanodot is formed on a cross-shaped W/Ta channel (Fig. 1A) (*40*). The nominal dot diameter D, channel width, and channel length are 200 nm, 250 nm, and 600 nm, respectively. An image of a fabricated nanodot sample taken by scanning electron microscopy is displayed in Fig. 1B. After defining the Hall-cross with a nanodot, coplanar waveguides are formed for high-frequency measurements.

Our experimental setup for electrical driving of Mn_3Sn is shown in Fig. 1C. We apply a pulse voltage with the width of 0.1 to 10 ns using a pulse generator through a radio frequency port of the bias tee. The state of the chiral-spin structure in Mn_3Sn is detected through the anomalous Hall effect (*42*) by measuring the voltage between the two Hall probes under a dc current of 100 μA, corresponding to the current density in the W/Ta layer of 3.8 MA cm^{-2}, applied to the dc port of the bias tee. The output side of the waveguide is terminated by an oscilloscope with an impedance of 50 ohms, which is used to monitor the transmitted waveforms of the injected pulses. Shown in Fig. 1D is the captured transmitted waveform of the applied pulse with nominal width of 0.1 ns (details on the captured waveforms with various nominal pulse widths are summarized in fig. S2). The pulse voltage is applied in the $[11\bar{2}0]$ direction of the hexagonal Mn_3Sn film, which is the most effective configuration for the Slonczewski-like SOT to induce the chiral-spin rotation (*28*, *29*).

Figure 2A shows the Hall resistance R_H versus the out-of-plane magnetic field H_z in a Mn_3Sn nanodot with D = 200 nm, where D is the nanodot diameter. Negative anomalous Hall resistance and binary state in the hysteresis loop are observed, which is consistent with our previous study on the thermal stability of Mn_3Sn nanodots (*43*), in which the uniaxial perpendicular anisotropy and the exchange stiffness for the antiferromagnetic order were estimated as 370 J m^{-3} and 3.5 pJ m^{-1}, respectively, leading to the domain wall width of ~300 nm. The switching field in the present study is evaluated to be about 350 mT (Fig. 2A).

Hall resistance versus applied current in Mn_3Sn nanodot

Before performing all-electrical experiments in the gigahertz range, we establish the field-free continuous rotation and field-assisted bipolar switching of the Mn_3Sn nanodots in the dc regime. Figure 2B shows R_H versus J_{HM} in a Mn_3Sn nanodot with D = 200 nm, where J_{HM} denotes the current density flowing into the W/Ta heavy-metal layers (supplementary text S3 and S4). The field along x direction H_x is also

---

[1] Advanced Institute for Materials Research, Tohoku University, Sendai, Japan. [2] International Center for Young Scientists, National Institute for Materials Science, Tsukuba, Japan. [3] Research Center for Magnetic and Spintronics Materials, National Institute for Materials Science, Tsukuba, Japan. [4] Laboratory for Nanoelectronics and Spintronics, Research Institute for Electrical Communication, Tohoku University, Sendai, Japan. [5] Department of Electronic Engineering, Graduate School of Engineering, Tohoku University, Sendai, Japan. [6] Frontier Research Institute for Interdisciplinary Sciences, Tohoku University, Sendai, Japan. [7] Center for Science and Innovation in Spintronics, Tohoku University, Sendai, Japan. [8] Division for the Establishment of Frontier Sciences of Organization for Advanced Studies at Tohoku University, Sendai, Japan. [9] National Institutes for Quantum Science and Technology, Takasaki, Japan. [10] Advanced Science Research Center, Japan Atomic Energy Agency, Tokai, Ibaraki, Japan. [11] Center for Innovative Integrated Electronic Systems, Tohoku University, Sendai, Japan. [12] Inamori Research Institute for Science, Kyoto, Japan. ***Corresponding author. Email: takeuchi.yutaro@nims.go.jp (Y.T); yutaymn@tohoku.ac.jp (Y.Y.); s-fukami@riec.tohoku.ac.jp (S.F.)**

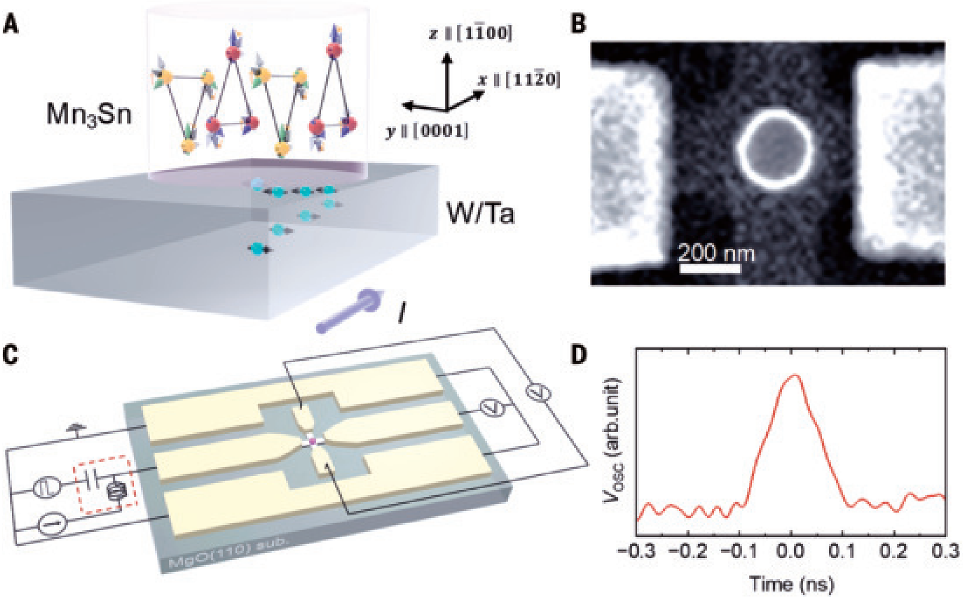

Fig. 1. Sample layout and measurement system. The system is used for electrical control of coherent antiferromagnetic chiral-spin rotation in a Mn$_3$Sn nanodot. (**A**) Illustration of Hall device with a Mn$_3$Sn nanodot and a W/Ta channel. (**B**) Scanning electron microscopy image of a fabricated Hall device. (**C**) Schematic of the Hall device, coplanar waveguide, and measurement system. sub., substrate; V, voltage; *I*, current. (**D**) A transmitted waveform of the applied pulse of 0.1 ns. The measurement is performed at room temperature. V_{OSC}, transmitted voltage measured with oscilloscope.

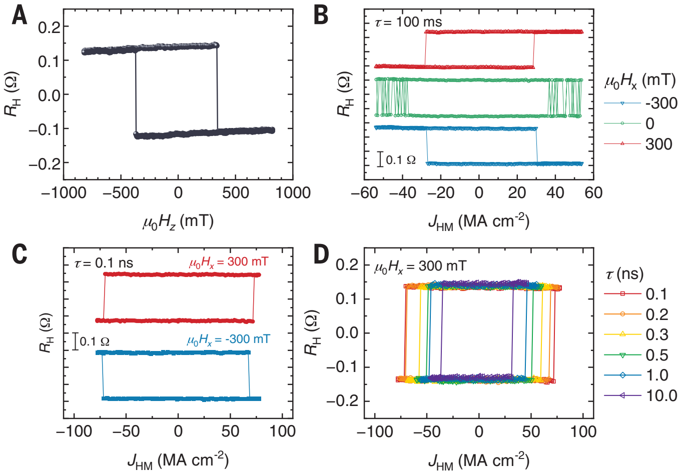

Fig. 2. Field- and SOT-induced switching of a Mn$_3$Sn nanodot. (**A**) R_H-H_z curve of prepared Mn$_3$Sn nanodot. (**B** and **C**) In-plane magnetic field dependence of R_H-J_{HM} curves for pulse width τ of 100 ms and 0.1 ns, respectively. (**D**) R_H-J_{HM} curves for various τ. Both R_H-H_z and R_H-J_{HM} curves are measured for a Mn$_3$Sn nanodot with a nominal diameter of 200 nm. The measurement is performed at room temperature.

applied to the $[11\bar{2}0]$ direction of Mn$_3$Sn, i.e., parallel to the current. For $\mu_0 H_x = 0$ mT, the binary randomization of R_H is observed once the pulse current amplitude exceeds the threshold, regardless of its direction. This is attributed to the SOT-driven continuous rotation of the chiral antiferromagnetic order in Mn$_3$Sn (*28*, *44*). The randomization between the binary states shows that the predominant magnetic anisotropy is twofold with the easy axis normal to the film (*24*, *29*) and that the Mn$_3$Sn nanodot has a single-domain structure (*43*). With finite H_x, a bipolar switching of R_H is obtained, in which the polarity of the hysteresis curve depends on the sign of H_x. This characteristic of the field-assisted switching is consistent with that reported in the previous studies on Hall bar devices (*23*–*26*, *29*, *44*) and can be explained as a result of the SOT-driven rotation being balanced by the external field that prefers the uncompensated net magnetization of Mn$_3$Sn pointing parallel to H_x.

We then move onto experiments with short current pulses in the range of nanoseconds to subnanoseconds. We first check the field-assisted switching by the short current pulses. Shown in Fig. 2C are R_H-J_{HM} curves with the pulse width $\tau = 0.1$ ns and $\mu_0 H_x = \pm 300$ mT; the R_H-J_{HM} curves at $\mu_0 H_x = 300$ mT with various τ are displayed in Fig. 2D. J_{HM} is calculated from the amplitude of the transmitted waveform. Bipolar switching is observed for all the τ down to 0.1 ns at $J_{HM} < 75$ MA cm^{-2}. In the following sections, the relationship between the pulse width and the threshold current density is extensively investigated.

Switching probability versus pulse width and amplitude

For deeper investigation into the dynamics of the chiral-spin structure in Mn$_3$Sn nanodots in the gigahertz regime, we measure the switching probability *P* as a function of J_{HM}, τ, and H_x by multiple applications of current pulses (see supplementary text S5 and fig. S5 for more details). Here, *P* is defined as the ratio of the number of successful switching out of at least 50 attempts of pulse application for a given set of J_{HM}, τ, and H_x. The antiferromagnetic ordering is initialized by applying a 0.1-s pulse current with an amplitude of 42 MA cm^{-2} under $\mu_0 H_x = 300$ mT.

Figure 3, A to D, shows the *P* versus J_{HM} for τ = 0.1, 0.2, 0.3, and 1.0 ns, respectively, under $\mu_0 H_x = 0$ and 300 mT. A general tendency for the case with $\mu_0 H_x = 300$ mT is that *P* initially increases with J_{HM}, reaches 1 and starts decreasing as J_{HM} further increases. The range of J_{HM} achieving $P = 1$ expands with a reduction of τ. This observation indicates that the antiferromagnetic order acquires a lower probability to switch back to the original state with the shorter pulse widths. Under a longer and larger pulse, the chiral antiferromagnetic order experiences a larger driving force to rotate for a longer time, resulting in less predictability for the final state. For $\mu_0 H_x = 0$ mT, nondeterministic behavior ($P \sim 0.5$) above a threshold is observed at τ = 1.0 ns as expected from Fig. 2B; notably, there is a $P = 1$ range at τ = 0.1 and 0.2 ns, achieving all-electrical switching, which at this timescale has been seen only in current-induced, heat-driven reversal of GdFeCo (*45*).

The dependencies of *P* on τ, J_{HM}, and H_x are summarized by two-dimensional (2D) color maps in Fig. 3, E to H. In the regions where J_{HM} is sufficiently large (the upper regions of the color maps), *P* oscillates with τ between relatively high values (switched regions) and relatively low values (switched-back regions). At $\mu_0 H_x = 0$ mT (Fig. 3E), we confirm a periodic appearance of switched and switched-back regions at least seven times as labeled by the arrows, indicating a highly coherent rotation of chiral-spin structure in the 50 trials. The oscillation of *P* becomes less appreciable as τ increases. The switched and switched-back regions are shifted toward the right side (longer τ) with decreasing J_{HM}. As $\mu_0 H_x$ increases from 0 to 300 mT, the switched (switched-back) regions expand (shrink). This is because the in-plane magnetic field breaks the $\pm x$ symmetry, assisting the "up" to "down" spin rotation (switching) and hindering the "down" to "up" rotation (switching-back).

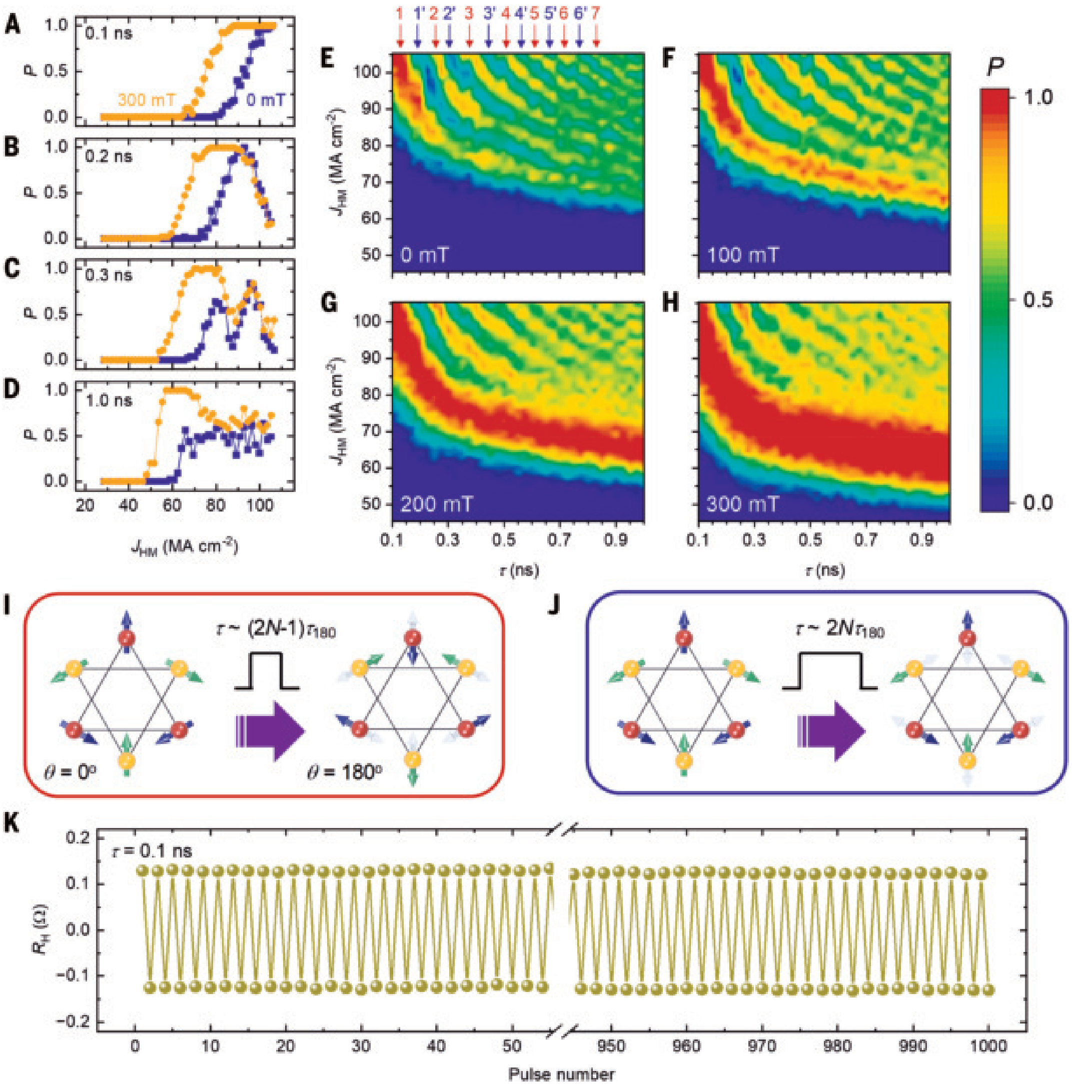

Fig. 3. Switching probability and field-free switching. (**A** to **D**) P versus J_{HM} for various τ. (**E** to **H**) 2D mapping of P versus J_{HM} and τ for various in-plane magnetic field H_x. The red and blue arrows above (E) point at switched and switched-back regions through coherent chiral-spin rotation, respectively. The numbers without (with) the prime symbol denote 180° coherent chiral-spin rotation being completed one, three, …, $2N$–1 (two, four, …, $2N$) times. (**I** and **J**) Schematic illustration of switching and switching-back process through controlling the coherent chiral-spin rotation of $\mathrm{Mn_3Sn}$ by short current pulse of $\tau \sim (2N-1)\,\tau_{180}$ and $2N\tau_{180}$, respectively. θ and τ_{180} denote the angle of the antiferromagnetic order parameter in the kagome plane and the time period for 180° rotation under the given J_{HM}, respectively. (**K**) Pulse-number dependence of Hall resistance in $\mathrm{Mn_3Sn}$ nanodot at zero magnetic field. Here, current pulse $J_{\mathrm{HM}} = 112$ MA cm^{-2}, and $\tau = 0.1$ ns is applied to the Hall devices. The measurement is performed at room temperature.

The switching and switching-back processes through the coherent chiral-spin rotation are schematically illustrated in Fig. 3, I and J. It is theoretically predicted that the frequency of the SOT-driven chiral-spin rotation increases with J_{HM} (*28*). Exploiting this unconventional current dependence of the antiferromagnetic dynamics, the switching and switching-back of the antiferromagnetic order can be all electrically controlled by current pulses with $\tau \sim (2N\text{–}1)\tau_{180}$ and $2N\tau_{180}$, respectively, where N is a positive integer and τ_{180} is the time period for 180° rotation under the given J_{HM}. In Fig. 3, E to H, the first, second, …, N-th switched (switched-back) regions therefore correspond to the 180° coherent chiral-spin rotation being completed one, three, …, $2N$–1 (two, four, …, $2N$) times. This is consistent with our numerical calculation considering the SOT-driven chiral-spin rotation in a single-domain antiferromagnet without any thermal assistance (fig. S6). The calculation also shows that the switching characteristic is insensitive to the rise and fall times of the pulse (fig. S7), indicating a minor impact of the thermally assisted SOT (*25*, *26*) in our experiment. Notably, although the experimentally observed switching characteristic may appear to be similar to the ferromagnetic switching by a short electric-field pulse (*46*, *47*), our scheme for the antiferromagnetic system does not require an external magnetic field.

Next, we demonstrate the reproducibility of the field-free switching based on the coherent driving of the chiral-spin structure. We repeat the write-and-read cycle 1000 times at zero field, where a writing current pulse of $\tau = 0.1$ ns and $J_{\mathrm{HM}} = 112$ MA cm^{-2} is utilized. Figure 3K shows a portion of the data, with R_{H} varying with the pulse number; the full results are shown in fig. S8. The result clearly manifests the full switching of the antiferromagnetic state taking place at each pulse application. We observe no error in the 1000 attempts, thanks to the high coherence of the chiral-spin dynamics.

Switching current density versus pulse width

We now study the switching in more detail and start by examining the dependence of the switching current density J_{C} on the pulse width τ.

Here, $J_C(\tau)$ is defined as the value of J_{HM} at which P first reaches 0.5 at fixed τ. Figure 4A shows the measured τ dependence of J_C for each H_x. The presence of H_x diminishes J_C because in the current configuration H_x assists the switching, as discussed in the previous section. We find that reducing τ from 1 to 0.2 ns (0.1 ns) leads to an increase in J_C by a factor of about 1.2 (1.4). This increasing rate is markedly lower than that for ferromagnetic switching. For example, in a three-terminal magnetic tunnel junction comprising Ta/W/CoFeB/MgO and designed to be switched by both spin-orbit and spin-transfer torques, the reduction of τ from 1 to 0.2 ns was reported to result in an increase in J_C by a factor of about 2.6 (*39*). A similar sizable increase in J_C was also reported in a perpendicularly magnetized Pt/Co/AlO_x nanodot (*36*), multilevel magnetization switching in exchange-biased Pt/Co/Ir-Mn (*48*), field-free SOT switching in a CoFeB/Ti/CoFeB nanodot (*49*), and SOT-driven domain-wall motion in ferrimagnetic Co-Gd (*50*). In the case of ferromagnetic switching by the conventional spin-transfer torque or the so-called type-y SOT switching (*5*, *6*), the rate of J_C increase is even higher (*35*, *37*–*39*). A thorough comparison of the pulse-width dependence of the switching current density reported in previous studies on ferromagnets and this work is shown in fig. S9, showcasing a qualitative difference between the ferromagnets and chiral antiferromagnets. The physical mechanism behind the greater suppression of J_C in Mn_3Sn can be mainly attributed to the inertial nature of the chiral-spin rotation, a universal property of antiferromagnetic dynamics. This will be discussed in more detail in the "Theoretical considerations" section.

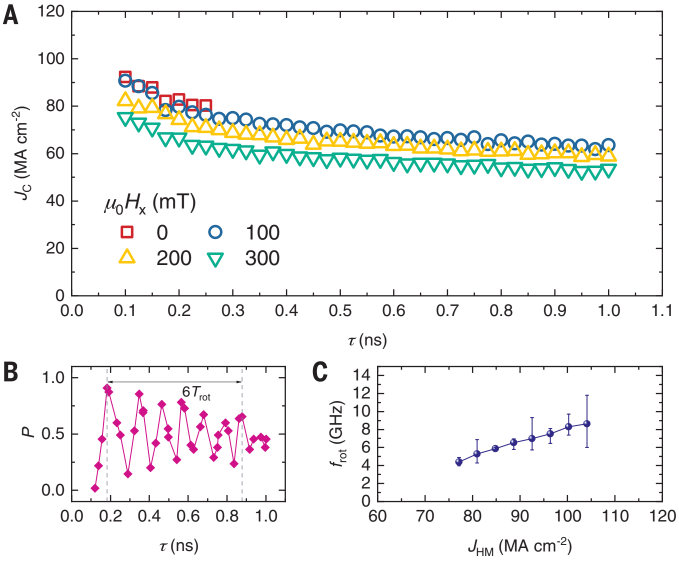

Fig. 4. Relationship among pulse width, amplitude, and switching properties. (**A**) τ dependence of switching current density J_C for various H_x. (**B**) P versus τ for J_{HM} = 104 MA cm^{-2}. (**C**) Current dependence of chiral-spin rotation frequency f_{rot}. No magnetic field is applied for (B) and (C). More details on f_{rot}, including the definition of the error bars, are found in supplementary text S10.

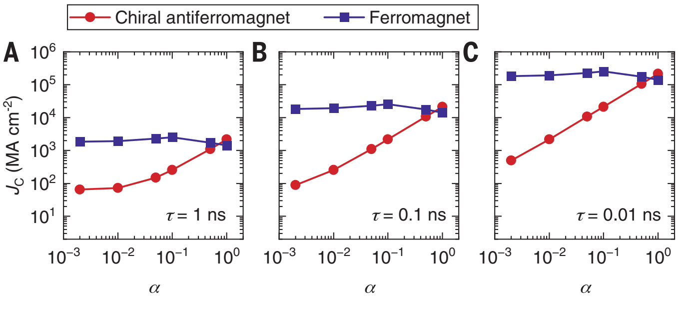

Fig. 5. Numerical calculation of switching current. (**A** to **C**) Calculated switching current density versus Gilbert damping constant in chiral antiferromagnet and ferromagnet for τ = 1, 0.1, and 0.01 ns, respectively.

Rotation frequency versus current density

In this section, we evaluate the frequency f_{rot} of the chiral-spin rotation in the Mn_3Sn nanodots with respect to the applied current. For this purpose, we extract the P versus τ at $\mu_0H_x = 0$ mT for various J_{HM} shown in Fig. 3E. In Fig. 4B, we show P versus τ at J_{HM} = 104 MA cm^{-2} as an example, where seven peaks are identified in the oscillation of P. We evaluate f_{rot} from the τ interval between the first and last peaks. Results of the P versus τ evaluated in the same fashion for various J_{HM} are summarized in fig. S10. Because of the inertial nature in antiferromagnetic dynamics (which will be discussed below), f_{rot} may not be a very accurate quantitative indicator of the actual frequency of the chiral-spin rotation. However, the J_{HM} dependence of f_{rot} (Fig. 4C) displays an important physical feature: f_{rot} increases with J_{HM}, which is consistent with the theoretical prediction (*28*, *51*). This tunability of the frequency with the current could lead to a different type of electrically tunable spintronic oscillators, in contrast to the conventional ones, for which ferromagnetic resonance is the basic working principle and thus the frequency of the spin dynamics is intrinsic to the system determined by material parameters such as the magnetic anisotropy (*11*, *46*, *52*, *53*).

Theoretical considerations

Next, we theoretically show that the threshold current density with a given pulse width is almost universally lower in antiferromagnets than in ferromagnets in the subnanosecond regime because of the inertial nature of the former's equation of motion. The magnetization of a ferromagnet obeys the Landau-Lifshitz-Gilbert (LLG) equation, a first-order differential equation in time. By contrast, the dynamics of the angular variable θ of the antiferromagnetic order parameter in the kagome plane is described by a second-order differential equation in time (*54*, *55*), $(\gamma H_E)^{-1}\partial_t^2\theta = -\alpha\partial_t\theta - \frac{\gamma H_K}{2}\sin 2\theta - \gamma H_S$; the left-hand side is the inertial term, where γ is the gyromagnetic ratio and H_E the effective field associated with the antiferromagnetic exchange coupling. The three "forces" on the right-hand side originate from, respectively, the damping torque on each sublattice magnetic moment, where α is the Gilbert damping constant; the uniaxial anisotropy characterized by the effective field H_K; and the SOT with the Slonczewski-like effective field H_S is the Slonczewski-like effective field. The antiferromagnetic dynamics are therefore mathematically described as a point mass moving in potential hills arising because of the magnetic anisotropy. For successful antiferromagnetic switching, the point mass needs to be supplied with sufficient kinetic energy by the SOT to overcome the potential barrier, and the pulse width can be shorter than the time it takes for the point mass to pass through a peak of the potential (*30*, *31*). In our present experiment, the observed antiferromagnetic advantage over ferromagnets can be attributed to the role that the α term plays in the antiferromagnet, i.e., a frictional force that resists the dynamics of θ. Smaller α, therefore, can generally lead to faster and more energy-efficient driving of θ, hence to smaller $J_C(\tau)$. This is in stark contrast to the ferromagnetic SOT-switching with the injected spin orthogonal to the magnetization (*3*, *6*), where $J_C(\tau)$ depends little on α (*56*).

In Fig. 5, the α dependence of $J_C(\tau)$ obtained by numerical simulations is shown for three different τ, for which we computed the dynamics of the magnetization (sublattice magnetic moments) for a ferromagnet (antiferromagnet). The details of the calculations are given in supplementary text S6 and S11 to S14. For the antiferromagnet, the parameter values are chosen to reproduce our experimental results with Mn_3Sn. To give a fair comparison between the two systems, for the ferromagnet we used parameter values that give the same effective magnetic anisotropy energy and Slonczewski-like SOT as for Mn$_3$Sn. For the unrealistically large $\alpha = 1$, $J_\mathrm{C}(\tau)$ takes similar values for the antiferromagnet and ferromagnet. As α decreases, $J_\mathrm{C}(\tau)$ for the antiferromagnet is linearly reduced until it hits the minimum value to overcome the energy barrier (~64 MA cm^{-2}), whereas for the ferromagnet it exhibits little dependence on α. Because $\alpha \ll 1$ for most magnetic materials of interest, $J_\mathrm{C}(\tau)$ is considerably and almost universally smaller for antiferromagnets. The experimental $J_\mathrm{C}(\tau)$ is reproduced quantitatively by the simulation with $\alpha = 0.002$ (fig. S11). Because the discussion here is based on the fundamental inertial nature of antiferromagnetic dynamics, it holds true with any driving forces, including spin-transfer torque (*1*, *35*, *39*) and electric field–induced driving (*46*, *47*). Furthermore, it was found that $J_\mathrm{C}(\tau)$ monotonically increases with H_K (fig. S12). We also found that $J_\mathrm{C}(\tau)$ for the antiferromagnet is insensitive to H_E (fig. S13), confirming that the exchange-enhanced effect has a minor impact here. Dependencies of $J_\mathrm{C}(\tau)$ on some other micromagnetic parameters are also shown in fig. S13, demonstrating that our conclusions are quantitatively robust against changes in those parameters. Simulated antiferromagnetic dynamics in time domain with several different pulses are given in fig. S14.

Discussion and outlook

In this work, we show a gigahertz-range electrical coherent driving of a chiral antiferromagnet under the spin-orbit torque using Mn$_3$Sn nanodots. The results were consistently described by coherent dynamics of the chiral-spin structure with an electrically tunable rotation frequency. Using this scheme, we demonstrate a highly reproducible, field-free gigahertz switching of the chiral antiferromagnet. We also show that the driving current for the antiferromagnet is much less sensitive to the pulse width in the high-speed regime, owing to the inertial spin dynamics that are universal to antiferromagnets in general. Furthermore, the switching field of Mn$_3$Sn nanodot, 350 mT in this work, is one to two orders of magnitude larger than that of the ferromagnetic counterparts (*5*, *6*, *39*, *57*), as a result of the vanishingly small magnetization in Mn$_3$Sn and the correspondingly small Zeeman energy splitting, offering high robustness against external fields. Our results experimentally show the advantage of antiferromagnetic spintronics over the conventional ferromagnetic counterpart.

REFERENCES AND NOTES

1. E. B. Myers, D. C. Ralph, J. A. Katine, R. N. Louie, R. A. Buhrman, *Science* **285**, 867–870 (1999).
2. H. Ohno *et al.*, *Nature* **408**, 944–946 (2000).
3. I. M. Miron *et al.*, *Nature* **476**, 189–193 (2011).
4. A. Manchon, S. Zhang, *Phys. Rev. B.* **78**, 212405 (2008).
5. L. Liu *et al.*, *Science* **336**, 555–558 (2012).
6. S. Fukami, T. Anekawa, C. Zhang, H. Ohno, *Nat. Nanotechnol.* **11**, 621–625 (2016).
7. J. E. Hirsch, *Phys. Rev. Lett.* **83**, 1834–1837 (1999).
8. V. M. Edelstein, *Solid State Commun.* **73**, 233–235 (1990).
9. T. Jungwirth, X. Marti, P. Wadley, J. Wunderlich, *Nat. Nanotechnol.* **11**, 231–241 (2016).
10. V. Baltz *et al.*, *Rev. Mod. Phys.* **90**, 015005 (2018).
11. J. Han, R. Cheng, L. Liu, H. Ohno, S. Fukami, *Nat. Mater.* **22**, 684–695 (2023).
12. C. Kittel, *Phys. Rev.* **73**, 155–161 (1948).
13. A. F. Andreev, V. I. Marchenko, *Sov. Phys. Usp.* **23**, 21–34 (1980).
14. K. Jhuria *et al.*, *Nat. Electron.* **3**, 680–686 (2020).
15. D. Polley *et al.*, *Sci. Adv.* **9**, eadh5562 (2023).
16. P. Wadley *et al.*, *Science* **351**, 587–590 (2016).
17. J. Železný *et al.*, *Phys. Rev. Lett.* **113**, 157201 (2014).
18. S. Y. Bodnar *et al.*, *Nat. Commun.* **9**, 348 (2018).
19. M. Meinert, D. Graulich, T. Matalla-Wagner, *Phys. Rev. Appl.* **9**, 064040 (2018).
20. K. A. Omari *et al.*, *J. Appl. Phys.* **127**, 193906 (2020).
21. X. Z. Chen *et al.*, *Phys. Rev. Lett.* **120**, 207204 (2018).
22. T. Moriyama, K. Oda, T. Ohkochi, M. Kimata, T. Ono, *Sci. Rep.* **8**, 14167 (2018).
23. H. Tsai *et al.*, *Nature* **580**, 608–613 (2020).
24. T. Higo *et al.*, *Nature* **607**, 474–479 (2022).
25. B. Pal *et al.*, *Sci. Adv.* **8**, eabo5930 (2022).
26. G. K. Krishnaswamy *et al.*, *Phys. Rev. Appl.* **18**, 024064 (2022).
27. P. Zhang *et al.*, *Phys. Rev. Lett.* **129**, 017203 (2022).
28. Y. Takeuchi *et al.*, *Nat. Mater.* **20**, 1364–1370 (2021).
29. J.-Y. Yoon *et al.*, *Nat. Mater.* **22**, 1106–1113 (2023).
30. A. V. Kimel *et al.*, *Nat. Phys.* **5**, 727–731 (2009).
31. K. Olejník *et al.*, *Sci. Adv.* **4**, eaar3566 (2018).
32. Y. Wang *et al.*, *Science* **366**, 1125–1128 (2019).
33. K. Lee *et al.*, *Nat. Nanotechnol.* **16**, 1337–1341 (2021).
34. Y. Behovits *et al.*, *Nat. Commun.* **14**, 6038 (2023).
35. H. Tomita *et al.*, *Appl. Phys. Lett.* **102**, 042409 (2013).
36. K. Garello *et al.*, *Appl. Phys. Lett.* **105**, 212402 (2014).
37. S. Shi, Y. Ou, S. V. Aradhya, D. C. Ralph, R. A. Buhrman, *Phys. Rev. Appl.* **9**, 011002 (2018).
38. H. Honjo *et al.*, "First demonstration of field-free SOT-MRAM with 0.35 ns write speed and 70 thermal stability under 400°C thermal tolerance by canted SOT structure and its advanced patterning/SOT channel technology" in *2019 IEEE International Electron Devices Meeting (IEDM)*, San Francisco, CA, USA, 7 to 11 December 2019 (2019), pp. 28.5.1–28.5.4.
39. C. Zhang, Y. Takeuchi, S. Fukami, H. Ohno, *Appl. Phys. Lett.* **118**, 092406 (2021).
40. See the supplementary materials.
41. J. Yoon *et al.*, *Appl. Phys. Express* **13**, 013001 (2020).
42. S. Nakatsuji, N. Kiyohara, T. Higo, *Nature* **527**, 212–215 (2015).
43. Y. Sato *et al.*, *Appl. Phys. Lett.* **122**, 122404 (2023).
44. G. Q. Yan *et al.*, *Adv. Mater.* **34**, 2200327 (2022).
45. Y. Yang *et al.*, *Sci. Adv.* **3**, e1603117 (2017).
46. Y. Shiota *et al.*, *Nat. Mater.* **11**, 39–43 (2011).
47. S. Kanai *et al.*, *Appl. Phys. Lett.* **101**, 122403 (2012).
48. Y. Wang *et al.*, *Nat. Electron.* **5**, 840–848 (2022).
49. Q. Yang *et al.*, *Nat. Commun.* **15**, 1814 (2024).
50. K. Cai *et al.*, *Nat. Electron.* **3**, 37–42 (2020).
51. D.-Y. Zhao, P.-B. He, M.-Q. Cai, *Phys. Rev. B* **104**, 214423 (2021).
52. S. I. Kiselev *et al.*, *Nature* **425**, 380–383 (2003).
53. A. A. Tulapurkar *et al.*, *Nature* **438**, 339–342 (2005).
54. O. V. Gomonay, V. M. Loktev, *Low Temp. Phys.* **41**, 698–704 (2015).
55. Y. Yamane, O. Gomonay, J. Sinova, *Phys. Rev. B* **100**, 054415 (2019).
56. T. Taniguchi, S. Mitani, M. Hayashi, *Phys. Rev. B* **92**, 024428 (2015).
57. C. Zhang *et al.*, *Appl. Phys. Lett.* **109**, 192405 (2016).
58. Y. Takeuchi *et al.*, Electrical coherent driving of chiral antiferromagnet, NIMS Materials Data Repository (MDR) (2025); https://doi.org/10.48505/nims.5415.

ACKNOWLEDGMENTS

We thank Y. Nakano, T. Tanno, I. Morita, R. Ono, M. Musya, H. Kodaira, F. Shibata, S. Kasai, and S. Mitani for their technical support and helpful discussions. **Funding:** This work was supported by JSPS Kakenhi grant 19H05622 (S.F., J.I., S.K.); JSPS Kakenhi grant 21J23061 (J.-Y.Y.); JSPS Kakenhi grant 22K14558 (Y.T.); JSPS Kakenhi grant 22KK0072 (Y.Y., Y.T.); JSPS Kakenhi grant 22KF0035 (S.F., J.H.); JSPS Kakenhi grant 23KJ0216 (T.U.); JSPS Kakenhi grant 24KJ0432 (Y.S.); JSPS Kakenhi grant 24K16999 (J.H.); JSPS Kakenhi grant 24H00039 (S.F., Y.T., Y.Y., S.K., J.I.); JST PRESTO grant JPMJPR24H6 (Y.T.); JST PRESTO grant JPMJPR21B2 (S.K.); MEXT Initiative to Establish Next-Generation Novel Integrated Circuits Centers (X-NICS) grant JPJ011438 (S.F.); Iketani Science and Technology Foundation grant 0331108-A (Y.Y., Y.T., J.-Y.Y.); Iketani Science and Technology Foundation grant 0361247-A (Y.T., Y.Y.); Casio Science and Technology Foundation grants 39-11 and 40-4 (Y.T.); Seiko Instruments Advanced Technology Foundation, Research Grants 2024 (Y.T.); and Research Institute of Electrical Communication, Cooperative Research Projects (S.F.). **Author contributions:** Conceptualization: Y.T., Y.Y., S.F.; Data curation: Y.T., Y.S., Y.Y.; Formal analysis: Y.T., Y.S., Y.Y., S.F.; Funding acquisition: Y.T., Y.S., Y.Y., J.-Y.Y., T.U., J.H., S.K., J.I., H.O., S.F.; Investigation: Y.T., Y.S., Y.Y., Y.K.; Methodology: Y.T., Y.Y., S.F.; Project administration: Y.T., Y.Y., H.O., S.F.; Resources: Y.T., Y.S., Y.Y., J.-Y.Y., Y.K., T.U., K.V.D.Z., S.K., H.O., S.F.; Software: Y.T., Y.S., Y.Y.; Supervision: H.O., S.F.; Validation: Y.T., Y.S., Y.Y.; Visualization: Y.T., Y.S., Y.Y., S.F.; Writing – original draft: Y.T., Y.Y., J.H., J.I., S.F.; Writing – review & editing: Y.T., Y.S., Y.Y., J.-Y.Y., Y.K., T.U., K.V.D.Z., J.H., S.K., J.I., H.O., S.F. **Competing interests:** The authors declare that they have no competing interests. **Data and materials availability:** All of the data needed to evaluate the conclusions in this work are available in the main text or the supplementary materials and have also been deposited to the National Institute for Materials Science (NIMS) Materials Data Repository (MDR) (*58*).

SUPPLEMENTARY MATERIALS

science.org/doi/10.1126/science.ado1611
Materials and Methods; Supplementary Text; Figs. S1 to S14

Submitted 19 January 2024; accepted 16 June 2025

10.1126/science.ado1611

CONSERVATION GENETICS

Fitness benefits of genetic rescue despite chromosomal differences in an endangered pocket mouse

Aryn P. Wilder[1]*, Debra M. Shier[1,2], Shauna N. D. King[1], Olga Dudchenko[3,4], Erik R. Funk[1], Ann Misuraca[1], Marlys L. Houck[1], William B. Miller[5], Caitlin J. Curry[1], Julie Fronczek[1], Ruqayya Khan[3], David Weisz[3], Robert N. Fisher[6], Erez Lieberman Aiden[3,4,7,8], Oliver A. Ryder[1], Cynthia C. Steiner[1]

Two-thirds of Earth's species have undergone population declines, leaving many vulnerable to genomic erosion and inbreeding depression. Genetic rescue can boost the fitness of small populations, but perceived risks of outbreeding depression can limit its use. We quantified these trade-offs in hundreds of endangered Pacific pocket mice (*Perognathus longimembris pacificus*) by combining whole-genome sequences with fitness data. The impacts of genomic erosion in remnant populations were reversed in an admixed breeding program, suggesting the potential benefits of genetic rescue. However, differences in chromosome numbers increase the risk of genetic incompatibilities. Fitness analyses suggested that although admixed karyotypes may have reduced fertility, non-admixed mice with low heterozygosity and high genetic load had even lower fitness, pointing to a greater risk of extinction if populations remain isolated.

Population decline and extirpation are major drivers of rapid biodiversity loss across the globe (*1*). An estimated 69% of populations have declined in the past five decades (*2*), losing 6 to 10% of standing genetic variation (*3*, *4*). Small populations are vulnerable to genomic erosion, in which strong genetic drift and inbreeding can lead to a loss of genetic diversity, an accumulation of genetic load, and reduced fitness (*5*–*8*). These impacts can be alleviated by genetic rescue through facilitated gene flow from an outside population (*9*–*11*). However, despite calls for its expanded use in conservation (*12*, *13*), genetic rescue remains underutilized (*14*), in part because of concerns that outbreeding depression may harm recovery (*9*). Established guidelines for genetic rescue exclude cases in which the receiver and source populations have been isolated for >500 years, live in distinct environments, or have fixed chromosomal differences (*15*). On the basis of these guidelines, many populations in need of genetic rescue are not considered good candidates. More precise implementation of genetic rescue requires a more detailed understanding of the genomic processes underlying the fitness trade-offs of inbreeding and outbreeding. These insights are largely limited to model species (*16*–*20*) that have differences in demographic history and genetic load that limit their relevance to threatened taxa (*21*).

To quantify the trade-offs of continued isolation versus genetic rescue, we estimated the genomic predictors of fitness under inbreeding and outbreeding in the endangered Pacific pocket mouse (*Perognathus longimembris pacificus*). Historically distributed along an ~200-km stretch of coastal Southern California (*22*, *23*), the Pacific pocket mouse occupied 30 known localities in the 1930s (Fig. 1A), but habitat destruction led to its widespread extirpation, and it was thought to be extinct for 20 years before its rediscovery in 1993 (*22*). Three known remnant populations persist at Dana Point (12 ha), Santa Margarita (885 ha), and South San Mateo (105 ha) (Fig. 1A), isolated by geography and urban development (*22*). We generated whole-genome sequence data for 468 Pacific pocket mice to examine the potential impacts of genetic rescue as a conservation tool.

Genomic erosion in small populations can be ameliorated by admixture

Remnant populations of Pacific pocket mice are small and isolated. Demographic history estimated from the genomes of 44 wild mice (sequenced at mean = 12.7 × coverage; tables S1 and S2 and fig. S1) suggest population bottlenecks within the past 25 to 50 generations (Fig. 1, C). Contemporary effective population sizes (N_e) based on linkage disequilibrium (*24*) are extremely small in Dana Point ($N_e = 12.3$) and South San Mateo ($N_e = 21.3$) and modest in the Santa Margarita population ($N_e = 254.8$; Fig. 1C and figs. S2 and S3), consistent with long runs of homozygosity (ROH) in the genome (Fig. 1E). Gene flow can generate false signatures of population decline (*25*), but models that account for gene flow also support recent bottlenecks (Fig. 1D). Whereas gene flow between the neighboring Santa Margarita and South San Mateo populations ceased only recently, Dana Point has been isolated from them for much longer (tables S3 to S5) but was likely once connected to populations now extirpated. The impacts of recent isolation and small population size are reflected in the genomes of an additional 148 wild mice sampled since 1996 and sequenced at low coverage (mean = 1.01 × coverage); genotype likelihood–based principal components analyses (PCAs) revealed divergence over time within Dana Point and South San Mateo, indicating genome-wide changes driven by genetic drift (fig. S4).

Consistent with strong genetic drift, remnant populations show signs of genomic erosion. Mice from Dana Point and South San Mateo had lower genome-wide heterozygosity and higher ROH-based inbreeding coefficients (F_{ROH}) than the larger Santa Margarita population (Tukey test; all $P < 1 \times 10^{-12}$; Fig. 2, C and D, and figs. S5 to S9). Given their recent N_e, theory predicts a 4.1% loss of heterozygosity per generation for Dana Point and a 2.3% loss for South San Mateo (*26*). Heterozygosity declined 18% from 2012 to 2020 in South San Mateo (linear regression; $P = 0.028$), and although temporal representation of high-coverage genomes in Dana Point was inadequate to test statistically, samples collected in 2012–2013 had 44% lower heterozygosity than the single Dana Point sample from 1999 (Fig. 2C). The potential functional impacts of genetic drift and inbreeding are underscored by elevated genetic load, estimated by homozygous-derived alleles that cause nonsynonymous changes at evolutionarily conserved sites (phyloP score ≥ 4) in protein-coding genes (*27*, *28*). Burdens of homozygous genetic load were greater in the smaller populations (Tukey test; all $P < 1 \times 10^{-12}$; Fig. 2E), and the number of high-frequency deleterious alleles increased in the populations over time (fig. S10). Together, these results suggest a loss of diversity and increased homozygous genetic load over the past several decades.

The low heterozygosity, high inbreeding coefficients, and high homozygous genetic load were reversed by admixture. An ex situ conservation breeding program was established in 2012 by admixing founders from the three remnant populations (Dana Point, $n = 11$; South San Mateo, $n = 14$; and Santa Margarita, $n = 17$; table S6) to provide a source for reintroductions to unoccupied habitats (*29*–*31*). The ex situ population also provided an opportunity to test admixture in a common environment (*32*). Along with the 42 higher-coverage (mean = 12.9 × coverage) genomes of the wild-born founders, we sequenced 278 mice born in the conservation breeding program

---

[1] Conservation Science Wildlife Health, San Diego Zoo Wildlife Alliance, Escondido, CA, USA. [2] Department of Ecology & Evolutionary Biology, University of California Los Angeles, Los Angeles, CA, USA. [3] The Center for Genome Architecture, Department of Molecular and Human Genetics, Baylor College of Medicine, Houston, TX, USA. [4] Center for Theoretical Biological Physics, Rice University, Houston, TX, USA. [5] US Fish & Wildlife Service, Carlsbad, CA, USA. [6] Western Ecological Research Center, US Geological Survey, San Diego, CA, USA. [7] Department of Biosciences, Rice University, Houston, TX, USA. [8] Department of Biochemistry and Molecular Biology, University of Texas Medical Branch; Galveston, TX, USA. ***Corresponding author. Email: awilder@sdzwa.org**

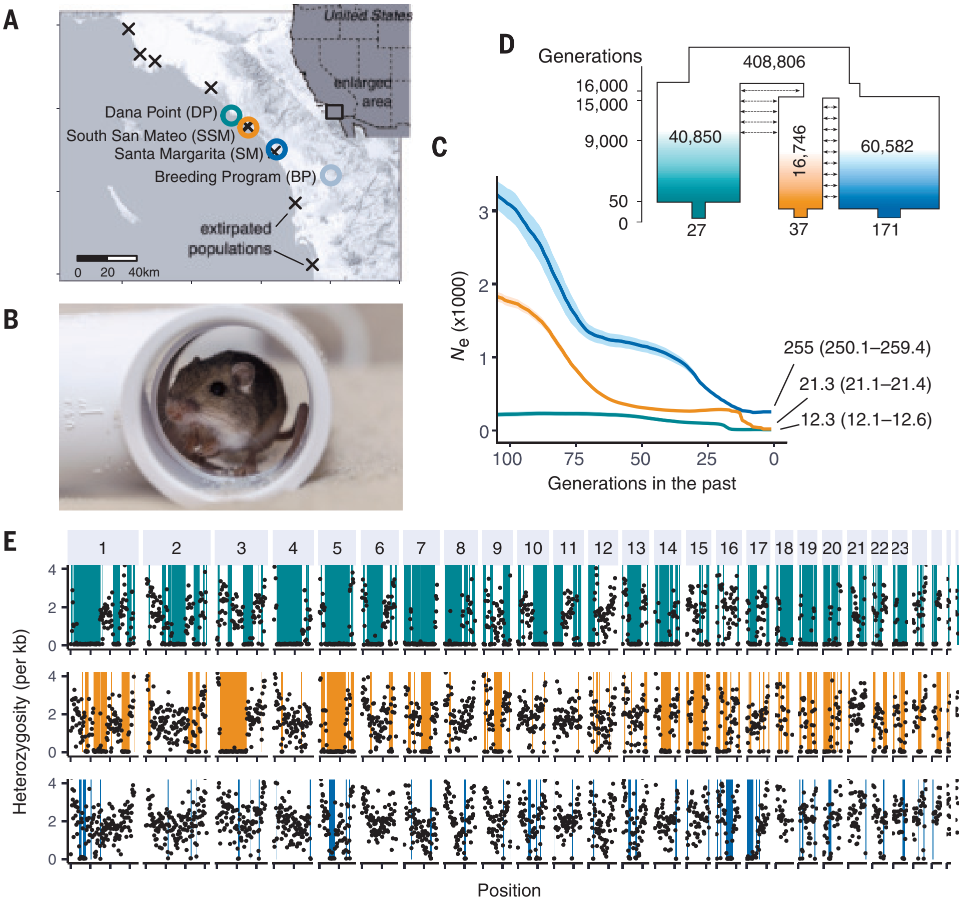

Fig. 1. Remnant populations of Pacific pocket mice are small, isolated, and inbred. (**A**) Three wild remnant populations in California at Dana Point, South San Mateo, and Santa Margarita and the conservation breeding program. (**B**) A Pacific pocket mouse in the conservation breeding program. [Photo credit: San Diego Zoo Wildlife Alliance] (**C**) Linkage disequilibrium–based effective population sizes (N_e) suggest declines, and extremely small recent N_e (N_e and 95% confidence intervals are given for the most recent generation). (**D**) Demographic models of the site-frequency spectrum support recent population bottlenecks and isolation of populations once larger and more connected. Box widths and numbers represent population sizes, and arrows show gene flow through time. (**E**) Heterozygosity in 1-Mb windows for the median individual in each population. Top to bottom, Dana Point, South San Mateo, and Santa Margarita. Long ROH (>1 Mb; highlighted bars) points to high inbreeding in Dana Point and South San Mateo.

(hereafter “breeding program”) at low coverage (mean = 1.16 × coverage) and imputed genotypes using pedigree information (*33*). Test samples imputed from low-coverage sequence data showed good agreement with genotypes called from high-coverage genomes (>98% identical genotypes and allelic dosage $r^2 > 0.94$; table S7 and fig. S11). Admixture of differentiated remnant populations in the breeding program (Fig. 2, A and B, and fig. S12) led to a boost in genetic diversity and masking of homozygous genetic load (Fig. 2, C to E). Offspring in the breeding program had higher heterozygosity (Tukey test; $P < 1 \times 10^{-4}$), lower inbreeding coefficients ($P < 1 \times 10^{-9}$), and lower homozygous genetic load ($P < 1 \times 10^{-9}$) compared with the founding populations, suggesting that genetic rescue through facilitated gene flow could help to mitigate genomic erosion in the wild (Fig. 2, C to E).

A fission yields different chromosome numbers fixed across populations

Variation in chromosome numbers (i.e., karyotypes) in the Pacific pocket mouse (*34*, *35*) raises concerns about outbreeding depression from genetic rescue (*15*). We generated karyotypes from 26 mice from the wild populations and the breeding program (table S8). All four karyotyped mice from Dana Point had diploid numbers of 2n = 58, with 15 metacentric and 13 acrocentric autosomal pairs (Fig. 3B), whereas all six from South San Mateo and all six from Santa Margarita had diploid numbers of 2n = 56, with 16 metacentric and 11 acrocentric autosomal pairs (Fig. 3A) (*36*). Poor cell growth in some samples introduced chromosomal artifacts arising in culture. To circumvent this problem, we characterized large-scale structural variation using high-throughput chromosome conformation capture (Hi-C) for 17 individuals (*37*, *38*), 11 with known karyotypes (table S8). Relative to South San Mateo and Santa Margarita, Dana Point samples showed a reduced number of Hi-C contacts between two regions of chromosome 2, consistent with a chromosome fission in a gene desert at 63.68 to 63.94 Mb (Fig. 3, C and D, and figs. S13 and S14). The ancestral diploid number is thought to be 2n = 56 (*39*, *40*), suggesting that a fission split the ancestral submetacentric pair number 2 into two acrocentric pairs, resulting in the same number of autosomal arms (*n* = 86) with an additional pair of chromosomes in Dana Point karyotypes.

Linked single-nucleotide polymorphisms (SNPs) flanking the fission breakpoint suggest that the populations are fixed for different karyotypes. The breakpoint is located within a highly differentiated 740-kb span distinguishing Dana Point from the other populations (Fig. 3E and fig. S15). A PCA of SNPs within this region groups 32 individuals according to their karyotypes (fig. S16), suggesting that they are diagnostic. Genotype likelihood–based PCA of all samples clusters all Dana Point samples (*n* = 74) into the group of homozygous fission mice with the extra chromosome pair, and all Santa Margarita (*n* = 82) and South San Mateo (*n* = 34) samples cluster into the homozygous ancestral group. Only the breeding program had heterozygous karyotypes with diploid number 2n = 57 (36 of 278 mice from the breeding program); all had admixed ancestry (Dana Point × South San Mateo and/or Santa Margarita) in their pedigree (figs. S17 to S19 and table S9). These results strongly suggest that Dana Point is fixed for the fission and extra chromosome pair, whereas Santa Margarita and South San Mateo are fixed for the ancestral karyotype.

Genetic rescue of the smallest, most inbred population (Dana Point) would require crossing populations fixed for different karyotypes, which could result in outbreeding depression if the karyotypes are genetically incompatible (*15*). Improper meiotic segregation of chromosomes can result in aneuploid gametes and reduced fertility of fission-fusion heterozygotes (*41*) and can restrict gene flow and even lead to speciation (*42*–*44*). Coincidentally, a fusion forming human chromosome 2 distinguishes the diploid numbers of humans (2n = 46) and chimpanzees (2n = 48) (*45*, *46*). The impact can also be small or undetectable, especially for simple centric fusions (*13*, *44*). For example, selection against fission-fusion heterozygotes is small in wild house mice (*Mus musculus*) and common shrews (*Sorex araneus*)

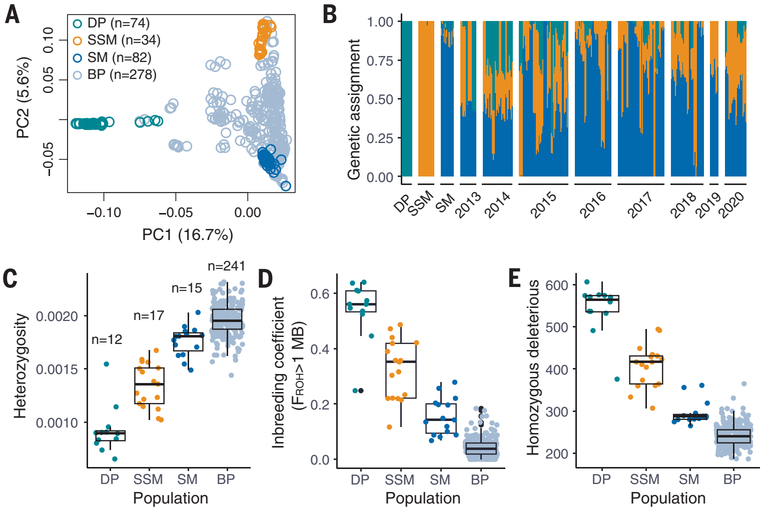

Fig. 2. Low diversity and high genetic load in small populations of Pacific pocket mice are reversed by admixture in a conservation breeding program. (**A**) Genotype likelihood–based PCA of genomic variation across populations. (**B**) Admixture of the differentiated founder populations, Dana Point (DP), South San Mateo (SSM), and Santa Margarita (SM), in mice born each year in the breeding program (BP). (**C** to **E**) Summary statistics from imputed genotypes. Compared with wild remnant populations, individuals in the admixed breeding program had the highest heterozygosity (C), lowest inbreeding coefficients [F_{ROH} (D)], and lowest homozygous moderate-impact conserved mutations (phyloP score ≥4) (E). The horizontal line and lower and upper hinges in each boxplot represent the median and first and third quartiles, respectively. The whiskers extend to 1.5x the interquartile range. Black points denote outliers. Sample sizes in (B) to (E) are given in (C). Note that the Dana Point sample with highest heterozygosity and lowest inbreeding and genetic load was collected in 1999, 13 or 14 years before the other Dana Point samples.

(*41*, *47*), and even populations with complex fusions can show high admixture (*48*). In the Pacific pocket mouse, chromosomal heterozygotes were morphologically identical to other karyotypes and produced viable offspring over four or more generations and multiple meioses (fig. S17). Recombination of chromosome 2 haplotypes indicated proper pairing of homologous chromosomes during meiosis (Fig. 3G and fig. S18). Although fitness in the wild could differ, strong selection against chromosomal heterozygotes was not apparent in the ex situ environment.

The cost of inbreeding exceeds outbreeding depression

Survival and reproduction in the breeding program suggest that despite differences in chromosome numbers, outbred mice have higher fitness than inbred mice. We used mixed-effects Poisson and Cox proportional hazards models to test heterozygosity, inbreeding coefficients, homozygous genetic load, and karyotype against survival and reproduction in admixed and non-admixed mice (n = 253) bred over 8 years. We accounted for environmental effects by including the population of origin as a random factor in all models. Considering each variable individually in separate models, mice with higher heterozygosity ($P = 5.97 \times 10^{-4}$), lower F_{ROH} ($P = 0.051$), and lower homozygous genetic load ($P < 0.05$) had more offspring (table S10), and mice with lower F_{ROH} ($P = 0.002$) and lower homozygous genetic load ($P < 0.004$) had higher survival (Fig. 4 and table S11). Models of survival and reproduction that included genomic variables consistently outperformed models only accounting for

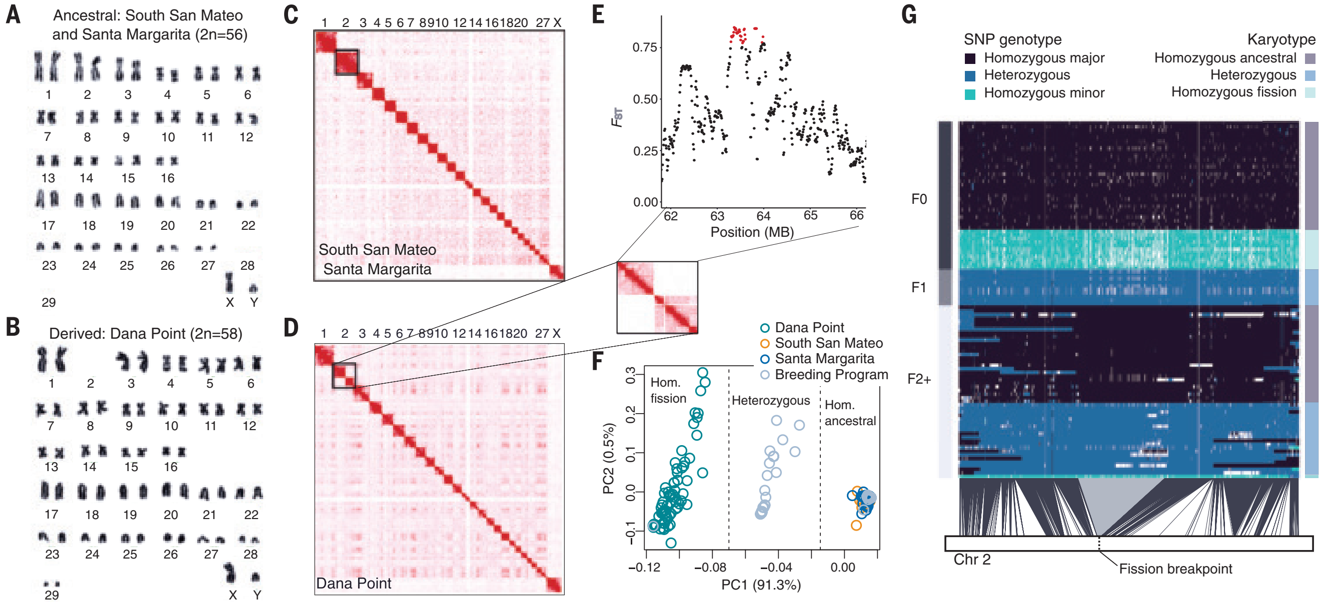

Fig. 3. A chromosomal fission yields different chromosome numbers between wild populations of Pacific pocket mice. (**A**) Ancestral karyotype typical of South San Mateo and Santa Margarita with diploid number 2n = 56. (**B**) Derived karyotype typical of Dana Point with diploid number 2n = 58. Submetacentric pair number 2 in (A) is replaced by two acrocentric pairs in (B). Chromosomes are sorted by size. (**C** and **D**) Hi-C contacts mapped to the 2n = 56 reference genome. Contact maps for South San Mateo and Santa Margarita (C) show an intact chromosome 2, whereas Dana Point (D) shows fission of chromosome 2. Refer to https://t.3dg.io/ppm-Fig-3 for interactive maps. (**E**) Highly differentiated SNPs (red points) between Dana Point versus South San Mateo and Santa Margarita in 50-kb sliding windows flank the fission breakpoint. (**F**) PCA of flanking SNPs distinguishes karyotypes; all Dana Point mice cluster with homozygous fission karyotypes, all South San Mateo and Santa Margarita mice cluster with homozygous ancestral karyotypes, and only admixed mice from the breeding program cluster with heterozygous karyotypes. (**G**) Differentiated SNPs on chromosome 2 show recombination of fission and ancestral haplotypes in F_2+ generations. Side colors indicate the generation (left) and karyotype (right) of each mouse. The locations of flanking SNPs used for karyotyping are highlighted in gray.

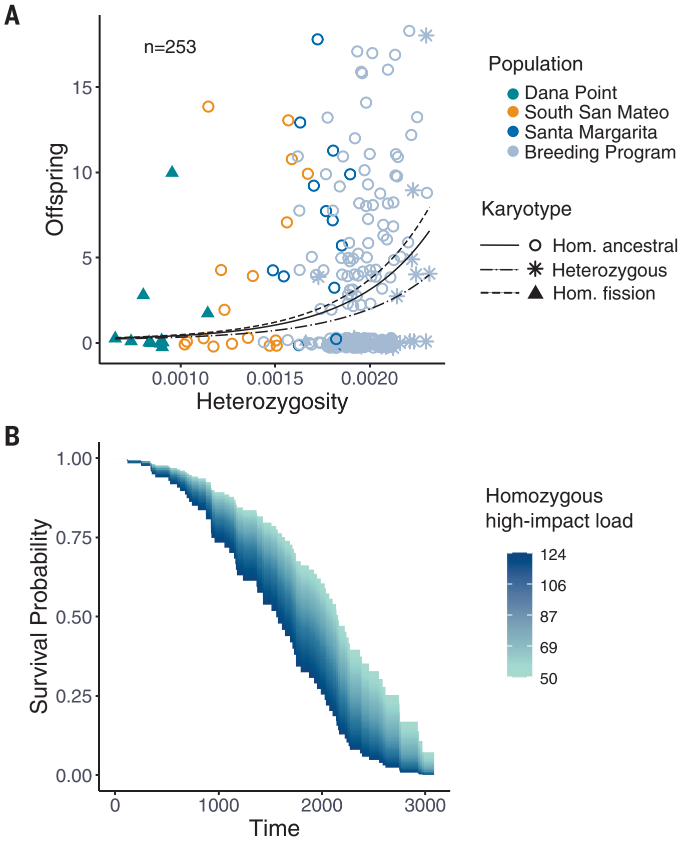

Fig. 4. Effects of inbreeding and outbreeding on survival and reproduction in Pacific pocket mice. (**A**) Mice with higher heterozygosity produced more offspring in models accounting for population of origin and time in the breeding program. Mice with heterozygous karyotypes produced fewer offspring than homozygous karyotypes (fitted curves), but the cost was outweighed by the boost in overall genetic diversity associated with outbreeding (table S16). (**B**) Mice with lower levels of homozygous high-impact deleterious alleles had higher survival probabilities in models accounting for population of origin and age upon entering the breeding program.

environment (tables S12 to S15). When controlling for the effects of genome-wide genetic diversity, heterozygous karyotypes had fewer offspring than the two homozygous karyotypes, but the reduction in reproductive success was masked by the associated boost in heterozygosity (Fig. 4A and table S14). The models predict that the heterozygous karyotype would have fewer offspring than a homozygous fission karyotype with the same genetic background. However, given the higher genome-wide heterozygosity typical of the outbred mouse with a heterozygous karyotype, it had on average 3.6 offspring, markedly more than the 0.50 offspring predicted for a mouse with a homozygous karyotype and genetic variation typical of the Dana Point population (table S16). The trends in reproductive success were similar when we restricted the analysis to captive-born mice (table S17), indicating that they were not driven solely by environmental effects. These results suggest that for the smallest population, the benefit of a boost in genetic diversity and masking of deleterious alleles outweighs the cost of admixing different karyotypes.

A major caveat of fitness in the ex situ environment is that it may not reflect nature. Although we controlled for breeding opportunities (table S18), differences in reproductive conditions could affect reproductive outcomes, and survivorship is higher under human care (*49*, *50*). Future studies will examine fitness correlations in admixed populations introduced to the wild with multiple years of survival and reproduction. Moreover, although the mice were collected across the range of each population, the breeding program had a limited number of initial founders. This was especially true for the Dana Point population, which, despite efforts to increase its ex situ representation through inter- and intrapopulation matings, had only three of 11 founders reproduce. Our findings are nonetheless consistent with those of other studies (*18*). Correlations between heterozygosity or inbreeding and survival have been observed across taxa (*49*, *51*, *52*), and reduced fertility has been seen in chromosomal heterozygotes (*13*, *41*, *44*); both may be occurring simultaneously in the Pacific pocket mouse.

Our empirical data suggest that genomic erosion in two populations could be alleviated by genetic rescue using different strategies. The data lend support for genetic rescue of Dana Point despite chromosomal differences with potential source populations. Without subsequent migration or population growth, however, genetic diversity and its fitness benefits would likely wane (*9*), potentially before the rare karyotype is removed by selection. Alternatively, F_2-backcrossed mice with the homozygous fission karyotype could serve as a source of migrants (fig. S17). Requiring at least two generations of ex situ breeding and more migrants (each carrying a portion of migrant alleles), this strategy introduces new genetic diversity without chromosomal variation, but the time required for breeding may make it impractical. For South San Mateo, translocations from Santa Margarita, a population recently connected by gene flow, may help to boost genetic diversity and relieve inbreeding (table S16). The weight of evidence suggests that continued isolation of these populations may lead to extinction over the long term; genomic erosion is likely already underway, and N_e is insufficient to maintain genetic diversity and avoid inbreeding (*26*). For a subspecies already extirpated from most of its range, the unique genetic variation in these populations may be critical reservoirs of adaptive potential against future environmental perturbation.

Conclusions

Even as global loss of biodiversity outpaces recovery, conservationists often prioritize maintaining genetic uniqueness at the expense of population size and resiliency (*53*). Studies across species suggest that inbreeding depression is more frequent and more severe than outbreeding depression (*13*, *54*). Using empirical data to isolate the genomic predictors and mechanisms of inbreeding and outbreeding depression allows us to weigh their respective impacts and potentially apply genetic rescue even when outbreeding depression is a risk. Our study presents a case in which the benefits of genetic rescue outweigh those of continued isolation despite fixed differences in chromosome numbers across populations, underscoring the advantage of less genetically restrictive conservation strategies in the midst of a conservation crisis.

REFERENCES AND NOTES

1. G. Ceballos, P. R. Ehrlich, R. Dirzo, *Proc. Natl. Acad. Sci. U.S.A.* **114**, E6089–E6096 (2017).
2. R. E. A. Almond, M. Grooten, D. Juffe Bignoli, T. Petersen, “Living planet report 2022: Building a nature-positive society” (World Wildlife Fund, 2022); https://www.wwf.org.uk/sites/default/files/2023-05/WWF-Living-Planet-Report-2022.pdf.
3. M. Exposito-Alonso *et al.*, *Science* **377**, 1431–1435 (2022).
4. D. M. Leigh, A. P. Hendry, E. Vázquez-Domínguez, V. L. Friesen, *Evol. Appl.* **12**, 1505–1512 (2019).
5. A. P. Wilder *et al.*, *Science* **380**, eabn5856 (2023).
6. R. Bürger, M. Lynch, *Evolution* **49**, 151–163 (1995).
7. S. Wright, *Genetics* **16**, 97–159 (1931).
8. M. Kardos *et al.*, *Nat. Ecol. Evol.* **7**, 675–686 (2023).
9. D. A. Tallmon, G. Luikart, R. S. Waples, *Trends Ecol. Evol.* **19**, 489–496 (2004).
10. A. R. Whiteley, S. W. Fitzpatrick, W. C. Funk, D. A. Tallmon, *Trends Ecol. Evol.* **30**, 42–49 (2015).
11. R. Frankham, *Mol. Ecol.* **24**, 2610–2618 (2015).
12. K. Ralls *et al.*, *Conserv. Lett.* **11**, e12412 (2018).

13. R. Frankham *et al.*, *Genetic Management of Fragmented Animal and Plant Populations* (Oxford Univ. Press, 2017).
14. S. W. Fitzpatrick, C. Mittan-Moreau, M. Miller, J. M. Judson, *J. Hered.* **114**, 354–366 (2023).
15. R. Frankham *et al.*, *Conserv. Biol.* **25**, 465–475 (2011).
16. J. Aspi, *Heredity* **84**, 273–282 (2000).
17. D. B. Jørgensen, M. Ørsted, T. N. Kristensen, *J. Evol. Biol.* **35**, 868–878 (2022).
18. T. C. Marshall, J. A. Spalton, *Anim. Conserv.* **3**, 241–248 (2000).
19. S. W. Margulis, J. Altmann, *Anim. Behav.* **54**, 397–408 (1997).
20. R. J. Sheffer, P. W. Hedrick, A. L. Velasco, *Anim. Conserv.* **2**, 121–129 (1999).
21. P. W. Hedrick, A. Garcia-Dorado, *Trends Ecol. Evol.* **31**, 940–952 (2016).
22. P. Brylski, L. Hays, J. Avery, "Pacific pocket mouse (*Perognathus longimembris pacificus*) recovery plan" (US Fish & Wildlife Service, 1998); https://ecos.fws.gov/docs/recovery_plan/980928c.pdf.
23. J. L. Patton, R. N. Fisher, *Therya* **14**, 131–160 (2023).
24. E. Santiago *et al.*, *Mol. Biol. Evol.* **37**, 3642–3653 (2020).
25. I. Novo *et al.*, *Genet. Sel. Evol.* **55**, 86 (2023).
26. R. Frankham, C. J. A. Bradshaw, B. W. Brook, *Biol. Conserv.* **170**, 56–63 (2014).
27. P. Cingolani, *Methods Mol. Biol.* **2493**, 289–314 (2022).
28. D. P. Genereux *et al.*, *Nature* **587**, 240–245 (2020).
29. D. M. Shier, "Behavioral ecology and translocation of the Pacific pocket mouse (*Perognathus longimembris pacificus*) for the period January 2007 - December 2007" (Conservation and Research for Endangered Species, San Diego Zoo, 2008).
30. D. M. Shier, S. Leivers, S. King, R. Chock, J. P. Montagne, "Captive breeding, anti-predator behavior and reintroduction of the Pacific pocket mouse (*Perognathus longimembris pacificus*) for the period July 1, 2014 – November 30, 2016" (California Department of Fish and Wildlife, Wildlife Management, Nongame Wildlife Unit Report 2016-10, 2016); https://nrm.dfg.ca.gov/FileHandler.ashx?DocumentID=138387.
31. R. Y. Chock, D. M. Shier, G. F. Grether, *Anim. Behav.* **137**, 197–204 (2018).
32. A. P. Wilder *et al.*, *Conserv. Genet.* **21**, 589–601 (2020).
33. A. Whalen, R. Ros-Freixedes, D. L. Wilson, G. Gorjanc, J. M. Hickey, *Genet. Sel. Evol.* **50**, 67 (2018).
34. M. L. McKnight, M. R. Lee, *J. Mammal.* **73**, 625–629 (1992).
35. J. L. Patton, *Southwest. Nat.* **12**, 429–438 (1967).
36. A. P. Wilder *et al.*, *Genome Biol. Evol.* **14**, evac122 (2022).
37. S. S. P. Rao *et al.*, *Cell* **159**, 1665–1680 (2014).
38. N. C. Durand *et al.*, *Cell Syst.* **3**, 99–101 (2016).
39. M. L. McKnight, *Evolution* **49**, 816–826 (1995).
40. R. Matthey, in *Advances in Genetics*, M. Demerec, Ed. (Elsevier, 1951), pp. 159–180.
41. M. W. Nachman, J. B. Searle, *Trends Ecol. Evol.* **10**, 397–402 (1995).
42. A. Mackintosh *et al.*, *Mol. Biol. Evol.* **40**, msad043 (2023).
43. J. M. de Vos, H. Augustijnen, L. Bätscher, K. Lucek, *Philos. Trans. R. Soc. Lond. B Biol. Sci.* **375**, 20190539 (2020).
44. R. J. Baker, J. W. Bickham, *Proc. Natl. Acad. Sci. U.S.A.* **83**, 8245–8248 (1986).
45. J. J. Yunis, O. Prakash, *Science* **215**, 1525–1530 (1982).
46. F. Kasai *et al.*, *Chromosome Res.* **8**, 727–735 (2000).
47. J. B. Searle, *Hereditas* **113**, 121–132 (2008).
48. S. Potter, C. Moritz, M. D. B. Eldridge, *Biol. Lett.* **11**, 20150731 (2015).
49. J. A. Jiménez, K. A. Hughes, G. Alaks, L. Graham, R. C. Lacy, *Science* **266**, 271–273 (1994).
50. W. B. Miller, M. Pavelka, "2004 Monitoring study of the Pacific pocket mouse (*Perognathus longimembris pacificus*) at Marine Corps Base Camp Pendleton, San Diego County, California: Final report" (California Department of Fish and Game, 2007); https://nrm.dfg.ca.gov/FileHandler.ashx?DocumentVersionID=42557.
51. P. A. Scott, L. J. Allison, K. J. Field, R. C. Averill-Murray, H. B. Shaffer, *Science* **370**, 1086–1089 (2020).
52. B. Hansson, L. Westerberg, *Mol. Ecol.* **11**, 2467–2474 (2002).
53. A. R. Weeks, J. Stoklosa, A. A. Hoffmann, *Front. Zool.* **13**, 31 (2016).
54. E. Liddell, P. Sunnucks, C. N. Cook, *Biol. Conserv.* **256**, 109072 (2021).

ACKNOWLEDGMENTS

We thank the San Diego Zoo Wildlife Alliance animal care and field staff (J. Chang, R. Chock, A. Diamond, E. Drum, C. Dyslin, R. Gosselin, E. Gray, A. Heath, A. Kozuch, M. LaCava, S. Leivers, M. Lucero, M. Swartz, and T. Wang) for samples and phenotypic data; C. Brehme, D. Rogers, K. Merrill, San Diego Natural History Museum, and the Museum of Vertebrate Zoology for samples; S. Turbek for help with analyses; and S. Hunjan, M. Korody, A. Chandrashekar, and E. Choi for lab support. C. Kozak, J. Patton, M. Nachman, and C. Conroy shared genomic data from the California Conservation Genomics Project. A. Vandergast, L. Nunney, J. Patton, S. Fitzpatrick, M. Supple, and the Pacific Pocket Mouse Working Group provided helpful feedback. A. Martin provided advice on AlphaPeel. Reviews from M. Kardos and two other reviewers improved the manuscript. Hi-C data were generated in collaboration with the DNA Zoo Consortium. DNA Zoo acknowledges support from Illumina, IBM, and the Pawsey Supercomputing Center. The findings and conclusions in this article are those of the authors and do not necessarily represent the views of the US Fish and Wildlife Service. Any use of trade, firm, or product names is for descriptive purposes only and does not imply endorsement by the US government. **Funding:** This work was supported by the California Department of Fish and Wildlife (grant P1850301 to A.P.W. and grants P1182023, P1482002, and P1750401 to D.M.S.); the Morris Animal Foundation (grant D19ZO-082 to A.P.W.); the US Fish & Wildlife Service (grant F15AC00734 to D.M.S.); the US Navy (cooperative agreement 62473-20-2-0016 to D.M.S.); the National Science Foundation (Postdoctoral Research Fellowship in Biology Award NSF DBI-2208925 to E.R.F.); the Welch Foundation (grant Q-1866 to E.L.A.); the National Institutes of Health (NIH) Encyclopedia of DNA Elements Mapping Center (award UM1HG009375 to E.L.A.); the US-Israel Binational Science Foundation (award 2019276 to E.L.A.); the Behavioral Plasticity Research Institute (NSF grant DBI-2021795 to E.L.A.); the NSF Physics Frontiers Center (award NSF PHY-2019745 to E.L.A.); and the NIH Centers of Excellence in Genomic Science (CEGS grant RM1HG011016-01A1 to E.L.A.). **Author contributions:** Conceptualization: A.P.W., D.M.S., W.B.M., O.A.R., C.C.S.; Formal analysis: A.P.W., O.D., E.R.F., C.J.C., A.M., M.L.H.; Investigation: A.P.W., D.M.S., S.N.D.K., O.D., A.M., J.F., R.K., D.W., E.L.A., C.J.C.; Resources: D.M.S., S.N.D.K., W.B.M., R.N.F., O.D., E.L.A., C.J.C.; Writing – original draft: A.P.W.; Writing – review & editing: All authors. **Competing interests:** E.L.A. and O.D. hold patents related to Hi-C. E.L.A. is on the scientific advisory board of Colossal Biosciences. The other authors declare no competing interests. **Data and materials availability:** The data presented here are detailed in the supplementary materials. All genomic sequence data are available on the National Center for Biotechnology Information (NCBI) website under PRJNA1263912, PRJNA512907, and PRJNA1003920. Hi-C maps are available on the GEO Database under GSE302104. Analysis scripts are available at https://github.com/apwilder/PPM_PopulationGenomics and https://github.com/erikrfunk/PPM_fastsimcoal2.

SUPPLEMENTARY MATERIALS

science.org/doi/10.1126/science.adn4666
Materials and Methods; Figs. S1 to S19; Tables S1 to S18; References (*55–107*);
MDAR Reproducibility Checklist

Submitted 20 December 2023; resubmitted 6 January 2025; accepted 27 June 2025

10.1126/science.adn4666

NEUROSCIENCE

Dysfunction in primate dorsolateral prefrontal area 46 affects motivation and anxiety

Christian M. Wood[1]*†, Rana Banai Tizkar[1]*†‡, Martina Fort[1], Xinhu Zhang[1], Kevin G. Mulvihill[1], Naixuan Liao[1], Gemma J. Cockcroft[1], Lauren B. McIver[1], Stephen J. Sawiak[1], Angela C. Roberts[1,2]*

The dorsolateral prefrontal cortex (dlPFC) is a higher-order brain structure targeted for noninvasive stimulation for treatment-resistant depression. Nonetheless, its causal role in emotion regulation is unknown. We discovered that inactivating dlPFC area 46 in marmosets blunts appetitive motivation and heightens threat reactivity. The effects were asymmetric—dependent on the left hemisphere only—and were mediated through projections to pregenual cingulate area 32. The antidepressant ketamine blocked the appetitive motivational deficits through mechanisms within subcallosal cingulate area 25, an area linked with treatment success in dlPFC noninvasive stimulation. Our data uncover an integrated prefrontal network for area 46 that contributes to positive and negative emotion regulation that may be core to our understanding of symptoms and therapeutic strategies for treatment-resistant depression and anxiety.

The dorsolateral prefrontal cortex (dlPFC) is considered part of a network involved in higher-order processes, such as attention, abstract thoughts, and consciousness (*1*, *2*). This region is known to be involved in the mental representation of information (*3*), such as in working memory, and provides a capacity for the regulation of different types of thoughts through inhibitory control mechanisms (*4*). It is also a target for noninvasive brain stimulation for the treatment of refractory depression (*5*, *6*). dlPFC transcranial magnetic stimulation (TMS) can improve depressive and comorbid anxiety symptoms (*5*, *7*) as well as normalize hyperactivity in another brain region, the subcallosal cingulate cortex (scACC), including area 25 (A25), which is known to be both overactive in depression and itself a target for deep brain stimulation for treating refractory depression (*8*–*11*). Better treatment responses are observed from dlPFC stimulation sites, such as area 46 (A46), that are more anticorrelated with scACC activity (*12*, *13*), whereas patients responding to scACC deep brain stimulation show increased activity in the dlPFC alongside reductions in scACC activity (*8*). In addition, functional asymmetry has been observed across the left and right dlPFC, with a recent framework positing hemispheric differences in affective and nonaffective processing of information (*7*), with antidepressant responses primarily associated with the left hemisphere and inhibitory control processes with the right hemisphere (*4*).

The antidepressant effects of activating the dlPFC are consistent with reductions in activity within dlPFC reported in subjects with depression, as revealed with both resting-state functional magnetic resonance imaging (rs-fMRI) and task-based fMRI (*14*, *15*). However, what are the neurobiological mechanisms by which the dlPFC can regulate positive and negative emotion? Certainly, correlative human neuroimaging studies have implicated the dlPFC in the generation and regulation of emotion through processes such as cognitive reappraisal (*16*), distraction (*17*), and suppression of both negative stimuli (*18*) and emotional memories (*19*). However, its causal involvement in emotion regulation and its functional interaction with A25 of the scACC and other prefrontal and cingulate structures remain unknown.

Appetitive motivation is reduced by A46 inactivation, which can be ameliorated by ketamine in A25

We first studied the role of A46 in appetitive behaviors, with a deficit in this behavioral domain highly relevant to the core symptom of anhedonia in depression (*20*, *21*). To do this, we assessed a marmosets' willingness to work for reward and their preference to consume rewarding substances. To selectively inactivate A46 neurons, we infused into A46 of six marmosets an adeno-associated virus (AAV) containing the inhibitory chemogenetic channel hM4Di (*22*) under a calcium calmodulin kinase II promoter (CaMKII) (fig. S1 and table S1), which primarily targets excitatory pyramidal cells (Fig. 1A). After this, marmosets were treated with the hM4Di activator deschloroclozapine (DCZ; 10 μg/kg intramuscularly) (*23*) to inactivate A46 projections. We measured the physical effort component of motivation (*24*) through a progressive ratio (PR) task in which an increasing number of responses to a touchscreen stimulus are required to receive a milkshake reward (Fig. 1B and fig. S2). Performance after drug treatment was compared with the previous day's performance to limit the impact of any interweek variability. DCZ treatment reduced total responses when compared with vehicle treatment (30 min before testing) (Fig. 1C), as well as rewards received (fig. S3A). These effects occurred without significantly altering the rate of responding, although a variable decline was observed (fig. S3B), which suggests that deficits in motor processes per se were unlikely to be the major contributor to the overall decline in total responding. In addition, this reduced motivation through hM4Di activation by DCZ was in the absence of any changes in consummatory behavior, with the marmoset's preference for sucrose unaffected during a 1-hour test in the home cage after DCZ treatment (Fig. 1D); the overall volume of solution consumed also was unaffected (fig. S3C). These data suggest that the DCZ-mediated deficit in the PR task was unlikely to be related to satiety, with the maximum reward volume on the PR task (3.75 ml, 25 rewards) being under 10% of the total volume consumed (~54 ml) on the sucrose preference test. Before receiving the hM4Di-containing viral infusion in A46, we showed that DCZ has minimal off-target effects on the PR task with no behavioral measure affected (fig. S4), indicating the specificity of the hM4Di-mediated effects.

This motivational blunting after A46 inactivation is similar to that seen after A25 overactivity (*25*) and is consistent with previous neuroimaging data in marmosets that showed an inverse relationship between A46 and A25 activity (*26*). Given that anticorrelated activity between these two regions is also an indicator of neuromodulatory treatment success (*12*, *27*), the next series of experiments determined their functional interaction with respect to treatment response. Instead of neuromodulation, we explored the ability of the fast-acting antidepressant ketamine to ameliorate the A46-mediated blunting of motivation (*25*). Systemic treatment with ketamine (0.5 mg/kg intramuscularly, 24 hours before testing) ameliorated the blunted motivation induced by DCZ treatment, restoring both total responses (Fig. 1E) and the number of rewards received to normal levels (fig. S3D). These effects occurred with a variable but nonsignificant effect on response rate (fig. S3E), whereas ketamine treatment alone did not affect any behavioral variable. To determine any interaction with A25 in this treatment response, we infused A25 with ketamine directly through surgically implanted cannulae, 24 hours before testing. The A25 ketamine infusion (Fig. 1F) blocked DCZ-induced blunting of responses (0.5 μg/μl) (Fig. 1G) and rewards received (fig. S3F), with the response rate not significantly affected albeit variably reduced (fig. S3G).

---

[1]Department of Physiology, Development and Neuroscience, University of Cambridge, Cambridge, UK. [2]Girton College, University of Cambridge, Cambridge, UK. ***Corresponding author. Email: cmw84@cam.ac.uk (C.M.W.); rb869@cantab.ac.uk (R.B.T.); acr4@cam.ac.uk (A.C.R.)** †These authors contributed equally to this work. ‡Present address: Aix Marseille University, CNRS, Institut de Neurosciences de la Timone (INT), Marseille, France.

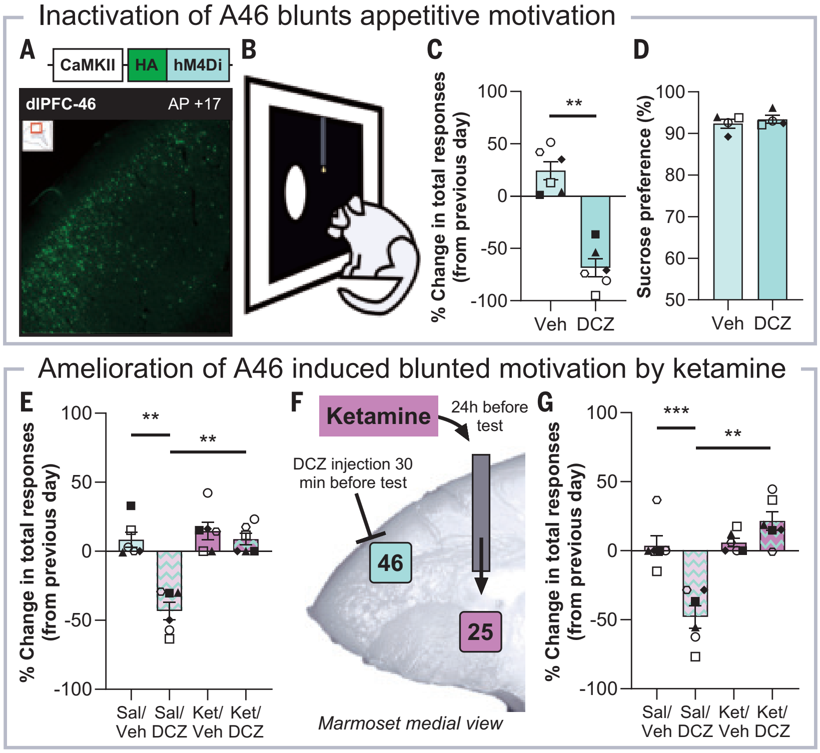

Fig. 1. Chemogenetic inactivation of A46 blunts appetitive motivation that can be ameliorated with ketamine treatment systemically and with direct A25 infusion. (**A**) Schematic of hM4Di viral construct with photomicrograph of fused hemagglutinin (HA)–tag expression in A46. (Inset) Coronal section showing region of interest. (**B**) Marmosets respond to a touchscreen stimulus a progressively increasing number of times for reward in the PR task. (**C**) DCZ treatment decreased touchscreen responses compared with that of vehicle (Veh; $n = 6$ marmosets, 10 μg/kg intramuscularly 30 min before testing; paired t test, $P = 0.0016$, $d = 2.52$). (**D**) Preference for 6% sucrose over water was unaffected by DCZ treatment ($n = 4$ marmosets, paired t test, $P = 0.408$). (**E**) Intramuscular ketamine (Ket) 24 hours before testing blocked the DCZ-induced reduction in responses [$n = 6$ marmosets; repeated measures ANOVA (rmANOVA) pretreat × treat interaction, $F_{(1,5)} = 15.24$, $P = 0.011$, $\eta^2 = 0.753$; post hoc: Sal/Veh versus Sal/DCZ, $P = 0.001$, $d = 2.62$; Sal/DCZ versus Ket/DCZ, $P = 0.002$, $d = 2.41$; Sal/Veh versus Ket/Veh, $P = 0.508$]. (**F**) Schematic for assessing A25's involvement in A46-induced motivational deficits through ketamine infusion. (**G**) Intra-A25 ketamine infusion blocked DCZ-induced reduction in responses ($n = 6$ marmosets; rmANOVA, pretreat × treat interaction, $F_{(1,5)} = 50.34$, $P < 0.001$, $\eta^2 = 0.91$; post hoc: Sal/Veh versus Sal/DCZ, $P < 0.001$, $d = 3.35$; Sal/DCZ versus Ket/DCZ, $P = 0.005$, $d = 1.99$; Sal/Veh versus Ket/Veh, $P = 0.794$). Data displayed as means ± SEM and individual data points, with significant Sidak corrected post-hoc comparisons indicated with an asterisk.

Reduced motivation by pathway inactivation of A46 to A32 is blocked by ketamine in A25

These data suggest that an interaction between A46 and A25 may contribute to motivated behaviors and their dysfunction. We thus explored their direct and indirect interaction through pathway-specific manipulations induced by infusions of DCZ (100 nM) into A46 neuron terminal regions through surgically implanted cannula into A25 (direct pathway) and ACC region area 32 (A32; indirect pathway) (postmortem cannula locations can be found in fig. S5). A25 receives relatively sparse projections from A46, whereas A32 receives projections from A46 into deep cortical layers and projects extensively into A25 across all layers (*28*, *29*). A32 has been proposed to form an indirect pathway by which A46, and dlPFC more broadly, may provide cognitive control over emotion through this serial pathway to A25 (*29*). Because A32 has a dorsal (A32) and ventral aspect (A32v), these were targeted separately (Fig. 2A) (*30*), with terminal fibers observed primarily within deeper layers, as were those in A25 (fig. S6). In the PR task, infusion of DCZ into A32 reduced the total responses made by the marmosets when compared with that by vehicle ($n = 6$ marmosets) (Fig. 2B), as well as when compared with DCZ infusion in A32v and A25, which themselves did not differ from vehicle. A similar reduction after A32 DCZ infusion was observed for the number of rewards received, whereas the response rates were not significantly affected though variable (fig. S7, A and B).

Having established the role of the pathway from A46 to A32, but not the direct pathway from A46 to A25, in appetitive motivated behavior, we subsequently assessed its functional interaction with A25. We determined whether ketamine could ameliorate the blunting of appetitive motivation induced this time by means of inactivation of the specific A46 to A32 pathway when infused into A25 (Fig. 2C). Infusion of ketamine into A25 (0.5 μg/μl, 24 hour pretreatment) blocked the ability of an intra-A32 DCZ infusion to reduce total responses in the PR task ($n = 4$ marmosets) (Fig. 2D), with DCZ still able to induce the deficit in responses after a saline infusion into A25. Ketamine infusion in A25 did not affect responses when administered alone. These effects also extended to the number of rewards received (fig. S7C), whereas no clear impact on response rate was observed for any treatment or pretreatment (fig. S7D).

A46 inactivation heightens marmoset's response to ambiguous threat through a pathway to ventral A32

We next assessed whether this A46 network was involved in marmosets' responsivity in threatening situations. Anxiety is highly comorbid with depression, and dlPFC TMS improves comorbid anxiety symptoms (*5*, *7*). A25 overactivation in marmosets also heightens responsivity to threats (*25*). Using an unfamiliar human standing in front of the cage for 2 min as an ambiguous threat (Fig. 3A), we studied the effects of DCZ treatment on a range of behaviors, including the marmosets' cage position and vocalizations, which we combined into a threat reactivity score (fig. S8) (*31*). To account for individual variability, we calculated the difference in threat score between treatments for each marmoset. Systemic DCZ increased the marmosets' threat reactivity score (Fig. 3B), an effect driven by a reduction in movement around the cage (fig. S9A). We subsequently infused DCZ into A46 neuron terminals in A32, A32v, and A25. Only infusion of DCZ into A32v increased the threat score (Fig. 3C), whereas infusion into the more dorsal A32 and A25 had no effect. In this instance, the heightening of the threat score was driven more by a reduction in time spent at the front of the cage (fig. S9B).

Evidence of functional asymmetry in A46

We next wanted to establish whether functional specialization exists between hemispheres because typical neuromodulatory strategies for treatment-resistant depression are primarily unilateral (*32*). With a separate cohort of marmosets with intracerebral cannulae targeting A46 ($n = 7$ marmosets), we determined whether hemispheric differences were observed after unilateral and bilateral pharmacological inactivation of A46 through intracerebral infusion of γ-aminobutyric acid type A/B ($\text{GABA}_{\text{A/B}}$) receptor agonists muscimol and baclofen (MB) directly into A46. Infusions of MB into both left and bilateral A46 increased the threat score on the human intruder test, whereas right A46 infusion had no effect (Fig. 4A and fig. S10). These findings not only replicated the chemogenetic inactivation of A46 but also indicated functional lateralization. We subsequently determined whether this extended to the established A46 pathways mediating threat and reward processes (to

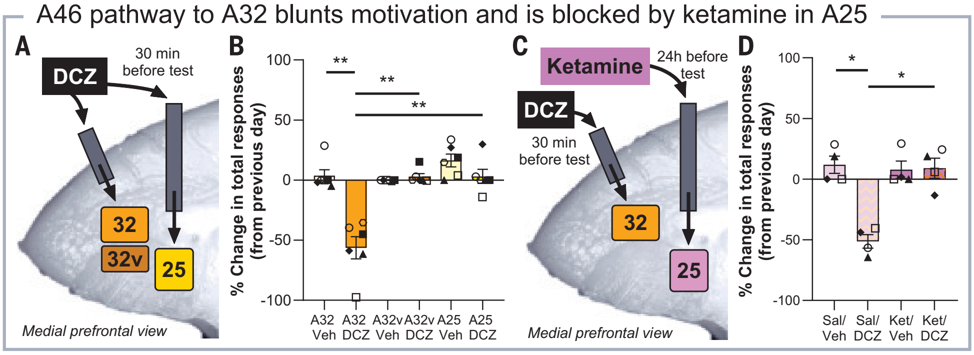

Fig. 2. Inactivation of an A46 to A32 pathway reduces appetitive motivation with this effect blocked by a ketamine infusion in A25. (**A**) Schematic of A46 terminal pathway manipulations through DCZ infusion (100 nM) in A32, A32v, or A25 of the marmoset. (**B**) DCZ infusion into A32 reduced the total responses marmosets made in comparison with the previous day, with DCZ into A32v and A25 showing no effect ($n = 6$ marmosets, rmANOVA, region × treatment interaction, $F_{(1.73, 8.63)} = 33.17$, $P < 0.001$, $\eta^2 = 0.869$; post hoc: A32 Veh versus DCZ, $P = 0.001$, $d = 2.77$; A32 DCZ versus A32v DCZ, $P = 0.003$, $d = 2.78$; A32 DCZ versus A25 DCZ, $P = 0.004$, $d = 2.65$). (**C**) Schematic for assessing A25's involvement in A46 to A32 pathway induced motivational deficits through A25 ketamine infusion. (**D**) Intra-A25 ketamine infusion blocked the ability of an A32 DCZ infusion from reducing responses ($n = 4$ marmosets, rmANOVA, pretreat × treat interaction, $F_{(1,3)} = 15.31$, $P = 0.030$, $\eta^2 = 0.836$; post hoc: Sal/Veh versus Sal/DCZ, $P = 0.014$, $d = 2.60$; Sal/DCZ versus Ket/DCZ, $P = 0.019$, $d = 2.32$; Sal/Veh versus Ket/Veh, $P = 0.461$). Data are displayed as mean ± SEM, and individual data points with significant Sidak corrected post-hoc comparisons are indicated with an asterisk.

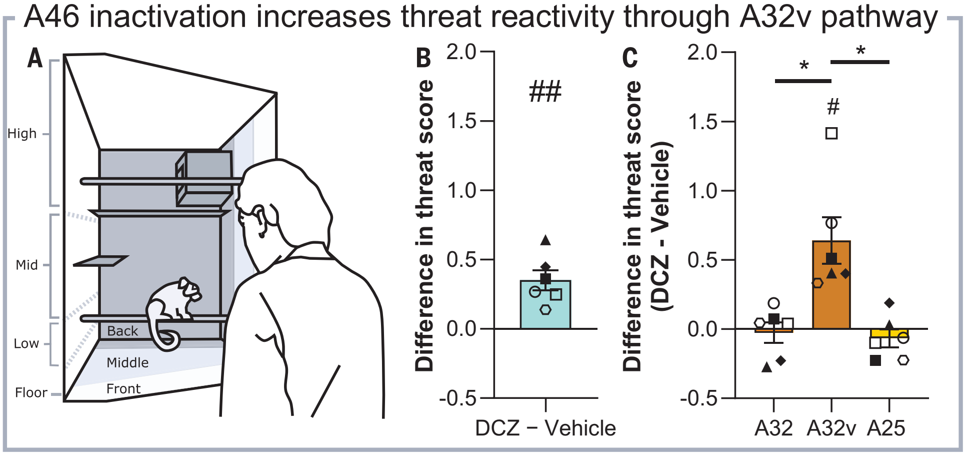

Fig. 3. Chemogenetic inactivation of A46 heightens responsivity to ambiguous threat through projections to ventral A32. (**A**) Schematic of the human intruder paradigm setup where an unfamiliar human maintains eye contact with a marmoset for 2 min. A difference score between treatments was used for each marmoset to account for individual variability ($n = 6$ marmosets). (**B**) DCZ treatment (10 μg/kg, intramuscularly) increased the threat score compared with vehicle treatment (one sample t test versus 0, $P = 0.005$, $d = 1.98$). (**C**) DCZ infusion into A32v alone heightened the threat score when compared with vehicle infusion, and also when compared with the effects of A32 and A25 DCZ infusion (rmANOVA, region effect, $F_{(1.7, 8.5)} = 12.52$, $P = 0.004$; post hoc, A32 versus A32v, $P = 0.022$, A32v versus A25, $P = 0.039$; A32v versus 0, $P = 0.012$, $d = 1.56$). Data are displayed as means ± SEM; individual data points with significant Sidak corrected pairwise comparisons are indicated with an asterisk, and one sampled t test versus hypothetical mean of 0 is indicated with a pound sign.

A32v and A32, respectively). DCZ infusion into left A32v heightened the threat score when compared with DCZ infusion into right A32v (Fig. 4B), whereas DCZ infusion into both left and bilateral A32 (but not right A32) decreased total responses when compared with vehicle on the PR task (Fig. 4C). These effects on motivation extended to the number of rewards received, with the response rate unaffected (fig. S11).

To complement this data, we looked to establish whether lateral specialization is an inherent part of the functional organization of A46 in the marmoset brain. To do this, we studied the functional connectivity patterns of rs-fMRI data in awake marmosets from an open-access database (*33*) through k-means clustering analysis. When constrained to two clusters, A46 functional connectivity across all 20 subjects revealed a bilateral dorsal-ventral division that was consistent with its known architectonic parcellation (Fig. 4D). Increasing to four clusters revealed hemispheric lateralization: Left and right dorsal A46 segments formed distinct clusters [Fig. 4E, cluster 1 (green) versus cluster 2 (blue)]. These clusters showed similar ipsilateral connectivity but differed primarily in contralateral connectivity, being more pronounced in the right hemisphere. The top 30 regions showing this lateralization can be found in fig. S12 and do not include A25, A32, or A32v, suggesting that overall, broad A46 network dynamics underlie this lateralization. Cluster robustness was validated by means of voxelwise bootstrap resampling using half of the data each time ($n = 5000$ bootstrap iterations) (Fig. 4, D and E, bottom, strong yellow and white shading).

Discussion

A46 within the dlPFC forms a functional network with A32 and A25 for regulating positive and negative emotion–related processes in marmosets. Inactivation of A46 blunts appetitive motivation and heightens responsivity to uncertain threat, two behavioral phenotypes highly relevant to our understanding of anhedonia and anxiety in depression. This functional network uses separate A46 projections to dorsal and ventral A32 to regulate these emotion-related behaviors. Additionally, we highlight the important role of A25 within this network to ameliorate A46 inactivation-induced appetitive motivational deficits, acting as a putative site of action for the fast-acting antidepressant, ketamine. Moreover, we provide evidence of functional asymmetry because the global and pathway-specific effects of A46 inactivation are left but not right dependent. Together, these effects provide functional evidence for the hypothesized interaction between these regions (*29*, *34*).

The function of A46, and the dlPFC more generally, has been associated with maintaining an online representation of information that can be used to regulate many different behaviors and is highly sensitive to stress (*35*–*37*). In this work, we demonstrated that marmoset A46 is necessary for maintaining an escalating amount of effort to acquire rewards while not directly being involved in the hedonic value of rewarding substances themselves. These findings are in agreement with the correlatory evidence that dlPFC activity in humans represents both cognitive and physical effort during decision-making (*38*) and that dlPFC

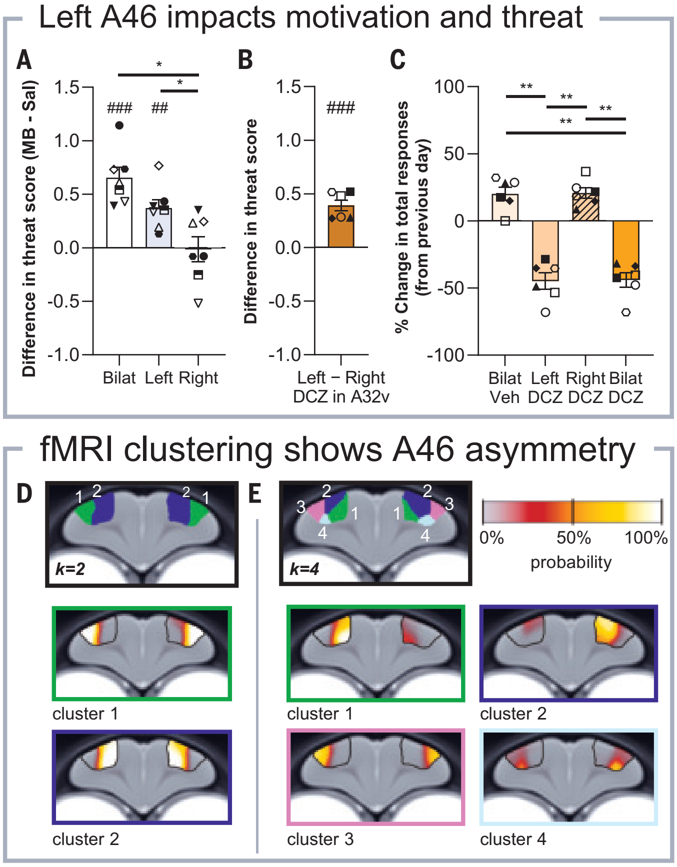

Fig. 4. Causal evidence for functional asymmetry across A46 hemispheres through unilateral behavioral analysis and correlatory evidence from resting-state functional connectivity clustering. (**A**) Bilateral and left A46 inactivation by means of MB infusion enhanced responsivity to threat, whereas right A46 inactivation had no effect (rmANOVA, region effect, $F_{(1.8, 10.7)} = 13.5$, $P = 0.0014$; post hoc, Bilat versus Right, $P = 0.013$; Left versus Right, $P = 0.041$). (**B**) DCZ infusion into left A32v increased threat responsivity when compared with right A32v (one sampled t test versus 0, $P = 0.008$). (**C**) Left and bilateral A32 DCZ infusions reduced responses in the PR task, with right DCZ infusion having no effect (rmANOVA, region effect, $F_{(2.9, 14.3)} = 42.8$, $P < 0.001$; post hoc, Bilat Veh versus Left DCZ, $P = 0.003$; Bilat Veh versus DCZ, $P = 0.004$; Left versus Right DCZ, $P = 0.003$; Right versus Bilat DCZ, $P = 0.002$). (**D**) k-means clustering of A46 resting-state functional connectivity data in 20 subjects, with $k = 2$ indicating separate bilateral clusters that align with architectonically defined ventral (green) and dorsal A46 (blue) with high confidence (yellow and white on probability color bar), revealed with clustering probability obtained from bootstrap resampling. (**E**) $k = 4$ clustering exposes A46 connectivity differences between predominantly right (green) and left (blue) hemispheres with high confidence. Black outline indicates A46. Behavioral data are displayed as means ± SEM and individual data points.

neurons in macaque monkeys encode motivational variables, with increasing activity during lower value trials—the latter hypothesized to increase tolerance for periods of reduced reward (*39*). Moreover, they appear consistent with the blunting of cognitive effort that humans were willing to exert after dlPFC dysfunction induced by noninvasive stimulation (*40*). Thus, the current deficit may be due to impaired integration of effort and reward value in the PR task resulting in an intolerance for the escalating effort cost for each reward. That said, the PR data shown here cannot directly parse the discussed motivational deficit from an increased intolerance for the delay in reward or enhanced fatigue.

The dlPFC, and A46 by extension, has also been associated with the cognitive regulation of negative emotional responses, in which it acts to appraise or reappraise uncertain threat (*41*) or suppress episodic recall and affective content (*42*). Reduction of this top-down cognitive control from A46, induced by either pharmacological or chemogenetic inactivation, likely impaired the marmosets' ability to appropriately appraise the uncertain threat context or adequately suppress threat-related circuits from altering their behavioral strategy, resulting in intolerance to the uncertain threat of the human intruder and a heightened response (*31*).

That A46 inactivation induced both anhedonia-like and anxiety-like effects raises the question as to whether these two phenotypes are related. The dlPFC is active during approach-avoidance tasks in humans that involve conflict between reward and threat (*43*), with decreased activity correlated with anhedonia in individuals with depression (*44*). Nonetheless, our current findings reveal these phenotypes as doubly dissociable at the level of downstream pathways, highlighting their independence; the A46 pathway to A32 regulates appetitive motivation, whereas the A32v pathway regulates responsivity to threats. A32v is a relatively small and understudied structure in marmosets, with prior data suggesting the involvement of dorsal A32 in regulating negative affect (*45*, *46*); thus, further characterization of this region will be required in the future. In macaque monkeys, a similar ventral but not dorsal region of A32 was observed to be selectively involved in generating avoidant behavior, an effect that was ameliorated with anxiolytic drug treatment (*47*). In humans and macaques, A32 has been identified as a connector hub, and our findings support the hypothesis that A32 is positioned to integrate the frontal cortex across distinct functional modalities, including the mediation of cognitive control over emotion (*48*). Afferents from A46 to A32 have been identified as predominantly feedforward, with neurons in the superficial layers of A46 projecting primarily to the deep layers of A32 (*29*). Comparative analysis of A32 terminals on excitatory and inhibitory neurons of all layers of A25 suggests that A32 may have a primarily inhibitory impact on A25, mediating the link between the cognitive control functions of A46 with emotion processing in A25 (*29*).

The exact circuits underpinning treatment efficacy of dlPFC neuromodulation are still being established despite their clinical use for depression for more than 15 years (*5*, *6*). However, repetitive TMS (rTMS) treatment efficacy across dlPFC sites is primarily observed for those areas anticorrelated with scACC activity, including A25 (*27*). We have demonstrated that direct ketamine infusion into A25 produced long-term changes that blocked the appetitive motivational deficits arising from A46 inactivation, an interaction likely mediated through A32, which is consistent with this region's major interconnectivity with both A46 and A25 in macaques (*29*) and aligning with marmoset connectivity data (*49*). Marmoset and macaque studies have reported, respectively, reduced activity or functional connectivity in A46 after A25 overactivation, which further illustrates this functional interaction (*26*, *50*). The underlying mechanism by which ketamine within A25 has its ameliorative effects is currently unclear, although ketamine can drive long-term spinogenesis in ventromedial prefrontal regions in rodents (*51*). Given that overactivation of A25 can mediate different components of anhedonia-like behavior in marmosets and produce an overall aversive affective state (*25*, *34*), the ability of ketamine to alter A25's downstream response to A46 inactivation may be the mechanism of this ameliorative process. Although this would be consistent with A25 acting as a downstream effector of the hierarchical pathway from A46, through A32, nevertheless it cannot be ruled out that A25 acts instead as a more general modulatory hub. Only future development of transsynaptic technologies will be able to functionally differentiate these possibilities.

Asymmetry has been observed not only in the functions of human dlPFC but also their dysfunction in disorders such as depression. This has resulted in neuromodulatory strategies being hemisphere dependent, with left-sided rTMS the more established treatment option (*5*, *6*). We provide evidence for functional asymmetry within A46 of the marmoset dlPFC, shown both with pharmacological manipulation and chemogenetics as well as functional imaging in a larger independent cohort of marmosets. We have shown that reactivity to uncertain threat and appetitive motivation is governed selectively by the left hemisphere. Consistently, recent evidence implicates appetitive motivation in humans with left dlPFC (*52*) and improvements in effortful motivation in depressed individuals by left dlPFC rTMS (*53*). Although we observed no particular behavioral process dependent on right A46 function here, rs-fMRI connectivity patterns nevertheless revealed overall greater cross-hemisphere connectivity in the right hemisphere, although the functional relevance of this remains to be determined. However, it is of interest that right dlPFC in humans is differentially activated during inhibitory control mechanisms, including that for emotional memories (*4*).

This study has identified a functional network for A46 within the left hemisphere that is involved in the regulation of positive and negative emotion–related behaviors in marmosets and provides insight into the mechanisms by which ketamine may act to ameliorate motivational anhedonia. These data provide a window onto the neurocircuitry within prefrontal and cingulate cortices that regulate emotion-related behaviors, providing a functional framework for understanding not only how dysfunction in A46, and the dlPFC more generally, can affect symptom-related behaviors in depression and anxiety but also how various treatment strategies may have their therapeutic action.

REFERENCES AND NOTES

1. X. Liu, M. T. Banich, B. L. Jacobson, J. L. Tanabe, *Cereb. Cortex* **16**, 827–834 (2006).
2. S. Bodovitz, *J. Theor. Biol.* **254**, 594–598 (2008).
3. A. F. T. Arnsten, M. J. Wang, C. D. Paspalas, *Neuron* **76**, 223–239 (2012).
4. M. C. Anderson, J. G. Bunce, H. Barbas, *Neurobiol. Learn. Mem.* **134** (Pt A), 145–161 (2016).
5. J. P. O'Reardon *et al.*, *Biol. Psychiatry* **62**, 1208–1216 (2007).
6. J. Mutz *et al.*, *BMJ* **364**, l1079 (2019).
7. L. K. White, W. Makhoul, M. Teferi, Y. I. Sheline, N. L. Balderston, *Neuropharmacology* **224**, 109355 (2023).
8. H. S. Mayberg *et al.*, *Neuron* **45**, 651–660 (2005).
9. W. C. Drevets, J. L. Price, M. L. Furey, *Brain Struct. Funct.* **213**, 93–118 (2008).
10. C. Hamani *et al.*, *Biol. Psychiatry* **69**, 301–308 (2011).
11. S. Alagapan *et al.*, *Nature* **622**, 130–138 (2023).
12. M. D. Fox, R. L. Buckner, M. P. White, M. D. Greicius, A. Pascual-Leone, *Biol. Psychiatry* **72**, 595–603 (2012).
13. S. Kito, T. Hasegawa, Y. Koga, *Brain Stimul.* **5**, 547–553 (2012).
14. M. Koenigs, J. Grafman, *Behav. Brain Res.* **201**, 239–243 (2009).
15. S. Grimm *et al.*, *Biol. Psychiatry* **63**, 369–376 (2008).
16. A. Golkar *et al.*, *PLOS ONE* **7**, e48107 (2012).
17. P. Kanske, J. Heissler, S. Schönfelder, A. Bongers, M. Wessa, *Cereb. Cortex* **21**, 1379–1388 (2011).
18. P. R. Goldin, K. McRae, W. Ramel, J. J. Gross, *Biol. Psychiatry* **63**, 577–586 (2008).
19. H. G. Engen, M. C. Anderson, *Trends Cogn. Sci.* **22**, 982–995 (2018).
20. M. T. Treadway, D. H. Zald, *Neurosci. Biobehav. Rev.* **35**, 537–555 (2011).
21. S. J. Rizvi, D. A. Pizzagalli, B. A. Sproule, S. H. Kennedy, *Neurosci. Biobehav. Rev.* **65**, 21–35 (2016).
22. B. N. Armbruster, X. Li, M. H. Pausch, S. Herlitze, B. L. Roth, *Proc. Natl. Acad. Sci. U.S.A.* **104**, 5163–5168 (2007).
23. Y. Nagai *et al.*, *Nat. Neurosci.* **23**, 1157–1167 (2020).
24. M. Husain, J. P. Roiser, *Nat. Rev. Neurosci.* **19**, 470–484 (2018).
25. L. Alexander *et al.*, *Neuron* **101**, 307–320.e6 (2019).
26. L. Alexander *et al.*, *Nat. Commun.* **11**, 5386 (2020).
27. A. Weigand *et al.*, *Biol. Psychiatry* **84**, 28–37 (2018).
28. M. K. P. Joyce, H. Barbas, *J. Neurosci.* **38**, 1677–1698 (2018).
29. M. K. P. Joyce, M. Á. García-Cabezas, Y. J. John, H. Barbas, *J. Neurosci.* **40**, 8306–8328 (2020).
30. G. Paxinos, C. Watson, M. Petrides, M. Rosa, H. Tokuno, *The Marmoset Brain in Stereotaxic Coordinates* (Elsevier, 2012).
31. S. K. L. Quah, G. J. Cockcroft, L. McIver, A. M. Santangelo, A. C. Roberts, *Front. Behav. Neurosci.* **14**, 34 (2020).
32. J. Downar, S. H. Siddiqi, A. Mitra, N. Williams, C. Liston, *Curr. Top. Behav. Neurosci.* **66**, 233–277 (2024).
33. D. J. Schaeffer *et al.*, *Neuroimage* **252**, 119030 (2022).
34. A. F. T. Arnsten, M. K. P. Joyce, A. C. Roberts, *Neurosci. Biobehav. Rev.* **145**, 105000 (2023).
35. J. D. Wallis, E. K. Miller, *Eur. J. Neurosci.* **18**, 2069–2081 (2003).
36. A. Etkin, C. Büchel, J. J. Gross, *Nat. Rev. Neurosci.* **16**, 693–700 (2015).
37. M. K. P. Joyce, S. Uchendu, A. F. T. Arnsten, *Biol. Psychiatry* **97**, 359–371 (2025).
38. T. T. J. Chong *et al.*, *PLOS Biol.* **15**, e1002598 (2017).
39. K. Amemori, S. Amemori, A. M. Graybiel, *J. Neurosci.* **35**, 1939–1953 (2015).
40. A. Soutschek, P. N. Tobler, *Hum. Brain Mapp.* **41**, 4630–4640 (2020).
41. K. N. Ochsner *et al.*, *Neuroimage* **23**, 483–499 (2004).
42. M. C. Anderson, S. B. Floresco, *Neuropsychopharmacology* **47**, 180–195 (2022).
43. R. L. Aupperle, A. J. Melrose, A. Francisco, M. P. Paulus, M. B. Stein, *Hum. Brain Mapp.* **36**, 449–462 (2015).
44. M. Ironside *et al.*, *Biol. Psychiatry* **87**, 399–408 (2020).
45. C. U. Wallis, R. N. Cardinal, L. Alexander, A. C. Roberts, H. F. Clarke, *Proc. Natl. Acad. Sci. U.S.A.* **114**, E4075–E4084 (2017).
46. C. U. Wallis, G. J. Cockcroft, R. N. Cardinal, A. C. Roberts, H. F. Clarke, *Cereb. Cortex* **29**, 4818–4830 (2019).
47. K. Amemori, A. M. Graybiel, *Nat. Neurosci.* **15**, 776–785 (2012).
48. W. Tang *et al.*, *eLife* **8**, e43761 (2019).
49. H. Skibbe *et al.*, *PLOS Biol.* **21**, e3002158 (2023).
50. S. Amemori, A. M. Graybiel, K. I. Amemori, *Nat. Commun.* **15**, 4201 (2024).
51. R. N. Moda-Sava *et al.*, *Science* **364**, eaat8078 (2019).
52. D. A. Pizzagalli, R. J. Sherwood, J. B. Henriques, R. J. Davidson, *Psychol. Sci.* **16**, 805–813 (2005).
53. R. Bi *et al.*, *J. Affect. Disord.* **356**, 414–423 (2024).
54. C. M. Wood, X. Zhang, S. J. Sawiak, A. C. Roberts, Dysfunction in primate dorsolateral prefrontal area 46 impacts motivation and anxiety. *Mendeley Data* (2025); https://doi.org/10.17632/7p2h8pktdk.1.

ACKNOWLEDGMENTS

We thank members of the Roberts lab for their support in conducting the research. We thank the Cambridge University Biological Services staff for their unwavering support and care for the marmosets. **Funding:** This research was funded in whole or in part by a Wellcome Trust Investigator award (224432/Z/21/Z) to A.C.R. and a UKRI Medical Research Council Programme grant (MR/V033492/1) to A.C.R. **Author contributions:** Conceptualization: R.B.T. led in involvement of dlPFC and its asymmetrical function in emotion regulation, and A.C.R. and C.M.W. led in the chemogenetic interrogation of dlPFC pathway in emotion regulation and treatment responsivity. Data curation: C.M.W., R.B.T., M.F., X.Z., N.L., A.C.R. Formal analysis: C.M.W., R.B.T., X.Z., S.J.S., A.C.R. Funding acquisition: A.C.R. Investigation: C.M.W., R.B.T., M.F., X.Z., K.G.M., N.L., G.J.C., L.B.M., A.C.R. Methodology: C.M.W., R.B.T., X.Z., S.J.S., A.C.R. Project administration: C.M.W., A.C.R. Resources: S.J.S., A.C.R. Software: C.M.W., R.B.T., X.Z., S.J.S. Supervision: C.M.W., S.J.S., A.C.R. Validation: C.M.W., A.C.R. Visualization: C.M.W., R.B.T., M.F., X.Z., S.J.S. Writing – original draft: C.M.W., R.B.T., A.C.R. Writing – review & editing: C.M.W., R.B.T., A.C.R., M.F., X.Z., K.G.M., N.L., S.J.S. **Competing interests:** The authors declare they have no competing interests. **Data and materials availability:** All data and connectivity analysis code are available in the main text and supplementary materials or are deposited at (*54*). Raw rs-fMRI connectivity data can be found at https://www.marmosetbrainconnectome.org/download.html. Viral construct containing hM4Di was acquired from VectorBuilder (vector information found at https://en.vectorbuilder.com/vector/VB221010-1182nft.html).

SUPPLEMENTARY MATERIALS

science.org/doi/10.1126/science.adx4142
Materials and Methods; Tables S1 to S2; Figs. S1 to S12; References (*55*–*65*);
MDAR Reproducibility Checklist; Data S1

Submitted 20 March 2025; accepted 23 June 2025

10.1126/science.adx4142

Overcoming energy disorder for cavity-enabled energy transfer in vibrational polaritons

Guoxin Yin[1]†, Tianlin Liu[2]*†, Lizhu Zhang[3], Tianyu Sheng[2], Haochuan Mao[2], Wei Xiong[1,2]*

Energy disorder is ubiquitous in chemistry and physics. It can suppress polariton delocalization by disrupting molecular coherence–limiting polariton-modified properties. We investigated how energy disorders affect vibrational polariton dynamics by probing ultrafast dynamics in 2,6-di-*tert*-butylphenol in liquids (inhomogeneous) and solids (homogeneous) using two-dimensional infrared spectroscopy and molecular dynamics simulations. In liquids, energy disorder disrupted delocalization, preventing vibrational energy transfer. By contrast, with reduced inhomogeneity, vibrational strong coupling in solids restored delocalization and enabled energy transfer. We established a stringent delocalization criterion, requiring collective coupling strengths exceeding three times inhomogeneous linewidths to sustain polariton coherence. This finding highlights energy disorder's detrimental effects and outlines strategies to overcome localization—either by minimizing disorder through chemical control or by achieving sufficient couplings using advanced photonic structures.

Vibrational polaritons are formed through strong coupling between resonant molecular vibrational modes and photonic modes (*1*–*3*). The vibrational strong coupling (VSC) is claimed when the light-matter coupling strength (characterized by the Rabi splitting, Ω_R) exceeds the dissipation rates of uncoupled molecular vibrations and cavity modes (*4*). VSC is typically established under collective coupling conditions ($g_0\sqrt{N}$, where g_0 is the single-molecule dipole coupling strength) involving a large number of molecular oscillators on the order of $N = 10^{10}$ (*1*). In the past decade, extensive experiments have demonstrated that polaritons can modify ground-state chemical reactivity (*5*–*8*), mediate energy transfer (*9*–*12*), and manipulate material properties (*13*–*17*), many of which were achieved in liquids or solids where vibrational transition energy disorder exists.

However, the role of energy disorder in polaritons, manifested as the inhomogeneous broadening in spectroscopy, has been largely neglected because polariton spectra remain intact if VSC criteria are met (*18*). Recently, theoretical studies have suggested that inhomogeneous systems may undergo similar dynamics inside and outside optical cavities (*19*–*23*), and a few null experimental results have been reported in systems with large inhomogeneity (*24*). A theoretical study by our group demonstrated that polariton delocalization is extremely susceptible to inhomogeneity and can only be sustained when the Rabi splitting exceeds three times the inhomogeneous linewidth (referred to as delocalization criterion hereafter), much more stringent than conventional VSC criteria (*25*). However, systematic experimental investigations are still lacking to resolve the impact of inhomogeneity on polariton-enabled dynamics.

Cavity-enabled energy transfer is a phenomenon that has been observed in both inter- and intramolecular schemes among several polaritonic systems (*10*–*12*, *26*, *27*). Notably, the vibrational energy transfer (VET) has only been demonstrated in highly homogeneous systems (*10*, *12*). Theoretically, Cao attributed the coherent cavity-enhanced energy transfer to delocalized polariton wave functions (*28*). Hence, inhomogeneity is expected to exert a large detrimental effect on delocalization (*21*) and, consequently, energy transfer. In this study, combining two-dimensional infrared spectroscopy (2D IR) (*29*–*31*) and molecular dynamics (MD) simulations, we studied the effect of the inhomogeneous broadening on polariton dynamics—specifically, the ultrafast energy transfer and conformational exchange. Crucially, we experimentally verified that the delocalization criterion is critical to overcome energy disorder and to restore energy transfer.

Results

We studied deuterated 2,6-di-*tert*-butylphenol (DTBP) (Fig. 1A), a phenol derivative with ultrafast conformational exchange dynamics that have been extensively investigated using 2D IR (*30*). Notably, this compound can form a crystalline solid close to the homogeneous limit (Fig. 1B), and its saturated dodecane solutions (liquid) represent the inhomogeneous limit owing to various hydrogen-bond (H-bond) interactions (Fig. 1C). Furthermore, the compound can either undergo conformation switches by H-bond dissociation and association or VET (Fig. 1, D and E). Thus, it provides an ideal test bed to understand how inhomogeneous broadening influences polariton-modified dynamics (Fig. 1F).

Ultrafast dynamics in liquids

To start with, we studied dynamics of deuterated DTBP in dodecane solutions (Fig. 2A). We observed a free DTBP peak (F) at 2691 cm^{-1} and a red-shifted complex (C) peak at 2680 cm^{-1} (Fig. 2B, top) using Fourier transform infrared spectroscopy (FTIR) (supplementary materials, sections S3.2 and S8.2.1). The spectral shift due to the H bond in complexes makes the OD stretch mode a sensitive probe of the two conformations. Using 2D IR (*32*), we quantified that the OD stretch of free DTBP has a 10 cm^{-1} inhomogeneous linewidth and a 6 cm^{-1} homogeneous linewidth, whereas the complex peak is characterized by 15 cm^{-1} and 8 cm^{-1}, respectively (section S4.2), both of which are inhomogeneously broadened as a result of H-bond interactions.

We then measured the time evolution of OD frequencies using 2D IR at the magic angle (*32*) and analyzed the 1-2 transition signals (positive ΔA) at 2570 to 2600 cm^{-1}, which are separated from the 0-1 transition by a ~100 cm^{-1} anharmonicity. At a waiting time (t_2) of 11 ps (Fig. 2C), we observed two diagonal peaks, (F,F) at 2597 cm^{-1} and (C,C) at 2583 cm^{-1}, from free and complexes; furthermore, two off-diagonal peaks, (F,C) and (C,F), arise from the ultrafast conformational switch. The diagonal peak volumes monotonically decrease with time, and the exchange peaks grow for ~1 ps and decay afterward. Fitting the dynamics of the (F,F) diagonal peak and the (F,C) off-diagonal peak (colored lines in Fig. 2D) yields the same time constants as fitting the (C,C) and (C,F) peaks (fig. S22), which suggests that the system remains at equilibrium under 2D IR measurements (*30*, *31*). On the basis of the kinetic model illustrated in Fig. 2A and detailed in section S7.2, we determined an F → C rate (k_{fc}) of 0.29 ± 0.06 ps^{-1} and a C → F rate (k_{cf}) of 0.95 ± 0.19 ps^{-1} at a deuteration level of 67% based on the equilibrium constant $K_{eq} = [F]/[C] = 3.25$ (section S4.2) (*33*). Additional measurements at a lower deuteration level (34%) result in similar exchanges rates ($k_{fc} = 0.27 \pm 0.02$ ps^{-1} and $k_{cf} = 0.87 \pm 0.08$ ps^{-1}; gray lines in Fig. 2D). These results reassure us that exchange peaks result from conformational switch rather than Förster resonance energy transfer (FRET) because the latter strongly depends on distances between deuterated species and is expected to rapidly decelerate at reduced deuteration levels (*34*, *35*).

Next, we measured the exchange rates under VSC (*36*). The liquid-phase DTBP was placed inside a Fabry–Pérot cavity of ~24-µm thickness. The transmission spectrum (Fig. 2B, middle) shows the lower polariton (LP) and upper polariton (UP) peaks at 2670 cm^{-1} and 2709 cm^{-1},

---

[1] Program in Materials Science and Engineering, University of California San Diego, La Jolla, CA, USA. [2] Department of Chemistry and Biochemistry, University of California San Diego, La Jolla, CA, USA. [3] Department of Chemistry, University of Pennsylvania, Philadelphia, PA, USA. ***Corresponding author. Email: w2xiong@ucsd.edu (W.X.); til073@ucsd.edu (T.L.)**
†These authors contributed equally to this work.

respectively, yielding $\Omega_R = 39\ \mathrm{cm}^{-1}$ that exceeds linewidths of both vibrational modes (complex, $19\ \mathrm{cm}^{-1}$; free, $14\ \mathrm{cm}^{-1}$) and the cavity mode (~$8\ \mathrm{cm}^{-1}$), satisfying VSC requirements. Weighted by the Hopfield coefficients of light and matter, the polariton lifetime is estimated to be ~1.4 ps and is considered in the dynamic analysis (sections S7.3 and S7.4). Upon pumping the UP (2700 to $2720\ \mathrm{cm}^{-1}$), a double derivative–shaped pump-probe signal was observed (Fig. 2B, bottom), attributed to the Rabi splitting contraction as a result of decreased ground-state population (*37*, *38*). Notably, the signal near the LP due to the excited-state absorption of dark modes, commonly observed in other polariton systems (*38*, *39*), is absent because of the large anharmonic shift of OD stretch modes.

To extract dynamics inside the cavity, we used the transfer matrix method (TMM) (section S6) (*40*) to fit both linear and pump-probe spectra. However, negligible rate alteration was observed. The reduced ground-state population (negative ΔA) of free molecules (Fig. 2E, blue) which are predominantly excited through the UP, monotonically decreases with time. Meanwhile, the dynamics of complex (Fig. 2E, orange) rise within the first 1 ps and decay afterward as a result of the F↔C exchange (section S7.1). We extracted the exchange rates as $k_{fc} = 0.28 \pm 0.03\ \mathrm{ps}^{-1}$ and $k_{cf} = 0.91 \pm 0.11\ \mathrm{ps}^{-1}$, which show negligible modification under VSC compared with outside-cavity rates. Similar rates were measured when the LP was excited (gray dotted lines in Fig. 2E). Overall, at $\Omega_R = 39\ \mathrm{cm}^{-1}$, the average exchange rates are $k_{fc} = 0.28 \pm 0.04\ \mathrm{ps}^{-1}$ and $k_{cf} = 0.91 \pm 0.14\ \mathrm{ps}^{-1}$. Additionally, exchange dynamics were investigated at three other Rabi splittings between 25 and $45\ \mathrm{cm}^{-1}$ (Fig. 2F); however, no dynamics were modified regardless of the coupling strength.

To interpret these null results, we placed the inhomogeneous linewidths of OD stretches on a delocalization map (Fig. 2G and section S9.1) with respect to coupling strengths $\left(2g_0\sqrt{N}\right)$ of the free and complex species. This map describes the delocalization as a function of full width at half maximum of inhomogeneous broadening ($\mathrm{FWHM}_{\mathrm{inhomo}}$) and coupling strengths, using the normalized inverse participation ratio (nIPR = 0 to 1, representing localization and delocalization limits) as a metric of delocalization (*23*, *25*). According to the map, none of the liquid-phase VSC systems are coupled strong enough to suppress the polariton localization (e.g., $\mathrm{nIPR}_{\mathrm{LP}} = 0.01$ and $\mathrm{nIPR}_{\mathrm{UP}} = 0.20$ at $\Omega_R = 39\ \mathrm{cm}^{-1}$) because of inhomogeneous broadening. Notably, at $\Omega_R = 45\ \mathrm{cm}^{-1}$, although free species gain moderate delocalization through polaritons, complex remains localized, resulting in no rate modification, consistent with Cao's prediction that delocalization of both energy donors and acceptors (i.e., complex and free) is the key driving force of polariton-mediated VET (*28*). Therefore, we hypothesize that these null results originate from the large energy disorder in liquids, which fails the delocalization criterion.

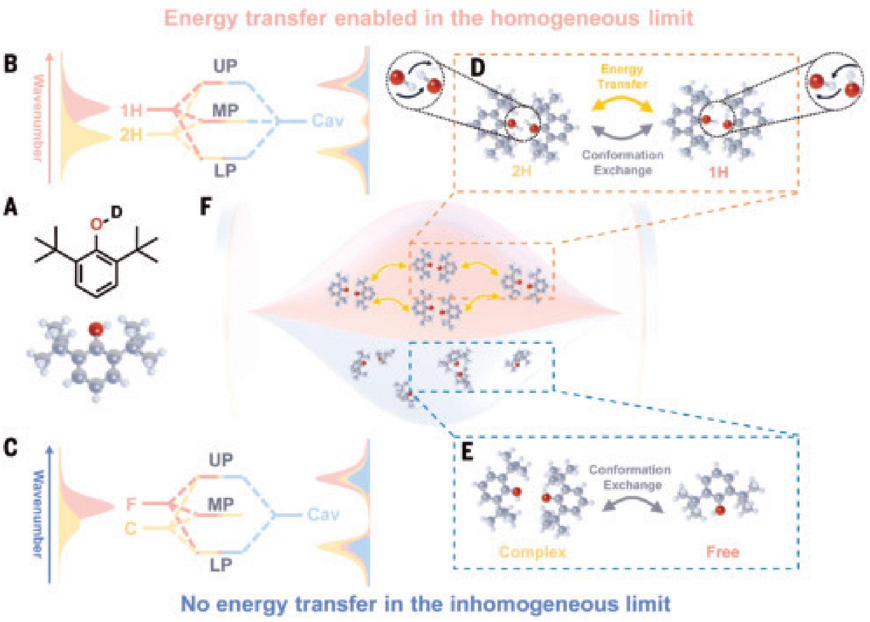

Fig. 1. Schematics of DTBP polariton dynamics at inhomogeneous and homogeneous limits. (**A**) The chemical structure of DTBP. (**B** and **C**) Crystalline solids (homogeneous limit) (B) or dodecane solutions (inhomogeneous limit) (C) form polaritons under VSC. The resultant UP, LP, and MP have primary contributions from 1H (or F) and the cavity, 2H (or C) and the cavity, and both molecular modes for the solid and solution samples, respectively. (**D** to **F**) Reduced inhomogeneity of solids enables additional polariton-enabled VET pathways along with the conformational exchange dynamics (D), whereas there is only conformation exchange dynamics in the liquid sample (E). This contrast highlights the detrimental effect of disorder on liquid-phase DTBP polariton-mediated dynamics.

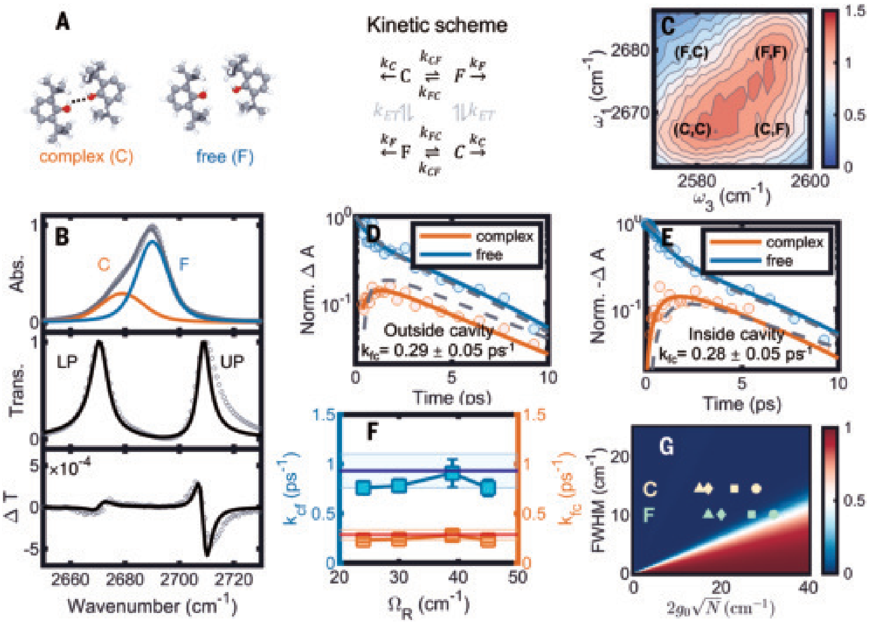

Fig. 2. Ultrafast dynamics in liquids. (**A**) Molecular structures of complex and free species. The kinetic model includes conformational switch (k_{cf}, k_{fc}), energy transfer (k_{ET}), and vibrational relaxation (k_c, k_f). (**B**) (Top) FTIR of the DTBP solution. The transmission (middle) and transient (bottom) spectra of polaritons ($\Omega_R = 39\ \mathrm{cm}^{-1}$) upon pumping the UP. Open circles indicate raw data, and solid lines indicate fits. (**C** and **D**) The 2D IR (C) at the 1-2 transition region, $t_2 = 11$ ps, and extracted outside-cavity exchange dynamics (D) of 67% (colored) and 34% (gray) deuterated samples. Deuteration level does not affect rates ($k_{fc} = 0.29 \pm 0.05\ \mathrm{ps}^{-1}$). (**E**) The inside cavity ($\Omega_R = 39\ \mathrm{cm}^{-1}$) exchange dynamics by pumping the UP (colored) and LP (gray). Different initial excited polariton states yield the same rate $k_{fc} = 0.28 \pm 0.05\ \mathrm{ps}^{-1}$. (**F**) Comparisons between outside (blue and red lines with uncertainty shadings) and inside (squares with error bars) rates show no significant difference. Error bars represent ±1 standard deviation. (**G**) The delocalization map shows localized polaritons. Inhomogeneous linewidths of complex (yellow, $14.5\ \mathrm{cm}^{-1}$) and free (green, $10.1\ \mathrm{cm}^{-1}$) are plotted against their light-matter coupling strengths $\left(2g_0\sqrt{N}\right)$. Overall Rabi splittings: triangle = $25\ \mathrm{cm}^{-1}$, diamond = $30\ \mathrm{cm}^{-1}$, square = $39\ \mathrm{cm}^{-1}$, and circle = $45\ \mathrm{cm}^{-1}$.

Ultrafast dynamics in solids

To test this hypothesis, we turned to the solid-phase DTBP, which has smaller inhomogeneous linewidths. The solid-phase samples are crystals with a grain size of ~50 μm (fig. S1), comparable to our probe beam size. MD simulations (section S8.2.1) suggest that DTBP pairs are building blocks of the crystal that have two conformations (Fig. 3A): a doubly H-bonded form (2H) and a singly H-bonded form (1H). These two conformations are readily distinguishable in the FTIR spectrum (Fig. 3B, top), with OD stretch modes at 2674 cm^{-1} for 2H and 2689 cm^{-1} for 1H (sections S3.1 and S8.2.2). The linewidths are visibly narrower than those in liquids. Indeed, we confirmed with 2D IR that 2H is associated with a 5 cm^{-1} inhomogeneous linewidth and a 6 cm^{-1} homogeneous linewidth, and the corresponding linewidths for 1H are 7 and 8 cm^{-1}, respectively. In addition, the equilibrium constant is determined as $K_{\mathrm{eq}} = [2\mathrm{H}]/[1\mathrm{H}] = 1.03$ (section S4.1).

Outside the cavity, conformational switch-induced off-diagonal peaks are evident at $t_2 = 11$ ps (Fig. 3C). Upon narrow-band pumping 2H (*41*), exchange rates ($k_{\mathrm{ex}} = k_{1\mathrm{H},2\mathrm{H}} = k_{2\mathrm{H},1\mathrm{H}}$) were measured to be 0.16 ± 0.02 ps^{-1} at the 67% deuteration level. Similarly, reducing the deuteration level (43%) did not alter exchange rates (gray dashed lines in Fig. 3D), indicating that conformational exchange is still predominant, with no apparent VET between the two conformers. This is corroborated by nonzero longtime anisotropy values that depend on crystal orientations (Fig. 3F), reflecting a ~120° orientational change of OD during the switch between 1H and 2H conformations (section S8.2.5) (*42*).

Next, we investigated the dynamics under VSC conditions with $\Omega_R = 39$ cm^{-1}, exceeding the linewidths of OD stretch modes (~11 cm^{-1}) and the cavity mode (9 cm^{-1}). Similar to the liquid phase system, the polariton lifetime is ~1.4 ps. In addition to the LP and UP, a middle polariton (MP) peak is visible because of the small inhomogeneous linewidths (*10*, *12*). Under this condition, we observed that VSC accelerated exchange rates, markedly contrasting the null results in liquids. Upon excitation at the LP, the ground-state population bleach of 2H appears to decay faster (Fig. 3E) than its counterpart outside the cavity (Fig. 3D). Simultaneously, the 1H population exhibits a faster rise. Both dynamics indicate faster exchange. In fact, the extracted dynamics lead to a three-times-faster exchange rate of 0.52 ± 0.11 ps^{-1} compared with that outside the cavity.

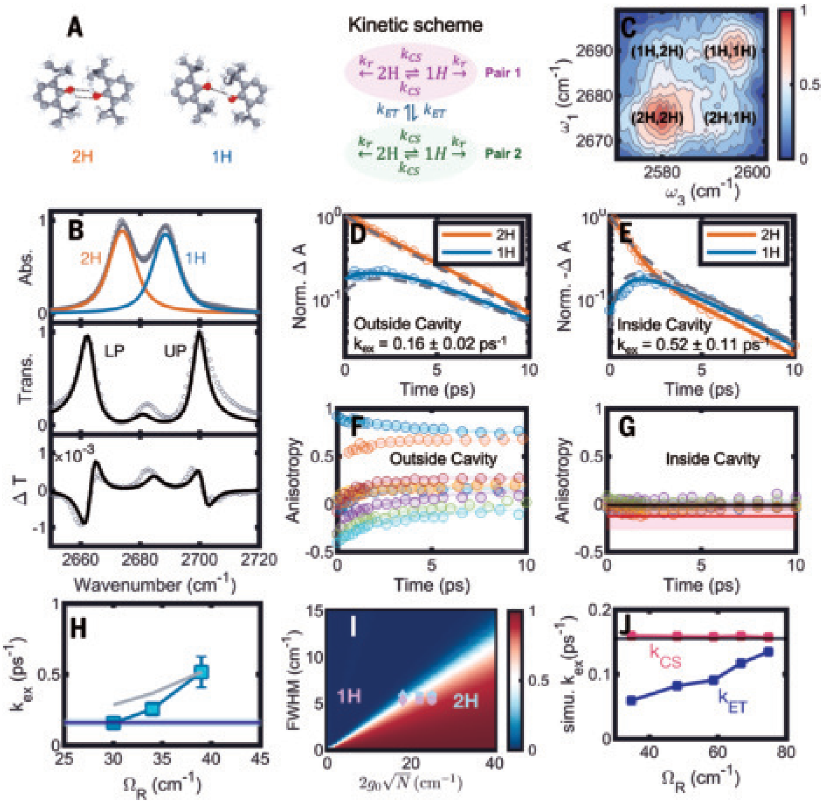

Fig. 3. Ultrafast dynamics in solids. (**A**) Molecular structures of the 2H and 1H conformations. The kinetic model includes conformation exchange (k_{CS}), energy transfer (k_{ET}), and vibrational relaxation (k_r). (**B**) (Top) FTIR spectrum of the solid DTBP. The transmission (middle) and transient (bottom) spectra of polaritons ($\Omega_R = 39$ cm^{-1}) upon pumping the LP. Raw data are indicated by open circles, and fits are indicated by solid lines. (**C** and **D**) The 2D IR (C) at the 1-2 transition, $t_2 = 11$ ps, and extracted outside-cavity exchange dynamics (D) of 67% (colored) and 43% (gray) deuterated samples. Different deuteration level yields the same $k_{\mathrm{ex}} = 0.16 \pm 0.02$ ps^{-1}. (**E**) The inside-cavity ($\Omega_R = 39$ cm^{-1}) exchange dynamics by pumping the LP (colored) and UP (gray) yield an average $k_{\mathrm{ex}} = 0.52 \pm 0.11$ ps^{-1}, which is three times faster than the outside-cavity rate. (**F**) The anisotropy outside the cavity due to conformational exchange depends on crystal orientations. (**G**) The anisotropy inside the cavity plateaus close to 0, reflecting energy transfer–induced orientational randomization of OD modes. The black line indicates the averaged integrated cross peak signals, and the red line indicates MD predictions. Different colors [(F) and (G)] represent different orientations. (**H**) Comparison between outside-cavity (blue line) and inside-cavity (blue squares) exchange rates, the latter increase with Rabi splittings. Error bars represent ±1 standard deviation. FRET prediction (gray) deviates from experiments. (**I**) The delocalization map confirms delocalized polaritons for the solid samples. The inhomogeneous linewidths of 2H (blue, 5.4 cm^{-1}) and 1H (pink, 5.9 cm^{-1}) are plotted against their light-matter coupling strengths $\left(2g_0\sqrt{N}\right)$. Overall Rabi splittings: diamond = 30 cm^{-1}, square = 34 cm^{-1}, and circle = 39 cm^{-1}. (**J**) Simulated outside-cavity (gray) and inside-cavity k_{CS} (pink) and inside-cavity k_{ET} (blue).

We used anisotropy measurements to identify the nature of this accelerated exchange. In contrast to outside-cavity results, the inside-cavity anisotropy remains close to 0 (Fig. 3G). This observation is also in sharp contrast to that of liquid samples, which starts from close to 0.4 and exponentially decays (fig. S15). This contrast suggests larger orientational randomization of OD modes compared with conformational exchange because energy transfer can occur between any 2H and 1H pairs at random locations (section S8.2.5). With different crystal orientations, we calculated energy transfer related anisotropies to plateau at −0.13 ± 0.13 (Fig. 3G, red line), agreeing well with our measurements of −0.01 ± 0.05 (Fig. 3G, black line). Thus, VSC enables an intermolecular VET channel, agreeing with previous studies (*10*, *12*).

Notably, the exchange rate exhibits a diminishing trend (Fig. 3H) with reduced coupling strengths, consistent with theoretical results based on an increased density-of-states argument (*43*). This trend can be qualitatively understood by placing the spectral parameters of the solid-phase VSC system on the delocalization map (Fig. 3I). Clearly, the new VET channel is opened when the polaritons are delocalized because the collective coupling strength is sufficient to overcome the effects of small inhomogeneity. For example, at $\Omega_R = 39$ cm^{-1}, the $\mathrm{nIPR}_{\mathrm{LP,UP}} = 0.54$, which is sufficiently large delocalization to drive cavity-enabled VET. Correspondingly, when $2g_0\sqrt{N}$ is reduced to ~30 cm^{-1}—i.e., ~3$\mathrm{FWHM}_{\mathrm{inhomo}}$—the polaritons become localized ($\mathrm{nIPR}_{\mathrm{LP,UP}} = 0.1$) and the VET becomes unmeasurable. Other disorders, such as dipole orientational disorder, reduce the collective coupling strength and Rabi splitting. However, the three-times criterion for delocalization remains valid, although the absolute number of delocalization size is reduced (section S9.2).

Complementary MD simulations support that the rate enhancement is due to the cavity-mediated VET. The calculated 2H→1H conformational exchange rate is 0.16 ps^{-1} outside the cavity (*44*), agreeing with our experimental results. Inside the cavity, polariton dynamics were simulated (Fig. 3I) using the CavMD method (*45*). However, the conformational exchange rates remain unchanged as $0.16 \pm 0.00(2)$ ps^{-1} (section S8.2.3). Next, energy transfer was investigated by sending an external pulse to interact with the LP for 1 ps (*46*). After the polariton pumping, energy is exchanged among the cavity photon and the OD stretch modes of the 1H and 2H species (section S8.2.4). The resultant 1H↔2H energy exchange rates monotonically increase from 0.06 ps^{-1} at $\Omega_R = 35$ cm^{-1} to 0.14 ps^{-1} at $\Omega_R = 75$ cm^{-1}. Simulated energy transfer rates are generally slower than experimental results; nevertheless, they exhibit a similar increasing trend at larger Rabi splittings. Notably, this trend aligns with predictions by the generalized resonant energy transfer theory (section S10) (*28*) and is consistent with a recent theoretical study on strongly coupled quantum dots (*47*). Although simulations indicate no modification in the conformational switch inside the cavity, future experiments under varying temperature and coupling conditions can clarify this further.

The observed new VET channel could also arise from FRET because by enhancing the collective coupling strength through increased deuteration, it decreases the effective distance between deuterated molecules and favors FRET. However, the measured deuteration level dependence deviates from FRET predictions (Fig. 3H), which highlights the distinctive nature of VSC-enabled VET. In fact, even the shortest hydroxyl distance between 2H and 1H (7 Å) exceeds the typical Förster radius of OD stretch modes (3 Å) (*35*). Therefore, by leveraging molecular coherence, this cavity-mediated VET overcomes distance limitations of FRET (*11*). Similar polariton-enabled energy transfer beyond FRET limits has also been reported in exciton-polariton systems (*27*, *48*).

Conclusions

By resolving ultrafast exchange dynamics of DTBP in liquid and solid forms under VSC, we showed that large inhomogeneous linewidths can diminish polariton delocalization and prevent rate modification. To overcome localization and restore cavity-enabled VET, a threefold, more stringent delocalization criterion needs to be met by either reducing energy disorder or enhancing coupling strengths. Given the prevalence of inhomogeneous broadening in molecular systems, the present study highlights the importance of enhanced cavity fields (e.g., plasmonic and photonic hotspots) and miniaturized cavity volume for future design of polariton systems to harness energy transfer and achieve chemical control. For rational design of polariton chemistry, reactions relying on VET are prime candidates because VSC may alter their pathways through influencing VET (*12*, *49*). It is noteworthy that entering ultrastrong coupling may be necessary to overcome energy disorder–led localization in many systems, necessitating theoretical methods beyond the Tavis-Cummings model, such as the Pauli-Fierz Hamiltonian. More broadly, the concept of using cavity fields to mitigate localization induced by energy disorder—or, generally speaking, defects—may extend well beyond chemistry, with implications for photophysics, photobiology, and materials science. Beyond energy transfer, other collective phenomena, such as polariton propagation, spatial coherences, and conductivity, could also be potential metrics of delocalization and benefit from the coherent delocalization enabled by polaritons.

REFERENCES AND NOTES

1. W. Xiong, *Acc. Chem. Res.* **56**, 776–786 (2023).
2. B. Xiang, W. Xiong, *Chem. Rev.* **124**, 2512–2552 (2024).
3. B. S. Simpkins, A. D. Dunkelberger, I. Vurgaftman, *Chem. Rev.* **123**, 5020–5048 (2023).
4. P. Törmä, W. L. Barnes, *Rep. Prog. Phys.* **78**, 013901 (2015).
5. A. Thomas *et al.*, *Science* **363**, 615–619 (2019).
6. W. Ahn, J. F. Triana, F. Recabal, F. Herrera, B. S. Simpkins, *Science* **380**, 1165–1168 (2023).
7. A. Thomas *et al.*, *Angew. Chem. Int. Ed.* **55**, 11462–11466 (2016).
8. K. Nagarajan, A. Thomas, T. W. Ebbesen, *J. Am. Chem. Soc.* **143**, 16877–16889 (2021).
9. A. D. Dunkelberger, B. T. Spann, K. P. Fears, B. S. Simpkins, J. C. Owrutsky, *Nat. Commun.* **7**, 13504 (2016).
10. B. Xiang *et al.*, *Science* **368**, 665–667 (2020).
11. X. Zhong *et al.*, *Angew. Chem. Int. Ed.* **56**, 9034–9038 (2017).
12. T. T. Chen, M. Du, Z. Yang, J. Yuen-Zhou, W. Xiong, *Science* **378**, 790–794 (2022).
13. T. Fukushima, S. Yoshimitsu, K. Murakoshi, *Chem. Sci.* **14**, 11441–11446 (2023).
14. S. Kumar *et al.*, *J. Am. Chem. Soc.* **146**, 18999–19008 (2024).
15. T. Fukushima, S. Yoshimitsu, K. Murakoshi, *J. Am. Chem. Soc.* **144**, 12177–12183 (2022).
16. K. Sandeep *et al.*, *J. Phys. Chem. Lett.* **13**, 1209–1214 (2022).
17. K. Hirai, H. Ishikawa, T. Chervy, J. A. Hutchison, H. Uji-I, *Chem. Sci.* **12**, 11986–11994 (2021).
18. R. Houdré, R. P. Stanley, M. Ilegems, *Phys. Rev. A* **53**, 2711–2715 (1996).
19. G. Engelhardt, J. S. Cao, *Phys. Rev. B* **105**, 064205 (2022).
20. W. Liu, J. Chen, W. Dou, *J. Phys. Chem. C* **128**, 12544–12550 (2024).
21. G. Engelhardt, J. Cao, *Phys. Rev. Lett.* **130**, 213602 (2023).
22. J. B. Pérez-Sánchez, F. Mellini, N. C. Giebink, J. Yuen-Zhou, *Phys. Rev. Res.* **6**, 013222 (2024).
23. R. Duan, J. N. Mastron, Y. Song, K. J. Kubarych, *J. Phys. Chem. Lett.* **14**, 1046–1051 (2023).
24. A. Dutta *et al.*, *Nat. Commun.* **15**, 6600 (2024).
25. T. Liu, G. Yin, W. Xiong, *Chem. Sci.* **16**, 4676–4683 (2025).
26. W. C. Swope, H. C. Andersen, P. H. Berens, K. R. Wilson, *J. Chem. Phys.* **76**, 637–649 (1982).
27. D. M. Coles *et al.*, *Nat. Mater.* **13**, 712–719 (2014).
28. J. Cao, *J. Phys. Chem. Lett.* **13**, 10943–10951 (2022).
29. K. Kwak, J. Zheng, H. Cang, M. D. Fayer, *J. Phys. Chem. B* **110**, 19998–20013 (2006).
30. J. Zheng *et al.*, *Science* **309**, 1338–1343 (2005).
31. J. Pan, A. P. Charnay, W. Zheng, M. D. Fayer, *J. Am. Chem. Soc.* **146**, 35329–35338 (2024).
32. P. Hamm, M. Zanni, *Concepts and Methods of 2D Infrared Spectroscopy* (Cambridge Univ. Press, 2011).
33. M. Grechko, M. T. Zanni, *J. Chem. Phys.* **137**, 184202 (2012).
34. S. Woutersen, H. J. Bakker, *Nature* **402**, 507–509 (1999).
35. R. L. A. Timmer, H. J. Bakker, *J. Phys. Chem. A* **114**, 4148–4155 (2010).
36. A. B. Grafton *et al.*, *Nat. Commun.* **12**, 214 (2021).
37. G. Stemo *et al.*, *J. Phys. Chem. A* **128**, 1817–1824 (2024).
38. H. Mao, W. Xiong, *J. Chem. Phys.* **161**, 104201 (2024).
39. B. Xiang *et al.*, *Proc. Natl. Acad. Sci. U.S.A.* **115**, 4845–4850 (2018).
40. G. Khitrova, H. M. Gibbs, F. Jahnke, M. Kira, S. W. Koch, *Rev. Mod. Phys.* **71**, 1591–1639 (1999).
41. S. Woutersen, Y. Mu, G. Stock, P. Hamm, *Chem. Phys.* **266**, 137–147 (2001).
42. C. Yan, J. Nishida, R. Yuan, M. D. Fayer, *J. Am. Chem. Soc.* **138**, 9694–9703 (2016).
43. W. X. Ying, P. F. Huo, *Commun. Mater.* **5**, 110 (2024).
44. C. A. F. de Oliveira, D. Hamelberg, J. A. McCammon, *J. Chem. Phys.* **127**, 175105 (2007).
45. T. E. Li, J. E. Subotnik, A. Nitzan, *Proc. Natl. Acad. Sci. U.S.A.* **117**, 18324–18331 (2020).
46. T. E. Li, A. Nitzan, J. E. Subotnik, *Nat. Commun.* **13**, 4203 (2022).
47. K. Peng, E. Rabani, *J. Chem. Phys.* **161**, 154107 (2024).
48. X. Zhong *et al.*, *Angew. Chem. Int. Ed.* **55**, 6202–6206 (2016).
49. T. E. Li, S. Hammes-Schiffer, *J. Am. Chem. Soc.* **145**, 377–384 (2023).
50. G. Yin *et al.*, Overcoming energy disorder for cavity-enabled energy transfer in vibrational polaritons, Zenodo (2025). https://doi.org/10.5281/zenodo.15393090

ACKNOWLEDGMENTS

Funding: G.Y. and T.L. were supported by a Department of Defense Multidisciplinary University Research Initiative (DOD MURI) grant from the Air Force Office of Scientific Research (FA9550-22-1-0317). H.M. was supported by the National Science Foundation (CHE-2101988). L.Z. was supported by the National Science Foundation (DMR-1844514). T.S. was supported by the Office of Naval Research (N000142412262). W.X. acknowledges the generous support from the Brown Institute for Basic Science (award no. S643177). Awards FA9550-22-1-0317, CHE-2101988, N000142412262, and S643177 were awarded to W.X. **Author contributions:** W.X. conceived the original idea and supervised the overall research. G.Y., T.L., and W.X. designed the experiments. G.Y., T.L., and T.S. conducted experimental work. G.Y., T.L., and W.X. analyzed experimental data. H.M. wrote the initial version of the TMM code. T.L. and L.Z. performed theoretical work. This work used SDSC Expanse CPU at San Diego Supercomputer Center (SDSC) through allocation CHE240181 from the Advanced Cyberinfrastructure Coordination Ecosystem: Services and Support (ACCESS) program, which is supported by US National Science Foundation grants 2138259, 2138286, 2138307, 2137603, and 2138296. G.Y., T.L., L.Z., and W.X. interpreted and discussed the experimental and theoretical results and wrote the final manuscript. **Competing interests:** The authors declare no competing interests. **Data and materials availability:** All data needed to support the conclusions of the main text and supplementary materials are available on request. Data have been uploaded to Zenodo (*50*).

SUPPLEMENTARY MATERIALS

science.org/doi/10.1126/science.adx3137
Materials and Methods; Supplementary Text; Figs. S1 to S42; Tables S1 to S6; References (*51*–*78*); Movies S1 and S2

Submitted 10 March 2025; accepted 19 June 2025

10.1126/science.adx3137


CAREER
PLANNING

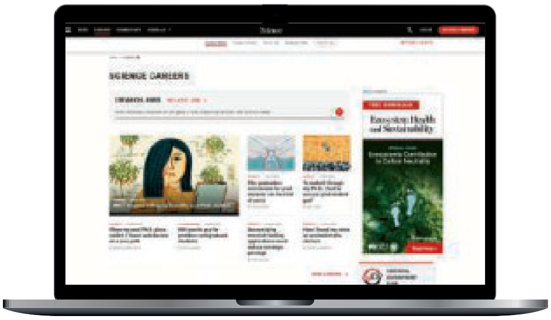

WORKING LIFE

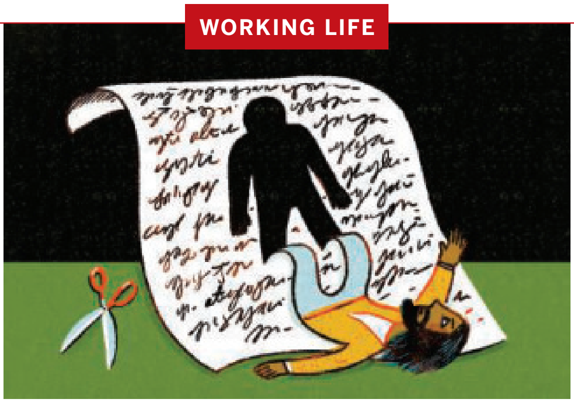

ILLUSTRATION: ROBERT NEUBECKER

Authorship, erased

Hari Ram C. R. Nair

The day the paper was published should have been a moment of pride. Instead, it felt like a quiet erasure. There it was: the data set I had helped shape, the computer scripts I had debugged and refined, the analytical framework I had spent months developing—all neatly embedded in a peer-reviewed journal article. But my name was absent. The feeling of exclusion was painful enough—but what stung more was that I had seen it coming, yet had felt powerless to stop it.

In 2020, during my doctoral studies at a major European university, a more senior Ph.D. student asked for help coding the analysis for his thesis. We had several in-depth discussions about the work, and he promised me co-authorship if the results were published. He even suggested the outcomes might fit into a chapter of my own dissertation, and that he would inform my supervisors once the work matured. I believed him.

Over the next year, I invested hours of focused effort into writing, modifying, and validating the scripts that underpinned the analysis. But crucially, the collaboration remained informal. Most conversations happened over voice calls. Any emails I sent went unacknowledged. There was no official record of our agreement or the work's scope. In hindsight, I now see that this lack of documentation was not an accident—it was deliberate.

A few years later, I learned the research was being prepared for publication. But my enthusiasm quickly turned to dismay when I realized the student I had helped—who was lead author on the paper—had no intention of including me as a co-author. When I spoke up, he claimed responsibility for coding the analysis, and said there was no written proof that I had worked on it.

One co-author acknowledged my contribution and attempted to intervene. My supervisor supported me, too. But the student still refused to include me. Eventually, I decided my efforts were better focused on my current work, and I gave up fighting.

My name was nowhere on the published paper—not even in the acknowledgments.

The betrayal had real consequences. Believing the work would lead to a joint publication, I had spent valuable time on it during my own thesis writing, delaying my Ph.D. by at least 6 months. Even worse was the emotional toll: frustration, helplessness, and a deep sense of injustice.

My story isn't unique. Authorship discussions too often rely on informal agreements, and many early-career scientists are unaware of standard authorship criteria. Even when research groups do have formal guidelines about who should be a named author, they're often not discussed until after a manuscript is already in draft, and students may be too hesitant to assert their rights in hierarchical lab cultures.

After my experience, my colleagues and I began to think about strategies to stop others being unjustly denied authorship. Eventually we came up with a set of procedures we now follow for every project in our lab to make sure all contributors receive fair recognition. We create a shared document outlining roles and authorship expectations right from the start, and agree on milestones when authorship will be further discussed, such as at key analysis phases or before manuscript drafting.

I also try to lead by example, discussing authorship openly with students and junior colleagues, and ensuring they receive the appropriate training in research ethics. I make sure they keep records of their contributions and read journals' authorship guidelines, and that they are aware of institutional support they can turn to if they encounter problems, such as research integrity offices or ombuds.

We've been trialing this new approach for a few months now, and the feedback from other lab members has been really positive. I'd encourage everyone to consider doing something similar. Authorship is more than a line on a CV—it is an ethical necessity. Every cleaned data set, debugged script, and refined figure deserves acknowledgment. And every early-career researcher deserves the confidence that their work will not just be used—but respected. □

Hari Ram C. R. Nair is a postdoctoral researcher at the Chalmers University of Technology.